Deutsches Zentrum
für Luft- und Raumfahrt
German Aerospace Center

Universität
zu Köln

Dynamic light scattering on macroscopic particles

Inaugural-Dissertation

zur

Erlangung des Doktorgrades

der Mathematisch-Naturwissenschaftlichen Fakultät
der Universität zu Köln

vorgelegt von

Lisa Künstler (geb. Dossow)

aus Rostock

Köln, 2023

Berichterstatter/in:	Prof. Dr. Matthias Sperl
(Gutachter/in)	Prof. Dr. Barbara Milow

Tag der mündlichen Prüfung: 05. Mai 2023

Abstract

Many of the assumptions, that form the basis of the methodology of dynamic light scattering (DLS), do not apply to particles whose radii exceed the wavelength of light by several orders of magnitude. In this thesis, the existing DLS concept is questioned in view of its applicability to macroscopic particles.

Since inhomogeneities and surface structures of macroscopic particles can be resolved by the wavelength of scattered light, the particle surface is considered as an additional, independent scattering object. Accordingly, the correlation function does not only decay due to motions of the macroscopic particles relative to one another, but also due to the motion of the surface's scattering entities. In DLS experiments with single, macroscopic spheres at least one full decay of the autocorrelation function can be observed. The existence of a second decay on smaller time scales is based on the complexity of the particle's surface structure. The late decay, which is attributed to the translation of the particle, is evaluated in terms of number fluctuation effects. Formulations for the analysis of the scattered light's detected intensity signal and for the description of the resulting autocorrelation function are presented.

The development of the decay on small time-scales, which can be traced back to the motion of the surface elements with respect to the particle's barycenter, is explained by a model developed within the scope of this work. Different scenarios regarding the particle's spin axis and varying parameters are discussed. The validity of the model is tested experimentally. From the knowledge gained, the translational and rotational granular temperature is estimated in a final exemplary experiment.

Kurzfassung

Viele Annahmen, die die Grundlage der Methodik der Dynamischen Lichtstreuung (DLS) formen, gelten nicht für Partikel, deren Teilchengröße die Wellenlänge des Lichts um mehrere Größenordnungen übersteigt. In dieser Arbeit wird auf das bestehende DLS Konzept eingegangen und bezüglich der Anwendbarkeit auf makroskopische Partikel hinterfragt.
Da Inhomogenitäten und Oberflächenstrukturen makroskopischer Teilchen mit der Wellenlänge von gestreutem Licht auflösbar sind, wird die Partikeloberfläche als zusätzliches, eigenständiges Streuobjekt betrachtet. Dementsprechend ist nicht nur ein Zerfall der Korrelationsfunktion durch Bewegungen der makroskopischen Teilchen relativ zu einander gegeben, sondern auch durch die Bewegung der Oberflächenstreuzentren.
In DLS Experimenten mit einzelnen, makroskopischen Kugeln kann mindestens ein vollständiger Zerfall der Autokorrelationsfunktion festgestellt werden. Die Existenz eines zweiten Zerfalls auf kleineren Zeitskalen basiert auf der Komplexität der Oberflächenstruktur des Partikels. Der späte Zerfall, welcher der Translation des Teilchens zugeordnet wird, wird im Rahmen von Anzahlfluktuationseffekten evaluiert. Formulierungen zur Analyse des detektierten Intensitätssignals des gestreuten Lichts, sowie zur Beschreibung der resultierenden Autokorrelationsfunktion, werden gezeigt. Die Entstehung des Zerfalls auf kleinen Zeitskalen, der sich auf die Bewegung der Oberflächenelemente bzgl. des Partikelschwerpunkts zurückführen lässt, wird mithilfe eines entwickelten Modells erläutert. Verschiedene Szenarien bzgl. der Rotationsachse des Teilchens und variierender Parameter werden diskutiert. Das Modell wird experimentell auf seine Gültigkeit überprüft. Aus den gewonnenen Erkenntnissen kann schlussendlich in einem finalen Beispielexperiment die granulare Translations- sowie Rotationstemperatur gewonnen werden.

Contents

1. Introduction

Granular media consist of a great number of randomly arranged solid macroscopic particles exhibiting different characteristics as varying shapes, colors or consistencies [1]. Common examples are coffee powder or beans, cereals, pills, sand or agglomerations of debris, e.g. Saturn's rings. In contrast to continuous media, granular media show characteristics of both, solids and fluids, depending on the degree of exposure to external forces such that, in particular, the transition between solid-like to liquid-like phases is of great interest for science and industry to study e.g. energy transfers [2].

A way to gain better understanding of the fluid state of granular media is to investigate the particles' motions within the flow. However, granular systems are generally opaque such that directly imaging the macroscopic grain motions within the bulk is difficult, if not even impossible since only the outer layer or surface may be observed. Thus, non-invasive optical methods, e.g. X-ray microtomography [3, 4], light scattering [5, 6] or magnetic resonance imaging [7, 8] are considered to characterize dynamic and structural properties within samples. The techniques above are able to resolve the motions on microscopic scales. Many experiments to measure the granular temperature with DLS or diffusing-wave spectroscopy (DWS), as extension of DLS to multiple-scattering problems, were performed on fluidized beds containing sand or glass particles [5, 9–14].

However, DLS was developed primarily for the investigation of soft matter, e.g. colloidal suspensions, emulsions or polymer solutions. The diameters of the comprised solid impurities measure approximately one wavelength of the incident radiation such that the suspended solids are still affine to thermal fluctuations, inducing Brownian motion [15, 16]. The approach for analyzing the intensity fluctuations caused by the

particles' Brownian motion was successfully tested numerous times [17–21]. Thus, scientists aimed for extending the concept to granular systems with grain sizes significantly larger than formerly considered in the theoretical assumptions, on which the methodology relies. However, when the theory was applied to granular gases, whose dynamics is particularly affected by gravitational and frictional effects, the consideration of purely Brownian motion is insufficient. Thus, incomplete interpretations regarding the results of DLS measurements on granular packings with respect to dynamic properties, e.g. collision lengths or the granular temperatures, may have occurred.

In this thesis, this gap in the theory shall be approached from a different perspective. If the established theory and all assumptions, made for particles of sizes comparable to the wavelength, may be reconsidered in view of macroscopic particles, a better understanding of the formation and time scales of the recorded autocorrelation functions from experiments probing granular media may be established. Due to their large diameters, macroscopic particles may be viewed as an agglomeration of numerous tiny scattering entities, where particular surface formations, asperities or inclusions of materials with different optical properties become resolvable. Thus, depending on the structure and its optical attributes, a single granular particle may yet be sufficiently complex to induce a full decay of a recorded auto-correlation function. In the past, scattering effects on the surface have been neglected and only the entire particle has been considered as scattering object. Therefore, this study focuses on DLS experiments on single macroscopic particles with diameters of the order of millimeters, where surface scattering will be particularly investigated.

But how does a single rigid granular scatterer, which is supposedly a discrete structure of scattering entities, particularly affect a DLS measurement? Is the recorded intensity signal evaluable such that the dynamics causing the decay of the auto-correlation function may be fully understood? Further, is the shape of the function's decay comparable to an exponential function if we expect a diffusive scattering particle? Is there only a single decay or is the problem more complex by providing more than one correlation function decay in a single measurement from a single macroscopic particle? If so, are further decays' shapes and decorrelation times dependent on the material of the particle? In addition, we expect the particle to perform different type of motions,

like translation and potentially rotation about its own barycenter. Thus, questions like "How do those motions in particular affect the correlation functions?" and "Is it possible to extract discrete velocities from those motions?" also arise. If the latter may be affirmed, an estimation of the respective granular temperature with the method of dynamic light scattering may be possible for a granular system in our laboratory setup.

In order to give satisfying answers to those questions, this thesis is structured as the following:

First, the fundamental principles of the granular temperature involving the definition of granular media (Chs. 2.1.1 and 2.1.2), light propagation as electromagnetic wave (Ch. 2.2.1), light scattering on spheres (cf. Ch. 2.2.2) and surfaces (cf. Ch. 2.2.3) as well as the method of dynamic light scattering (Ch. 2.3) will be recapitulated to give solid background knowledge for the experiments and their discussions. Further, the encountered difficulties in performing DLS on granular particles with the existing theory are summarized in Ch. 2.4.

In Ch. 3, considerations and thoughts about the geometry of experimental setup as well as the selection of specific optical components are presented. Additionally, a test with a colloidal suspension is performed to show the good functioning of the setup in sense of the classic DLS principle.

DLS experiments on single macroscopic spheres of selected soft and hard materials will be discussed in Ch. 4. The effect of the presence of only a single moving macroscopic particle in the observation volume is shown. Analytic formulations to describe the particle's translation within the in Ch. 3 presented setup will be given.

Ch. 5 provides a model to evaluate the effects of particle rotation. Particular correlation function expressions for distinct spin axis orientations within the setup geometry will be provided. The dependence of the autocorrelation function on specific parameters as the particle radius or rotational velocity will be discussed.

The concept from Ch. 5 is then tested experimentally in Ch. 6 via DLS measurements. The obtained results are validated with the particle image velocimetry (PIV) method.

Another application of the model will be provided in Ch. 7, where an idealized hourglass-like system is investigated and granular temperatures are determined.

The essential findings from all chapters will be summarized in Ch. 8, accompanied by a brief outlook.

References

[1] J. Duran and R. P. Behringer. "Sands, powders, and grains: An introduction to the physics of granular materials". In: *Physics Today* 54.4 (2001), pp. 63–64.

[2] J. Bridgwater. "Particle technology". In: *Chemical engineering science* 50.24 (1995), pp. 4081–4089.

[3] J. Cutress and R. Pulfer. "X-ray investigations of flowing powders". In: *Powder Technology* 1.4 (1967), pp. 213–220.

[4] S. G. Grantham and F. Forsberg. "Measurement of granular flow in a silo using Digital Speckle Radiography". In: *Powder technology* 146.1-2 (2004), pp. 56–65.

[5] D. Goldman and H. Swinney. "Signatures of Glass Formation in a Fluidized Bed of Hard Spheres". In: *Physical Review Letters* 96.14 (Apr. 2006). issn: 0031-9007. doi: 10.1103/PhysRevLett.96.145702.

[6] K. Kim, J. K. Moon, J. J. Park, H. K. Kim, and H. K. Pak. "Jamming transition in a highly dense granular system under vertical vibration". In: *Physical Review E* 72.1 (2005), p. 011302.

[7] E. Ehrichs, H. Jaeger, G. S. Karczmar, J. B. Knight, V. Y. Kuperman, and S. R. Nagel. "Granular convection observed by magnetic resonance imaging". In: *Science* 267.5204 (1995), pp. 1632–1634.

[8] C. R. Müller, J. F. Davidson, J. S. Dennis, P. Fennell, L. F. Gladden, A. N. Hayhurst, M. D. Mantle, A. Rees, and A. J. Sederman. "Real-time measurement of bubbling phenomena in a three-dimensional gas-fluidized bed using ultrafast magnetic resonance imaging". In: *Physical review letters* 96.15 (2006).

[9] M. J. Biggs, D. Glass, L. Xie, V. Zivkovic, A. Buts, and C. Kounders. "Granular temperature in a gas fluidized bed". In: *Granular Matter* 10.2 (2008), pp. 63–73.

[10] V. Zivkovic, M. Biggs, D. Glass, P. Pagliai, and A. Buts. "Particle dynamics in a dense vibrated fluidized bed as revealed by diffusing wave spectroscopy". In: *Powder Technology* 182.2 (Feb. 2008), pp. 192–201. ISSN: 00325910. DOI: 10.1016/j.powtec.2007.12.007.

[11] V. Zivkovic, M. Biggs, D. Glass, and L. Xie. "Particle dynamics and granular temperatures in dense fluidized beds as revealed by diffusing wave spectroscopy". In: *Advanced Powder Technology* 20.3 (2009), pp. 227–233.

[12] V. Zivkovic, K. Berry, D. Glass, and M. Biggs. "Determining key variables of the kinetic theory of granular flow using DWS". In: *AIP Conference Proceedings*. Vol. 1542. 1. American Institute of Physics. 2013, pp. 1266–1269.

[13] N. Menon and D. J. Durian. "Particle Motions in a Gas-Fluidized Bed of Sand". In: *Physical Review Letters* 79.18 (Nov. 1997), pp. 3407–3410. ISSN: 0031-9007. DOI: 10.1103/PhysRevLett.79.3407.

[14] L. Xie, M. J. Biggs, D. Glass, a. S. McLeod, S. U. Egelhaaf, and G. Petekidis. "Granular temperature distribution in a gas fluidized bed of hollow microparticles prior to onset of bubbling". In: *Europhysics Letters (EPL)* 74.2 (Apr. 2006), pp. 268–274. ISSN: 0295-5075. DOI: 10.1209/epl/i2005-10526-y.

[15] B. J. Berne and R. Pecora. *Dynamic light scattering: with applications to chemistry, biology, and physics*. Courier Corporation, 2000.

[16] L. Cipelletti, V. Trappe, and D. J. Pine. *Scattering techniques*. John Wiley & Sons, Inc.: New York, NY, USA, 2016.

[17] D. Chowdhury, C. M. Sorensen, T. Taylor, J. Merklin, and T. Lester. "Application of photon correlation spectroscopy to flowing Brownian motion systems". In: *Applied optics* 23.22 (1984), pp. 4149–4154.

[18] O. Robin and P. Paquin. "Evaluation of the particle size of fat globules in a milk model emulsion by photon correlation spectroscopy". In: *Journal of dairy science* 74.8 (1991), pp. 2440–2447.

[19] P. A. Hassan, S. Rana, and G. Verma. "Making sense of Brownian motion: colloid characterization by dynamic light scattering". In: *Langmuir* 31.1 (2015), pp. 3–12.

[20] K. Elamin and J. Swenson. "Brownian motion of single glycerol molecules in an aqueous solution as studied by dynamic light scattering". In: *Physical Review E* 91.3 (2015).

[21] D. Arzenšek, R. Podgornik, and D. Kuzman. "Dynamic light scattering and application to proteins in solutions". In: *Seminar, Department of Physics, University of Ljubljana*. 2010, pp. 1–18.

2. Fundamental principles and considerations

The question of how a granular system interacts with light and what may be learned from this process has been investigated in the last decades by several researchers [1–10]. However, the answer to this problem is not as straight forward as one might initially think. Concepts, which were successfully tested and applied to dynamic systems with particles of sizes comparable to the wavelength of light, e.g. colloids or emulsions [7, 11–14], do not work properly for light scattering on granular media. Many assumptions fail due to the greater spatial dimensions of the particles resulting in now resolvable surface structures and inner anomalies. A new methodology may help to solve the problem in understanding the physics of the actual situation of dynamic light scattering on granular systems.

The fundamental theories and applications implicated in this problem will be described in the following. After a brief introduction to granular media and the granular temperature, the interaction of light with matter will be elaborated. Along the way, the experimental method dynamic light scattering (DLS) for single-scattering problems and its extensional method diffusing-wave spectroscopy (DWS) for multiple-scattering situations will be introduced such that in the final subchapter we gain insight of the experimental and theoretical challenges of DLS/DWS on granular systems.

2.1. Temperature of granular media

Microscopically, temperatures provide an estimation of the systems average kinetic energy and thus, the molecules' velocities. The disordered dynamics of granular media however impede the estimation of a single temperature [15]. The concept of the granular temperature [16] was developed to find a statistical measure for the velocity distribution within a dynamic granular medium. While the temperature of a fluid or gas may be easily measured, probing the granular temperature is comparably difficult such that it has been subject to many studies in the past years [17–21].

In order to understand the fundamental nature of granular media, which will be investigated in light scattering experiments in later chapters (cf. Ch. 4, 6 and 7), a brief introduction will be provided in the subsequent section. This introduction will be followed by another section explaining the basic idea of the granular temperature, which motivates the studies in the final chapter (Ch. 7) of this thesis.

For the brief introduction to granular media and the granular temperature below, we follow Andreotti [15] as principal reference. Further references will be highlighted.

2.1.1. Granular media

Granular media may be defined as a system that is composed of a large number of discrete macroscopic particles surrounded by a gas or a liquid [22, 23]. Thus, granular media include a wide range of systems from fine powders consisting of particles of micrometre size, to piles of large rocks on Earth or in space. Sand grains and coffee beans as daily life examples for granular systems are shown in Fig. 2.1.

When considering granular media, we consider a system whose particles are not driven by thermal random motion. Particles smaller than $1\,\mu$m, e.g. molecules, suspended in a fluid undergo Brownian motion changing their position and orientation randomly with time [24]. In contrast, granular particles exceed diameters of $1\,\mu$m such that gravity and friction outrange the thermal random motion. Their dynamics are driven primarily by collisions, e.g. with other particles or confining physical boundaries as for example a container wall [15, 22, 25–29]. With the increased particle dimensions, respective to

(a) Heap of sand

(b) Coffee beans

Figure 2.1.: The two images show daily life examples of granular media. The left photo presents a heap of sand piling up. The photo on the right shows coffee beans falling from a cup onto resting coffee beans on a plate. [credits: Mirko Künstler]

sub-micron particles, the surficial and the internal structures of the particular particle, e.g. surface roughness and impurities, gain prominence. In particular, for optical methods such as direct imaging methods or indirect scattering methods, e.g. dynamic light scattering which will be used as method of investigation in the following chapters (cf. Chs. 4 to 7), those particle features have a significant impact on the recorded data [30].

Depending on local applied stress, granular media conduct as either an elastic solid or as a fluid [31]. In case of an elastic solid, the granular medium can create a very stable and strong supporting structure due to the particles being in close contact. If the particles start to lose contact due to external forces, induced by e.g. shearing or vibration, the system starts to flow as observed for example for avalanches. During the transition from one state to the other, the granular medium shows a combination of solid and fluid behavior. The particles in the material begin to move freely as individual particles as the speed of deformation increases. The transition from solid-like to fluid-like is used to study e.g. energy transfers in the system [32].

A dynamic granular system is modelled by the so-called rapid flow or granular gas [33]. The particles are modelled spheres of the same size. In a granular gas, the mean free

path of the particles is much larger than the typical particle size [34]. The mean free path describes the average distance over which a particle travels before changing its direction, e.g. due to inter-particle collisions. This model considers the particles to behave in a way that is somewhat analogous to a collection of molecules and has been therefore approached by extending the kinetic theory of dense gases. The kinetic theory of gases describes the thermodynamic behavior of gases whose atoms or molecules move in constant and fast random motions. The kinetic temperature of a gas is proportional to the mean kinetic energy of the molecules, which is directly linked to the magnitude of the molecules' speed by $T \sim v^2$.

Einstein [35] notes that the properties of a collection of suspended macroscopic particles are similar to those of suspended molecules. However, one must keep in mind that ordinary gases are generally systems in thermodynamic equilibrium. In thermodynamic equilibrium, macroscopic physical quantities do not depend on time [24]. An example for a granular system in equilibrium state is a resting pile of sand. The particles do not perform Brownian motion, but there is also no transfer of matter or energy among the particles. A driven sand volume, for example the falling sand grains in Fig. 2.1, however, is considered to be a system in non-equlibrium. The particles in a granular gas contain many degrees of freedom such that their dynamics are dominated by collisions causing a dissipative loss of energy. Thus, their dynamics are generally non-linear and irreversible [36]. Consequently, the kinetic temperature always dissipates when no external source of energy is compensating that loss. For example, shaking a box of coffee beans creates a motion that seemingly has a temperature. However, this motion will quickly stop when the shaking stops [18, 23].

The dynamics in such a non-equilibrium system of granular particles may be characterized by the granular temperature, which will be shortly introduced in the next section Ch. 2.1.2.

2.1.2. Granular temperature

The term kinetic temperature of a gas is only reasonably used if on average the kinetic energy is the same for each molecule in the gas (or each degree of freedom), such

that the equipartition of energy is respected. The equipartition theorem states that in thermal equilibrium, energy is shared equally among all degrees of freedom. The amount of energy hidden in the translational motion of a particle should therefore be equal to that in its rotational motion.

The flow behaviour of granular media is primarily affected by the random motion of the particles due to the energy loss during inter-particle collisions [37]. Thus, the dynamic evolution of granular gases is fundamentally different from molecular gases. Since granular media are therefore generally far from equilibrium, the statistical measure of the kinetic temperature becomes irrelevant here [26].

However, the random motion can be characterized by the so-called granular temperature, which is a measure of the random parts of the velocities of the grains in a fluidized granular system [18]. The granular temperature Θ was first formally defined by Ogawa [16, 38, 39]

$$\Theta = \langle (\vec{v_i} - \langle \vec{v_i} \rangle)^2 \rangle \quad i = 1\,,\,\ldots\,,\,N. \tag{2.1}$$

Eq. 2.1 states the mean squared deviation of the particle's velocity $\vec{v_i}$ with respect to the bulk's mean velocity $\langle \vec{v_i} \rangle$ of all N particles. Thus, the dimension of the granular temperature is a squared velocity. For the sake of simplification, the term enclosed in the angular brackets in Eq. 2.1 may here be rewritten as $\delta v^2 = (v - \langle v \rangle)^2$. Commonly, the granular temperature for a monodisperse system is formulated as [18, 40]

$$\Theta_d = \frac{1}{d} \langle \delta v^2 \rangle. \tag{2.2}$$

d denotes the spatial dimension and $\langle X \rangle$ is the average of the entity X such that in a monodisperse three-dimensional system, the granular temperature would read as $\Theta_{3D} = \frac{1}{3} \langle \delta v^2 \rangle$ [41].

The determination of the granular temperature of a granular gas in an experiment depends on the determinability of the velocity of the particles. According to Eq. 2.1, the velocity of each particle has to be measured independently such that the mean velocity and subsequently the velocity fluctuations may be determined. If one aims for identifying the granular temperature of an avalanche, theoretically, the velocity of each ice particle has to be measured.

2.2. Optics of granular matter

Optics is a major discipline that studies the propagation and properties of light. In electromagnetic field theory, light is described as a wave propagating through space. When light interacts with matter, secondary radiation is emitted which is called scattered light [42–44]. Within this thesis, data obtained from a technique, which is based on the scattering of light on particles, called dynamic light scattering (DLS), is used. This chapter provides an understanding of the inner workings of the method including the fundamental physical concepts of light scattering. Method limitations based on the existing theory for the interpretation in view of granular particles (cf. Ch. 2.1.1) will be highlighted.

In the sections below, the scattering process of electromagnetic waves, and in particular light, is first explained, followed by a brief description of the scattering on discrete particles, which is the basis for the established theory for DLS, cf. Ch. 2.3. A short introduction to the scattering on surfaces will be provided at the end of this chapter.

2.2.1. Scattering of electromagnetic fields

This chapter shall provide a brief overview on how an electromagnetic wave can be described and what characteristics may be deduced from that description by considering electromagnetic waves in vacuum. Afterwards, the interaction of electromagnetic waves with matter is summarized.

Electromagnetic waves in vacuum

In the classical field theory of electromagnetism, light is considered to be an electromagnetic (EM) wave that propagates through space and interacts with matter [44]. Before that interaction is further explained, the derivation of that wave form from the Maxwell equations in vacuum, and consequent characteristics of such a wave, are dedudced.

Following Bohren and Huffman [44] and Morin [45] throughout this section, the solution to the Maxwell equations in free space describes the propagation of electromagnetic

fields, in particular the electric field $\vec{E}$ and magnetic field $\vec{B}$, as waves. Assuming a charge- and current-free (ρ=0 and $\vec{j} = 0$, respectively) vacuum situation, the Maxwell equations are given as:

$$\nabla \cdot \vec{E} = 0 \tag{2.3}$$

$$\nabla \cdot \vec{B} = 0 \tag{2.4}$$

$$\nabla \times \vec{E} = -\frac{\partial \vec{B}}{\partial t} \tag{2.5}$$

$$\nabla \times \vec{B} = \epsilon_0 \mu_0 \frac{\partial \vec{E}}{\partial t}. \tag{2.6}$$

The constant ϵ_0 describes the permittivity in vacuum, μ_0 denotes the permeability in vacuum. The aim is to find a form of the equations, where the electric and magnetic fields are separated. This is achieved by using wave equations known as Helmholtz-equations

$$\frac{\partial^2 \vec{E}}{\partial t^2} = \frac{1}{\mu_0 \epsilon_0} \nabla^2 \vec{E} \tag{2.7}$$

$$\frac{\partial^2 \vec{B}}{\partial t^2} = \frac{1}{\mu_0 \epsilon_0} \nabla^2 \vec{B}. \tag{2.8}$$

The square root of the prefactor on the right-hand side of both equations determines the velocity of the wave in vacuum:

$$c = \sqrt{\frac{1}{\mu_0 \epsilon_0}} \approx 3 \cdot 10^8 \frac{m}{s}. \tag{2.9}$$

The solution to the Helmholtz equations are plane waves, as approximation for spherical waves in the far-field. This ansatz also satisfies the relations of the fields in the Maxwell equations. The plane waves solving the Maxwell equations are expressed as:

$$\vec{E} = \vec{E}_0 e^{i\phi} = \vec{E}_0 e^{i(\vec{k}\vec{r} - \omega t)} \tag{2.10}$$

$$\vec{B} = \vec{B}_0 e^{i\phi} = \vec{B}_0 e^{i(\vec{k}\vec{r} - \omega t)} \tag{2.11}$$

$\vec{E}_0$ and $\vec{B}_0$ describe the corresponding field's amplitude. Both are vectorial expres-

sions, which contain information about the field's polarization characteristics. The exponential term is called phase term, since it provides information about the phase $\phi = (\vec{k}\vec{r} - \omega t)$ of the field. The vector $\vec{r} = (x, y, z)$ defines the position, ω determines the angular frequency and t defines the time. The wave's frequency may be determined from the angular frequency by $\nu = \frac{\omega}{2\pi}$. The vector $\vec{k} = (k_x, k_y, k_z)$ denotes the wave vector, which describes the direction of propagation of the plane wave. Its magnitude is given by the wavenumber $|\vec{k}| = \frac{2\pi}{\lambda}$ including the wavelength λ.

EM radiation comprises a wide range of wave types classified by their wavelength or their frequency [46]

$$\nu = \frac{c}{\lambda}. \tag{2.12}$$

Only a small portion of the broad spectrum of EM waves is visible to the human eye. The spectrum range depicted in Fig. 2.2 comprises wavelengths of $\approx 10^2$ m to $\approx 10^{-13}$ m. The visible light spectrum, though, only ranges from approx. 350 nm (violet light) to approx. 750 nm (red light). Radiation with greater wavelengths is considered to be infrared light (up to millimeters), microwaves (millimeters to meters) or radio waves (meters and beyond). Shorter wavelengths, which are linked to a greater energy level, include ultra-violet radiation (wavelengths down to 10 nanometers), x-rays and gamma radiation (less than 1 nanometer).

The insertion of Eq. 2.10 into Eq. 2.7 gives $\omega^2 = \frac{|\vec{k}|^2}{\mu_0 \epsilon_0}$ and therefore by using Eq. 2.9:

$$\omega = c|\vec{k}| \tag{2.13}$$

Eq. 2.13 is called the dispersion relation in vacuum [46]. A point travelling in the direction of $\vec{k}$ has to move at a speed v, named the phase velocity, in order to remain at the same phase in the wave. In vacuum, the phase velocity equals the constant c, contrary to the wave propagation in matter, where the phase velocity depends on the material properties. Therefore, Eq. 2.13 states that EM waves in vacuum are dispersionless. The dispersion of EM waves in matter will be introduced further below.

We learn more about the relation between electric and magnetic fields in a plane wave by inserting the expressions for the plane waves (Eqs. 2.10 and 2.11) into the first two Maxwell equations, such that $\vec{k} \cdot \vec{E} = 0$ and $\vec{k} \cdot \vec{B} = 0$. Further, using Eqs. 2.10

and 2.11 in the third and fourth Maxwell equation, we receive $\vec{k} \times \vec{E}_0 = \omega \vec{B}_0$ and $\vec{k} \times \vec{B}_0 = \omega \vec{E}_0$. Those equations define the condition for the transversality of the plane waves describing that the electric and the magnetic field oscillate perpendicularly to each other and perpendicularly to the wave's propagation direction:

$$\vec{E} \perp \vec{B} \perp \vec{k}. \tag{2.14}$$

EM waves transport energy upon the object they are interacting with. The rate of the energy transport per area is defined by the Poynting vector [47]

$$\vec{S} = \frac{1}{\mu_0} \vec{E} \times \vec{B}. \tag{2.15}$$

The direction of the Poynting vector determines the direction of the propagation of the EM wave and thus also the direction of the energy transport. Due to the transversal nature of the wave, $|\vec{E} \times \vec{B}|$ is equal to E·B, such that the Poynting vectors absolute value is defined as

$$|\vec{S}| = S = \frac{1}{c\mu_0} E^2. \tag{2.16}$$

However, in practice, it is more convenient to quantify the mean energy transport per time. Therefore, we consider the mean, denoted here by $\langle ... \rangle$, of the Poynting vector's absolute value, which is also called the intensity I [46, 48]:

$$I = \langle S \rangle = \frac{1}{c\mu_0} E^2 = \epsilon_0 c E_0^2 \tag{2.17}$$

Eq. 2.17 shows that the intensity in vacuum is proportional to the squared magnitude of the electric field's amplitude. The light intensity is an important measure which will be the basis of dynamic light scattering measurements, see Ch. 2.3.

Interaction of electromagnetic waves and matter

A description of the interaction of light with a dielectric is provided by the Maxwell equations, which include information on the material's dielectric constant and perme-

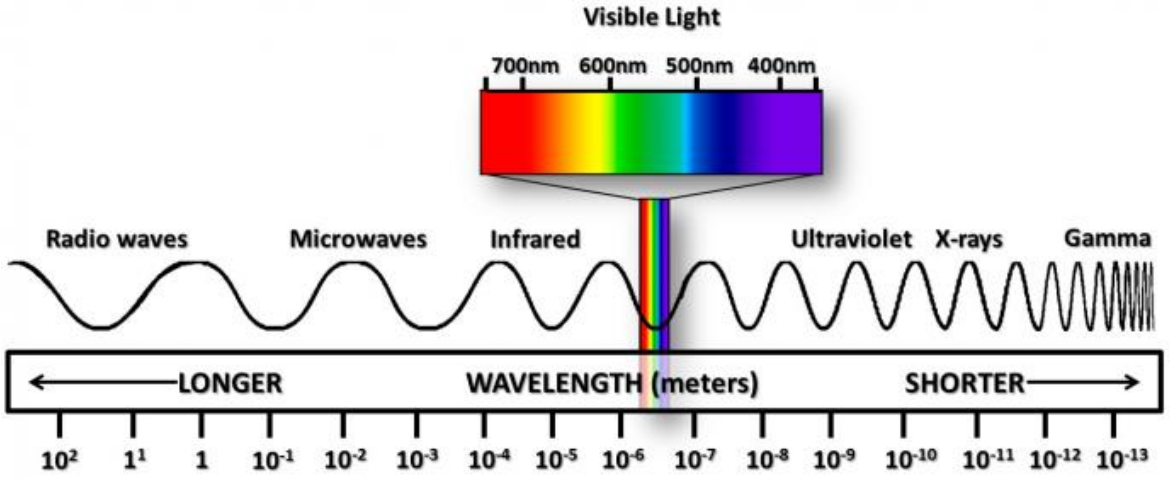

Figure 2.2.: Overview of the electromagnetic spectrum. The spectrum is classified by wavelengths ranging from 10^2 m (radio waves) to 10^{-13} m (gamma waves). The visible light spectrum is found at intermediate wavelengths of 750 nm (red light) to 350 nm (violet light). [49]

ability defined in the constitutive relations [44, 46]:

$$\vec{D} = \epsilon \cdot \vec{E} \qquad \vec{B} = \mu \cdot \vec{H} \tag{2.18}$$

The electric displacement $\vec{D}$ and the magnetic intensity $\vec{H}$ are related to $\vec{E}$ and $\vec{B}$ by the permittivity and the magnetic permeability $\mu = \mu_0\mu_r$. The permittivity or dielectric constant of a material comprises the electric polarizability of a dielectric $\epsilon = \epsilon_0\epsilon_r$ as combination of the electric permittivity in vacuum ϵ_0 and in the respective medium ϵ_r. The vectors $\vec{E}$ and $\vec{B}$ denote here the electric field strength and the magnetic flux density. The Maxwell equations in matter are then given as:

$$\vec{\nabla} \cdot \vec{D} = \rho \tag{2.19}$$

$$\vec{\nabla} \cdot \vec{B} = 0 \tag{2.20}$$

$$\vec{\nabla} \times \vec{E} = -\frac{\partial \vec{B}}{\partial t} \tag{2.21}$$

$$\vec{\nabla} \times \vec{H} = \vec{j} + \frac{\partial \vec{D}}{\partial t} \tag{2.22}$$

ρ and $\vec{j}$ represent, respectively, the electric charge density and the electric current density. The Maxwell equations above may be solved with the same logic as presented above. However, μ_0 and ϵ_0 in Eqs. 2.7 and 2.8 have to be replaced by the material-dependent expressions μ and ϵ, respectively.

When passing from one medium to another, a sudden change in μ and ϵ forms, microscopically, a discontinuity [44]. The subscripts 1 and 2 denote the respective media. The electromagnetic fields are however required to satisfy the Maxwell equations where both properties are continuous. Thus, the following boundary conditions must be fulfilled at the medium boundary [50]:

$$\hat{n} \times (\vec{E}_1(x) - \vec{E}_2(x)) = 0 \tag{2.23}$$
$$\hat{n} \times (\vec{H}_1(x) - \vec{H}_2(x)) = \vec{j} \tag{2.24}$$
$$\hat{n} \cdot (\epsilon\vec{E}_1(x) - \epsilon\vec{E}_2(x)) = \rho \tag{2.25}$$
$$\hat{n} \cdot (\epsilon\vec{H}_1(x) - \epsilon\vec{H}_2(x)) = 0 \tag{2.26}$$

such that the fields' tangential components are required to be continuous across the boundary. The variable x is thereby a location on the surface and $\hat{n}$ describes the normal vector on the surface. From that boundary condition, it follows as well that energy is conserved across that boundary.

Following the logic in the optics chapter of Halliday [46], the wave's phase velocity in matter v is given by

$$v = \frac{1}{\sqrt{\epsilon\mu}} = \frac{1}{\sqrt{\epsilon_0\epsilon_r\mu_0\mu_r}}. \tag{2.27}$$

The ratio of the phase velocity of the wave in the medium respective to the phase velocity in vacuum c is quantified by the refractive index η describing the retardation of the EM wave in a specific dielectric. With Eq. 2.27, η may be reformulated in terms of μ and ϵ:

$$\eta = \frac{c}{v} = \sqrt{\frac{\epsilon\mu}{\epsilon_0\mu_0}} \tag{2.28}$$

By using Eq. 2.28 in combination with the wave's frequency $\nu = \frac{v}{\lambda}$, we may write

$$\lambda = \frac{c}{\eta\nu}. \tag{2.29}$$

Consequently, the wavelength is indirectly proportional to the refractive index the wave is propagating through. η depends on the wavelength and thus on the frequency ν, such that $\eta = \eta(\nu)$, formulating the dispersion in matter. An EM wave passing through a material induces charge oscillations, which are slightly out of phase (delayed) with respect to the driving electromagnetic field. The oscillating charges reradiate a wave but with a phase delay such that the wave propagates slower. Thus, the wave has a reduced wavelength in the medium but the frequency remains the same. Consequently, the refractive index is not universal for all wavelengths of visible light. However, dispersion only occurs for polychromatic light, which contains a number of distinct wavelengths. In case of monochromatic light, though, there are no dispersion effects expected.

According to Berne and Pecora [1], everytime electromagnetic waves interact with a medium, the wave will undergo scattering. The scattering of EM waves is a process related to inhomogenities in the system the wave is passing through. Everything apart from vacuum comprises heterogenities and thus all matter will scatter EM waves. Matter is, in terms of light scattering, considered to consist of electric dipoles. Electric dipoles are objects with an asymmetrical distribution of charges, in particular with positive charge on one and negative charge on the other end. If those charges are exposed to an external electric field $\vec{E}$, the dipole starts to oscillate at the frequency of the incident light. The quantity determining the separation of charges within the dipole is the dipole moment

$$\vec{\mu} = \alpha \vec{E} \tag{2.30}$$

with α being the polarizability tensor. In case of spherical volumes, α is reduced to a scalar quantity since the induced dipole moment is always parallel to the applied electric field.

The dipoles re-radiate electromagnetic energy in form of waves with the same wavelength as the incident radiation [44]. The reradiated EM wave is then called the scattered wave. The scattering pattern is determined by the incident wave's phase and amplitude as well as by the dipole moment. For a point dipole, the light is scattered in all directions. An extended dipole, however, re-radiates with a symmetric intensity distribution having the maximum intensity along the direction of the dipole moment.

This direction is also called the forward scattering direction. The intensity decreases as the angle between the dipole moment and the scattering direction increases. The scattered light's strength depends on the external electric field $\vec{E}$ of the EM wave [1]. The scattering process is therefore a combination of an excitation and a re-radiation mechanism. If the light is incident on multiple charges, the total scattered electric field is then a superposition of all scattered fields of the accelerated charges.

The scattering process may be classified as elastic or inelastic, as described by e.g. Bohren and Huffman [44]. When the ideal case of elastic scattering is assumed, the wavelength of the scattered radiation equals that of the incident radiation. In contrast, scattering is considered to be inelastic, if the wavelength, and thus the transported energy, will have changed, e.g. due to absorption processes. Quasi-elastic scattering describes a modified version of the idealized elastic scattering, where the wavelength is still not impacted by the interaction with matter, but phase changes occur. For example, quasi-elastic scattering is assumed for the method of dynamic light scattering, which will be introduced in Ch. 2.3.

The scattering behavior of a medium may be analyzed if Eq. 2.10 for the incident wave as well as for the scattered wave is known. The aim is to identify the phase difference caused by the scattering event. If we assume quasi-elastic scattering, ω=const. such that the information contained in $\vec{k}$ is of interest. When light is scattered, a difference in the direction of propagation of the scattered light $\vec{k}_s$ towards the incoming light $\vec{k}_i$ is registered. This difference is described by the scattering vector

$$\vec{q} = \vec{k}_s - \vec{k}_i \tag{2.31}$$

with the wave number

$$|\vec{q}| = q = 2k\sin\left(\frac{\Theta}{2}\right) = \frac{4\pi}{\lambda}\sin\left(\frac{\Theta}{2}\right) \tag{2.32}$$

if both wave moduli are assumed to be equal ($|\vec{k}| = |\vec{k}_s| = |\vec{k}_i|$). Eq. 2.32 is called Bragg condition [1]. The scattering vector depends on the wavelength and the scattering angle Θ. Θ is described as the angle enclosed by the incident and scattered wave vector. q will change from 0 to 1 for angles from $\Theta = 0°$ to $\Theta = 180°$, respectively.

The angular distribution of the light, which is scattered by a particle, depends strongly on the particle's size, shape and the materials it is composed of [44]. There are two options to describe scattering of light on media: Either, the wave is scattered by a dipole, such that the theory of Rayleigh scattering may be applied (cf. Ch. 2.2.2.1), or the wave is interacting with continuous media, such that the scattering process may be explained with Mie theory (cf. Ch. 2.2.2.2). The principles of both theories will be briefly discussed in the following sections.

2.2.2. Scattering on particles

In this chapter, the focus lies on the influence of the scattering particle's size [43, 51]. First, the interaction of scatterers much smaller than or comparable to the wavelength of the incident radiation is briefly described within the theory of Rayleigh scattering and the Rayleigh-Gans-Debye approximation (Ch. 2.2.2.1), respectively. The interaction of the electromagnetic wave with continuous media will be shortly discussed within the frame of Mie theory (Ch. 2.2.2.2). The fundamental principles of geometrical optics as an approach for scattering on large particles will be introduced in the final section Ch. 2.2.2.3.

2.2.2.1. Scattering on small particles

This chapter is oriented on the work of Egelhaaf [7]. We assume quasi-elastic scattering such that the scattering process can be described by the phase difference between the incident light and the scattered light. The incident light is assumed to be a plane wave of the form of Eq. 2.10. Possible scattering effects of the surrounding fluid are neglected.

Volume elements

The scattering behavior of particles with a very small radius compared to the wavelength of the incident light ($r \ll \lambda$), referred here to as point-like volume elements, shall be briefly discussed. Due to the small radii, the particles are comparable to a dipole (cf. Ch. 2.2.1) and thus re-radiate light in all directions [7].

The scattered electric field $\mathrm{d}\vec{E}(\vec{r},t)$ of a very small volume element $\mathrm{dV}(\vec{r})$, at a position $\vec{r}$ respective to an electric field at the origin, e.g. the detector (in the far-field) as depicted in Fig. 2.3, is according to Egelhaaf defined as

$$d\vec{E}(\vec{r},t) = \vec{E}_0\rho(\vec{r})\frac{1}{s}e^{-i(k_s s-\omega t+\Delta\phi)}dV \tag{2.33}$$

with $\rho(\vec{r})$ giving the material-dependent scattering length density, or also scattering ability, of the volume element and s describing the distance of dV to the origin. The variable k_s describes the magnitude of the scattered wave vector. The term $e^{i\Delta\phi}$ contains information about the phase difference caused by the scattering process.

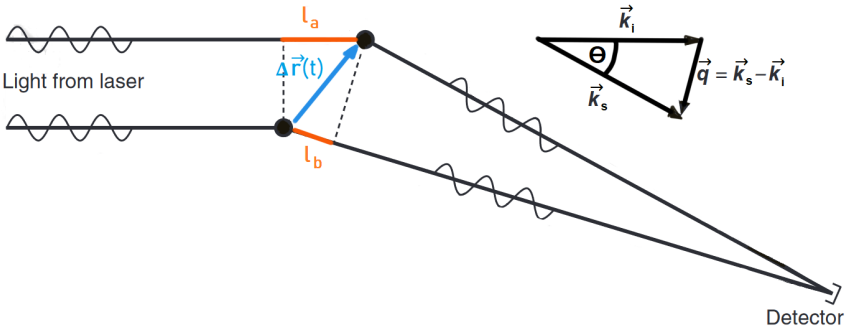

Figure 2.3.: Schematic drawing of light being scattered on a volume element at two distinct time points. The volume element travelled a distance $\Delta\vec{r}(t)$ within a specific time t. The light incidents from the left with the wave vector $\vec{k}_i$. The scattered light that is registered by a detector in the far-field is represented by the wave vector $\vec{k}_s$. The scattering angle Θ is enclosed by the respective incident and scattered wave vectors. The resulting scattering vector is represented by $\vec{q}$. The additional path segments the light has to travel to reach the volume elements after it moved is denoted by l_a. The additional path length of the scattered light between both states is respectively named l_b. The thereby caused phase shifts are indicated by the wavelets superposing the corresponding wave vectors. (modified from [8])

Fig. 2.3 shows a volume element dV (black dot) at a position $\vec{r}$, respective to a reference point (detector), that has moved a particular distance $\Delta\vec{r}(t)$ within time t. The change of location is indicated by the blue arrow. Light is incident from the left side with a specific phase indicated by the wavelets travelling towards the element. The incident

light's wave vector is denoted by $\vec{k_i}$. The light is scattered, when interacting with the volume element, such that the scattered light propagates under a scattering angle Θ and with wave vector $\vec{k_s}$ towards the detector. In order to reach the volume element at its later position, the incident light has to travel an additional distance l_a, indicated in orange, respective to travelling to the volume element's initial location. Further, the scattered light has then to travel an extra distance l_b to reach the detector. This significant path length difference ΔL provokes a relative phase difference between both scattered waves observed at the detector. The phase difference $\Delta\phi$ is then the sum of the projections of $\vec{r}(t)$ on $\vec{k_i}$ and $\vec{k_s}$:

$$\Delta\phi = \frac{2\pi}{\lambda}\Delta L(t) = \vec{k_i}\cdot\vec{r} - \vec{k_s}\cdot\vec{r} \tag{2.34}$$

$$= (\vec{k_i} - \vec{k_s})\cdot\vec{r} \tag{2.35}$$

$$= -\vec{q}\cdot\vec{r} \tag{2.36}$$

As consequence of quasi-elastic scattering, the scattered electric field of the volume element independent of experimental setup dependencies is expressed by [7]:

$$d\vec{E}(\vec{q},t) \sim \rho(\vec{r})e^{-i\vec{q}\vec{r}}dV \tag{2.37}$$

depending on the volume elements position in space and its scattering length density as well as on the scattering vector, such that the scattering angle Θ and the wavelength of the light are essential. The scattering vector $\vec{q}$ defines positions $\vec{r}$ with an identical phase factor. Since we only consider a single volume element here, the scattering length of the entire volume element is $\rho(\vec{r})\,dV$.

Extended particles

In order to extend the applicability of the Rayleigh scattering to particles that are relatively small, but can be larger than considered within the Rayleigh scattering limits, and of arbitrary shape, the Rayleigh-Gans-Debye approximation (RGD) was developed [44]. The RGD approximation is an approximate solution for light scattering problems. This theory is valid, if the refractive index η of the scatterer is almost equal to the refractive index of the surrounding environment such that $m = \frac{\eta_i}{\eta_o} \approxeq 1$. Additionally,

the scatterer's characteristic linear dimension d must be sufficiently small compared to the wavelength λ such that

$$\begin{aligned} |m-1| &\ll 1 \\ \frac{2\pi}{\lambda} d|m-1| &\ll 1. \end{aligned} \tag{2.38}$$

The "heuristic" consequences of Eq. 2.38, according to Bohren and Huffman [44], are on one hand that the incident wave is not notably reflected at the medium boundary. On the other hand, there will be no significant change in the phase or amplitude of the incident wave, when entering the particle. The latter may also be rephrased in terms of the first order Born approximation, such that the incident wave will (almost) not be distorted by interacting with the particle. This way, the particle may be considered "optically soft" and the approximation is applicable to irregular shaped particles. For example, the DLS theory designed for diluted samples with small particles like colloids relies on the principles of the RGD approximation [7, 44].

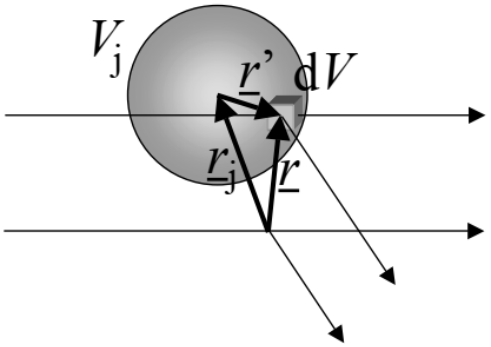

Figure 2.4.: A volume element's dV position within an extended particle V_j. The positional vector $\vec{r}$ is decomposed into the positional vectors of the center of mass $\vec{r}_j$ and the distance between the particle's center and the volume element $\vec{r}'$. Note: The vectors in the figure above are indicated by lines below the name of the property. To be consistent with the nomenclature in this thesis, the vectors will be specified throughout the text by arrows above the property. [7]

RGD assumes that each segment of each scattering particle "sees" (nearly) the same incident wave. Following Egelhaaf [7] further, such an extended particle describes an

entity of many volume elements dV($\vec{r}$), which here possess a dependence on the location within the extended particle. Consequently, the path lengths of the incident and the scattered light differ for each scattering volume element respective to the other volume elements. Therefore the light's phases, see Eq. 2.36, also differ.

Again, the total electric field received (in the far-field) by the observer is a superposition of all scattered electric fields. Therefore, we may determine the total scattered electric field by summing up all contributions of the scattered electric fields $\vec{E}_j(\vec{q},t)$ of the individual volume elements j. The relative positions of the elements within a rigid particle V_j, cf. Fig. 2.4, is given by:

$$\vec{r}(t) = \vec{r}_j(t) - \vec{r}\,' \tag{2.39}$$

The vector $\vec{r}_j$ represents the location of a reference point. The particle's center of mass is a typical choice [7]. $\vec{r}\,'$ defines the position of the volume element respective to the particle's center of mass. A complex internal and superficial particle structure, which gains prominence with increasing particle radius, leads therefore to other scattering scenarios than it applies to a very small and homogeneous particle. Irregular particle shapes supposedly further enhance this effect. If all scattered electric fields are added together to express the total scattered field, we obtain by using Eq. 2.39:

$$\vec{E}_j(\vec{q},t) = \int_{V_j} d\vec{E}(\vec{q},t) \sim \int_{V_j} \rho(\vec{r}\,') e^{-i\vec{q}\vec{r}(t)} dV \tag{2.40}$$

$$= e^{-i\vec{q}\vec{r}_j(t)} \int_{V_j} \rho(\vec{r}\,') e^{-i\vec{q}\vec{r}\,'(t)} dV = b_j(\vec{q}) e^{-i\vec{q}\vec{r}_j\,'(t)} \tag{2.41}$$

The integral term may be abbreviated as $b_j(\vec{q})$ since it represents a single extended particle's contribution as Fourier transform of $\rho(\vec{r}\,')$ [7]. $b_j(\vec{q})$ describes the mass distribution within the particle and thereby, its position should not affect the result. The scattered electric field of an extended particle V_j may then be according to Egelhaaf expressed as:

$$\vec{E}_j(\vec{q},t) \sim b_j(\vec{q}) e^{-i\vec{q}\vec{r}_j(t)} \tag{2.42}$$

This equation is very similar to the equation for a single volume element (cf. Eq. 2.37). In case of an extended particle though, the scattering length is $\vec{q}$-dependent.

Ensemble of particles

If light scattering on a particle ensemble is to be investigated, the approach is very similar to the approach above, where we added up several scattering volumes to one big particle ($r \cong \lambda$). Several big particles are added up to an ensemble of big particles, where, thereby, the sum of the contributions of the particles as well as their scattering volumes have to be considered.

If we apply the same logic as before and take the sum of discrete contributions of all N particles into account before calculating the integral, we gain

$$\vec{E}(\vec{q},t) = \sum_{j=1}^{N} \vec{E}_j(\vec{q},t) \sim \sum_{j=1}^{N} b_j(\vec{q}) e^{-i\vec{q}\vec{r}_j(t)} \tag{2.43}$$

$$= \sum_{j=1}^{N} \left(\int_{V_j} \rho(\vec{r}\,') e^{-i\vec{q}\vec{r}\,'} dV \right) e^{-i\vec{q}\vec{r}_j(t)}. \tag{2.44}$$

This equation is again similar to Eqs. 2.37 and 2.41. The amplitude term $b_j(\vec{q})$ stays mathematically the same, however, the contribution of each particle has now to be summed as well. The phase term is again expressed by $e^{-i\vec{q}\vec{r}_j(t)}$.

As mentioned above, the theory behind the dynamic light scattering method presented in Ch. 2.3 relies on RGD. In view of DLS experiments on granular media, which exhibit grain sizes of the order of several micrometers or more, the validity and in particular the upper bound of RGB respective to the particle diameter is of great interest. We consider Eq. 2.38. For glass particles ($\eta_{\text{glass}} \approx 1.5$) surrounded by air ($\eta_{\text{air}} \approx 1.0$), we receive $|1.5 - 1| = 0.5$. Thus, Eq. 2.38 reduces to

$$\frac{\pi}{\lambda} d \ll 1.$$

According to the equation above, the particle's diameter has to be of an order of less

than $\frac{\lambda}{\pi}$. If light with $\lambda = 532\,\text{nm}$ illuminates the glass sphere, the particle diameter should not exceed magnitudes of approx. $\frac{5}{\pi} \cdot 10^{-7}\,\text{m}$ for RGD to be valid. Consequently, granular particles with diameters of several microns or even millimeters would clearly not be suitable for the applicability of this theory. So in general, this principle breaks down as soon as the particles obtain diameters, which are of the order of the incident light. Then, the particle interior gains significance, whose optical structure may differ significantly from that of the particle's surrounding [1].

2.2.2.2. Mie theory

The Mie theory [52] is the generalized solution of the scattering of an EM wave by homogeneous, spherical particles. The theory provides a definite solution to the Maxwell's equations for the multipole radiation caused by the electric polarization of the molecules in the scattering particles, when an electromagnetic wave is interacting with it. The scattered field is represented as an infinite series of the multipole radiation. Mie theory includes all possible ratios of the particle radius to the wavelength of the incident light. Thus, Mie scattering permits computations for spherical scatterering objects a few orders of magnitude larger than the incident wavelength [53, 54].

According to van de Hulst [42], the most notable outcome of the complexity of the series of multipoles are the Mie resonances, which characterize particles sizes that scatter the light particularly weakly or strongly and allow, thus, a classification of scattering regimes. The Mie resonances are visualized in Fig. 2.5. Mie resonances notably occur primarily for spheres with a radius of $r \approx \lambda$ (shaded red). For $r \ll \lambda$ (shaded green), the resonances become negligible. With growing particle diameter ($r \gg \lambda$), the amplitudes of the Mie resonances fade out and saturate eventually at a constant value of ≈ 1 (blue shaded region).

A measure to classify those regimes is the scattering parameter

$$x = \frac{2\pi r}{\lambda}. \tag{2.45}$$

as it may be found in commonly consulted field-related literature as e.g. Bohren and Huffman [44] or Born and Wolf [48], which were also here consulted for the following

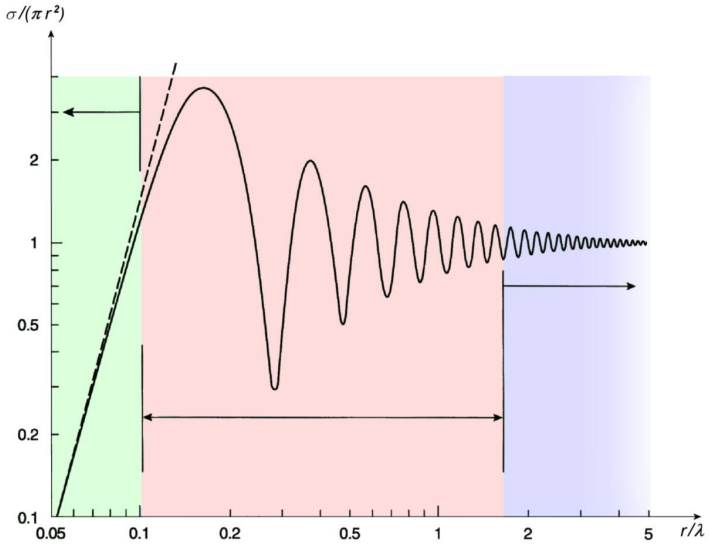

Figure 2.5.: The relative scattering cross-section $\sigma_{\text{rel}} = \frac{\sigma}{\pi r^2}$ in dependence of the particle radius r normalized by the wavelength λ. The effects of the multipole series of Mie theory may be classified into three categories: Rayleigh scattering (green), Mie Scattering including the Mie resonances (red) merging into the geometrical optics regime (blue) for large radii. [55]

theory. The scattered wave is a sum of partial waves whose amplitudes are defined by scattering coefficients. The scattering coefficients are determined by the refractive index of the homogeneous object and the scattering parameter. Therefore, the scattering parameter gives a rough idea of the relation between the particle circumference and the wavelength of the light wave. In particular, the scattering ability is determined by the relative scattering cross-section σ_{rel}. The total scattering cross-section σ describes how much of the incident energy flux density is extinguished due to scattering and absorption by the particle. σ is weighted by the particle's geometric cross-section such that the relative scattering cross section representing the ordinate in Fig. 2.5, is defined as

$$\sigma_{rel} = \frac{\sigma}{\pi r^2}. \tag{2.46}$$

The values on the abscissa in Fig. 2.5 give the size ratio of the particle diameter to the light's wavelength. The size ratio as well as the refractive index η of the particle determine the spatial distribution of the scattered light.

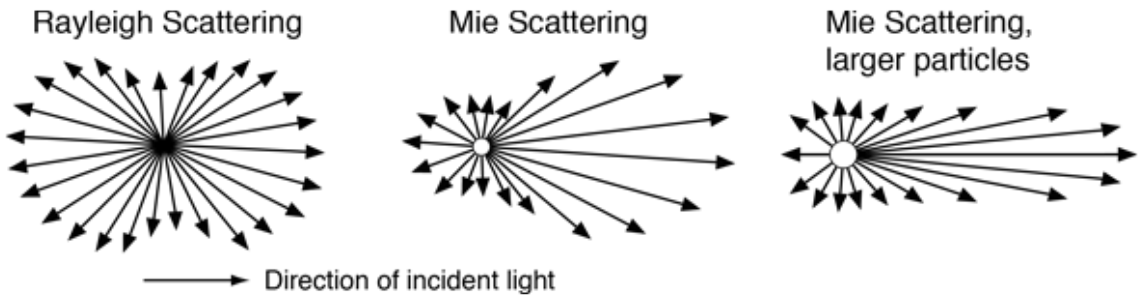

Figure 2.6.: The distribution of the scattered light in dependence of the particle size. The light incidents from the left. The black arrows depict the travelling direction of the scattered light. With increasing particle radius, the preference of scattering in the forward direction increases. On the left, Rayleigh scattering for particle sizes much smaller than the wavelength is shown. In the middle, Mie scattering of a particle with a diameter comparable to the wavelength of the radiation shows a respectively higher portion of scattered light in the forward direction. Mie scattering with strong forward scattering for larger particles is presented on the right side. [56]

There is a preference of radiation scattering in the forward direction that arises as well with increasing particle radius, as depicted in Fig. 2.6. The forward direction is defined as the propagation direction of the incident light [44]. The effect determines the spatial scattering intensity with an angular dependence of observation. For Rayleigh scatterers ($x \ll 1$), the intensity of the scattered light will be nearly the same for all directions due to the dominant dipole terms in the multipole equations, whereas for increasing particle sizes ($x \approx 1$) the geometry of the scattering pattern will be more rather intricatly shaped due to the higher order multipoles involved. The magnitude of the observed intensity depends highly the angle of observation. Though, for very large scatterers ($x \gg 1$), the extent of forward scattering is that great, that almost all light is scattered in the forward direction. This constitutes the basis of the concept of geometrical optics where the light is assumed to travel along a specific direction as a light ray. The definition of a ray will be given in Ch. 2.2.2.3. Since the Mie resonances for scatterers orders of magnitudes greater than the incident light's wavelength approach a finite value, it may be assumed that in those scenarios, the light will be scattered in a single direction with a specific intensity. If we consider a particle with a radius of 1 mm as a great Mie-scatterer respective to the wavelength of green light, as it is often used in DLS

experiments (cf. Ch. 2.3), the ratio of radius to wavelength is $\frac{r}{\lambda} = \frac{10^{-3}}{5 \cdot 10^{-7}}\,\mathrm{m} = 2 \cdot 10^{3}\,\mathrm{m}$, which exceeds the displayed scale in Fig. 2.5 by orders of magnitude. Thus, such a Mie-scatterer is expected to scatter strongly in the forward direction only.

Mie theory would provide a complete solution to problems regarding such large particle dimensions as obtained by granular particles. However, assuming a particle with a diameter of 1 mm, the number of terms in the series expansion would exceed about 12 000 terms [44]. Those calculations would clearly take a tremendous amount of patience. Apart from the massive extent of terms for the calculation, this theory is still bound to the assumption of perfectly spherical scatterers. In case of naturally occurring granular matter, however, the particles' shapes will deviate more or less from a sphere. Thus, the application of Mie theory to the scattering of granular particles is rather problematic. However, for particles much larger than the wavelength, the Mie theory merges into the limit of geometric optics, which comprises reflection and refraction solved by ray-tracing. Geometric optics will be introduced in the next section. The boundary conditions on the sphere's surface become less relevant or converge due to the lack of curvature into the problem of scattering on surfaces, which will be further discussed in Ch. 2.2.3.

2.2.2.3. Geometrical optics

In situations, where the object's dimensions are much larger than the wavelength of light ($r \gg \lambda$), geometrical optics, also stationary phase optics [57], is an excellent approach. Geometrical optics assumes that the light's propagation paths may be approximated as rays ($\lambda \to 0$) [48]. A ray models the vector, which is perpendicular to the plane wave and is therefore pointing in the direction of energy flow [58]. The ray's diameter w is considered much larger than the wavelength ($w > \lambda$) of the incident radiation, such that variations on the length scales of λ in the field's amplitude at the rays's margin are minute compared to the magnitude of the amplitude itself. Further, the ray's width is considered to be much smaller than the particle's radius ($r \gg w$). The physics of light reflection, refraction and scattering are in general sufficiently described as for wave optics, however, geometrical optics does not account for the effects of diffraction or interference [48].

The principle of geometrical optics is consolidated by four axioms [58]: First, rays propagate directly in an homogeneous medium obeying Fermat's principle. Secondly, at the boundary of two homogeneous and isotropic media, the light is reflected or refracted as stated in Snell's law, which will be further described below. Thirdly, the path of light is invertible, meaning that every ray also obeys the same laws of physics as its direction of travel is reversed. Lastly, when light rays cross each other's path, no deflection is caused.

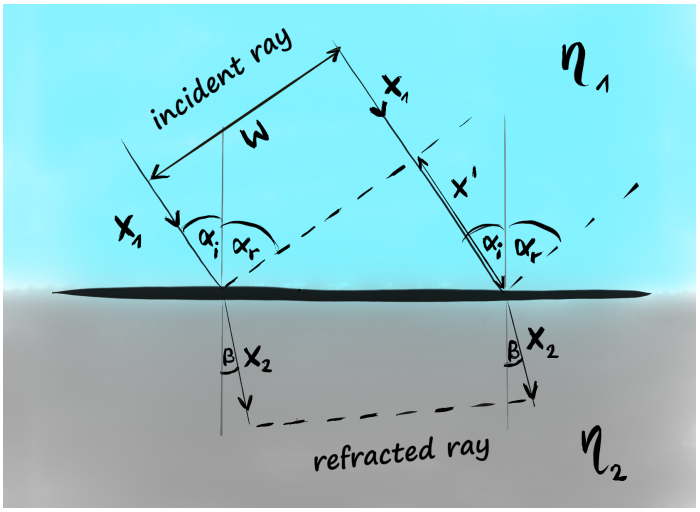

Figure 2.7.: A schematic sketch of Snell's law. The incoming ray of width w incidents on the media boundary with a velocity v_1 in the medium of refractive index η_1 at an incident angle of α_i after travelling a distance x_1. The reflection angle is denoted as α_r. The distance x' describes the geometrical offset distance of the ray's right boundary that is caused due to the inclined ray's normal respective to the surface normal of the boundary. The respective properties for the refracted ray are denoted by the subscript 2. The refracted ray will be deflected towards the surface normal by an angle β.

For now, we are only interested in transparent media, in order to neglect significant absorption processes. If a beam of light propagates from one medium to another, for example from air to water, two phenomena are observed. First, the beam is reflected. Second, the beam is partially transmitted through the medium and is partially reflected.

According to the law of reflection [48]

$$\sin(\alpha_i) = \sin(\alpha_r) \tag{2.47}$$

the light's angle of incidence α_i equals the angle of the reflected ray α_r respective to the surface normal, as shown in Fig. 2.7. The incident beam is described by its angle respective to the axis of incidence or the surface normal. In the extreme case of the incident beam aligning with the surface normal such that $\alpha_i = \alpha_r = 0°$, the beam will be reflected back at itself. If $\alpha_i = \alpha_r = 90°$, the beam will only slightly touch upon the surface and travel parallel to the surface boundary.

Optical refraction of light occurs, when light passes from one material to another. Consequently, two phenomena are observed: The propagation speed v of the beam but also its propagation direction will change. We consider a surface boundary between medium 1 and medium 2 in which a light ray of width w propagates with the velocities $\mathrm{v}_1 = \frac{x_1}{t_1}$ and $\mathrm{v}_2 = \frac{x_2}{t_2}$. x_1, x_2 are the travelled distances and t_1, t_2 denote the travelling times, respectively, in each medium. x' is the additional distance the ray's boundary further to the right (cf. Fig. 2.7) has to travel before reaching the surface boundary. The ratio between the refractive indices η_1 and η_2 will give the degree of alteration of the propagation direction. If $\eta_1 < \eta_2$, such that the light travels from an optically thinner medium into an optically thicker medium, the transmitted ray will be refracted towards the normal and $\beta < \alpha_i$. In the opposite case ($\eta_1 > \eta_2$), the ray will be deflected respective to the normal. By using common trigonometric functions, we find

$$\sin(\alpha_i) = \frac{x'}{d} = \frac{v_1 t'}{d} \qquad \sin(\beta) = \frac{x_2}{d} = \frac{v_2 t_2}{d} \tag{2.48}$$

with d being the distance between two ray points meeting the material boundary. Further, $t' = t_2$ because the two points travel to x_2 and x' in the same amount of time, respectively. The change of propagation direction as the consequence of the change of the phase velocity is described by Snell's law [48]:

$$\frac{\eta_1}{\eta_2} = \frac{\sin(\alpha_i)}{\sin(\beta)} = \frac{v_1}{v_2}. \tag{2.49}$$

In the general case of reflection, the incident angle is equal to the reflected angle $\alpha_i = \alpha_r$, because $v_1 = v_2$ and $\eta_1 = \eta_2$. In the special case of total reflection, the medium that the ray is leaving has a greater refractive index than the medium, that the ray is entering, such that $\eta_1 > \eta_2$. In addition, the incidence angle α_i is sufficiently

large, such that the following condition is fulfilled: $\sin(\beta) = \frac{\eta_1}{\eta_2}\sin(\alpha_i) > 1$. The light will then be fully reflected at the medium boundary [46]. The principle of total internal reflection is for example used in fiber optics, which deals with the transmission of light along fibers made of plastic or glass, which is very useful in the usage of endoscopes.

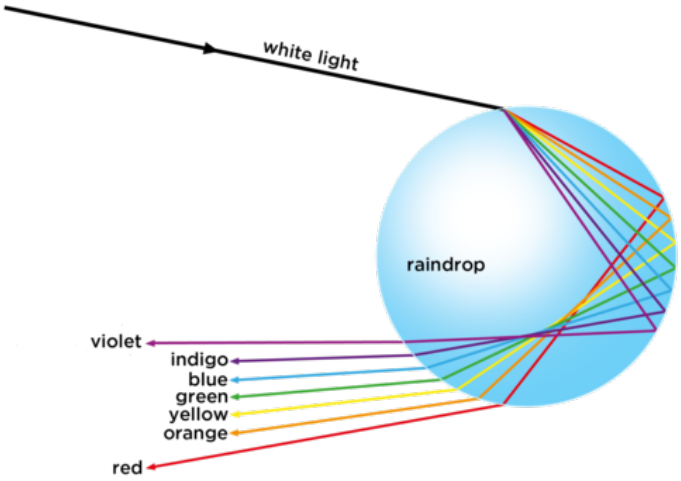

Figure 2.8.: A schematic sketch of the light propagating within a raindrop in the atmosphere generating a rainbow for a perceiver on the ground. The polychromatic light radiated from the sun enters the droplet from the left side. The light will then be diffracted into its spectral colors after being partially refracted at the media boundary. The light will then be internally reflected (and refracted) twice before leaving the droplet. The spectral colors, ranging from violet to red, may then be perceived by an observer on the ground. [59]

The rainbow is an excellent example on which the concept of geometrical optics may be briefly applied to macroscopic particles. Water droplets in the air of millimeter sizes and approximated as spheres, are illuminated by sun light, see Fig. 2.8. When the polychromatic light reaches the air-water boundary, the light will be partially refracted and partially reflected in accordance with Snell's law, cf. Fig. 2.7 and Eq. 2.49. The effect of dispersion causes the refracted light to be separated into its spectral colors ranging from red (greatest wavelength) to violet (shortest wavelength). According to Eq. 2.29, the violet light will be scattered the strongest and the red light the weakest. At the backside of the droplet at the water-air boundary, that light will be again partially refracted and partially reflected. The reflected portion will further propagate

through the droplet reaching another water-air boundary where another reflection and refraction of the light takes place. The portion of light, which leaves the rain droplet after being internally reflected twice, is the light an observer on the ground perceives as rainbow. That rainbow, is however only the rainbow of first order with the highest perceived intensity. Light, which has be internally reflected more than two times when leaving the droplet results in higher order rainbows [46].

2.2.3. Scattering on surfaces

The surface is here defined as homogeneous boundary between two isotropic materials and therefore as boundary between two layers of distinguished refractive indices. Surface scattering is described as the scattering process happening only at that boundary and not further within the second medium, as volume scattering does [57]. Generally in nature, both processes occur simultaneouly, however, one of them is dominant. For example, when observing bare soil, which may be assumed to be a homogeneous body, surface scattering dominates.

Similar to scattering on discrete particles, the scattering of light on surfaces may be also described by solving the Maxwell equations (Eqs. 2.19 to 2.22). We consider a plane wave to be incident on a rough surface. As already noted in Ch. 2.2.1, the EM fields should satisfy the boundary conditions, i.e. continuity conditions, when crossing a boundary [50]:

$$\hat{n} \times (\vec{E}_1 - \vec{E}_2) = 0 \tag{2.50}$$

$$\hat{n} \times (\vec{H}_1 - \vec{H}_2) = \vec{j}_s \tag{2.51}$$

$$\hat{n} \cdot (\epsilon\vec{E}_1 - \epsilon\vec{E}_2) = \rho_s \tag{2.52}$$

$$\hat{n} \cdot (\epsilon\vec{H}_1 - \epsilon\vec{H}_2) = 0 \tag{2.53}$$

j_s denotes the electric surface current density and ρ_s the surface charge density, respectively. The vector $\hat{n}$ represents the unit normal vector of the surface S. ϵ describes dielectric properties of the material. The problem of the boundary conditions may be solved with help of the Green's function.

According to Beckmann and Spizzichino [60], for observations from the far-field the scattered electric field in a point at a location P may be expressed as Helmholtz integral

$$\vec{E}(P) = \frac{1}{4\pi} \int\int \left(\vec{E}_{\mathrm{S}} \frac{\partial \psi}{\partial \hat{n}} - \psi \left(\frac{\partial E}{\partial \hat{n}} \right)_{\mathrm{S}} \right) dS \tag{2.54}$$

with a spherical wave of radius r′ and wave vector $\vec{k}$

$$\psi = \frac{1}{r'} e^{i\vec{k}r'}. \tag{2.55}$$

In order to evaluate the integral, the surface field $\vec{E}_{\mathrm{S}}$ and its normal derivative at the surface $\left(\frac{\partial \vec{E}}{\partial \hat{n}}\right)_{\mathrm{S}}$ have to be identified, which are in general not known. By assuming that the surface does not have sharp edges compared to the light's wavelength (Kirchhoff's assumption), the two unknown properties may be approximated. It is assumed that the field in a surficial point equals the field, which would be present on a tangent plane at that point. Thus, the field and its normal derivative would be:

$$\vec{E}_{\mathrm{S}} = (1+F)\vec{E}_i \qquad \text{and} \quad \left(\frac{\partial \vec{E}}{\partial \vec{n}} \right)_{\mathrm{S}} = (1-F)\vec{E}_i \vec{k}_i \cdot \hat{n} \tag{2.56}$$

with $\hat{n}$ the normal to the surface at point P. $\vec{E}_i$ and $\vec{k}_i$ describe the incident field and wave vector. F is the Fresnel reflection coefficient, which gives the portion of reflected light if the surface was smooth. Even though, we consider a rough surface, the approximation is valid since we assume local smoothness of the surface. The intensity of the scattered light is determined by the surface field, which is dependent on the surface currents. The light's angle of incidence θ_0, the wave's polarization and electrical properties (e.g. permittivity or permeability) encoded in the refractive index η of the surface determine the surface currents, such that F=F(θ_0, η).

Following Ticconi et al. [57], at a surface boundary of any roughness, the light's path will be deflected by means of Snell's law (see Eq. 2.48). In the case of a perfectly smooth surface, see Fig. 2.9 a), the reflection will be specular (mirror-like) accompanied by a symmetric angle to the incident angle. The specular reflection's intensity is determined by the Fresnel reflectivity, which increases with an increasing ratio of

complex permittivity. If the surface roughness increases as little as in Fig. 2.9 b), two components coexist: the component of specular reflection and a scattering component. The specular component is called the coherent component. The component of scattered light is named diffuse or the incoherent component. In a statistical sense, the specular component describes the mean value of the scattered field whereas the diffuse component represents the deviation of this mean due to the rough surface's randomness [61, 62]. The diffuse components' magnitudes will be smaller than that of the specular component. The degree of roughness determines the ratio between both components. In case of a completely rough and thus diffuse surface, as in Fig. 2.9 c), ideally, only diffuse components will remain without any component of specular reflection. Thus, the radiation will be scattered in all directions.

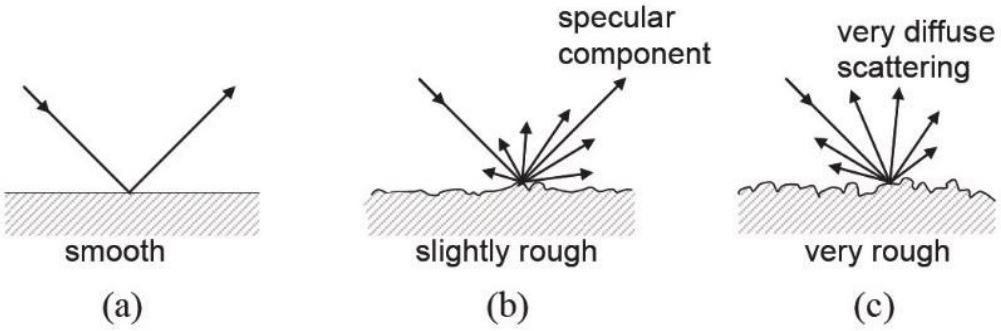

Figure 2.9.: A schematic sketch of the portion of specular and diffusive scattered light depending on the surface roughness. Figure a) shows a smooth surface with only reflected light. In b), the roughness is slightly increased such that smaller diffuse components add to the specular component. c) shows the case of a very rough surface with very diffuse scattering where no specular component is observable. [63]

A surface is here considered to be statistically rough if the surface profile obeys a statistical distribution, like a Gaussian distribution. According to Goodman [64], the scattering at such a rough surface permits to make the following assumptions for the scattered fields: First, the phases of the elementary scatterers are uniformly distributed between $[-\pi, \pi]$. Further, the phases and amplitude terms are statistically independent of each other but also of all other phases and amplitudes caused at other points.

There are two main approaches to model statistically rough surfaces that light interacts

with, which are described below. When introducing both models, we will follow the work of Nayar et al. [65]. Additional references will be highlighted. All models may be classified in two main categories: Either they comprise a well-known surface structure or the surfaces are approximated as planes with random irregularities. In the latter, the surface is described by a statistical distribution of either its slope, respective to its average slope, or by its height, respective to a mean height serving as reference.

The slope distribution model assumes the surface to consist of small planar micro-facets. An infinetesimal surface is then composed of numerous micro-facets. Each facet has a normal vector $\hat{n}_i$, which deviates from the groups mean normal vector $\bar{n}$ by an angle δ in orientation. δ is assumed to be a random variable. In case of an isotropically rough surface, the angle's probability distribution is rotationally symmetric respective to $\bar{n}$ and thus, it may be expressed as normal distribution with $\langle\delta\rangle = 0$ such that

$$\rho_\delta(\delta) = \frac{1}{\sqrt{2\pi\sigma_\delta}} e^{-\frac{\delta^2}{2\sigma_\delta^2}} \tag{2.57}$$

with σ_δ being the standart deviation of δ. The greater σ_δ is, the rougher the surface is modelled. In contrast to the height distribution model presented below, this model depends only on a single variable. However, the advantage of this model is that the scattering of the incident radiation depends on the local slope instead of the local height of the surface, such that this model is assumed to be more directly applicable to surface reflection problems.

If the surface is modelled by its height probability distribution $\rho_h(h)$ of height h(x,y), which is given as random function by the Cartesian coordinates x and y, the surface shape is determined as:

$$\rho_h(h) = \frac{1}{\sqrt{2\pi\sigma_h}} e^{-\frac{h^2}{2\sigma_h^2}} \tag{2.58}$$

Thereby, it is also assumed that h is normally distributed such that $\langle h\rangle = 0$. The variable σ_h is the standart deviation of the root-mean-square (RMS) of h and describes the roughness of the surface. The spatial correlation function C determining the degree of correlation between the heights of two points separated by a distance s is then:

$$C(s) = e^{-\frac{s^2}{l^2}} \tag{2.59}$$

with l being the correlation length, describing the distance necessary for C to drop to the value $\frac{1}{e}$. So, if both points are further apart than the correlation length, both heights may be assumed to be statistically independent of each other. By changing the parameters σ_h and l, which describe the statistical variation of the surface height's random component relative to $\langle h \rangle$ [57], the model appearance may be altered. In case of an extremely smooth surface, all points are correlated with each other such that the correlation length will be infinite $l = \infty$. The greater σ_h and the smaller l, the rougher the surface in mechanical terms [62].

So, roughness is a measure of the statistical variation in the topographic configuration of a surface in units of wavelength since the resolvability of the roughness changes with the incident radiation's wavelength [66]. Thus, in case of electromagnetic waves, the ratio between both properties matters [62]. A measure to describe the degree of roughness of a surface respective to the incident radiation's wavelength is the Rayleigh roughness criterion [67].

The criterion gives an estimation regarding if a surface may be considered rough or smooth with respect to the incident radiation's wavelength and incident angle respectively to the surface normal. When the radiation is incident on a rough surface under an angle θ_0, the specularily reflected light will be scattered from the surface at the same angle (law of reflection), as depicted schematically in Fig. 2.10. We now assume two parallel wavelets of which one is scattered from a reference plane (solid line) and the other being scattered from another plane parallel (dashed line) to that reference plane in a distance Δh. The different path lengths cause a phase difference $\Delta\phi$ in the scattered light. The path difference is given by $\Delta L = 2\Delta h \cos(\theta_0)$, such that the phase difference is identified as:

$$\Delta\phi = \frac{4\pi}{\lambda}\Delta h \cos(\theta_0) \tag{2.60}$$

If the reference plane marks the average height of the roughnesses, Δh can be considered to be the root mean square (RMS) surface height. As a conventional value: If $\Delta\phi$ is less than $\frac{\pi}{2}$ the surface is considered smooth [68]. Therefore, the Rayleigh criterion [69] of the form

$$\Delta h \geq \frac{\lambda}{8\cos(\theta_0)} \tag{2.61}$$

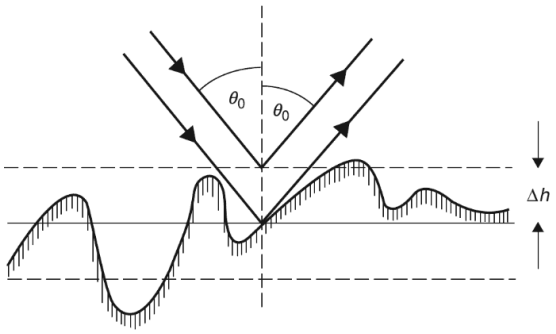

Figure 2.10.: A schematic drawing of light scattered on a rough surface. If incident radiation with an angle of θ_0 is reflected from a rough surface with a height deviation of Δh, the degree of roughness of that surface may be estimated with the Rayleigh criterion. The path difference of two rays scattered at distinct heights is given by $2\Delta h\cos(\theta_0)$. [68]

states that a surface is rough if the condition above is valid. If $\Delta h < \frac{\lambda}{8}$, roughnesses can not be resolved and thus the surface is considered to be optically smooth. Consequently, for a wavelength of visible light of $\lambda = 0.5\,\mu$m the roughness has to be at least as great as 60 nm to be notable. If however another type of EM radiation with greater wavelength is incident, such small height deviations as for visible light may not be resolved anymore and the surface seems smooth. Further, if the angle of incident θ_0 changes to larger values for a certain wavelength, the lower threshold of resolvable roughnesses also increases. Therefore, roughnesses perceived under a smaller angle may then not be noticable anymore such that the surface as well appears to be smooth [68].

2.3. Fundamentals of dynamic light scattering (DLS)

Over the past centuries, different optics-based methods to investigate the structure and the dynamics of samples were developed. The methods may be categorized in two types [8]: First, there are direct methods like microscopies which provide real-space images of the matter and measure therefore the real-space structures of particles. The other type of methods are indirect methods or scattering methods, e.g. neutron, X-ray or light scattering which measure the Fourier transform of samples. Light scattering methods have some advantages over direct methods: On one hand, they are able to give a much better quantative measurement of the average structures and dynamics because they are able to average over many more particles compared to the real-space measurements. On the other hand, even though direct methods are improving on this continuously, scattering methods are rather able to measure 3-dimensional structures on a broad range of time lasting from nanoseconds to hours. Further, apart from the extremes, scattering techniques do not have to suffer from trade-offs between either an extensive sample volume or an extensive dynamical range.

The method of light scattering can be subcategorized into two concepts [1, 7, 8]: First, static light scattering (SLS) will quantatively probe the structural properties of the sample system, like the form and structure factor of the material, by observing the intensity fluctuations I(Θ) of the scattered light from varying observation angles Θ. The structure factor gives mathematical description of a material's scattering ability regarding the incident radiation. The form factor $F(\vec{q}) = \frac{\langle b^2(\vec{q})\rangle}{\langle b^2(0)\rangle}$ is a mathematical expression that compensates for irregularity of an object's shape and structure by considering intra-particle interferences [7]. Secondly, dynamic light scatting (DLS) will investigate the dynamical properties of the sample, like motion type and speed or particle sizes, by analyzing the intensity fluctuations I(t) of the scattered light over time t from a fixed location. Regarding the characterization of particles with sizes smaller than a few microns, dynamic light scattering became a standard analysis method to determine their sizes, as well as their mobility on microscopic length scales [70].

Following Berne and Pecora [1] and Cipelletti [8], the best choice of the scattering technique, however, depends generally on the characteristic length scales of the sample or rather on the wavelength of the radiation. If the wavelength of the light equals

approximately the particle size, the most precise outcome is expected [1]. For example, by the use of X-rays with wavelengths of approx. 0.1 nm (see. Fig. 2.2), atomic and molecular length scales are probed. In case of light scattering with an average wavelength of 500 nm, structures with length scales of several μm are probed. Those structures might be colloids, polymers or surfactant solutions. Further, we note that visible light interacts much stronger, usually 4 to 5 orders of magnitude stronger, with matter than x-ray radiation. The consequence is that light scattering may be very sensitive to sparse concentrations of scatterers like very dilute solutions mixed with small particles and thus multiple scattering might be an issue.

So, in order to investigate the granular temperature of a granular system, the evolution of the system dynamics is relevant. An optical measurement technique capable to provide information about the system's dynamics is dynamic light scattering. DLS comprises the ability of analyzing the motion type and speed of the particles. Therefore, the focus of the following sections lies on this method. The bulk of theory which is presented in the following sections refers to very large extent to the works of Berne and Pecora [1], Egelhaaf [7] and Cipelletti [8].

2.3.1. The method's principles

The DLS method may collect data on the dynamics of systems within a short period of time. The very basic DLS setup consists of three components: A coherent light source (laser), the sample and the detector system, cf. Ch. 3. The monochromatic light illuminates the sample, which contains particles that act as scatterers in the dilute solution. The scattered light will then be registered by the detector. The intersection between the incident and the scattered laser beam is called scattering volume [1].

As discussed in Ch. 2.2.1, the incident radiation is a plane wave (cf. Eq. 2.10). The detected scattered fields at a given time is the superposition of the electric fields of all illuminated particles [1]. Thus, the total field depends on the particles' locations. The relative motion of the particles with respect to each other will provoke a phase difference in the scattered electric fields registered by the detector. Since the particles are assumed to continously move by translation, rotation or vibration via e.g. thermal fluctuations,

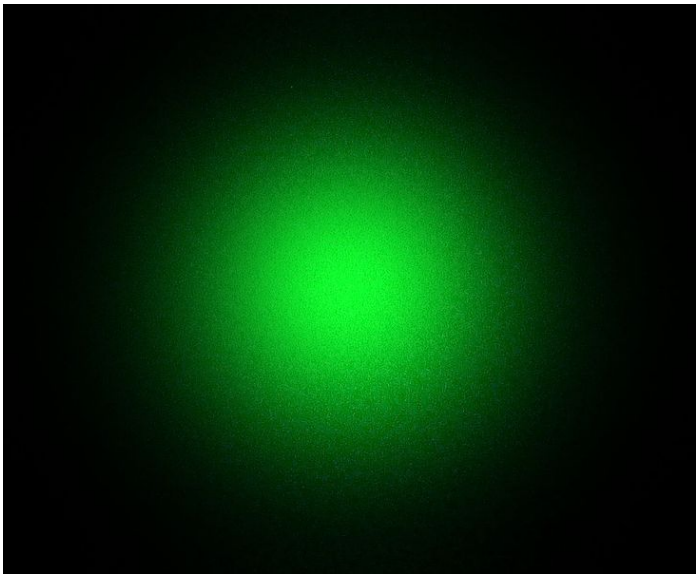

Figure 2.11.: A photograph of a speckle pattern produced with a 5 mW green laser pointer beam profile. The maximum intensity is found in the geometrical center of the pattern. The brightness decreases exponentially towards the outer bounds. [71]

the scattered field at the detector will fluctuate with time. In those fluctuations, information about the positions and orientations of the particles is encoded.

In the experiment, the scattered light registered at the detector is then perceived as a speckle pattern, see Fig. 2.11. The speckle pattern is a time-dependent map of local light intensity extrema. The phase difference causes the intensity to fluctuate with time t and in consequence the speckle pattern changes over time due to the constructive ($\Delta\phi = 0$) or destructive interference ($\Delta\phi = \pi$). The pattern will change most dramatically due to local displacements of $\Delta\vec{r} \sim \frac{\pi}{q}$. With the knowledge of q from Eq. 2.32, we are able to determine the theoretical range of length scales which may be investigated with DLS [8]

$$\Delta r_{min} \approx \frac{\lambda}{2\eta} \tag{2.62}$$

$$\Delta r_{max} \approx \frac{\pi}{k\Theta_{\min}} \sim 10^2 \frac{\lambda}{\eta} \tag{2.63}$$

with $q_{\min} = 2k \sin(\Theta_{\min}/2) \approx k\Theta_{\min}$. In case of visible light with wavelengths ranging

from ≈400 nm to ≈800 nm, the theoretically resolvable range in water would be 150 nm $< \Delta r <$ 30 μm [7].

The recorded intensity fluctuations may then serve to analyze the sample's dynamics by the calculation and interpretation of autocorrelation functions [1]. Correlation functions provide the degree of correlation between two dynamical properties over a period of time or spatial areas. The application of temporal autocorrelation functions on DLS data is discussed in the next chapter Ch. 2.3.2.

2.3.2. Time series analysis of the scattering intensity

The dynamics of a sample investigated with DLS are analyzed by autocorrelation functions. The theory of the analysis presented here follows Berne and Pecora [1] and Cipelletti [8]. As noted in the former section, the total electric field at the detector is a superposition of the electric field of the scattered light:

$$E(t) = \sum_{j=1}^{N} E_j e^{i\phi_j(t)} \tag{2.64}$$

In section Ch. 2.2.2.1, notations for the scattered electric fields for the cases of a single volume element, an extended particle and a particle ensemble were given. All expressions depend on the position $\vec{r}(t)$ of the particles. Thus, time varying electric fields will depend on the time-varying positions of the particles. If the particle positions change, a change of phase $\Delta\phi_j(t) = -\vec{q}\vec{r}_j(t)$ occurs. Here, we consider quasi-elastic scattering, such that $|\vec{q}| = q$.

The correlation function is supposed to compare the system's dynamical states at two different times separated by a delay time τ. The field autocorrelation function, which

is expressed by the phase shifts dependent on τ, equals

$$G_1(\tau) = \langle E(t)E^*(t+\tau)\rangle = \left\langle \left(\sum_j E_j e^{i\phi_j(t)}\right)\left(\sum_{j'} E_{j'} e^{i\phi_{j'}(t+\tau)}\right)\right\rangle \tag{2.65}$$

$$= \sum_j \langle |E_j|^2\rangle \langle e^{i(\phi_j(t)-\phi_{j'}(t+\tau)}\rangle \tag{2.66}$$

$$= \sum_j \langle |E_j|^2\rangle \langle e^{i\Delta\phi_j(\tau)}\rangle. \tag{2.67}$$

Hereby the assumptions were made, that the amplitudes and the phases of the individual fields are not correlated and also not correlated with those from other particles such that only terms with j=j' contribute. Further, all phases are assumed to be evenly distributed between $[-\pi, \pi]$. Consequently, the electric fields are Gaussian distributed and the central limit theorem is respected [64].

For very long measurements, where towards higher delay times τ, the maximum relaxation time of the system is widely exceeded, $\langle E^*(t+\tau)\rangle$ and $\langle E(t)\rangle$ become statistically independent. So, for very large τ, $\langle E(t)E^*(t+\tau)\rangle = \langle E(t)\rangle\langle E^*(t+\tau)\rangle = 0$ because the electric field is then equally positive or negative. Usually, not the autocorrelation function of the form of Eq. 2.67 is considered but its normalized version

$$g_1(t,\tau) = \frac{\langle E(t)E^*(t+\tau)\rangle}{\langle |E(t)|^2\rangle}. \tag{2.68}$$

By the division by the squared mean amplitude of the fields, we assure that the autocorrelation function is independent of the initially recorded field amplitude at time t=0. Thus, the decay of $g_1(\tau)$ ranges from 1 for small τ to 0 for τ being greater than the system's maximum relaxation time.

In case of Brownian motion, the phase angles will fluctuate randomly. If the scattering vector $\vec{q}$ is sufficiently large, the phase may take on values between 0 and 2π with equal probabilities. Thus, if we take the time average of the scattered electric field, when the particles perform a random walk, that is considered to be symmetrical about its origin, we receive

$$\langle \vec{E}(t) \rangle \sim \langle \sum_{j=1}^{N} E_j e^{-iq\vec{r}_j(t)} \rangle = 0 \tag{2.69}$$

and the decay has the form

$$g_1(t) = \langle e^{-\vec{q}\Delta\vec{r}_j(t)} \rangle \tag{2.70}$$

with $\Delta\vec{r}_j(t) = \vec{r}_j(t) - \vec{r}_j(0)$ and $\Delta\vec{r}_j(t)$ being a Gaussian random variable. For simple diffusion $\langle \Delta\vec{r}_j{}^2(t) \rangle = 6Dt$ and thus [7]

$$g_1(\tau) = e^{-\frac{q^2}{6}\langle \Delta\vec{r}_j{}^2(t) \rangle}. \tag{2.71}$$

In statistical mechanics, the mean squared displacement $\langle \Delta r^2 \rangle(\tau) = \langle |\vec{r}(t) - \vec{r}_0|^2 \rangle = \frac{1}{N}\sum_{j=1}^{N} |\vec{r}_j(t) - \vec{r}_j(0)|^2$ describes the deviation of a particle respective to a reference position over time. D reflects the diffusion coefficient for the self-diffusion of particles of diameter d described by the Stokes-Einstein equation

$$D = \frac{k_B T}{6\pi\eta d}. \tag{2.72}$$

k_B states the Boltzmann's constant. Hereby, the particles are assumed to not interact with each other by e.g. collisions or streaming currents. This assumption infact opposes the nature of granular media (cf. Ch. 2.1.1). Experimentally, the avoidance of inter-particle collisions may be achieved by using samples, where the sample dimensions are sufficiently large such that all of the N particles will not interact.

In general, diffusion processes may also be described by the Kohlrausch function [72]

$$g_1(\tau) \sim e^{\left(-\frac{t}{\tau}\right)^{\beta}} \tag{2.73}$$

where the dimension of the coefficient β determines the kind of diffusion process. The variable t denotes the time passing and τ gives the time interval needed for the exponential function to decay to its $\frac{1}{e}$-portion. If $\beta = 1$, we expect normal diffusion such that the mean squared displacement $\langle \Delta r^2 \rangle(\tau)$ grows linearly with τ, which represents

the above mentioned random walk geometry. If $\beta < 1$, subdiffusion or even confined diffusion, where the particles are expected to be trapped in some geometrical structure, is observed. Then, $\langle \Delta r^2 \rangle(\tau) \propto \tau^{\beta}$. In contrast, if $\beta > 1$ superdiffusion and if even $\beta = 2$ a ballistic motion is anticipated, where $\langle \Delta r^2 \rangle(\tau) \propto \tau^2$.

However, the only property, which can be directly measured in an experiment, is the intensity of the scattered light I(t)= $\sqrt{\frac{\epsilon}{\mu}}(E(t)E^*(t)) \sim |E(t)E^*(t)|$ registered by the detector. The intensity is expressed more precisely by

$$I(t) = \sum_j \sum_{j'} E_j(t) E_{j'}^*(t) e^{-i(\phi_j(t) - \phi_{j'}(t))}. \tag{2.74}$$

The mean intensity is then given by

$$\langle I(t) \rangle = \langle E(t)E^*(t) \rangle = \left\langle \left(\sum_j E_j e^{i\phi_j(t)} \right) \left(\sum_{j'} E_{j'} e^{i\phi_{j'}(t)} \right) \right\rangle. \tag{2.75}$$

The equation above simplifies if we assume the following incidences: If the particle properties and thus the amplitude E_j do not depend on the particle's position in space, we can average the phases and the amplitude separately:

$$\langle I(t) \rangle = \sum_j \langle |E_j|^2 \rangle \langle e^{i(\phi_j(t) - \phi_{j'}(t)} \rangle \tag{2.76}$$

Under the assumption, that all particles are identical in size, shape and scattering properties, nearly equal amplitudes for all scattering events are expected

$$\langle I(t) \rangle = \sum_j \langle |E_j|^2 \rangle = \langle I_j(t) \rangle \tag{2.77}$$

$$\equiv \langle I_t(t) \rangle \tag{2.78}$$

with $\langle I_t(t) \rangle$ being the total average intensity. In view of granular media, a uniform appearance of the particles in very improbable in nature. In laboratory experiments, however, the granular medium would need to be carefully selected to assure that this requirement is nearly met (cf. Ch. 2.1.1).

So, the faster the intensity fluctuates, the faster the particles move. In order to study

the evolution of the dynamics of the system, the intensity autocorrelation function G_2 is calculated. The intensity correlation function can then be defined as [73]

$$G_2(\tau) = \langle I(t)I(t+\tau)\rangle = \langle E(t)E^*(t)E(t+\tau)E^*(t+\tau)\rangle \tag{2.79}$$

$$= \left\langle \sum_j \sum_{j'} \sum_{j''} \sum_{j'''} E_j(t)E^*_{j'}(t)E_{j''}(t+\tau)E^*_{j'''}(t+\tau)e^{i(\phi_j(t)-\phi_{j'}(t)+\phi_{j''}(t+\tau)-\phi_{j'''}(t+\tau))} \right\rangle \tag{2.80}$$

The assumptions of the phase and the amplitudes being uncorrelated as well as the independence of the particles' motions, with respect to each other, are still considered to be valid. Therefore, we may split the averages over the amplitudes and the phase terms again, as done before in Eq. 2.66, and consider further only contributions from j=j′ and j″=j‴ as well as j=j‴ ≠ j′=j″. Also it is assumed, that the phases fluctuate much faster than the values for the amplitudes, such that the amplitude terms may be replaced by their initial values. All intermediate steps of the calculation can be retraced in the publication of Born et al. [73]. The equation above simplifies to:

$$G_2(\tau) = \langle I_t(t)I_t(t+\tau)\rangle + \left\langle \sum_j \sum_{j'} E_j(t)E^*_j(t)E_{j'}(t)E^*_{j'}(t)e^{i(\phi_j(t)-\phi_{j'}(t+\tau))}e^{i(\phi_{j'}(t)-\phi_{j'}(t+\tau))} \right\rangle \tag{2.81}$$

$$= \langle I(t)_t I_t(t+\tau)\rangle + \sum_j \sum_{j'} \langle I_j(t)I_{j'}(t)\rangle \left\langle e^{i(\phi_j(t)-\phi_j(t+\tau)}\right\rangle \left\langle e^{i(\phi_{j'}(t)-\phi_{j'}(t+\tau)}\right\rangle \tag{2.82}$$

$$= \langle I(t)_t I_t(t+\tau)\rangle + \sum_j \sum_{j'} \langle I_j(t)I_{j'}(t)\rangle \left|\langle e^{i(\Delta\phi_j(\tau)}\rangle\right|^2 \tag{2.83}$$

$$= \langle I(t)_t I_t(t+\tau)\rangle + |E(t)E^*(t+\tau)|^2 \tag{2.84}$$

In case of a stationary process, which means that averaging the intensity over time does not depend on the time t but on the delay time τ, the time dependence may be neglected such that the intensity autocorrelation function from Eq. 2.68 is $g_2(t,\tau) = g_2(\tau)$, with

$$g_2(\tau) = \frac{\langle I(0)I(\tau)\rangle}{\langle I(0)\rangle^2}. \tag{2.85}$$

The normalization by $\langle I(0)\rangle^2$ ensures an independence of the incident intensity. The

intensity correlation function takes, in theory, the ensemble average and, in practice, it calculates the time average of the intensity data. Usually, both approaches yield approximately the same results, however, there are specific cases, where discrepancies between both averages occur. A prominent example for the latter are glassy systems [8].

The range of values, that $g_2(\tau)$ may take on, depends on the behavior of the numerator. For very long delay times τ

$$\lim_{\tau\to\infty} g_2(\tau) = \lim_{\tau\to\infty} \frac{\langle I(0)I(\tau)\rangle}{\langle I(0)\rangle^2} = \lim_{\tau\to\infty} \frac{\langle I(0)\rangle\langle I(\tau)\rangle}{\langle I(0)\rangle^2} = 1 \tag{2.86}$$

such that the intensities $I(0)$ and $I(\tau)$ will be uncorrelated, if there is some sort of motion. If the system is stationary, nothing changes and $I(0) = I(\tau)$. If the delay times are close to zero

$$\lim_{\tau\to 0} g_2(\tau) = \lim_{\tau\to 0} \frac{\langle I(0)I(\tau)\rangle}{\langle I(0)\rangle^2} = \lim_{\tau\to 0} \frac{\langle I(0)^2\rangle}{\langle I(0)\rangle^2} = 2. \tag{2.87}$$

The equation above equals 2 if we use $\langle I(0)^2\rangle = 2\langle I(0)\rangle^2$ for a extremely high number of particles N$\to\infty$. For a detailed calculation, reference Egelhaaf [7].

Eq. 2.84 may be perceived as reformulation of the Siegert relation [74]

$$g_2(t,\tau) = 1 + |g_1(t,\tau)|^2 \tag{2.88}$$

$$= 1 + \left|\langle e^{-iq[\vec{r}(0)-\vec{r}(\tau)]}\rangle\right|^2 = 1 + f(\tau)^2 \tag{2.89}$$

which applies, if the scattered fields obey Gaussian statistics, such that the central limit theorem is valid [1, 75]. Further, it is assumed that the scattering volume has to be large respective to the particle diameters, such that the mean free path is regarded as suffciently large and, consequently, the particles only seldomly collide. Thus the particles may be considered to be statistically independent. The term $f(\tau) \equiv \langle e^{-iq[\vec{r}(0)-\vec{r}(\tau)]}\rangle$ is also called intermediate scattering function or dynamic structure factor, which is a mathematical expression containing information about inter-particle correlations and their time evolution [1].

2.3.3. Diffusing-wave spectroscopy (DWS)

In reality, it is often difficult to assure, that the detected light is only scattered once on its way through an object. When particles have diameters, which are comparable to the wavelength of the light, the scattering is usually so strong, that the single scattering condition is hurt. When the light is scattered multiple times, the system can not be characterized anymore by the scattering vector $\vec{q}$, since it is, due to its randomization, impossible to reconstruct the exact path, that the light took while propagating through the sample. In order to perform single scattering experiments, the free mean path ℓ must be much greater than the sample dimension. This assures, that the light may travel some time through the sample until the sequential collision with matter happens [11].

The method, which was developed by Pine and Weitz [76] to solve the problem of multiple scattering, is called diffusing-wave spectroscopy (DWS). We follow the theory presented in their work throughout this section. This method treats the random propagation of light and the dynamical effects caused in a turbid sample with statistical approximations in multiple scattering situations. This way, the mean squared displacement, which is a common measure for the characterization of the dynamics of turbid samples, may be retrieved. DWS is based on the assumption of the diffusion approximation [77], which assures that the light has been scattered a very large number of times. Therefore, its path within the medium may be described by a random walk. Materials that can be considered to be diffusive volume scatterers, may be recognized by their white appearance like teflon, milk or flour. The diffusion approximation assumes the light to diffuse through the medium. Therefore each scattering event is represented by an average scattering event. Thus, only the light's path length determines the number of relevant average scattering events, which contribute to each path. Those paths are then averaged in order to obtain the autocorrelation function of the system. Similar to the DLS method, phase changes of the scattered light based on the particles' relative motion respective to each other are registered and analyzed. This technique sums up all possible phase shifts $\Delta\phi_i(\tau)$. In the end, we receive an autocorrelation function, which describes the magnitude of phase differences based on the time lags τ.

The experimental setup for DWS is similar to the setup of an DLS experiment. Both

involve a coherent light source and a detector. However, because of multiple scattering, the scattering vector $\vec{q}$ is meaningless here and therefore also the scattering angle Θ. Thus, there are many possible options regarding the location of the laser respective to the detector. In practice, the transmission (T) and the back-scattering (BS) geometries are favored. Thereby, the detector will be placed on the opposite side of the sample with respect to the incident laser beam or, it will be placed in a small angle laterally to the laser beam, respectively. Each technique probes shorter and longer light paths with a different number ratio. In case of the transmission geometry, the probability that more longer paths are recorded is much higher, since all of the detected light must at least have travelled a distance equal to the sample thickness. Averaging over more longer paths resolves short length-scale motions better, since longer paths cause a faster decay. At longer times, the contributions of the long paths have already decayed and only short path contributions remain showing relatively long length-scale motions. However, with this geometry, one needs to know in advance discrete sample properties as e.g. the sample's absorption coefficient or the free mean path. In case of the back-scattering geometry, we do not need to know additional material dependent properties. This method probes short and long light paths, but with an increased number of short paths (which also contain a portion of only reflected and not even scattered light) over which is temporally averaged. Thus, with BS rather long length-scale motions are resolved.

Two length scales are indispensable to characterize the multiple scattering and the transport of light: First, the mean free path ℓ:

$$\ell = \frac{1}{\sigma\rho}. \tag{2.90}$$

σ represents the total scattering cross-section for a single particle in the assumed dilute suspension and ρ states the number density of the particles. Second, the distance, over which the light's direction of propagation is randomized, is called transport mean free path ℓ^*

$$\ell^* = \frac{\ell}{\langle 1 - \cos(\theta)\rangle}. \tag{2.91}$$

θ describes the mean scattering angle and the angular brackets indicate the ensemble average over many scattering events. In case of particle diameters of approximately the

size of the wavelength, single scattering is sufficient to randomize the light ($\ell = \ell^*$). In case of larger particles like granular particles: $\ell^* > \ell$. Thus, several scattering events are required due to the enhanced likeliness of forward scattering (cf. Fig. 2.6).

With those quantities, we may describe the total phase shift of a photon travelling from the laser through the sample towards the detector by assuming quasi-elastic scattering as

$$\phi(t) = k_0 s(t) = \sum_{j=0}^{N} \vec{k}_j(t) \cdot (\vec{r}_{j+1}(t) - \vec{r}_j(t)). \tag{2.92}$$

s represents the total path length for a photon scattering N times by

$$s = \sum_{j=0}^{N} |\vec{r}_{j+1}(t) - \vec{r}_j(t)| \tag{2.93}$$

and $\vec{k}_j$ being the wave vector after j scattering events. If all wave vectors have the same magnitude: $k_j = k_0$ for all j. As for DLS, we expect the total electric field at the detector to be a superposition of scattered electric fields, see Eq. 2.64. But instead of summing only over all particles, which have their own path, as done for DLS, we here need to sum over all light paths and over all particles in each path, since many particles may take the same path. Additionally, the field amplitude is now not only dependent of the laser intensity but also on the number of particles belonging to one path. If the particles are assumed to be independent and the fields form different paths are uncorrelated, the field autocorrelation function may be expressed as

$$g_1(t) = \sum_p \frac{\langle |E_p|^2 \rangle}{\langle I \rangle} \langle e^{i(\phi_p(0) - \phi_p(t))} \rangle \tag{2.94}$$

for the paths p. In case of a large number of diluted particles performing Brownian motion, $\langle \Delta\phi_p^2(t) \rangle$ depends only on the path length of light s and thus the field correlation function reflects a sum of path lengths instead of summing oven individual paths. Further,

$$g_1(t) = \sum_s P(s) e^{-\frac{s}{3l^*} k_0^2 \langle \Delta r^2(t) \rangle} \tag{2.95}$$

with P(s) being the path length distribution function through the sample. This way, the mean squared displacement $\langle \Delta r^2(t) \rangle$ may be obtained from DWS on dilute solu-

tions with particles performing random walks. Under those conditions, the intensity autocorrelation function $g_2(\tau)$ may be retrieved via the Siegert relation

$$g_1(\tau) = \left(\frac{\langle EE^*(\tau) \rangle}{\langle |E|^2 \rangle} \right) = \frac{1}{\beta} \left(\frac{\langle II(\tau) \rangle}{\langle I \rangle^2} - 1 \right) = \frac{1}{\beta} \left(g_2(\tau) - 1 \right). \tag{2.96}$$

β describes a constant, which is defined by the collection optics.

From Eq. 2.92, we see that the only parameters describing the particles themselves and their motions are their positions $\vec{r}_j(t)$. Therefore, an appropriate description of the scattering behavior by the mean squared displacement in Eq. 2.95 is only possible for particles of the orders of 10^{-7} m or less, when light incidents upon them and the scattering may be explained with Rayleigh, RGD or Mie theory. If large particles as e.g. granular particles are considered, the description fails since the positions and thus the relative motions of scattering entities situated on the particle's surface are here unnoticed.

2.4. Conclusion

DLS and DWS opened several doors in order to analyze the dynamics of different kinds of samples containing particles with radii comparable to the light's wavelength. Thus, it is very tempting to apply the existing DLS or DWS methodology also to systems with macroscopic particles, like granular systems [3–5, 78–80]. However, in the former sections, assumptions in the existing theory were highlighted, that become invalid for macroscopic particles, since their radii exceed the light's wavelength by several orders of magnitude. Usually, Mie theory or the geometrical optics approximation are used to investigate scattering on such large objects. However, in view of DLS on granular media, both methods are not sufficient. Mie theory only applies to homogeneous spheres, which usually oppose the nature of granular particles. The geometrical optics approximation considers the light to propagate as ray instead of a wave and therefore only provides stationary phases. DLS, though, exploits phase difference in the scattered light, which can not be provided by this ansatz.

The DLS theory was developed on the assumptions that small particles ($r \leq \lambda$) are driven by Brownian motion and whose scattering behavior may be explained by Rayleigh scattering or the Rayleigh-Gans-Debye approximation. Macroscopic particles ($r \gg \lambda$), however, exceed the upper size limit for this approximation by several orders of magnitude. Thus, the occurring scattering processes are not expected to be adequately described by the approximation. Further, granular media comprise macroscopic particles, that are not prone to thermal random motion. In fact, in granular systems, the kinetic energy dissipates, if it is not compensated for. In case of agitation, the particle dynamics are dominated by collisions. Thus, the particles may not be considered statistically independent of one another. Statistical independence, though, is the fundament of the interpretation of the phase differences in DLS and DWS experiments and, consequently, on the estimations of the mean squared displacements.

In the established theory, scattering objects are comparable to a dipole or a small group of dipoles, which are approximated as point source or a small homogeneous sphere. With increasing particle dimensions, the probability of occurring internal and surficial inhomogeneities increases. If existing, those features will scatter the light differently compared to the predominant material. Thus, a granular particle may be,

depending on the type of material, a local agglomeration of numerous scatterers with different scattering abilities.

Due to $r \gg \lambda$, the suggestion is to treat light scattering on a macroscopic particle as light scattering on a vast surface. The media boundary then consists of dipole-like entities scattering the light, such that the degree of roughness of the surface may be of interest. In contrast to the usually assumed Rayleigh scatterers, a macroscopic object's scattering center is not necessarily identical to the particle's barycenter, but may be situated on its surface. Thus, it may perform a motion relative to the particle's barycenter. The motion of those scattering entities causes time-dependent phase differences in the scattered fields, such that individual particle motion, e.g. rotation, vibration or spontaneous deformations, may be analyzed. However, those dependencies are not sufficiently included in the existing DLS or DWS theory used in experiments with granular media and have therefore to be compensated for in further studies.

In conclusion, we expect that the recorded intensity fluctuations do not only depend on phase differences caused by the relative motions among the particles, but also on the surface structures of each individual particle. Therefore, particle rotation and spontaneous deformations of soft particles, caused by collisions, can contribute to light intensity fluctuations. In order to gain the most reasonable results from DLS/DWS experiments on macroscopic particles, we either need to know in advance, what's the physics behind the autocorrelation function, that we are going to measure or the dynamics in our sample need to be fully deterministic. Consequently, we would be able to study why and how the autocorrelation function will decay based on the surface conditions of the particles and of dictated bulk particle motions.

In this study, the aim is to design experiments, where the influence of only a single macroscopic particle will be investigated. This way, only a limited number of options for the particles motion per time occurs and the investigation will be free of inter-particle interference effects. According to the statements above, a single macroscopic particle should already cause complex effects on the light scattering process and therefore on the decay of the obtained autocorrelation function. The complexity of the particles is initially decreased to the possible minimum by investigating spherical transparent particles, cf. Ch. 4. Later, we approach the nature of a granular particle again step-

wise by using spherical particles with a surface structure. Apart from the translational motion of the particle, it is expected that the rotation about its barycenter will also induce a change in the scattered light's intensity. With the developed model, cf. Ch. 5, a full explanation of how a single particle contributes to the autocorrelation function of our DLS experiment should be provided for analyzing the dynamics of granular particles. The concept of granular temperatures may be used as statistical measure to characterize the distribution of the kinetic energy among the degrees of freedom of the system, cf. Ch. 7.

References

[1] B. J. Berne and R. Pecora. *Dynamic light scattering: with applications to chemistry, biology, and physics*. Courier Corporation, 2000.

[2] G. Maret and P. E. Wolf. "Multiple light scattering from disordered media. The effect of brownian motion of scatterers". In: *Zeitschrift fuer Physik B Condensed Matter* 65.4 (Dec. 1987), pp. 409–413.

[3] M. J. Biggs, D. Glass, L. Xie, V. Zivkovic, A. Buts, and M. a. Curt Kounders. "Granular temperature in a gas fluidized bed". In: *Granular Matter* 10.2 (Jan. 2008), pp. 63–73. issn: 1434-5021. doi: 10.1007/s10035-007-0077-8.

[4] K. Kim and H. K. Pak. "Diffusing-wave spectroscopy study of microscopic dynamics of three-dimensional granular systems". In: *Soft Matter* 6.13 (2010), p. 2894. issn: 1744-683X. doi: 10.1039/b926799a.

[5] V. Zivkovic, M. Biggs, D. Glass, P. Pagliai, and A. Buts. "Particle dynamics in a dense vibrated fluidized bed as revealed by diffusing wave spectroscopy". In: *Powder Technology* 182.2 (Feb. 2008), pp. 192–201. issn: 00325910. doi: 10.1016/j.powtec.2007.12.007.

[6] A. Amon, R. Bertoni, and J. Crassous. "Experimental investigation of plastic deformations before a granular avalanche". In: *Physical Review E* 87.1 (Jan. 2013). issn: 1539-3755. doi: 10.1103/PhysRevE.87.012204.

[7] S. U. Egelhaaf. "Solution Scattering". In: *Soft condensed matter physics in molecular and cell biology*. Taylor & Francis, 2006, p. 38.

[8] L. Cipelletti, V. Trappe, and D. J. Pine. *Scattering techniques*. John Wiley & Sons, Inc.: New York, NY, USA, 2016.

[9] D. Bicout, E. Akkermans, and R. Maynard. "Dynamical correlations for multiple light scattering in laminar flow". In: *Journal de Physique I* 1.4 (1991), pp. 471–491.

[10] D. J. Pine, D. A. Weitz, P. M. Chaikin, and E. Herbolzheimer. "Diffusing wave spectroscopy". In: *Physical review letters* 60.12 (1988), p. 1134.

[11] D. Weitz, J. Zhu, D. Durian, H. Gang, and D. Pine. "Diffusing-wave spectroscopy: The technique and some applications". In: *Physica Scripta* 1993.T49B (1993), p. 610.

[12] L. Cristofolini, D. Orsi, and L. Isa. "Characterization of the dynamics of interfaces and of interface-dominated systems via spectroscopy and microscopy techniques". In: *Current opinion in colloid & interface science* 37 (2018), pp. 13–32.

[13] D. Orsi, F. Salerni, E. Macaluso, E. Santini, F. Ravera, L. Liggieri, and L. Cristofolini. "Diffusing wave spectroscopy for investigating emulsions: I. Instrumental aspects". In: *Colloids and Surfaces A: Physicochemical and Engineering Aspects* 580 (2019), pp. 123–574.

[14] F. Salerni, D. Orsi, E. Santini, L. Liggieri, F. Ravera, and L. Cristofolini. "Diffusing wave spectroscopy for investigating emulsions: II. Characterization of a paradigmatic oil-in-water emulsion". In: *Colloids and Surfaces A: Physicochemical and Engineering Aspects* 580 (2019), pp. 123–724.

[15] B. Andreotti, Y. Forterre, and O. Pouliquen. *Granular media: between fluid and solid*. Cambridge University Press, 2013.

[16] S. Ogawa. "Multitemperature theory of granular materials". In: *Proc. of the US-Japan Seminar on Continuum Mechanical and Statistical Approaches in the Mechanics of Granular Materials, 1978*. Gakajutsu Bunken Fukyu-Kai. 1978, pp. 208–217.

[17] N. V. Brilliantov, T. Pöschel, W. T. Kranz, and A. Zippelius. "Translations and rotations are correlated in granular gases". In: *Physical review letters* 98.12 (2007).

[18] I. Goldhirsch. "Introduction to granular temperature". In: *Powder Technology* 182.2 (2008), pp. 130–136.

[19] V. Zivkovic, M. Biggs, D. Glass, and L. Xie. "Particle dynamics and granular temperatures in dense fluidized beds as revealed by diffusing wave spectroscopy". In: *Advanced Powder Technology* 20.3 (2009), pp. 227–233.

[20] M. Zvonimir, G. François, J. Baker, E. Itai, and M. Benjy. "A granular thermometer". In: *Granular Matter* 23.2 (2021).

[21] I. Ippolito, C. Annic, J. Lemaitre, L. Oger, and D. Bideau. "Granular temperature: experimental analysis". In: *Physical Review E* 52.2 (1995), p. 2072.

[22] R. M. Nedderman et al. *Statics and kinematics of granular materials*. Vol. 352. Cambridge University Press Cambridge, 1992.

[23] E. S. Oran and J. P. Boris. "Fluid Dynamics". In: *Encyclopedia of Physical Science and Technology (Third Edition)*. Ed. by R. A. Meyers. Third Edition. New York: Academic Press, 2002, pp. 31–43. isbn: 978-0-12-227410-7. doi: https://doi.org/10.1016/B0-12-227410-5/00248-9.

[24] M. Doi. *Soft Matter Physics*. EBL-Schweitzer. OUP Oxford, 2013, pp. 93–94. isbn: 9780191503504. url: https://books.google.de/books?id=-21pAgAAQBAJ.

[25] W. B. Russel, D. A. Saville, and W. R. Schowalter. *Colloidal dispersions*. Cambridge university press, 1991.

[26] H. Jaeger. "Sand, jams and jets". In: *Physics World* 18.12 (2005), p. 34.

[27] É. Guyon and J.-P. Troadec. *Du sac de billes au tas de sable*. Odile Jacob, 1994.

[28] J. Duran. *Sands, powders, and grains: an introduction to the physics of granular materials*. Springer Science & Business Media, 2012.

[29] K. K. Rao, P. R. Nott, and S. Sundaresan. *An introduction to granular flow*. Vol. 490. Cambridge university press Cambridge, 2008.

[30] U. K. Krieger and A. A. Zardini. "Using dynamic light scattering to characterize mixed phase single particles levitated in a quasi-electrostatic balance". en. In: *Faraday Discuss.* 137 (2008), pp. 377–388. ISSN: 1359-6640, 1364-5498. DOI: 10.1039/B702148H. (Visited on 07/21/2021).

[31] H. M. Jaeger, S. R. Nagel, and R. P. Behringer. "Granular solids, liquids, and gases". In: *Reviews of modern physics* 68.4 (1996), p. 1259.

[32] J. Bridgwater. "Particle technology". In: *Chemical engineering science* 50.24 (1995), pp. 4081–4089.

[33] I. Goldhirsch. "Mesoscopic nature of granular flows". In: *Handbook of Powder Technology*. Vol. 10. Elsevier, 2001, pp. 245–253.

[34] T. Pöschel and S. Luding. *Granular gases*. Vol. 564. Springer Science & Business Media, 2001.

[35] A. Einstein. *Investigations on the Theory of the Brownian Movement*. Courier Corporation, 1956.

[36] H. Hinrichsen and D. E. Wolf. *The physics of granular media*. John Wiley & Sons, 2006.

[37] A. Zippelius. "Granular gases". In: *Physica A: Statistical Mechanics and its Applications* 369.1 (2006), pp. 143–158.

[38] P. K. Haff. "Grain flow as a fluid-mechanical phenomenon". In: *Journal of Fluid Mechanics* 134 (1983), pp. 401–430.

[39] S. Savage and D. Jeffrey. "The stress tensor in a granular flow at high shear rates". In: *Journal of Fluid Mechanics* 110 (1981), pp. 255–272.

[40] D. Serero, C. Goldenberg, S. H. Noskowicz, and I. Goldhirsch. "The classical granular temperature and slightly beyond". In: *Powder technology* 182.2 (2008), pp. 257–271.

[41] V. Zivkovic. "Study of granular temperature in dense fluidized beds by diffusing wave spectroscopy". PhD thesis. The University of Edinburgh, 2009.

[42] H. C. van de Hulst. "Light scattering by small particles". In: *Quarterly Journal of the Royal Meteorological Society* 84.360 (1957), pp. 198–199. DOI: https://doi.org/10.1002/qj.49708436025.

[43] M. Kerker. *The Scattering of Light, and Other Electromagnetic Radiation*. Physical chemistry. Academic Press, 1969. ISBN: 9780124045507. URL: https://books.google.de/books?id=XyJRAAAAMAAJ.

[44] C. F. Bohren and D. R. Huffman. *Absorption and scattering of light by small particles*. John Wiley & Sons, 2008.

[45] D. Morin. "Electromagnetic waves". In: *Harvard University Physics Course, affiliated with MIT Education* 8 (). URL: https://scholar.harvard.edu/files/david-morin/files/waves_electromagnetic.pdf.

[46] D. Halliday, R. Resnick, and J. Walker. *Halliday Physik. 2., überarbeitete und ergänzte Auflage*. 2009.

[47] J. H. Poynting. "XV. On the transfer of energy in the electromagnetic field". In: *Philosophical Transactions of the Royal Society of London* 175 (1884), pp. 343–361.

[48] M. Born and E. Wolf. *Principles of optics: electromagnetic theory of propagation, interference and diffraction of light*. Elsevier, 2013.

[49] NASA. *Electromagnetic Spectrum*. http://www.ces.fau.edu/nasa/module-2/radiation-sun.php. Accessed: 2022-09-02. 2022.

[50] C. A. Balanis. *Advanced engineering electromagnetics*. John Wiley & Sons, 1989.

[51] H. C. van de Hulst. *Light scattering by small particles*. Courier Corporation, 1981.

[52] G. Mie. "Beiträge zur Optik trüber Medien, speziell kolloidaler Metallösungen". In: *Annalen der Physik* 330.3 (1908), pp. 377–445.

[53] T. Wriedt. "Mie Theory: A Review". In: *The Mie Theory: Basics and Applications*. Ed. by W. Hergert and T. Wriedt. Springer Berlin Heidelberg, 2012, pp. 53–71. ISBN: 978-3-642-28738-1. DOI: 10.1007/978-3-642-28738-1_2.

[54] Y. Eremin. "SCATTERING | Scattering Theory". In: *Encyclopedia of Modern Optics*. Ed. by R. D. Guenther. Oxford: Elsevier, 2005, pp. 326–330. ISBN: 978-0-12-369395-2. DOI: https://doi.org/10.1016/B0-12-369395-0/00682-5.

[55] C. Wolff. *Rayleigh- versus Mie- Scattering*. https://www.radartutorial.eu/01.basics/Rayleigh-%20versus%20Mie-Scattering.en.html. Accessed: 2022-08-22. 2022.

[56] R. Nave. http://hyperphysics.phy-astr.gsu.edu/hbase/atmos/blusky.html. Accessed: 2022-10-05. 2022.

[57] F. Ticconi, L. Pulvirenti, N. Pierdicca, and V. Zhurbenko. "Models for scattering from rough surfaces". In: *Electromagnetic waves* 10 (2011), pp. 203–226.

[58] A. Schuster. *An introduction to the theory of optics*. E. Arnold, 1904, pp. 38–53.

[59] TuitionPhysics. *The Physics Behind Rainbow Formation*. https://tuitionphysics.com/2016-feb/the-physics-behind-rainbow-formation/. Accessed: 2022-09-30. 2016.

[60] P. Beckmann and A. Spizzichino. "The scattering of electromagnetic waves from rough surfaces". In: *Norwood* (1987).

[61] F. T. Ulaby, R. K. Moore, and A. K. Fung. "Microwave remote sensing: Active and passive. volume 1-microwave remote sensing fundamentals and radiometry". In: (1981).

[62] D. Didascalou, M. Dottling, N. Geng, and W. Wiesbeck. "An approach to include stochastic rough surface scattering into deterministic ray-optical wave propagation modeling". In: *IEEE Transactions on Antennas and Propagation* 51.7 (2003), pp. 1508–1515.

[63] M. A. Richards, J. Scheer, W. A. Holm, and W. L. Melvin. *Principles of modern radar*. Vol. 1. Citeseer, 2010.

[64] J. W. Goodman. "Statistical properties of laser speckle patterns". In: *Laser speckle and related phenomena*. Springer, 1975, pp. 9–75.

[65] S. K. Nayar, K. Ikeuchi, T. Kanade, et al. "Surface reflection: physical and geometrical perspectives". In: (1991).

[66] J. Bennett and L. Mattsson. "Introduction to Surface Roughness and Scattering 2nd edn (Washington, DC: Optical Society of America)". In: (1999).

[67] J. W. S. B. Rayleigh. *The theory of sound*. Vol. 2. Macmillan & Company, 1896.

[68] W. G. Rees. *Physical principles of remote sensing*. Cambridge university press, 2013, pp. 62–64.

[69] L. Rayleigh. "On the dynamical theory of gratings". In: *Proceedings of the Royal Society of London. Series A, Containing Papers of a Mathematical and Physical Character* 79.532 (1907), pp. 399–416.

[70] ISO22412:2017. *Particle size analysis – Dynamic light scattering (DLS)*. Standard. Geneva, CH: International Organization for Standardization, Feb. 2017.

[71] Zaereth. *A 5 mw green laser pointer beam profile, showing the TEM00 profile*. `https://de.wikipedia.org/wiki/Datei:Green_laser_pointer_TEM00_profile.JPG`. Accessed: 2022-09-02. 2012.

[72] G. Williams and D. C. Watts. "Non-symmetrical dielectric relaxation behaviour arising from a simple empirical decay function". In: *Transactions of the Faraday society* 66 (1970), pp. 80–85.

[73] P. Born, S. Reinhold, and M. Sperl. "Probing density waves in fluidized granular media with diffusing-wave spectroscopy". In: *Physical Review E* 94.3 (2016).

[74] A. Siegert. *On the fluctuations in signals returned by many independently moving scatterers*. Radiation Laboratory, Massachusetts Institute of Technology, 1943.

[75] J. W. Goodman. *Speckle phenomena in optics: theory and applications*. Roberts and Company Publishers, 2007.

[76] D. A. Weitz and D. J. Pine. "Diffusing wave spectroscopy". In: *Dynamic Light Scattering: The Method and Some Applications*. Ed. by W. Brown. Oxford: Oxford University Press, 1993, pp. 652–720.

[77] A. Ishimaru. *Wave propagation and scattering in random media*. Vol. 2. Academic press New York, 1978.

[78] P. Dixon and D. J. Durian. "Speckle Visibility Spectroscopy and Variable Granular Fluidization". In: *Physical Review Letters* 90.18 (May 2003). issn: 0031-9007. doi: 10.1103/PhysRevLett.90.184302.

[79] D. Goldman and H. Swinney. "Signatures of Glass Formation in a Fluidized Bed of Hard Spheres". In: *Physical Review Letters* 96.14 (Apr. 2006). issn: 0031-9007. doi: 10.1103/PhysRevLett.96.145702.

[80] N. Menon and D. J. Durian. "Diffusing-wave spectroscopy of dynamics in a three-dimensional granular flow". In: *Science* 275.5308 (1997), pp. 1920–1922.

3. Experimental setup for DLS on granular particles

A dynamic light scattering (DLS) setup consists of a laser light source, the sample which is to be illuminated, and a detection system which involves a correlator that is connected to a computer [1]. This configuration of items is used to record intensity fluctuations with time, and occasionally with space [2] of the light scattered by the sample. The on interference effects based intensity fluctuations are directly linked to the particles' motions within the observation volume and thus knowledge about the dynamics of the sample system may be retrieved.

The experimental setup used in later experiments of Chs. 4, 6 and 7 will be presented in Ch. 3.1. In order to show that the setup is well calibrated for DLS experiments, measurements with a colloidal suspension were taken as reference. The procedure will be presented in Ch. 3.2.

3.1. Hardware and alignment

In this chapter, the basic experimental setup for the experiments performed in this work is presented. Many thoughts and considerations were made in advance of assembling the setup which will be described in detail. Additionally, it should be mentioned here that the basics of this setup (i.e. camera equipment and DLS processing hardware) were initially chosen in view of light scattering measurements within the project "Soft Matter Experiments" (SOMEX) aboard the sounding rocket MAPHEUS and for drop tower campaigns at the Zentrum für angewandte Raumfahrttechnologie und Mikrogravitation

(ZARM) in Bremen, Germany. Therefore, some requirements were realized, which are necessary for microgravity (μg) experiments but are not in particular required for performing laboratory experiments. Additional information on this will be provided in the corresponding sections if necessary.

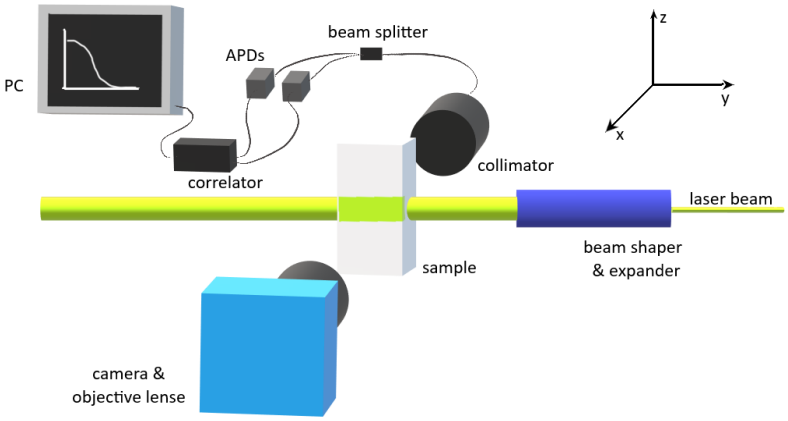

Figure 3.1.: The fundamental setup used from a side-view. The path of the laser light is shown by the green beam incident from the right-hand side. The width of that laser beam indicates the (un-)expanded condition of the beam. The camera, including a telecentric objective, as well as the collimator were mounted orthogonally to the laser's opto-mechanic axis but still in the same horizontal plane. The sample is placed in the center of the configuration where the laser's and collimator's opto-mechanic axes intersect. The light detection arrangement consists of a beam splitter, two Avalanche photo diodes (APD) and a correlator, which is attached to a computer (PC). The Cartesian frame of reference is depicted on the right-hand side.

3.1.1. Light scattering components

Fig. 3.1 shows all DLS devices that were used in the experimental setups in Chs. 4 to 6. The experiment starts with the laser beam, incident from the right, illuminating the sample. A laser is a coherent light source. Therefore, no random fluctuations of the light wave's phase due to a deterministic phase relation should be present. Based upon its monochromatic nature, laser light is a suitable source for revealing interference effects caused by particles scattering the light [1].

The vertically polarized laser Coherent Verdi G5 SLM [3] (rms noise <0.02%,

linewidth <5 MHz, power up to 5 W) with green light of wavelength λ =532 nm was used in the laboratory experiments and produces a laser beam with a Gaussian intensity profile. The beam will broaden for higher light intensities. For example, with a power of 1.5 W, the laser beam expands to approximately 3 mm width. If the diameter of the laser beam is small compared to the particle's diameter, the particle can not be completely illuminated. Since we aim for experiments on macroscopic particles of millimeter-sized diameters, we want to keep the observation volume, which is in the x- and z-dimension (cf. Fig. 3.1) directly determined by the laser beam width for single scattering experiments, as great as possible. However, a broadened Gaussian-shaped intensity profile does not provide a homogeneous illumination of the sample. The highest intensity is registered in the center of the distribution and lessens exponentially to the outer bounds. A Gaussian intensity profile would therefore entail an analysis of how the light intensity will vary across the entire observation volume. The intensity of the scattered light will then explicitly depend on a particle's position as well as its translational motion in the observation volume.

Therefore, a compact system of aspherical lenses was chosen to broaden and additionally shape the laser beam. The beam expander A|BeamExpander 532nm by Asphericon [4] is a combination of several lenses which may be selected and mixed freely for each application. The lense combination broadens, or, if used in the opposite way, focuses the laser beam with a set magnification factor. We chose two components with a magnification factor of 1.5 x and one of 2 x. This way, we were able to broaden the beam from approx. 3 mm to 14.7 mm for the operating laser with a power of 1.5 W. The modified width may be regarded as quite large compared to the particle diameters of approx. two millimeters in the experiments. The A|TopShape beam shaper by Asphericon [5] was installed in the back of the magnification lenses. This beam shaper ensures the most possible homogeneous illumination by using aspherical optics such that the Gaussian intensity profile is shaped to a so-called "flat top hat", comparable to a man's cylinder hat. Fig. 3.2 a) shows exemplarily the broadened laser beam propagating through a cuvette filled with a colloidal suspension. The measures of the cuvette are found in Ch. 3.2. For verifying the usage of these components in the setup, the photometer P501U by Westboro Photonics [6] was used to test wether we do use the correct configuration of magnification lenses and the shaper or if signi-

ficant abberations are present. The measurements show a clear flat top hat with well distributed intensity values, as presented in Fig. 3.2 b), such that the illumination of the sample may be considered homogeneous.

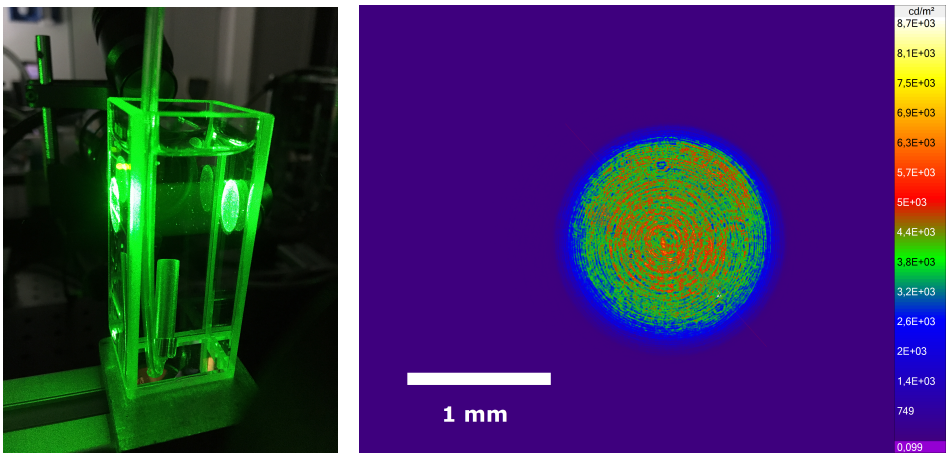

(a) (b)

Figure 3.2.: Left: A photo of the shaped and extended laser beam illuminating a colloidal suspension in a cuvette in the laboratory. The light is incident from the right and traverses the entire sample horizontally. Right: The with the photometer measured brightness of the broadened and shaped beam. The image shows the laser beam's top-hat profile. The scale bar indicates a distance of 1 mm. The color scale on the right gives the light intensity in cd/m^3.

The sample characteristics as well as the particle sizes and materials, which will be illuminated by the laser beam, vary from one experiment to another. Thus, they will be discussed separately in the corresponding sections.

In DLS experiments, the by the particles scattered light has to be detected with the same scattering vector irrespective of the positions of the particles in the expanded laser beam [1]. Therefore, light from a broad region of the laser volume needs to be collected. This is here achieved by using the 24 mm clear aperture fibre collimator 60FC-L-0-M100S-01 from Schäfter+Kirchhoff [7], which is installed in the same horizontal plane as the laser. The collimator is a spatial filter and will thus collect light only that is scattered parallel to its opto-mechanic axis. Due to the great aperture, the collimator collects light from a cylindrical volume with a base diameter larger than the width of the

laser beam. The vertical dimension of the detection volume is still specified by the laser beam's width. The collimator is placed several tens of centimeters apart from the actual sample. Thus, the collimator to sample distance is at least one order of magnitude greater than the particle size and the spatial scales on which the particles move. The collimator may be therefore considered to be located in the far-field such that we may assume the plane wave approach to be valid for this setup. The collimator is placed at an angle of 90° with respect to the incoming light. Thus, it detects in $\Theta = 90°$ scattered light and focuses it into a single-mode fiber. The fixed position at 90° was chosen due to practical reasons. When recording data in back-scattering direction, the probability that a great portion of only reflected and thus unscattered light is detected is quite high. If the detector is placed in transmission direction, additional studies of the absorption and mean free path of the sample must be performed. Here, $\Theta = 90°$ was selected since in that direction, the cuvette has a flat facet which avoids additional diffraction effects because of the cuvette's glass.

In order to avoid the detection of light that might have been scattered at any vessel's walls, the hardware linear polarizer LPVISC100 from Thorlabs [8] was installed in front of the collimator to maximize the dynamical contrast. The polarization direction of the laser and the polarizer are aligned perpendicular to the scattering plane. Due to this geometry, the experimental setup presented here is only sensitive to phase shifts that correspond to particle motions in x- and y-direction in the spatial plane of the laser-beam-collimator configuration, see Fig. 3.1. Thus, the probability to only detect light which has been scattered once in a 90° angle is maximized.

Another filter was installed in front of the collimator: the long pass filter FELH0500 [9] with cut-off wavelength of 500 nm by Thorlabs. That filter is supposed to only transmit light which has a wavelength greater than 500 nm. The longpass filter will assure, that no blue LED light, whose purpose will be discussed in Ch. 3.1.2, will pollute the DLS measurements.

The single-mode fiber, which is split into two parts by the beam splitter FBS-532-Y-011 532NM (Schäfter+Kirchhoff) [10], guides the light intensity information to two avalanche photo diodes (APD) ID QUANTIQUE ID100-MMF50-ULN from ID Quantique [11], (dark count rate < 20 Hz). The APDs transform the light signal into an

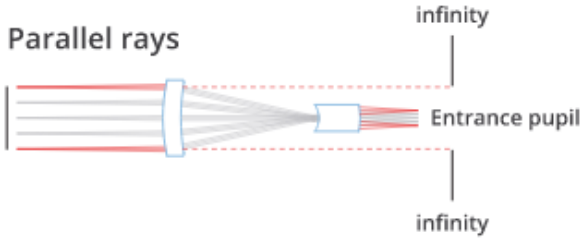

Figure 3.3.: Schematic drawing of the light ray propagation in a telecentric objective. Only rays parallel to the objective's opto-mechanic axis are collected and then focused. The entrance pupil lies in the infinite. [14]

electronical signal. That signal is then processed by the ALV-7002/USB correlator [12] (25 ns initial sampling time, 296 channels) which pseudo-cross-correlates [13] the detected fluctuations with a time resolution of 200 μs. The correlator provides the autocorrelation function $(g_2(\tau) - 1) \sim g_1(\tau)$ which is time-averaged over a full measurement run. The intensity trace of the entire measurement as well as the hardware autocorrelation function can then be accessed in the ALV software on a regular computer.

3.1.2. Camera and accessories

In order to fully understand the dynamics and every cause of a phase shift when probing samples with this setup, we want to verify our results visually and take photos with a high-speed camera simultaneously, or at least in the same experimental conditions. This enables to compare the information obtained from the DLS measurement with the information from image analysis. If both show equivalent results, we consider our setup to be well-calibrated.

First of all, an additional light source has to be installed such that the sample is illuminated sufficiently from all angles visible for the camera. For this purpose, we use LED diodes with a wavelength of 435 nm (blue) on the opposite side of the sample with respect to the incoming laser beam to achieve that necessary brightness. In the laboratory experiments, however, the LEDs were placed in a 45° angle off the opto-mechanic axis of the laser beam in the x-y-plane, such that no laser light which might has been reflected by the mounting of the LEDs, and then scattered another time on

the particle pollutes the DLS measurements (no multiple scattering). The particular wavelength for the LEDs was chosen to operate the DLS setup and the camera setup at the same time during the μg experiments aboard MAPHEUS or in the ZARM capsule. Other monochromatic LED light may be selected. The requirement is though that the light comprises a wavelength different of that of the laser light and that the corresponding long- or shortpass filter is installed. Due to the longpass filter in front of the collimator, the latter would only detect the scattered green light and, in our case, blue light would be only visible for the camera components.

The high-speed camera MotionBLITZ Cube 4 by Mikrotron [15] is a device with a Fast CMOS Sensor of the size 1,280 (H) x 1,024 (V) pixels or active area of 15.36 mm (H) x 12.29 mm (V). The physical size of the pixels is 12x12 μm such that it resolves images with 1.3 megapixel. The camera is able to record with up to 93,000 frames per second (FPS) depending on the size of the chosen region of interest (ROI). In case of full coverage of the sensor, the camera is able to record with 25-1,010 FPS which equals a temporal resolution of max. 0.99 ms. The recording time depends, due to the big amount of produced data that is supposed to be transferred, as well on the size of the ROI as on the number of FPS. For full resolution, measurements of 3.24 s may be performed, which are sufficient for our purposes. The shutter time may be selected from 2 μs to 1/FPS. The recorded data is transferred via the camera's Gigabit-Ethernet interface, that allows up to 1,000 MBit/s, to a standard computer.

In the following, the objective lense will only be called "objective" for abbreviation. The telecentric objective TC3MHR024-C by Opto Engineering [16] (length: 17.7 cm, aperture's diameter: 4.4 cm) was chosen to complete the visual observation system. Telecentric objectives are used to restrict the effects of perspective distortions. The entrance pupil is considered to be located in the infinite such that only those rays or beams, whose barycentric ray are exactly parallel to the opto-mechanic axis, are collected. Fig. 3.3 shows the functioning of a telecentric objective schematically with the light incident from the left. The objective's front diameter needs to be at least as big as the diagonal of the object field. Also, the image scale should not change when the object is moved axially. Thus, the feature of the image should always appear to have the same size independent of the object's distance to the objective. However,

since there is always a depth of focus plane for any objective, telecentric objectives also have a sector, where the object will be in the focus. If the object is found outside of the depth of focus, it will maintain its size but will appear blurry. The degree of blurriness increases with distance to the plane with maximum focus. This circumstance allows to observe the particle motion in systems with many granular particles in the dimension of the image depth, such that not only the lateral and vertical particle motion, but also the motion towards the detector would be determinable.

This objective was manufactured for camera sensors up to the size of 1.1" and 25.11 mm x 18.39 mm respectively. The effective f-stop is specified as 11. The operating distance determines which part of the sample lies within the depth of focus which is in our case only approx. 1.8 mm wide. The operating distance of this objective is 6.72 cm according to the manufacturer, which may be considered rather short. That short operating distance was necessary to fit the MAPHEUS rocket dimensions. Further, the short operating distance serves the fact that the closer the objective is positioned with respect to the object, the bigger the object will appear on the sensor due to the larger image section. Thus, the pixel density per object is higher. The aim here is to efficiently analyze the motion of the scatterers on photos to compare that information with the results from the light scattering measurements. Therefore, a high pixel density of a particle is necessary to guarantee a good resolution of the spatial motion of the particle but also of its surficial features.

We increased the pixel density per particle further by using the crop factor Ξ of the objective-camera-sensor combination [17–19]. Also called the "focal length multiplier", it will increase the aspect ratio of the objects on the camera's sensor. The crop factor does not physically change parameters, it will only alter the perspective, when a camera sensor of certain dimensions is combined with an objective of dimensions inappropriate for the sensor. The crop factor is the ratio of the size of the diagonal of a frame w.r.t the size of the sensor's diagonal:

$$\Xi = \frac{d_{\text{image}}}{d_{\text{sensor}}} \tag{3.1}$$

Usually, an objective is supposed to illuminate the entire area of the camera sensor. If an objective that has been constructed for a smaller sensor (f.ex. 2/3") but is used

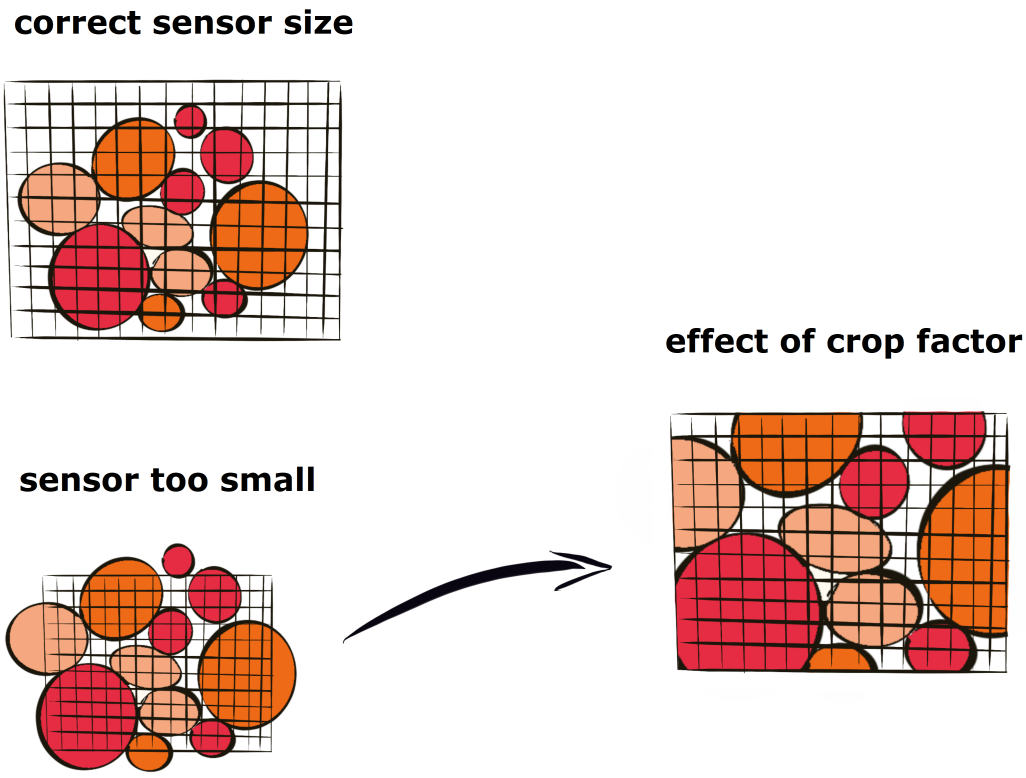

Figure 3.4.: The effect of the crop factor on an image. The grid superposing the actual image indicates the camera's sensor size compared to the image size. Both colored images on the left side have identical dimensions. The top left image is generated if the correct objective for a specific camera sensor is used. If the sensor is too small (bottom left), the image produced by the objective exceeds the sensor dimensions. The image that is mapped onto the sensor (right figure) is cropped. However, the cropped section is then mapped with a higher pixel density compared to the uncropped image. Thus, particular features may be investigated more accurately.

with a greater sensor (f.ex. 4/3"), not all pixels will be illuminated and vignetting is the consequence. If an objective, which was manufactured for a camera with a greater sensor size, is mounted to a camera with a smaller sensor size, we increase the apparent image size, see Fig. 3.4. A feature in the actual image, which has a discrete size, will then appear greater on the sensor, such that the margins of the projected image will not fit onto the sensor anymore and the overall image seems isotropic stretched. The information from the marginal image regions is lost. However, a feature in the mapped part of the image is then enlarged in the sense that more pixels represent this feature than in the case of a camera objective size fitting to sensor size. This way, we are able to increase our apparent resolution, which is not the actual physical resolution of the sensor, since the pixel size and the number of pixels, which add to the sensor, are hardware features and remain the same.

3.2. Validation experiment with a colloidal suspension

In order to test that the setup and the considerations made above for its functioning are sufficient and valid for DLS experiments, a calibration experiment was realized. A colloidal suspension was probed to show, that the standard DLS theory applies. The scatterers were observed in a OG740 cuvette from Hellma with a volume of 100 ml and measures of 10 x 5 x 3 cm^3. The cuvette was filled with filtered and deionized water to limit the contamination of the sample by suspended solids from tab water, which would contribute to the decay of the autocorrelation function in an unintended way.

The deionized water was mixed with 0.1 ml of diluted silica spheres (SiO_x 108) of an approximate diameter of 100 μm. The filled cuvette was placed in the center of the observational plane of the setup, see Fig. 3.1. The center is found where the elongated opto-mechanic axes of the laser beam and the collimator intersect. Due to the milky appearance of the solution indicating a high number of contained scattering entities, we expect to have a sufficient signal strength when already using smaller laser light intensities. Here, we choose a laser power of 400 mW. The ALV correlator will provide the autocorrelation function $(g_2(\tau) - 1) \sim g_1(\tau)$.

In DLS measurements with colloids, we expect a random walk of the particles due to

thermal fluctuations in the dilute sample. Since a sufficient amount of thousands of colloidal particles for good Gaussian statistics [20] is assured in only one drop of the concentrated colloid solution, the autocorrelation function is expected to ideally decay from 1 to 0.

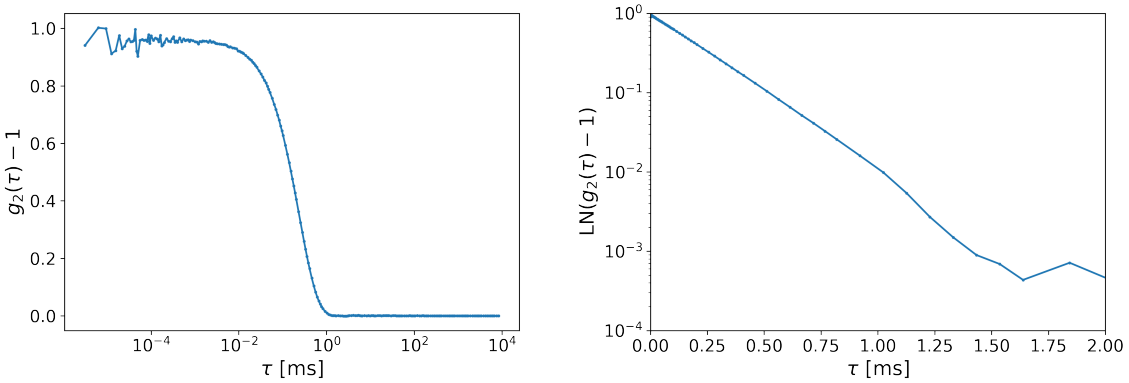

(a) (b)

Figure 3.5.: Left: The by the ALV correlator measured autocorrelation function $g_2(\tau) - 1$ of a colloidal suspension (diluted SiO_x 108 spheres) showing an exponential decay from 1 to 0. The setup was arranged as described in Fig. 3.1. Right: The graph shows the autocorrelation function on a linear x- and a logarithmic y-axis, which decays linearly up to 1 ms.

In Fig. 3.5 a), we see the expected decay from the experiment. The autocorrelation function has an intercept value of approximately 0.95 to 1.0 and decays to zero at about 1 ms. Expecting an exponential decay, which may be described by Eq. 2.73 by Williams and Watts [21], we can extract the decay parameter of the exponent t by:

$$\ln(g_2(\tau) - 1) = \ln\left(e^{-\frac{t}{\tau}}\right) = -\frac{t}{\tau} \tag{3.2}$$

In the logarithmic representation of the exponential function on linear time scales in Fig. 3.5 b), the function decays linearly up to 1 ms, which indicates a linear relation between the exponent and the logarithm of the autocorrelation function, as described by Eq. 3.2. If the colloidal particles are assumed to perform Brownian motion, we

know from Eq. 2.71 that the suitable exponential fit may be rewritten as

$$g_2(\tau) - 1 = e^{-q^2 D\tau} = e^{-\frac{q^2}{6}\langle \Delta r^2(\tau)\rangle}. \tag{3.3}$$

q is found by $q = \frac{4\pi\eta}{\lambda}\sin\left(\frac{90°}{2}\right)$ for our experiment where the collimator is located at 90°. If we then apply the logarithm to the equation above we receive the mean squared displacement

$$\langle \Delta r^2(\tau)\rangle = -\frac{6}{q^2}\ln(g_2(\tau) - 1). \tag{3.4}$$

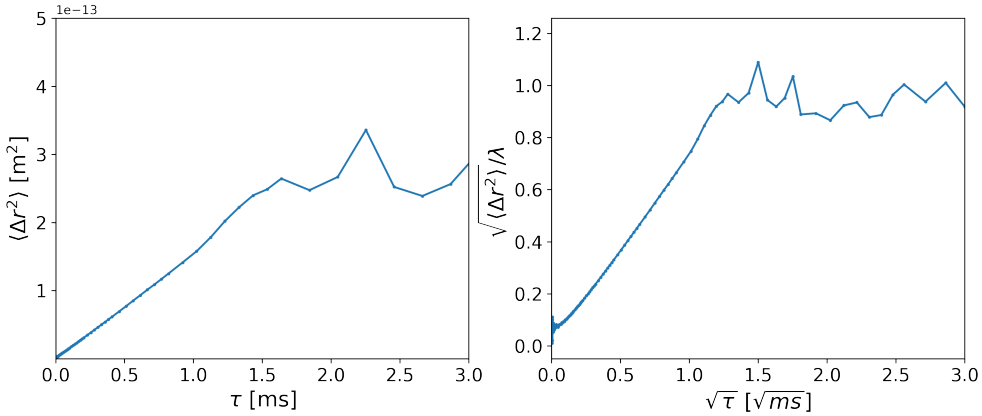

Figure 3.6.: Here, the calculated mean squared displacement (MSD) $\langle \Delta r^2\rangle$ for silica particles dissolved in filtered and ionized water is presented. On the left side, the results with the corresponding scale in m^2 are provided. On the right side, the root of the MSD was extracted to give information in form of a distance in meters, which was normalized by the wavelength λ.

The mean squared displacement for silica particles with an approximated diameter of 100 μm is presented in Fig. 3.6. We see a linear slope for short time lags up to $\tau = 1$ ms, which then converts into a plateau of $\approx 3 \cdot 10^{-13} m^2$. From Eq. 3.3, we assume that $D\tau \cong \lambda$. According to Egelhaaf [22], the autocorrelation function should decay to $\frac{1}{e}$ after the particles have moved at least a wavelength which is in our case $\lambda = 532$ nm. From the graph on the right-hand side in Fig. 3.6, we see that our apparatus is able to resolve motions of distances of approx. 0 to λ. This is shown by the average value of ≈1 for $\sqrt{\tau} > 1\sqrt{\text{ms}}$ when normalizing the square root of the MSD, which reflects a travelled distance, by the wavelength of λ.

In conclusion, the setup is able to produce data from a colloidal suspension with DLS, which may be interpreted as an analysis of the Brownian motion of the scatterers. The particles move linearly for approx. 1 ms until the signal converts into noise. Thus, this experiment validated that this setup is suitable for performing DLS measurements.

References

[1] B. J. Berne and R. Pecora. *Dynamic light scattering: with applications to chemistry, biology, and physics*. Courier Corporation, 2000.

[2] J. C. Marron and K. S. Schroeder. "Speckle from rough rotating objects". In: *Applied optics* 27.20 (1988), pp. 4279–4287.

[3] I. Coherent. *Verdi G SLM-Series*. https://www.coherent.com/content/dam/coherent/site/en/resources/datasheet/lasers/COHR_VerdiG_SLM-Series_DS_0220_1.pdf. Accessed: 2023-01-14. 2020.

[4] asphericon GmbH. *Beam Expansion: a|BeamExpander*. https://www.asphericon.com/en/products/beamtuning/beamexpansion. Accessed: 2023-01-14. 2022.

[5] asphericon GmbH. *Aspheric laser beam shaper: a|TopShape*. https://www.asphericon.com/en/products/beamtuning/beamshaping. Accessed: 2023-01-14. 2022.

[6] W. Photonics. *Imaging Photometer: P230U, P501U, P1230U*. https://wphotonics.com/wp-content/uploads/WP_-Smart_Series_Photometers_07-2020.pdf. Accessed: 2023-01-14. 2011.

[7] Schäfter+Kirchhoff. *Fiber Collimators*. http://probceff4.pic9.websiteonline.cn/upload/fk60fc_e.pdf. Accessed: 2023-01-14. 2017.

[8] I. Thorlabs. *LPVISC100 - Ø25.0 mm Unmounted Linear Polarizer, 510 - 800 nm*. https://www.thorlabs.com/thorproduct.cfm?partnumber=LPVISC100. Accessed: 2023-01-14. 2023.

[9] I. Thorlabs. *FELH0500 - Ø25.0 mm Premium Longpass Filter, Cut-On Wavelength: 500 nm*. https://www.thorlabs.com/thorproduct.cfm?partnumber=FELH0500. Accessed: 2023-01-14. 2023.

[10] Schäfter+Kirchhoff. *Fiber Collimators*. http://probceff4.pic9.websiteonline.cn/upload/fk60fc_e.pdf. Accessed: 2023-01-14. 2017.

[11] P. S. Ltd. *id100 series: single-photon detectors for visible light with best-in-class timing accuracy*. https://www.photonicsolutions.co.uk/upfiles/id100series.pdf. Accessed: 2023-01-14. 2022.

[12] ALV-GmbH. *ALV-MultiCorr Series Multiple Tau Digital Correlators*. https://www.alvgmbh.de/dwnload/alv7000specs.pdf. Accessed: 2023-01-14. 2014.

[13] ALV-GmbH. *PMT or APD based "Pseudo" Cross Correlation Detectors*. https://www.alvgmbh.de/Products/PMTs___APDs/Cross/cross.html. Accessed: 2023-01-14. 2014.

[14] Opto-Engineering. *Tutorial: Objektive der Telezentrie*. https://www.opto-e.de/ressourcen/tutorial-telezentrische-objektive. Accessed: 2022-08-15. 2022.

[15] M. GmbH. *High-Speed Recording Cameras MotionBLITZ Cube4*. https://www.daheng-imaging.com/uploadfile/2021/0804/20210804011646351.pdf. Accessed: 2023-01-14. 2022.

[16] Opto-Engineering. *TC3MHR024-C*. https://www.opto-e.com/de/produkte/tc3mhr-series/TC3MHR024-C. Accessed: 2023-01-14. 2022.

[17] T. Ang. *Advanced Digital Photography*. Amphoto Books, 2003. url: https://books.google.de/books?id=jVDD2B4chAoC.

[18] Wikipedia. *Crop factor*. https://en.wikipedia.org/wiki/Crop_factor. Accessed: 2023-01-02. 2022.

[19] D. Heller. *Digital Travel Photography*. A Lark Photography Book Series. Lark Books, 2007. isbn: 9781579909734. url: https://books.google.de/books?id=vX7sdIHrFPQC.

[20] J. W. Goodman. "Statistical properties of laser speckle patterns". In: *Laser speckle and related phenomena*. Springer, 1975, pp. 9–75.

[21] G. Williams and D. C. Watts. "Non-symmetrical dielectric relaxation behaviour arising from a simple empirical decay function". In: *Transactions of the Faraday society* 66 (1970), pp. 80–85.

[22] S. U. Egelhaaf. "Solution Scattering". In: *Soft condensed matter physics in molecular and cell biology*. Taylor & Francis, 2006, p. 38.

4. Isolation of a single macroscopic scatterer's translational and rotational motion

In this chapter, the impact that only a single macroscopic particle has on the recorded intensity autocorrelation functions (IACF) shall be determined. Due to its increased size, and therefore increased structural complexity, with respect to particles with dimensions comparable to the wavelength of light, distinct features in the IACF caused by the particle's motion are expected.

The within the frame of this thesis performed studies presented here were already published in Dossow et al. [1] such that it may be consulted as main reference. Additional references will be particularly highlighted. Two fundamental principles should be clarified with the following experiments, where conditions are produced such that only a single macroscopic scatterer may be observed at a time. First, we want to know if a single particle is scattering the light sufficiently such that it is detectable by the detector and that the motion of only a single scatterer may be investigated. The occurrence of the specific motional attribute of the periodicity will also be reviewed. Second, we want to investigate, if distinct optical properties of several types of macroscopic scatterers are observable and how they affect the measured autocorrelation function.

In the following section (Ch. 4.1), the idea of the investigation of a single macroscopic particle based on the concept of number fluctuations [2] is presented. Ch. 4.2 discusses the experimental setup used to perform the calibration experiment with air bubbles in Ch. 4.3 as well as the experiments with hard sphere scatterers composed of distinct

materials in Ch. 4.4. A conclusion about the findings will be drawn in Ch. 4.5.

4.1. The concept

The theory presented here is based on the concept of number fluctuations of a sample's scattering entities that contribute to the decay of the autocorrelation function (see Berne and Pecora [2] for reference). In a homodyne spectrum, for very dilute solutions the time-dependent intensity autocorrelation function consists of a sum of two components

$$g_2(\vec{q},t) = \langle N\rangle^2[1 + |F_s(\vec{q},t)|^2] + \langle \delta N(0)\delta N(t)\rangle \tag{4.1}$$

The first term describes the Gaussian approximation consisting of the intermediate scattering function $F_s(\vec{q},t)$, cf. Eq. 2.89, and the average number of scatterers $\langle N\rangle$. This term comprises information about the interference effects resulting from the scattering processes. The second term, called "extra term" or "probability after-effect function" [3], provides information about the deviation from the first term based on fluctuations of the particle numbers $\delta N(t)$ within the scattering volume. Those fluctuations should occur on scales of τ that represent the time a particle would need to cross that scattering volume. The Gaussian approximation term however, will decay on time scales τ_q that equal the time a particle needs to move a distance of q^{-1} with q being the absolute value of the scattering vector. Since $\tau_q \ll \tau$, the autocorrelation function should decay in two stages. For multiple particle systems having a sufficient concentration, the autocorrelation function will then decay as

$$g_2(\vec{q},t) = \begin{cases} 2\langle N\rangle^2 + \langle N\rangle & \text{if } t = 0 \\ \langle N\rangle^2 + \langle N\rangle & \text{if } \tau_q \ll t \ll \tau \\ \langle N\rangle & \text{if } t \gg \tau \end{cases} \tag{4.2}$$

The correction factor for less concentrated solutions is $\langle N\rangle^{-1}$. [2]

The dependency on the scattering vector $\vec{q}$ will be neglected in the following, since

$\Theta = 90°$ and thus $|\vec{q}| = q$ is always a fixed value in the experiments performed below. If we only consider a single particle such that N=1 in Eq. 2.64, we see that the scattered intensity becomes independent of $\vec{r}_j(t)$ and thus the electric field E(t) becomes time-independent. The intensity from a single particle I^P in the scattering volume turns out as

$$I^P = E(t)E^*(t) \propto |E_1|^2 \tag{4.3}$$

with the subscript 1 indicating a single particle. Here, the particle is considered to be spherical for simplicity. If the intensity of a single particle should still fluctuate this must be the consequence of time-dependent changes of the scattered electric field's amplitude $E_1(t)$. The reason may be structural anomalies like impurities, odd shapes, i.e. deviations from a perfect sphere, or features on the particle surface, which move within the scattering volume, becoming detectable by e.g. the particle rotating with an angular frequency $\vec{\omega}_j(t)$. The time-dependence may then be expressed as

$$I^P(t) = E(t)E^*(t) \propto |E(t)|^2 \tag{4.4}$$

Therefore, the individual motion of the particle as e.g. rotation, vibration or the deformation of soft particles resulting in for example oscillations caused by relaxation, should result in intensity fluctuations.

4.1.1. The blinking

In the following experiments, the effect of the presence of the particle only and the intensity fluctuations resulting from this is analyzed. Due to the horizontal orientation of the scattering plane as described in chapter 3 we know, that our setup is only sensitive to horizontal motions and not to vertical motions. Thus, the detector should only perceive the transition of a scatterer through the scattering volume from bottom to top (rising) or vice-versa (falling) as sudden flash or "blinking". The blinking describes

a sudden change of the scattered light intensity I(t) linked to the particle's presence

$$I(t) = N(t) \cdot I^P(t) \tag{4.5}$$

N(t) represents the number fluctuations [2], switching between 1, if a particle is currently located within the scattering volume, and 0 if there is no scatterer present. The duration of the blinking is determined by the transit velocity of the individual particle. Due to the great size of the particle, it may be only partially illuminated when entering or leaving the laser beam such that in those situations $0 < N(t) < 1$.

However, with a realistic intensity trace, the intensity will fluctuate between $I^P(t)$ and $I^n(t)$, since there will always be some intensity contribution caused by background noise, denoted by the subscript n, present. The number fluctuation function then changes to

$$N(t) = \begin{cases} 1 & \text{if there is a scatterer} \\ \frac{I^n}{I^P} & \text{if there is no scatterer} \end{cases} \tag{4.6}$$

The scattered light's intensity fluctuations may then be analyzed by the time-averaged autocorrelation $g_2(\tau)$, cf. Ch. 2.3.2:

$$g_2(\tau) = \frac{\langle I(t) \cdot I(t+\tau) \rangle}{\langle I(t) \rangle^2} \tag{4.7}$$

With Eq. 4.5, the equation above may be written as

$$g_2(\tau) = \frac{\left\langle N(t) \cdot I^P(t) \cdot N(t+\tau) \cdot I^P(t+\tau) \right\rangle}{\langle N(t) \cdot I^P(t) \rangle^2} \tag{4.8}$$

$$= \frac{\langle N(t) \cdot N(t+\tau) \rangle}{\langle N(t) \rangle^2} \cdot \frac{\langle I^P(t) \cdot I^P(t+\tau) \rangle}{\langle I^P(t) \rangle^2} \tag{4.9}$$

$$= g_2^N(\tau) \cdot g_2^P(\tau) \tag{4.10}$$

The simplification from Eq. 4.8 to Eq. 4.9 involves the assumption that the intensity scattered by the particle in the laser beam and the blinking function are stochastically

independent such that $\langle N(t) \cdot I^P(t)\rangle = \langle N(t)\rangle \cdot \langle I^P(t)\rangle$. Eq. 4.10 describes the general form of the intensity autocorrelation function caused by blinking. This equation, however, states that if one tries to isolate the scattering intensity of a single particle $g_2^P(\tau)$, the division of $g_2(\tau)$ by $g_2^N(\tau)$ will amplify the noise for data segments where $g_2^N(\tau)$ is small.

Therefore, we use an alternative approach by taking a closer look at the fluctuation terms of the autocorrelation function $g_2(\tau)$. Here, only important steps in the calculation are presented. The full solution method is included in the appendix of Dossow et al. [1]. The fluctuations can be described by $\delta N(t) = N(t) - \langle N(t)\rangle$ and $\delta I^P(t) = I^P(t) - \langle I^P(t)\rangle$ with the average values of the fluctuations being $\langle \delta N(t)\rangle = \langle \delta I^P(t)\rangle = 0$. The numerators of Eq. 4.9 may then be rewritten as

$$\langle N(t) \cdot N(t+\tau)\rangle = \langle N(t)\rangle^2 + \langle \delta N(t)\delta N(t+\tau)\rangle \tag{4.11}$$

$$\left\langle I^P(t) \cdot I^P(t+\tau)\right\rangle = \langle I^P(t)\rangle^2 + \langle \delta I^P(t)\delta I^P(t+\tau)\rangle \tag{4.12}$$

The multiplication of both properties will result in four terms

$$\langle N(t) \cdot N(t+\tau)\rangle \cdot \langle I^P(t) \cdot I^P(t+\tau)\rangle \tag{4.13}$$

$$\begin{aligned} &= \langle N(t)\rangle^2 \langle I^P(t)\rangle^2 + \langle I^P(t)\rangle^2 \langle N(t) \cdot N(t+\tau)\rangle \\ &+ \langle N(t)\rangle^2 \left\langle I^P(t) \cdot I^P(t+\tau)\right\rangle + \langle N(t) \cdot N(t+\tau)\rangle \left\langle I^P(t) \cdot I^P(t+\tau)\right\rangle \end{aligned} \tag{4.14}$$

If we expect $\langle N(t) \cdot N(t+\tau)\rangle$ to decay to 0 much slower than $\left\langle I^P(t) \cdot I^P(t+\tau)\right\rangle$, the first term may be replaced by its initial value at $\tau = 0$ resulting in $\langle N(t)\rangle^2$. If we then implement this result in Eq. 4.9, the intensity autocorrelation may be expressed alternatively as

$$g_2(\tau) = 1 + \frac{\langle \delta N(t)\delta N(t+\tau)\rangle}{\langle N(t)\rangle^2} + \left(1 + \frac{\langle \delta N(t)^2\rangle}{\langle N(t)\rangle^2}\right) \frac{\langle \delta I^P(t)\delta I^P(t+\tau)\rangle}{\langle I^P(t)\rangle^2} \tag{4.15}$$

In order to receive $g_2(\tau) - 1$ instead of only $g_2(\tau)$, we subtract 1 from both sides of the equation and finally rephrase all components of Eq. 4.15 for simplicity to

$$g_2(\tau) - 1 \quad \equiv \quad g_2^{\delta N}(\tau) + \left(1 + g_2^{\delta N}(0)\right) \cdot g_2^{\delta I^p}(\tau). \tag{4.16}$$

This expression provides a suitable form to isolate the contributions of blinking and of the scattering of single particles. We see that $g_2^{\delta I^P}$ is linked to the initial blinking value added a value of 1. For the extraction of $g_2^{\delta N}(\tau)$, a proper understanding of the functional form of the decay function is necessary. When a suitable expression is retrieved, the data may be fitted with the analytical function and $g_2^{\delta I^P}(\tau)$ may be separated by the use of Eq. 4.16. That functional form shall be identified in the subsequent section Ch. 4.1.2.

4.1.2. The shape of the expected autocorrelation function's decay

A vertical transition of the particle through the laser beam volume implicates a gradual intensity increase and decrease, respectively, when the particle that enters or leaves the laser beam has a finite diameter. Therefore, we expect an intensity signal of trapezoidal shape, where the plateau represents the time of full illumination of the particle in the measured intensity trace and the flanks showing that gradual transition between the laser beam and regions without light. The transition of a falling particle is visualized in Fig. 4.1 with the time passing by from the left of the image to the right. However, if the laser beam is small compared to the particle radius, rather Gaussian shaped, or the particle is just passing segments of the beam, the trapezoidal shape will merge into a triangular shape with a constant in- and decrease of the light intensity and peaking in a maximum value.

Since the intensity signal is assumed to have a trapezoidal shape, the autocorrelation function $g_2(\tau) - 1$ should then have the shape of the autocorrelation function of a trapezoid. The extended solution to the calculation of the analytic expression of the autocorrelation function of a trapezoid may be found in the appendix of Dossow et al. [1]. The most important steps are presented below.

Temporal autocorrelation functions are a measure of the correlation between observations of a time series which are separated by time units or time steps τ. The blinking (see Ch. 4.1.1), here called $g(\tau)$ for brevity, may be described generally as

$$g(\tau) \equiv \langle N(t)N(t+\tau)\rangle = \frac{1}{2T}\int_{-T}^{T} N(t)N(t+\tau)dt \tag{4.17}$$

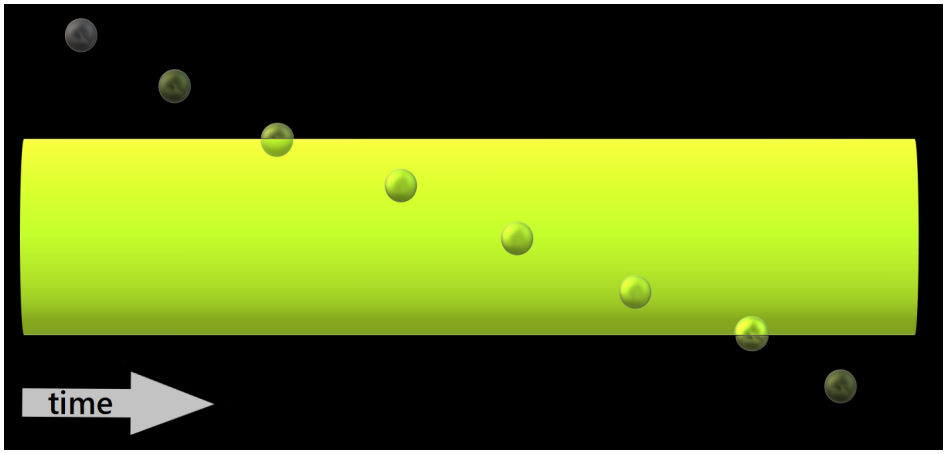

Figure 4.1.: This schematic sketch shows a stroboscobic image of a scatterer falling through the laser beam. The time passes from left to right in the picture. The particle is partially illuminated when approaching or leaving the beam. Maximum brightness is achieved within the laser beam volume. The degree of illumination of the particle is given by the distinct shades of green.

where the function N(t) is defined over the temporal interval [-T,T].

A trapezoid is the result of the crosscorrelation of two differently sized rectangular functions, as visualized in Fig. 4.2 a). So, the autocorrelation function of a trapezoid could be determined by the autocorrelation function of the crosscorrelation function of those two rectangle pairs (cf. Fig. 4.2 b)). Alternatively, we also know that a triangle is the result of the autocorrelation function of two rectangles. Therefore, the autocorrelation function of a trapezoid may also be expressed by the crosscorrelation of two triangles (cf. Fig. 4.2 c)). The relations between the rectangles, triangles and trapezoids thus allow to draw connections between their length and height parameters with the appropriate conversions. This way, we are able to draw conclusions about the signal shape, and thus the particle illumination time, from the fit of the autocorrelation functions.

In the following, we will first address the autocorrelation functions of simple geometrical shapes, in particular a rectangle and a triangle. Afterwards, the crosscorrelations of those geometries with different spatial dimensions are discussed, leading to the shape of a trapezoid and its autocorrelation function based on the former obtained expressions.

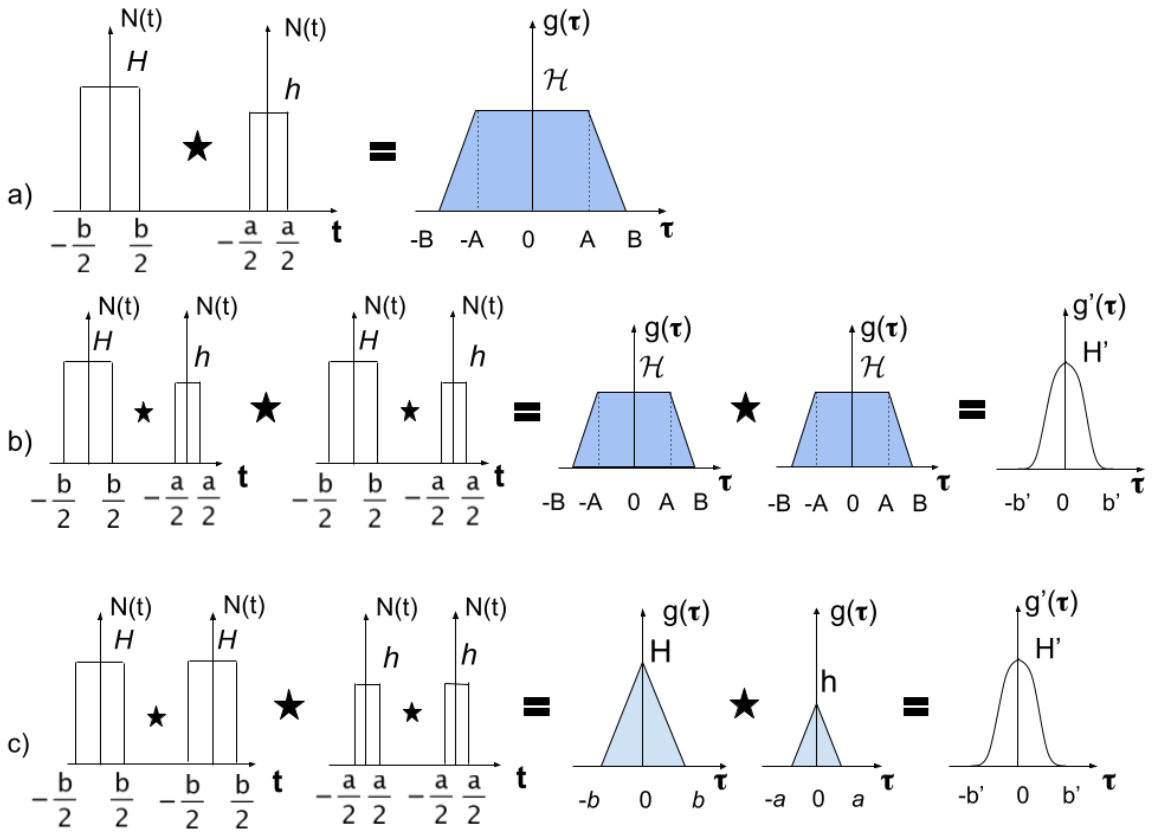

Figure 4.2.: Overview of the correlation functions of different geometries. The symbol $\star$ indicates the convolution of both geometries. $g(\tau)$ indicates the correlation function of two signals N(t). If $g(\tau)$ is correlated with another correlation function, the thereby resulting correlation function is named $g'(\tau)$. a) shows the crosscorrelation of two differently sized rectangular signals resulting in a trapezoid. b) shows the autocorrelation of the convolution of both rectangles from a), which is also equal to the autocorrelation of a trapezoid. c) shows the alternative calculation with respect to b) by calculating the crosscorrelation of either the autocorrelations of two differently sized rectangular signals or the crosscorrelation of two differently sized triangular signals. [1]

Autocorrelation function of a rectangular signal

When correlating two similar rectangular signals of the form

$$N_{rect}(t) = \begin{cases} H & \text{if } |\tau| \leq \frac{b}{2} \\ 0 & \text{else} \end{cases} \tag{4.18}$$

with a height H, a half-width of $\frac{b}{2}$ (see Fig. 4.2c)) such that the signal is only being defined between $-\frac{b}{2} \leq t \leq \frac{b}{2}$, the correlation function will be according to Eq. 4.17 a triangular function of half-width b and height H

$$g_{rect}(\tau) = \frac{bH^2}{2T}\left(1 - \frac{|\tau|}{b}\right) \tag{4.19}$$

for $0 \leq |\tau| \leq b$ and $g_{rect}(\tau) = 0$ elsewhere. A rectangular signal may be considered a good representation of the problem, if the particle passing the laser beam is quite small compared to the width of the laser beam, such that gradual illumination when entering or leaving the laser may be neglected. Additionally, the particles need to be fast in this case.

Autocorrelation function of a triangular signal

Due to the geometry of a triangle, the discontinuity happening at t=0 needs to be covered carefully. The shape of

$$N_{\text{tri}}(t) = H^2\left(1 - \frac{|t|}{b}\right) \tag{4.20}$$

is represented by height H and half-width b for $0 \leq |t| \leq b$ (elsewhere $N_{\text{tri}}(t) = 0$). When integrating the signals according to Eq. 4.17, the discontinuity at $t = 0$ provokes two distinguishable cases depending on the magnitude of τ. If $\tau \leq b - t$ the discontinuity will not be crossed, but if $\tau \geq b - t$ it will be passed such that an appropriate description

is necessary:

$$g_{\mathrm{tri}}(\tau) = \begin{cases} \frac{H^2}{2Tb^2}\left(\frac{|\tau|^3}{2} - b|\tau|^2 + \frac{2}{3}b^3\right) & \text{if } 0 \leq |\tau| \leq b \\ -\frac{H^2}{12Tb^2}(|\tau|^3 - 2b)^3 & \text{if } b \leq |\tau| \leq 2b \end{cases} \tag{4.21}$$

For time shifts τ greater than 2b, no correlation exists. The triangular signal type applies for very large particles transiting the laser beam where a constant gradient is present. The autocorrelation function of a triangle signal is a bell-shaped function with a maximum height of $\mathfrak{H} = \frac{bH^2}{3T}$ and a half-width of 2b with an inflection point at b. However, the correlation of two differently sized triangles will result in a differently shaped bell-like function equal to the autocorrelation function of a trapezoid signal.

Autocorrelation function of a trapezoidal signal

If we want to derive an expression for the autocorrelation function of a trapezoid-shaped signal we have two options as stated before. The first option presented is the derivation by the correlation of two correlation pairs of two differently shaped rectangular functions each as presented in Fig. 4.2 b). But, due to the possible commutation of correlations

$$\begin{aligned} g_{\mathrm{trap}} &= N_{\mathrm{trap}} \star N_{\mathrm{trap}} \\ &= (N_{\mathrm{rect}_1} \star N_{\mathrm{rect}_2}) \star (N_{\mathrm{rect}_1} \star N_{\mathrm{rect}_2}) \\ &= (N_{\mathrm{rect}_1} \star N_{\mathrm{rect}_1}) \star (N_{\mathrm{rect}_2} \star N_{\mathrm{rect}_2}) \\ &= N_{\mathrm{tri}_1} \star N_{\mathrm{tri}_2} \end{aligned}$$

we may take the short cut by cross-correlating two triangles of different sizes (as shown in Fig. 4.2 c). The symbol $\star$ indicates the convolution of the quantities. The subscripts 1 and 2 denote the two differently sized signals, respectively. The triangular signals are then defined similar to Eq. 4.20, for both types 1 and 2, in the limits from 0 to either a or b, respectively.

$$N_{\mathrm{tri}_1}(t) = h\left(1 - \frac{|\tau|}{a}\right) \qquad \text{for } 0 \leq |t| \leq a \tag{4.22}$$

$$N_{\mathrm{tri}_2}(t) = H\left(1 - \frac{|\tau|}{b}\right) \qquad \text{for } 0 \leq |t| \leq b \tag{4.23}$$

Elsewhere, $N_{\mathrm{tri}_1}(t)$ and $N_{\mathrm{tri}_2}(t)$ equal zero. The crosscorrelation according to Eq. 4.17 is defined by

$$g_{\mathrm{trap}}(\tau) = \frac{1}{2T}\int_{-T}^{T} N_{\mathrm{tri}_1}(t) N_{\mathrm{tri}_2}(t+\tau)dt \tag{4.24}$$

Here, one needs to be cautious about the relative sizes between N_{tri_1} and N_{tri_2} because this will significantly influence the shape of the resultant correlation function. If the width 2a of N_{tri_1} is significantly smaller than the width 2b of N_{tri_2} such that $a < (b-a)$, the crosscorrelation function would be the same as if the autocorrelation function of a trapezoid with a broader plateau with respect to its flank widths was calculated. If the triangles have significantly distinct sizes, the rectangular signals which are the basis for the triangular signals, would also have strongly differing dimensions. A trapezoid with a broader plateau and narrow flanks would then be the result. If however the flanks are much broader such that the plateau is respectively narrow, the two triangle signals may be expected to have similar dimensions as $a > (b-a)$.

The resulting correlation functions for both geometries are then calculated by taking into account the geometrical discontinuities of the signal types such that four cases for the step size magnitude $|\tau|$ ought to be calculated. For the ACF, where the width and the height of signal 1 is much smaller than signal 2, we obtain:

$$g_{\mathrm{trap}_{1\ll 2}}(\tau) = \begin{cases} \frac{\mathrm{hH}}{6abT}\left(\tau^3 - 3a\tau^2 + 3a^2b - a^3\right) & \text{for } 0 \le |\tau| \le a \\ \frac{\mathrm{hH}}{2bT}\left(a(b-\tau)\right) & \text{for } a < |\tau| \le (b-a) \\ \frac{\mathrm{hH}}{2abT}\left(\frac{\tau^3}{6} + \frac{a-b}{2}\tau^2 - \frac{a^2+2ab-b^2}{2}\tau \right. & \\ \left. + \frac{a^3+3a^2b+3ab^2-b^3}{6}\right) & \text{for } (b-a) < |\tau| \le b \\ \frac{\mathrm{hH}}{12abT}\left((a+b)-\tau\right)^3 & \text{for } b < |\tau| \le (b+a) \end{cases} \tag{4.25}$$

with the total width of 2(b+a) and a signal height of $H' = \frac{Hha}{2T}(1 - \frac{a}{3b})$ at $\tau = 0$. For $|\tau| > (b + a)$, $g_{\mathrm{trap}_{1\ll 2}}(\tau) = 0$. The resulting autocorrelation function has then also a bell-like shape. However, the slope of the decay will be steeper and slightly more linear than the decay of the autocorrelation function of a triangle. The difference is pictured in Fig. 4.3. The graphs show a comparison of all previously derived correlation functions with their respective signals and their parameters. It is clearly visible, that the autocorrelation function of a trapezoid signal is basically an intermediate case between the autocorrelation function of a rectangular signal, that results in a linear decaying function, and the autocorrelation function of a triangle that has rather a bell shape. This intermediate incidence does not only involve the function width but also the function height at $\tau = 0$. For rather equally sized signals 1 and 2, we obtain:

$$g_{\mathrm{trap}_{1\approx 2}}(\tau) = \begin{cases} \frac{\mathrm{hH}}{6abT}\left(\tau^3 - 3a\tau^2 + 3a^2b - a^3\right) & \text{for } 0 \le |\tau| \le (b-a) \\ \frac{\mathrm{hH}}{2abT}\left(\frac{\tau^3}{2} - \frac{a+b}{2}\tau^2 + \frac{(a-b)^2}{2}\tau \right. & \\ \left. + \frac{-a^3+3a^2b+3ab^2-b^3}{6}\right) & \text{for } (b-a) < |\tau| \le a \\ \frac{\mathrm{hH}}{2abT}\left(\frac{\tau^3}{6} + \frac{a-b}{2}\tau^2 - \frac{a^2+2ab-b^2}{2}\tau \right. & \\ \left. + \frac{a^3+3a^2b+3ab^2-b^3}{6}\right) & \text{for } a < |\tau| \le b \\ \frac{\mathrm{hH}}{12abT}\left((a+b)-\tau\right)^3 & \text{for } b < |\tau| \le (b+a) \end{cases} \tag{4.26}$$

The total width and the signal height at the intercept value are the same as for Eq. 4.25. Also, the expressions for the first (but with a different upper limit for τ) and the last function segment are described by the same terms in both cases. The intermediate segments, which describe the linear-looking part of the decay differ in their limits. Also, only the second part differs for each case, whereas the third equation stays the same for both.

Eqs. 4.25 and 4.26 are expressed in terms of the dimensions of triangular intensity signals a, b and hH. If the transition of the particle travelling through the laser beam is to be studied, the interest is high in expressing those equations in terms of the trapezoid signal parameters such that conclusions about the illumination time of the particle may be drawn. The trapezoid signal is defined as

$$N_{\mathrm{trap}}(t) = \begin{cases} \mathcal{H} & \text{for } 0 \le |t| \le A \\ \mathcal{H}\left(\frac{1}{1-\frac{A}{B}}\right)\left(1 - \frac{|t|}{B}\right) & \text{for } A < |t| \le B \end{cases} \tag{4.27}$$

with the choice of parameters as shown in Fig. 4.2 a). Here again, for $|t| > B$ the signal is 0. From above, we know that the trapezoidal signal is the result of the correlation of two dissimilar shaped rectangles $N_{rect1} = H$ for $0 \le |t| \le \frac{b}{2}$ and $N_{rect2} = h$ for

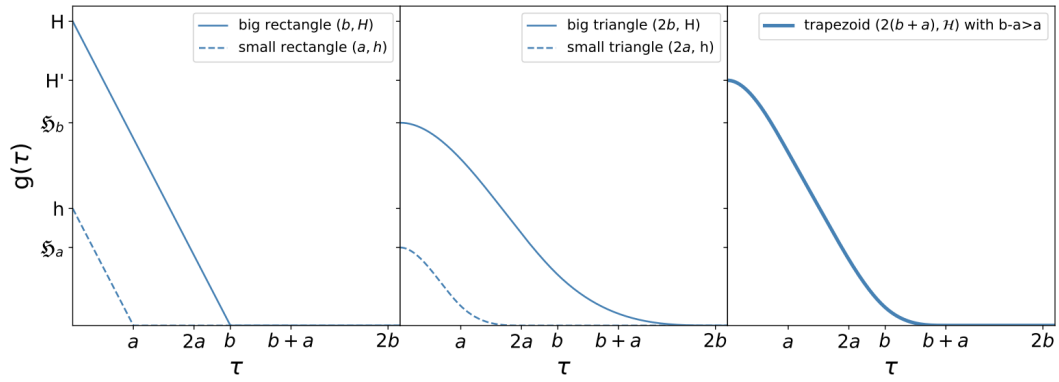

Figure 4.3.: An overview of the resulting correlation function plots depending on the signal geometries. The left panel shows the autocorrelation of a bigger rectangle with total width of b and height H and a smaller rectangle with the parameters a and h, respectively. The middle panel gives the autocorrelation functions of a small and a bigger triangle of total width 2a or 2b and respective heights h and H. The resulting bell shaped curves have their maximum height $\mathfrak{H}_a$ and $\mathfrak{H}_b$, respectively, at $\tau = 0$. Finally, the right panel illustrates the autocorrelation function of a trapezoid (total width: 2(b+a), height: $\mathcal{H}$) which is generated by the crosscorrelation of the two triangles from the middle panel. [1]

$0 \leq |t| \leq \frac{a}{2}$ and 0 elsewhere.

$$g_{\text{rect1+2}}(\tau) = N_{\text{trap}}(\tau) = \begin{cases} \frac{H \cdot h}{2T} \cdot a & \text{for } 0 \leq |\tau| \leq (\frac{b}{2} - \frac{a}{2}) \\ \frac{H \cdot h}{2T} \cdot (1/2(a+b) - \tau) & \text{for } (\frac{b}{2} - \frac{a}{2}) < |\tau| \leq (\frac{b}{2} + \frac{a}{2}) \end{cases} \tag{4.28}$$

By comparing Eqs. 4.27 and 4.28, we note:

$$A = \frac{b}{2} - \frac{a}{2} \tag{4.29}$$

$$B = \frac{a}{2} + \frac{b}{2} \tag{4.30}$$

such that the widths of the rectangular signals, or half-widths of the triangles respectively, a and b may be re-expressed as

$$a = B - A \tag{4.31}$$

$$b = B + A \tag{4.32}$$

The connection between the signal heights may be described as in the following: The rectangular signal parameters are linked to the height of the trapezoid $\mathcal{H}$ as

$$\mathcal{H} = hH \cdot a \tag{4.33}$$

such that the rectangle heights h and H are described by

$$H = h = \sqrt{\frac{\mathcal{H}}{B-A}} \tag{4.34}$$

and the heights of the triangles as

$$\begin{aligned} \mathrm{h} &= a \cdot h^2 = \mathcal{H} \\ \mathrm{H} &= b \cdot H^2 = \mathcal{H} \cdot \frac{B+A}{B-A} \end{aligned}$$

up to the prefactor $\frac{1}{2T}$. Due to the available conversions between the parameters of the geometries, we are now able to rewrite Eqs. 4.25 and 4.26 with the respective parameters A, B and $\mathcal{H}$ of a trapezoidal signal as

$$g_{\mathrm{trap}_{1\ll 2}}(\tau) = \begin{cases} \frac{\mathcal{H}}{6T(B-A)^2(B+A)} \left(\tau^3 - 3(B-A)\tau^2 \right. & \\ \quad \left. +3(B-A)^2(B+A) - (B-A)^3\right) & \text{for } 0 \leq |\tau| \leq \frac{B-A}{2} \\ \frac{\mathcal{H}}{2T(B+A)} \left((B+A) - \tau\right) & \text{for } \frac{B-A}{2} < |\tau| \leq A \\ \frac{\mathcal{H}}{2T(B-A)^2(B+A)} \left(\frac{\tau^3}{6} - \frac{A\tau^2}{2} \right. & \\ \left. -\frac{1}{2}\left((B-A)^2 - (B+A)^2\right)\tau + \frac{8B^3 - 2(B+A)^3}{3}\right) & \text{for } A < |\tau| \leq \frac{B+A}{2} \\ \frac{\mathcal{H}}{12T(B-A)^2(B+A)} \left(2B - \tau\right)^3 & \text{for } \frac{B+A}{2} < |\tau| \leq 2B \end{cases} \tag{4.35}$$

for the case of a trapezoid with steep flanks (B-A) and a narrow plateau of 2A such that $B - A < 2A$. If both triangles have similar dimensions $B - A > 2A$, i.e. a trapezoidal

signal with long flat flanks, the segments of the correlation function are defined as

$$g_{\mathrm{trap}_{1\approx 2}}(\tau) = \begin{cases} \frac{\mathcal{H}}{6T(B-A)^2(B+A)}\left(\tau^3 - 3(B-A)\tau^2 \right. & \\ \quad \left. +3(B-A)^2(B+A) - (B-A)^3\right) & \text{for } 0 \leq |\tau| \leq A \\ \frac{\mathcal{H}}{4T(B-A)^2(B+A)}\left(\tau^3 - 2B\tau^2 + 4A^2\tau \right. & \\ \quad \left. +\frac{1}{3}\left(8B^3 - 2((B-A)^3 + (B+A)^3)\right)\right) & \text{for } A < |\tau| \leq \frac{B-A}{2} \\ \frac{\mathcal{H}}{2T(B-A)^2(B+A)}\left(\frac{\tau^3}{6} - \frac{A\tau^2}{2} \right. & \\ \left. -\frac{1}{2}\left((B-A)^2 - (B+A)^2\right)\tau + \frac{8B^3 - 2(B+A)^3}{3}\right) & \text{for } \frac{B-A}{2} < |\tau| \leq \frac{B+A}{2} \\ \frac{\mathcal{H}}{12T(B-A)^2(B+A)}\left(2B - \tau\right)^3 & \text{for } \frac{B+A}{2} < |\tau| \leq 2B \end{cases} \tag{4.36}$$

Finally, Eqs. 4.25 and 4.26 or Eqs. 4.35 and 4.36 may be used to replace the number fluctuation term $g_2^{\delta N}(\tau)$ in Eq. 4.16 by using the corresponding equation above as fit function for the data. The applicability of this concept will be tested in Chs. 4.3 and 4.4 when the functions are applied to recorded data.

4.2. Experimental Setup

The experimental setup is, apart from the sample configuration, the same setup as presented in Chs. 3. The aim of the following experiments is to produce situations with only a single particle present to verify the concept presented in Ch. 4.1. The realization of experiments with similar aims were already performed by levitation experiments where the particles were kept in a defined position through e.g. levitation [4–6]. We first want to calibrate the setup by using air bubbles in water which are small enough to rise vertically (Ch. 4.3). Subsequently, rigid spheres of different materials and therefore distinct scattering properties will be tested to show, on one hand, how a scatterer impacts the measured intensity signal (Ch. 4.4.1) and if only the translation

or other motions can be observed. On the other hand the effects of the material-dependent scattering properties are observed (Ch. 4.4.2).

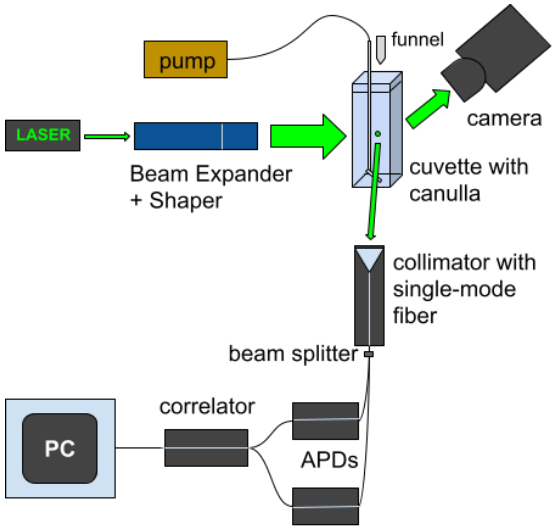

Figure 4.4.: Schematic drawing of the setup used for observing the effects of number fluctuations in the autocorrelation function. The setup is similar to that, which was presented in Ch. 3. Additionally, the two mechanisms to provide the scatterers are shown: First, the canulla, cuvette and syringe combination to produce air bubbles in distilled water. Second, the funnel mounted above the cuvette through which hard sphere scatterers are supposed to fall into the observation volume. [1]

For the calibration experiment in Ch. 4.3, the sample system consists of a 10 cm x 5 cm x 3 cm cuvette (the same as in Ch. 3.2), a canulla and a syringe pump `Chemyx Fusion 100` [7]. The air bubbles will be produced in distilled, filtered water to avoid great amounts of suspended solids that may cause an increased background noise in the data. The cuvette must be well aligned with the laser beam to guarantee a good setup symmetry in order to avoid additional scattering effects from the glass walls. The canulla, as presented in Fig. 4.4, is placed in one of the cuvette's corners with the tip bent about 90° facing upwards to assure a better adaptability of the canulla to the cuvette's floor. Additionally, effects on the bubble's flow dynamics by the vessel walls are avoided. The other end of the canulla is attached to the syringe driver by a common silicon tube. The constant pumping speed assures a periodic production of air bubbles in the water such that the influence of periodicity of the bubble presence

may be studied. Two types of canullas with diameters of 0.35 mm and 0.8 mm were used to gain more versatile data. With those canullas, we were able to produce bubble diameters of $d_{0.35}$ ≈0.75 mm and $d_{0.8}$ ≈3 mm, respectively. The cuvette as well as the canullas were, in advance, plasma treated to facilitate the rising of the bubbles such that strong oscillations of the bubbles after breaking away from the canulla's tip will be reduced.

The experiments from Chs. 4.4.1 and 4.4.2 have an even easier handling compared to the bubble production mechanism. The only hardware needed for the provision mechanism of the hard spheres is a small funnel which is mounted centrally above the center of the observation volume and the laser beam. The solid particles are dropped manually in the center of the scattering volume. Thereby, any container can be used to catch the falling sphere. The only requirement is that the container must be placed sufficiently low beneath the laser beam to avoid contact with the laser light.

4.3. Calibration experiment with air bubbles

In this chapter, we want to test two situations and how they influence the outcome of experiments with our setup: First, we want to know, if the setup is able to detect only a single macroscopic particle at a time, for example a single air bubble in water. Second, we want to know if periodicity in the bubble provision is affecting the results.

For the validation of our concept, we analyze the shape of the recorded intensity signals. In Chapter 4.1.1, we state that the intensity or, in particular, the signal that arises from intensity fluctuations should have a trapezoidal shape for macroscopic particles, with diameters a few times smaller than the laser beam width, due to the gradual illumination of the particles in the scattering volume, as seen in Fig. 4.5. The left image shows a streak of an air bubble created with a 0.8mm canulla rising through the observation volume. The process is documented with the high-speed camera. The beam width of $d_{beam} \approx 15$ mm can be confirmed from such images. While rising through the scattering volume from bottom to top, the illumination, and thus the intensity of the scattered light, increases until the bubble fully enters the scattering volume. The light intensity remains relatively high until the bubble starts to quit the illuminated

area and gradually vanishes. Thus, we expect the intensity signal of a single particle to have two ramps embracing a plateau just like a trapezoid.

This transition of the scattered light's intensity can be analyzed with the intensity trace data from the ALV correlator. On the right-hand side of Fig. 4.5, a detailed section of the intensity trace data showing a periodic bubble appearance and the calculated mean signal retrieved from the complete intensity trace are depicted. The latter was obtained in three steps by processing the data with `python`. First, a 1-D uniform filter `scipy.ndimage.uniform_filter1d(data, size=25)` was applied on the intensity trace to smooth the signal. Second, noisy segments in between the peaks, which might falsify the final signal when averaging all data points, are removed. This is done by setting a global threshold value at about half of the maximum intensity of the peaks. All data points above that threshold plus additional 150 data points on each side of the signal below that threshold are included in the new data set. Finally, the mean signal shape is calculated by averaging all peaks of the shortened data set. The averaged intensity signal for single scatterers clearly shows a trapezoid-like shape, which allows us to determine the time a scatterer needs to pass through the scattering volume. The plateau in this example ranges from approximately 20 ms to 45 ms. From the evaluation of the streaks with the image editing software `ImageJ`, we expect a bubble with an approx. diameter of 3 mm to transit the laser beam in approx. 25 ms.

In order to estimate the approximate diameter of the air bubbles mathematically and to validate the functionality of the setup by comparing the result to the diameter estimations from the video streaks, we use the calculation for the rate of sedimentation v_s [8]

$$v_s = \sqrt{\frac{4}{3}\left(\frac{\rho_p}{\rho_w} - 1\right)\frac{gd}{C_D}} \tag{4.37}$$

using the drag coefficient $C_D = \frac{18.5}{Re^{0.6}}$ and the Reynolds number $Re = \frac{\rho_w v_s d}{\eta}$, which characterizes the flow dynamics. The diameter of the particle may then be estimated by:

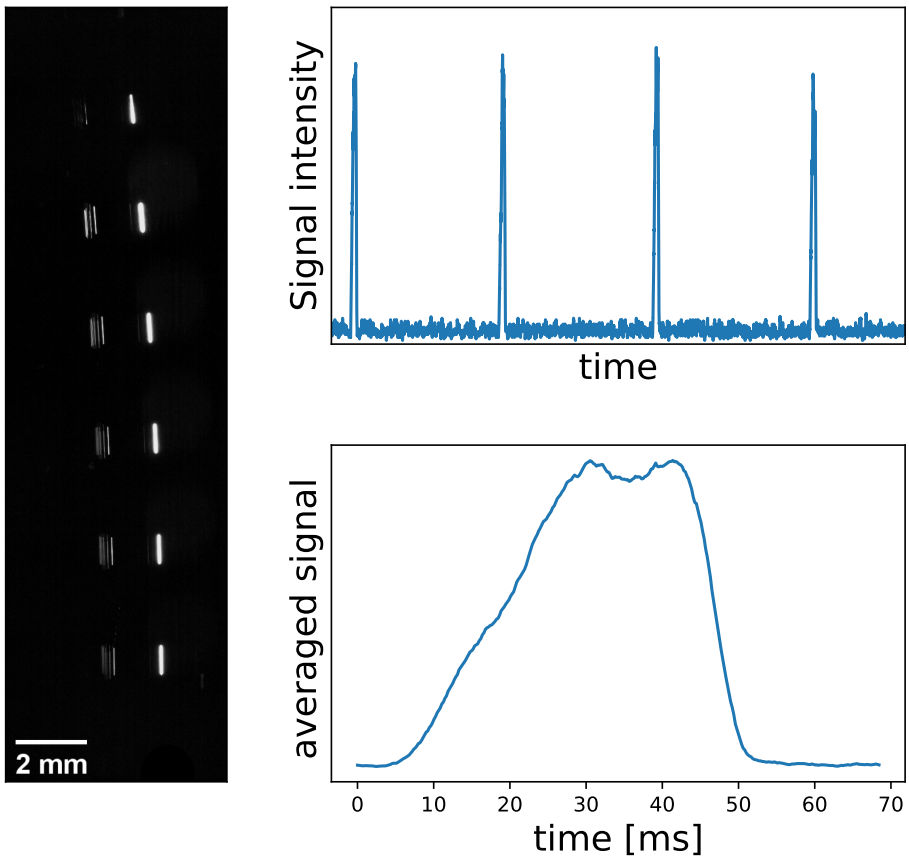

Figure 4.5.: The blinking caused by the air bubbles rising through the laser beam. On the left side, a superposed image sequence of an air bubble, produced with a 0.8 mm canulla, rising through the observation volume is presented. On the right, the upper figure shows a segment of a recorded intensity trace received by the hardware correlator. The air bubbles were produced in regular intervals. The lower panel shows the average signal shape, indicating that the transit of the bubble through the detection volume generates an approximately trapezoidal signal on the scales of milliseconds. [1]

$$d = \left(\frac{111}{8} \frac{v_p^{1.4} \eta^{0.6}}{g \rho_w^{0.6}} \left(\frac{\rho_p}{\rho_w} - 1 \right)^{-1} \right)^{\frac{5}{8}} \tag{4.38}$$

The densities of the water and the particles are denoted as $\rho_w = 997 \frac{kg}{m^3}$ and ρ_p, respectively. η connotes the viscosity of the medium, g represents the gravitational constant. The particle velocity v_p is estimated from the video steaks of the scatterers. The laser beam boundaries serve as reference to estimate the travelled distance of the particle and the number of the corresponding frames (recordings with 500 FPS) provides the respective time. Air bubbles ($\rho_p = 1204 \frac{kg}{m^3}$) generated with the 0.8 mm canulla usually need 38 ms (19 frames) to cross the approx. 14.8 mm wide laser beam. Therefore, by having a particle velocity of $v_p = 0.3 \, \frac{\text{mm}}{\text{ms}}$ and $Re \approx 700$, the bubbles should have an approximate diameter of $d_{0.8} \approx 3.1$ mm if following Eq. 4.38. In comparison, bubbles produced with the 0.35 mm canulla have a diameter of $d_{0.35} \approx 0.75$ mm ($v_p = \frac{190 \, \text{ms}}{14.8 \, \text{mm}} = 0.08 \, \frac{\text{mm}}{\text{ms}}$). For comparability, the diameter of the used 2 mm PTFE particles (manufacturer's information, $\rho_p = 2200 \frac{\text{kg}}{\text{m}^3}$) used in Ch. 4.4.2 was also calculated with Eq. 4.38. Based on the particle velocity of $v_p = \frac{50 \, \text{ms}}{14.8 \, \text{mm}} = 0.3 \, \frac{\text{mm}}{\text{ms}}$, the estimated diameter is 2.1 mm. Thus, the estimated result agrees well with the diameter given by the manufacturer. However, the calculation of the sedimentation rate considers spherical particles only. This does, in fact, not apply to bigger bubbles due to their aptitude regarding flow deformation [9], as seen in the streak. Thus, this approximation should be only considered as rough measure for the air bubbles. Though, the concept provides still a very good approximation for hard spheres as those PTFE spheres investigated.

Fig. 4.6 shows the a) theoretical and b) measured intensity autocorrelation function (IACF) $g_2(\tau) - 1$. In the simulation, the IACF depends on the mean particle number $\langle N \rangle$ over the whole measurement period ranging from 0.1 bubbles per measurement time T to 50 bubbles/T. The measured IACFs hinge on the pumping rate which will provide a similar assertion about the bubble number per measurement duration. The 0.8 mm wide canulla was used.

The graphs in Fig. 4.6 a) are the results of the calculation of the number fluctuations

from Eq. 4.1. For very dilute systems we use the following expression

$$g_2(\tau) = \frac{1}{2\langle N\rangle^2}\left[\langle N\rangle^2(1+e^{-\frac{q^2}{3}\langle v^2\rangle t^2}) + \langle N\rangle\left(1+\frac{2\langle v^2\rangle t^2}{3\sigma^2}\right)^{-\frac{3}{2}}\right] \tag{4.39}$$

The number fluctuations term $\langle \delta N(0)\delta N(t)\rangle$ is above substituted by [2]

$$\langle \delta N(0)\delta N(t)\rangle = \langle N\rangle\left[1+\frac{2\langle \Delta r^2(t)\rangle}{3\sigma_1^2}\right]^{-1}\left[1+\frac{2\langle \Delta r^2(t)\rangle}{3\sigma_2^2}\right]^{-\frac{1}{2}} \tag{4.40}$$

σ_1 is the focussed incident beam diameter and σ_2 the width of the collimation optics. If the particles follow linear trajectories for distances long compared to σ_1 and σ_2, we may assume that the particles perform not a Brownian motion but a ballistic motion such that the mean squared displacement in the intermediate scattering function in Eq. 4.1 is expressed by $\langle \Delta r^2\rangle = \langle v^2\rangle t^2$ such that Eq. 4.40 will provide $\langle v^2\rangle$. For the calculation in Eq. 4.39, we assume $\sigma_1 = \sigma_2 \equiv \sigma$ since in the experiment, the laser is broadened before the light is interacting with the particle such that both beam diameters are equal.

The IACFs in Fig. 4.6 a) decay at the same time for each value of $\langle N\rangle$ such that we may expect, in combination with our knowledge about the relation between the trapezoidal shape of the intensity signal and the scatterer transition through the scattering volume, that each bubble, independent of the pumping rate, needs the same time to pass through the laser beam. The duration is then given by the decay time τ_D at which $g_2(\tau)-1$ equals 0. If $\langle N\rangle$=1, a smooth transit of bubbles is observed, meaning that by the time a bubble leaves the scattering volume, a new bubble just enters it. A mean particle number of $\langle N\rangle$=0.1 corresponds to bubbles being present in the laser beam only $\frac{1}{10}$ of the recording duration. $\frac{9}{10}$ of that time, there is no bubble propagating within the laser beam. In contrast, if $\langle N\rangle$=50, 50 bubbles are entering, leaving and transiting the laser beam in the same moment. This is admittedly a quite extreme case. However, it shows well, that if there are that many particles involved, the intercept value of the decay shrinks. In contrast, for small $\langle N\rangle$ the intercept is increased. This may be explained by the proportionality of the IACF and the average particle number

$\langle N \rangle$ from Eq. 4.39

$$g_2(\tau = 0) = \frac{\langle I^2 \rangle}{\langle I \rangle^2} \sim \frac{1}{2\langle N \rangle} \tag{4.41}$$

With only a few particles, or more particular: a small N, the blinking can be easily perceived by the human eye. The frequency of the blinking is of course increasing with increasing N, such that with a sufficiently high N, only an apparent static illumination may be registered. Then, the number fluctuations become negligible, as indicated by Berne and Pecora [2] and no correlation is given as visualized by $\langle N \rangle$=50 in Fig. 4.6 a).

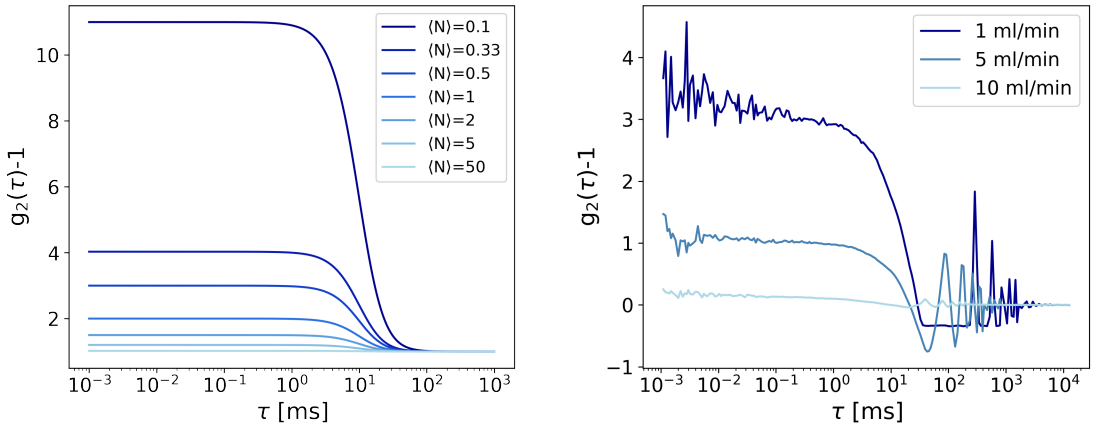

(a) simulated IACFs (b) measured IACFs

Figure 4.6.: Figure a) shows the theoretical decays of the intensity autocorrelation function depending on the mean particle number $\langle N \rangle$ over the whole measurement period. The calculations are based on the equations for number fluctuations by Berne & Pecora [2]. The mean particle number was varied from 0.1 particles to 50 particles. b) shows measured autocorrelation functions $g_2(\tau) - 1$, caused by macroscopic bubbles traversing the observation volume, depending on the pumping rate of the syringe ranging from 1 to 10 ml/min. For the measurements the 0.8 mm wide canulla was used.

Fig. 4.6 b) shows the measured IACF depending on the pumping rate of the syringe chosen here to vary from 1 ml/min to 10 ml/min. Apart from the oscillations of the IACF after the first decay, these IACFs show the same behavior as the simulated

IACFs. With increasing pumping rate, which is equivalent to an increased mean particle number, the intercept will shrink. Further, if there are numerous scatterers as in a high-frequency bubble series, the intercept will be nearly 0. The decay time will be, as calculated before, independent of the pumping rate with a value of $\approx 40\,\mathrm{ms}$. The oscillations of the IACF at later times do not appear in the simulations in Fig. 4.6 a). In Fig. 4.6 b), we see that the amplitude of the oscillations with respect to the magnitude of the initial decay will increase with increasing mean particle number. In case of 5 ml/min, we see that the initial decay and the first oscillation show a similar amplitude of approx. 1. Further, the intercept is also found at ≈1. Those indications refer to the occurrence of the scatterers over the full measurement duration. Meaning, there are as many situations without a bubble present, as there are with a bubble present such that both situations are statistically equally balanced. Since each oscillation's maximum is found at every other 40 ms, we see that the time a bubble needs to traverse the scattering volume is equal to the time a subsequent bubble needs to reach the position of the previous bubble. Consequently, a new bubble enters the laser beam just immediately after the previous bubble leaves the scattering volume. In case of 1 ml/min, the follow-up time ($\tau_F \approx 300\,\mathrm{ms}$) is much longer than the transit time ($\tau_D = \tau_T \approx 40\,\mathrm{ms}$). Thus, there is some temporal lag between succeeding bubbles in the laser beam such that the total time of situations without bubbles increases respective to the situation with a pumping rate of 5 ml/min.

If we compare the autocorrelation function of this experiment with the periodic particle insertion to experiments without periodic provision as in Fig. 4.9 (left panel) of Ch. 4.4.1, we see in the latter case no oscillations occurring after the initial decay. However, the first decay which contains the sought information about the transit time of the particle occurs independent of the periodicity. Infact, temporarily irregular occurring bubbles would cause a better agreement with the theory than periodic appearances.

Finally, we are able to understand the contribution of the number fluctuations $g_2^{\delta N}(\tau)$ to the measured autocorrelation function $g_2(\tau)-1$ and to separate it from the contribution of intensity fluctuations induced by the structure of particle $g_2^{\delta I^P}(\tau)$. In the left panel of Fig. 4.7, the measured autocorrelation function, including the calculated fit function and a reference measurement without scatterers to show the impact of background

noise, is presented. The reference measurement does not show any correlation or decay behavior if no scatterers are present.

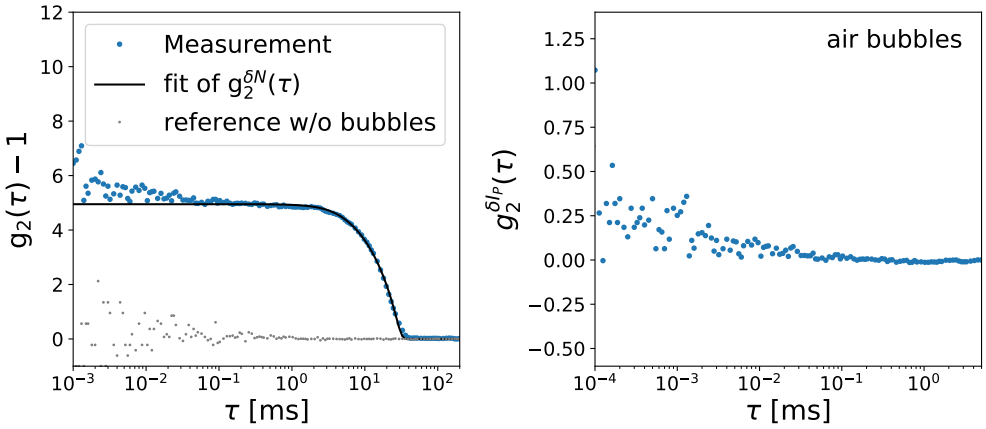

Figure 4.7.: The autocorrelation function for rising macroscopic bubbles in the setup. The measured data $g_2(\tau) - 1$ is presented by the blue dotted lines. The black solid line in the left panel shows the portion of the number fluctuations $g_2^{\delta N}(\tau)$ based on a fit with the analytical form of the autocorrelation function of a trapezoid. The light gray dotted line provides the measured ACF without any scatterers present in the observation volume. In the right panel, we see the correlation function for early times with the contributions from the number fluctuations removed. [1]

The bubble IACF function comprises a single decay caused by number fluctuations, as expected from transparent particles with no inner homogeneities or surface features. The shape of the decay can be fitted with the calculated form of the autocorrelation function of a trapezoidal intensity signal from Eq. 4.25. Thus, we expect the contributions from blinking only to affect the part of the correlation function at later times of the order of milliseconds. The right plot of Fig. 4.7 illustrates the isolated $g_2^{\delta I^P}(\tau)$ at very early times of the order of microseconds. No discrete decay of the $g_2^{\delta I^P}(\tau)$ is observable. $g_2^{\delta I^P}(\tau)$ was obtained by subtracting the number fluctuation contribution $g_2^{\delta N}(\tau)$ from the measured data and then normalizing it by the intercept at $\tau = 0$ of $g_2^{\delta N}(\tau)$ added 1. The function's intercept is found below noise level, cf. the left panel of Fig. 4.7. The magnitude of $(g_2(\tau) - 1) - g_2^{\delta N}(\tau)$ is of the order of maximum 2. $(g_2(\tau) - 1) - g_2^{\delta N}(\tau)$ equals the not normalized form of $g_2^{\delta I^P}(\tau)$. The magnitude of the noisy reference IACF ranges from negative values to about 2. Comparing both

magnitudes for specific τ-values, the noise's amplitude will generally be perceived to be slightly higher than that of $(g_2(\tau) - 1) - g_2^{\delta N}(\tau)$. Thus, the possibility exists that an early decay due to internal structures or shape oscillations may be hidden in the data at very early times. However, the noise level does not allow for analysis, since a decay would not be resolvable the setup used. However, literature regarding the natural resonances of bubble oscillations [10, 11] does not consider the variation of bubble shapes for such objects with diameters of millimeters for such short time scales. Thus, a hidden decay is rather improbable.

4.4. Experiments on rigid spheres

The experiment from the former chapter, where air bubbles rose in a container of water, showed that the setup is well calibrated for detecting the presence of a single scatterer in the scattering volume. We also learned that the periodic occurrence of the scatterers has no impact on the actual decay of the IACF but will only cause oscillations at later times. Further we know, that with the technical and theoretical tools given, we are able to distinguish the blinking's influence on the measured intensity autocorrelation function from other effects. In the following, we want to study further how the scattering properties of different materials affect the outcome of contributions from the particles' scattered intensity $g_2^{\delta I^P}(\tau)$. According to Berne and Pecora [2] and in particular Eq. 4.10, IACFs may decay in two stages if there are number fluctuations and additionally other mechanisms causing a phase difference in the scattered light. For this purpose, we first want to investigate a so-called ideal scatterer where we expect no distinct second early decay of the measured IACF (cf. Ch. 4.4.1). Only the translational motion of the ideal scatterer should cause a phase change and thus a decay in the autocorrelation function. Secondly, we want to investigate the effect of three different materials that should have diverging scattering properties due to their internal and surface structures (cf. Ch. 4.4.2).

4.4.1. The ideal scatterer

We are looking for a type of scatterer for that our experimental setup is sensitive to its translational motion only such that no other motion type induces a phase shift. Therefore, the particle should fulfill several requirements to be considered an "ideal scatterer" in relation to our experimental setup.

There are technical and data related requirements to identify an ideal scatterer. In the sense of data analysis, we seek a particle type for which the intercept of $g_2^{\delta I^P}(\tau)$ is approx. 0, such that only one clear decay is occurring in $g_2(\tau) - 1$, akin to the air bubble experiment in Ch. 4.3. However, in case of the bubbles, it was probably only a happenstance that the shape's oscillation was happening on time scales, which are not resolvable with our setup. Anyhow, shape oscillations should not be present in case of rigid spheres except for deformation processes which should be barred here. Thus, the first requirement for an ideal rigid sphere scatterer is to be as spherical as possible. If the particle does not possess surface asperities or exhibits a rather ellipsoidal shape, no rotation of the particle about its spin axis should be detectable. Further, internal impurities become notable with proceeding measurement time due to the time dependence of the impurity's position, in or on the particles surface with respect to the particle's barycenter. If there are no anomalies included in the particle, no additional interference effects are induced. Technically, the least susceptible particles to those features are transparent spheres.

After a long test series of different macroscopic and transparent spheres, we found that the 2 mm sapphire (Al_2O_3) ball lense by Edmund optics [13] with a refractive index of $\eta = 1.77$ fulfills the requirements best. A photo of the spheres used is provided in the bottom right panel of Fig. 4.10. Other glass sphere types' intercepts will still start at values $\gg 0$. One case of the previously tested glass spheres will be presented in Ch. 4.4.2. Ball lenses are by definition Mie-scatterers by focusing the incoming light in the forward direction just like a special type of thick biconvex lenses [14], as pictured in Fig. 4.8. They are produced from a single glass substrate with high precision such that no impurities, e.g. air bubbles, may be trapped inside. If surface asperities are produced, they are assumed to be minute to what the setup may resolve with the chosen laser light wavelength.

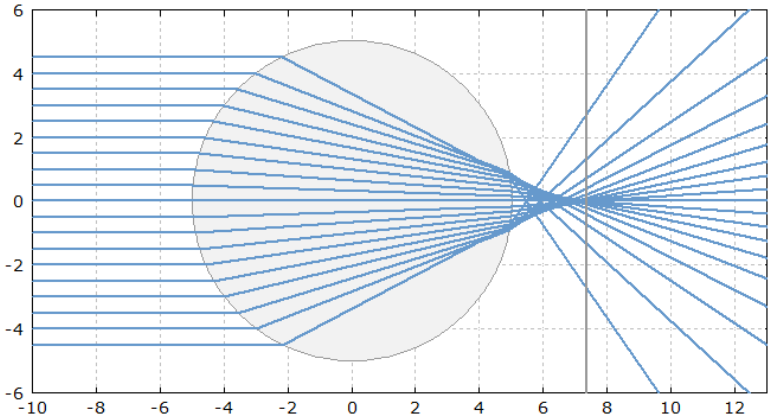

Figure 4.8.: A ball lense focusing of light. The horizontal and vertical scales indicate unitless distances. The paraxial rays incident from the left have a focus position as marked by the gray vertical line. The outer rays are more strongly refracted than the centered rays. [12]

Only a smaller portion of the light interacting with the ball lense will be scattered in a 90° angle. Thus, due to the laser-detector geometry of our setup, the intercept of the measured IACF with only a single particle will be low compared to other materials like for example those used in Ch. 4.4.2. The measured and processed autocorrelation function (ACF) is presented in Fig. 4.9. In the left panel, the measured ACF shows a quite noisy behavior for very early times and then merges into a clear decay from approx. 1 to 0 at $\tau \approx 10\,\mathrm{ms}$. The data is fitted with the ACF of a trapezoidal signal (cf. Eq. 4.35) shown by the black solid line representing $g_2^{\delta N}(\tau)$. The inset in the right plot shows a montage of subsequent time steps of the particle falling through the laser beam. We only see two light reflexes: one on the right side where the laser beam is incident and on the left side, where the light leaves the ball lense.

On the right side of Fig. 4.9, we see the normalized isolated contribution of the particle scattering $g_2^{\delta IP}(\tau)$. That contribution was calculated according to Eq. 4.15. On time scales of only a few μs, the data remains noisy. On average, the intercept may be considered $\cong$ 0 as sought for an "ideal scatterer". Of course, there may be some information about a tiny decay hidden in the noise. However, it is quite unlikely that a minute feature has such a great impact on the ACF since the noise level may be considered low already and additionally, the sphere is comparably "ideal" with respect

to the other tested scatterers, cf. Ch. 4.4.2.

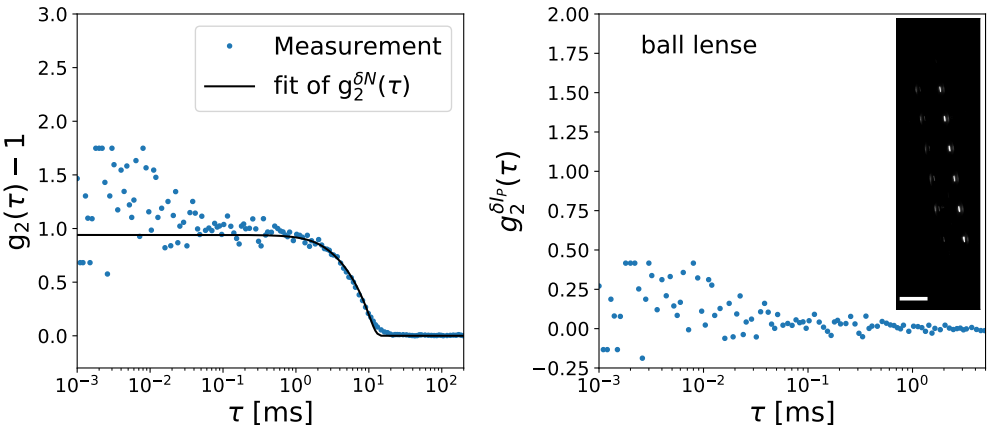

Figure 4.9.: The autocorrelation function of a falling ball lense. The measured data $g_2(\tau) - 1$ is presented by the blue dotted lines. The black solid line in the left window shows the contribution of the number fluctuations $g_2^{\delta N}(\tau)$ based on a fit with the analytical form of the autocorrelation function of a trapezoid. In the right window, we see the isolated contribution of the scattering of the particle showing values smaller than 0.5. The inset in the right window shows the streak of a falling ball lense. The bar at the bottom marks the distance of 2 mm. (modified from [1])

4.4.2. Regular scatterers

In Ch. 4.3 and 4.4.1, we have seen that there are soft and rigid spherical transparent particles, which will only cause relevant phase shifts due to their transit through the scattering volume. Thus, number fluctuations cause a single distinct decay of the IACF. However, we now want to investigate the complexity contrast with respect to ideal scatterers in the scattering behavior of "more real" granular particles. The positions of surface and internal features become then time-dependent. According to theory of Berne and Pecora [2], this incident results in a second decay in $g_2(\tau) - 1$.

The particles were chosen to show different scattering properties of materials but also to represent particles which are commonly used in other studies using DLS to investigate granular media [15–19]. However, those granular particles are still quite ideal in

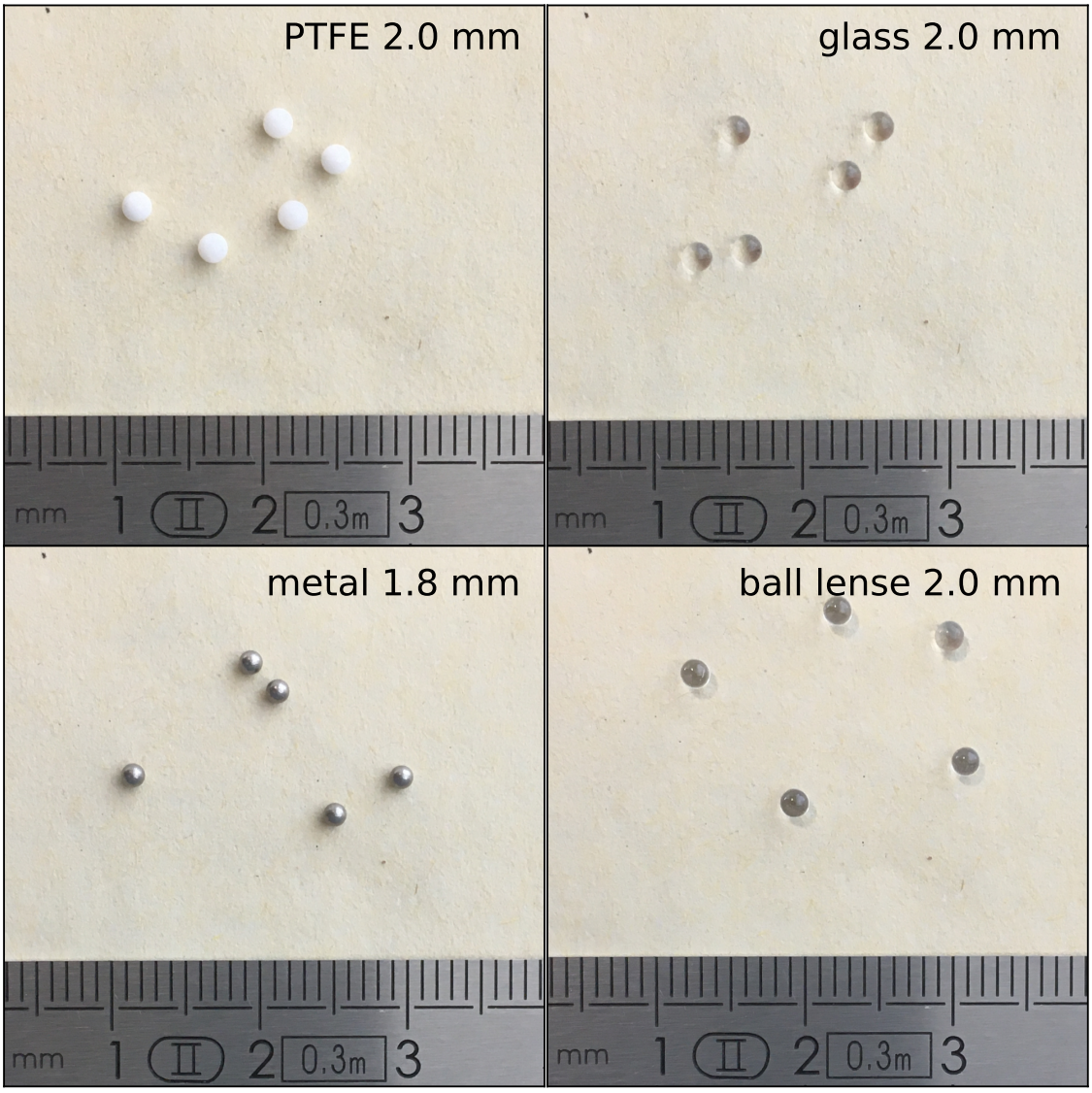

Figure 4.10.: Photos of the granular particles used in the experiments in Ch. 4.4. The ruler t the bottom of each photo gives information about the spatial scales. The top left photo shows teflon (plastic) spheres of diameter 2 mm. Next to it, regular glass spheres of the same dimensions are shown. The bottom left photo shows metal spheres (Mu-metal) with a slightly smaller diameter of approx. 1.8 mm and finally the sapphire ball lenses (Al_2O_3) in the bottom right panel. [1]

comparison to granular particles found in the nature as e.g. sand grains or pebbles. The particles tested in the here performed laboratory experiments are all spherical and within each species, the particles exhibit the same particle size and scattering properties such that the ensemble would be considered monodisperse.

In contrast to the transparent ideal scatterers, which were introduced in Ch. 4.4.1, so-called diffusive scattering particles shall be investigated in the following. Diffusive scattering particles are here understood as scattering entities which generate a great number of scattered electric fields contributing to the total scattered electric field such that the maximum speckle contrast is found to be approximately equal to unity. Thus, many small scattering elements are expected to scatter the incident radiation. For the analysis of diffusive scattering particles, polytetrafluoroethylene (PTFE) or also called Teflon spheres from TIS Wälzkörpertechnologie [20] of a diameter of 2 mm are used. Additionally, spherical custom-made Mu-metal particles for the MEGRAMA experiments [21] with a diameter of approx. 1.8 mm and Worf high-precision glass beads [22], also with a diameter of 2 mm, are chosen. Metals reflect the light at the surface such that no light may pass the surface and thus, only the light which is reflected in the direction of the detector may be collected. Anyhow, each illuminated scattering entity on the metal sphere's surface contributes. In case of the glass beads, the light will be refracted at the medium boundary as explained by Snell's law (Eq. 2.48). The refracted light will then propagate through the sphere until it will meet the media boundary at another surface point of the sphere again. There, the light leaves the sphere under a specific angle determined by Snell's law. Supposedly, the monochromatic light beam will encounter about two scattering events when interacting with a spherical glass bead. A visual comparison of all scatterers and additionally the ball lenses from Ch. 4.4.1 is presented in Fig. 4.10. When comparing the appearance of the glass beads and the ball lenses, even though they are both transparent and spherical, a clear difference in how the light is traversing the object is visible. This supports the assumption, that the individual scattering properties and thus the time-dependent scattering behavior adapted from individual particle motions has a significant impact on the IACF.

The data acquisition procedure is the same for all particles with the setup described in Ch. 4.3. The only modification to the setup is that instead of a pump and a canulla

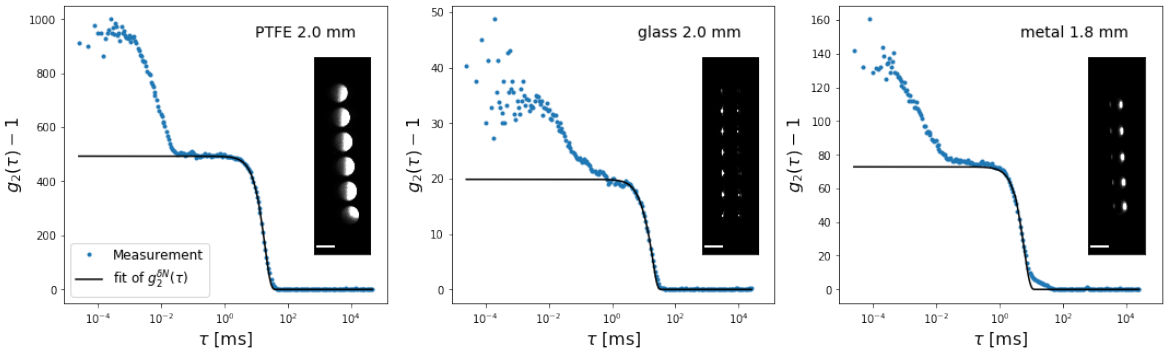

Figure 4.11.: The measured autocorrelation functions (ACF) of a teflon particle, a glass bead and a metal sphere. All graphs show the recorded data with two decays in a blue dotted line. The black solid line presents the contribution of the number fluctuations $g_2^{\delta N}(\tau)$ to the entire ACF $g_2(\tau) - 1$. The inset of each window shows a photo montage of a representative falling particle through the laser beam. The included white bar indicates the length of 2 mm. [modified from: [1]]

a funnel was used through which the particles were dropped. The funnel was mounted a few centimeters above the scattering volume with the tip pointing vertically towards the center of the observation volume. The particles were dropped one after another with a sufficient delay such that not more than one particle traverses the scattering volume. The resulting autocorrelation functions are shown in Fig. 4.11. From left to right, the ACF of teflon, mu-metal and glass spheres are depicted in blue. In contrast to the ACF from the ball lenses in Fig. 4.9, an explicitly shaped decay at very early times is visible such that the ACF decays twice. The black solid line represents the functional form of the number fluctuations (see Ch. 4.1.1) by the autocorrelation of a trapezoidal signal.

After quarrying the impact of the blinking, a fully developed decay remains, see Fig. 4.12. The decays' normalized forms allow to compare the shapes and the noise performance. Obviously, the shape for each species differs from the others. The intercept value's magnitude of the teflon ACF is much higher than those of the metal or glass spheres. White materials scatter stronger than e.g. transparent materials since they comprise numerous scattering entities on their surface and internally, such that the light's direction of propagation is quickly randomized and the probability that light is

scattered in a 90° angle towards the detector is much higher. The average intensity will decrease with the number of scattering entities of the object. Thus, the transparent scatterer will show here the smallest intercept value. This will also cause a susceptibility to a rather noisy behavior if only a few data points are generated as for the very early times in the recorded ACF. The more scattering entities are involved, the less noisy the ACF will be at very short times. At this point, the shape of the three ACFs may not be explained by exponential functions of the form of $e^{-\frac{t}{\tau}}$ or $e^{-v^2\tau^2}$. A discrete idea of what is happening during the scattering process and a understanding of what potentially causes phase shifts, plus how the phase shifts are produced, is inevitable to comprehend the shape of the decays.

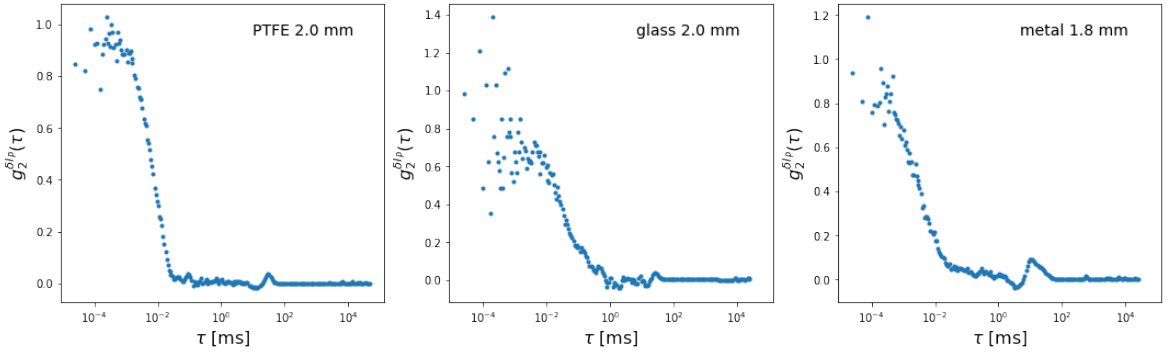

Figure 4.12.: The isolated portion of the individual scattering contributions $g_2^{\delta I^P}(\tau)$ in the autocorrelation function for falling macroscopic particles in the setup. The function's decay for teflon particles, glass beads and metal spheres are presented by the blue dotted lines. [modified from: [1]]

The photos in Fig. 4.13 were taken during a measurement run. The exposure time was approx. 200 μs such that the interference patterns of the scattered light was caught on camera at the back of the vessel wall. The speckle patterns' appearances support the theory of the materials having diverging scattering properties and therefore diverging number of contributing scattering entities. The speckle pattern of teflon (a) appears to be a random speckle pattern expected from diffusive scattering objects as depicted in Fig. 2.11. As in a colloidal suspension, the light is expected to perform a random walk within the teflon particle before it leaves in the direction of the scatterer. The glass bead's speckle pattern (b) reminds of the interference pattern in Young's double slit experiment [23]. The two concentrated scattering areas in the front and in the back of

the sphere respective to the incoming laser beam may act in the same way as the slits in the famous experiment. The metal sphere's speckle pattern (c) seems similar to that of the diffusive scattering object. However, its intensity is notably lower. Supposedly, less scattering entities scatter the light compared to a). The speckle pattern of the ball lense (d) hardly exists which supports the assumption of a Mie-scatterer.

Since there is always only one particle present in the scattering volume, the decay can not be induced by any interference effects between the scatterers in a particle ensemble, according to Eq. 4.1, such that only time-dependent features in or on the particle induce the decay. In the experiments performed, the particles did not suffer any deformation nor should falling solid spheres vibrate if not particularly excited to do so. Therefore, the only explanation left is that of the rotation of the scattering entities of a single particle about its barycenter, which entails either surface features causing a deviation from a homogeneous spherical shape or inner impurities, causes the decay of the ACF at very small time scales.

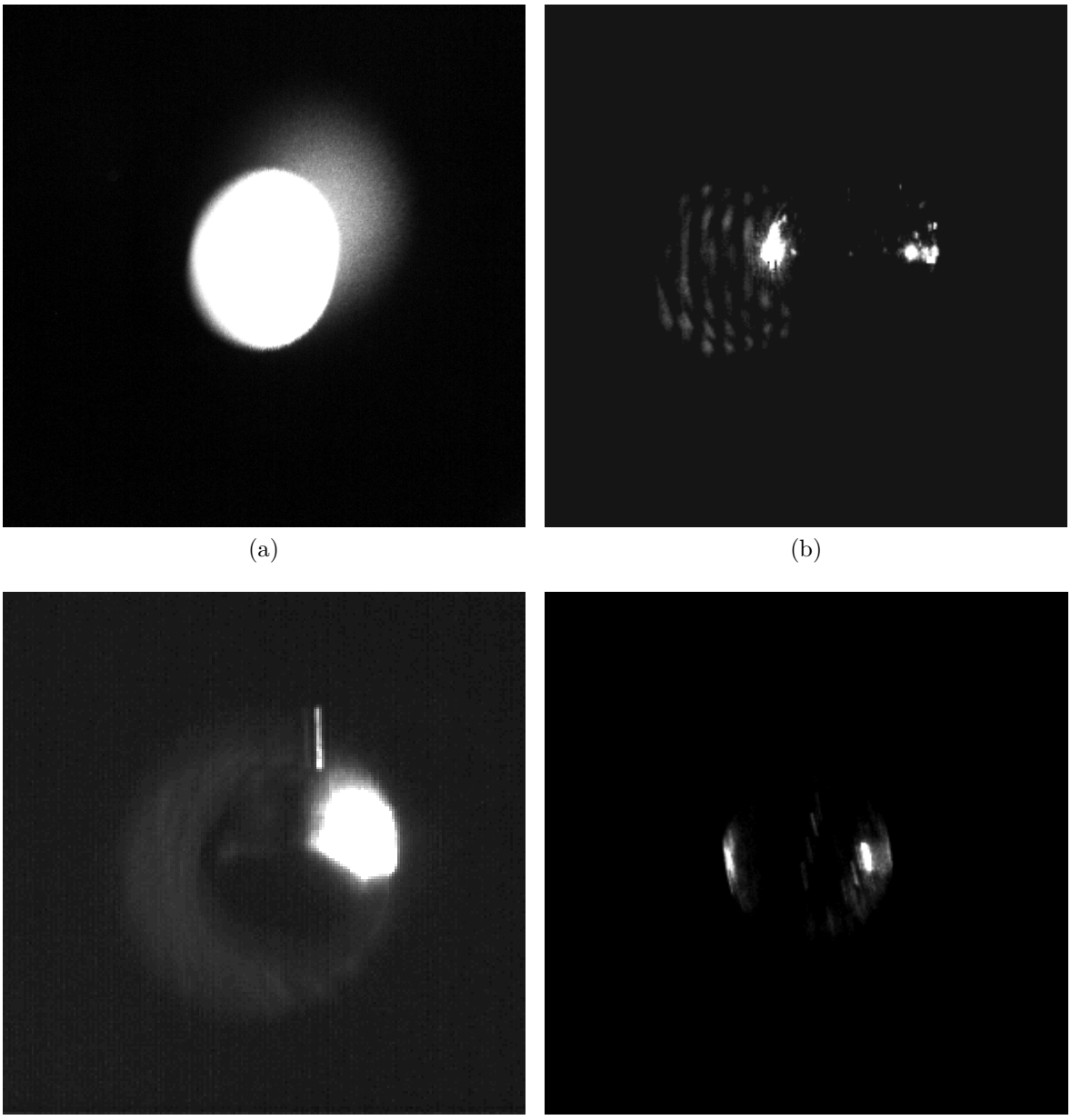

(a) (b)

(c) (d)

Figure 4.13.: Snap shots of the scattered light patterns of (a) a teflon sphere (b) a high-precision glass bead (c) a metal sphere (with a small air bubble sticking to the sphere's top) and (d) a ball lense. The images were taken with exposure times of approx. 500 μs during experiments where the spheres fell through the funnel into the cuvette filled with filtered and deionized water. The scattering patterns became visible on the cuvette's glass wall facing the collimator. The particles in a) and c) show broad spots of randomized speckles. b) shows a clear interference pattern with bands, similar to that pattern observed in Young's slit experiment [23]. In d), no pattern is noted.

4.5. Conclusion

The performed DLS experiments on single macroscopic particles showed, that the presence of such an object is sufficient to induce a full decay of the measured autocorrelation function (ACF). Since the experimental setup is not sensitive to vertical motions of the scattering objects, only the presence of the vertically dropping or rising particles causes a sudden, temporary jump in light intensity ("blinking"). This intensity fluctuation gives information about the dynamics of the object. No further particle, which potentially induces inter-particle interference effects, was ever present in the observation volume. Thus, the ACF's decay can, according to the theory of Berne and Pecora [2], be attributed to the fluctuating number of scatterers in the observation volume. We note further, that a periodic appearance of scatters from the same species has only secondary effects on the autocorrelation function and does not influence the actual decay.

The with this setup recorded decay may be described by the autocorrelation function of a trapezoidal intensity signal. The trapezoidal shape reflects the transit of the particle through the laser beam by showing distinct intensity variations of the scattered light. The trapezoid's flanks correspond to the particle approaching and leaving the laser volume. The plateau describes the period of the particle being fully illuminated within the beam. Since the width of the laser beam and the form of the particle's flight trajectory are known, the particle's velocity may be identified. The total width of the intensity signal determines the time scales of the autocorrelation function's decay.

Depending on the optical properties of the particle, a second decay at much earlier times ($\tau \approx 10^{-6}\,s$) will be induced. Transparent and pure particles ("ideal scatterers") still show only a single decay, which is attributed to their presence in the observation volume. Due to the missing surficial or internal structures, no additional scattering processes take place. Thus, only information about the translational motion of such a particle is provided by the data. If however, an opaque particle with a smooth or rough surface crosses the observation volume, clear decays at those early times are observed. The same applies for transparent particles that show irregular shapes, surface asperities or impurities. The most distinct decay was obtained for a particle with a diffusive scattering surface. The existence of additional decays, depending on

the complexity contrast between the particles, shows particularly the effect of surface scattering on macroscopic particles.

Since only number fluctuations induce the ACF's decay for the ideal scatterers, an ansatz for separating those contributions from the early decay, that is based on the individual optical properties of the particle, could be formulated. Therefore, the early decays for the different particle species may be analyzed individually. From Fig. 4.12, we see that the structure-dependent decay at very early times varies in shape, time scales and noise performance for the different species, such that each kind should be analyzed individually. In the further chapters, we will focus on the diffusive scattering particles.

In Ch. 5, a model will be presented that aims for identifying the phase fluctuations that a single rough macroscopic sphere induces. The model shall provide a proper analysis of the decay of diffusive scattering particles at early times. Thereby, rotation of this optically rough particle about its own axis is assumed. The model will be developed for different spin axis orientations with respect to the setup geometry. Subsequently, parameter studies will be conducted and the model is experimentally tested. In case of a sound theoretical model structure and proper experimental results, this concept may be the origin of another methodology to analyze granular media with light scattering.

References

[1] L. Dossow, R. Kessler, M. Sperl, and P. Born. "Dynamic light scattering from single macroscopic particles". In: *Applied Optics* 60.32 (2021), pp. 10160–10167.

[2] B. J. Berne and R. Pecora. *Dynamic light scattering: with applications to chemistry, biology, and physics*. Courier Corporation, 2000.

[3] S. Chandrasekhar. "Mod". In: *Physics* 15.1 (1943), p. 43.

[4] U. K. Krieger and A. A. Zardini. "Using dynamic light scattering to characterize mixed phase single particles levitated in a quasi-electrostatic balance". en.

In: *Faraday Discuss.* 137 (2008), pp. 377–388. ISSN: 1359-6640, 1364-5498. DOI: 10.1039/B702148H. (Visited on 07/21/2021).

[5] C. Maass, N. Isert, G. Maret, and C. Aegerter. "Experimental Investigation of the Freely Cooling Granular Gas". In: *Physical Review Letters* 100.24 (June 2008). ISSN: 0031-9007. DOI: 10.1103/PhysRevLett.100.248001.

[6] V. Lee, N. M. James, S. Waitukaitis, and H. M. Jaeger. "Collisional Charging of Individual Sub-Millimeter Particles: Using Ultrasonic Levitation to Initiate and Track Charge Transfer". en. In: *Physical Review Materials* 2.3 (Mar. 2018). ISSN: 2475-9953. DOI: 10.1103/PhysRevMaterials.2.035602.

[7] C. Inc. *Fusion Series USER MANUAL*. https://www.chemyx.com/downloads/FusionSeries_Manual.pdf. Accessed: 2023-01-16. 2016.

[8] K. Luckert. *Handbuch der mechanischen Fest-Flüssig-Trennung*. Vulkan-Verlag GmbH, 2004, pp. 106–108.

[9] R. Clift, J. R. Grace, and M. E. Weber. "Bubbles, drops, and particles". In: (1978).

[10] U. Kornek, F. Müller, K. Harth, A. Hahn, S. Ganesan, L. Tobiska, and R. Stannarius. "Oscillations of soap bubbles". In: *New Journal of Physics* 12.7 (2010).

[11] H. Lamb. "Hydrodynamics, Cambridge Univ". In: *Press* (1932), pp. 134–139.

[12] R. Photonics. *Ball Lenses*. https://www.rp-photonics.com/ball_lenses.html. Accessed: 2022-08-24. 2022.

[13] E. Optics. *Saphir-/Rubin-Kugellinsen und Halbkugellinsen*. https://www.edmundoptics.de/f/sapphire-and-ruby-ball-lenses/12451/. Accessed: 2023-01-02. 2023.

[14] H. Vortisch. "Beobachtung von Phasenübergängen in einzeln levitierten Schwefelsäuretröpfchen mittels Raman-Spectroskopie und elastischer Lichtstreuung". PhD thesis. 2002.

[15] R. Piazza, J. Stavans, T. Bellini, D. Lenti, M. Visca, and V. Degiorgio. "Light-scattering experiment on anisotropic spherical particles". In: *Trends in Colloid and Interface Science IV* (1990), pp. 89–94.

[16] W. Leutz and J. Rička. "On light propagation through glass bead packings". In: *Optics communications* 126.4-6 (1996), pp. 260–268.

[17] N. Menon and D. J. Durian. "Diffusing-Wave Spectroscopy of Dynamics in a Three-Dimensional Granular Flow". In: *Science* 275.5308 (Mar. 1997), pp. 1920–1922. issn: 00368075. doi: 10.1126/science.275.5308.1920.

[18] D. Goldman and H. Swinney. "Signatures of Glass Formation in a Fluidized Bed of Hard Spheres". In: *Physical Review Letters* 96.14 (Apr. 2006). issn: 0031-9007. doi: 10.1103/PhysRevLett.96.145702.

[19] J. Crassous. "Diffusive wave spectroscopy of a random close packing of spheres." In: *The European physical journal. E, Soft matter* 23.2 (June 2007), pp. 145–152. issn: 1292-8941. doi: 10.1140/epje/i2006-10079-y.

[20] T.-G. Wälzkörpertechnologie. *Kunststoffkugeln*. https://www.tis-gmbh.info/kunststoffkugeln/. Accessed: 2022-12-02. 2022.

[21] P. Yu, E. Stärk, G. Blochberger, M. Kaplik, M. Offermann, D. Tran, M. Adachi, and M. Sperl. "Magnetically excited granular matter in low gravity". In: *Review of Scientific Instruments* 90.5 (2019).

[22] W. G. GmbH. *Glaskugeln, Glasperlen, Mahlkugeln, Mischkugeln, Füllkugeln*. https://worf.de/wordpress/produkte/glaskugeln/. Accessed: 2023-01-03. 2022.

[23] D. Halliday, R. Resnick, and J. Walker. *Halliday Physik. 2., überarbeitete und ergänzte Auflage*. 2009.

5. Model for determining a rough sphere's rotation

Heretofore, in the context of the methods DLS and DWS the scattering performance of granular media was attempted to be explained with the principles of Mie theory as numerical solution to the Maxwell equations and the RGD approximation for "extended particles" (cf. Chs. 2.2.2, 2.3 and 2.3.3). In Mie theory however, the scattering performance as entire sphere is considered relevant and the computational power needed to describe light scattering on a single macroscopic particle is vast [1]. Additionally, Mie-scatterers only provide a single intensity value in a specific direction, cf. Ch. 2.2.2.2. That direction is identified by the corresponding spherical coordinates. If the sphere rotates, the spherical coordinates respective to that direction will change, however, the intensity's magnitude will not, such that no random speckle pattern is created, which is inevitable for the analysis of phase shifts between the incident and scattered light on rough surfaces. The RGD approximation considers non-spherical shapes, but the particle sizes are still only comparable to the wavelength of light, such that the particle may be considered to be internally and surficial homogeneous [1, 2]. In case of granular matter though, scattering from an usually imperfect spherical particle's surface itself in fact plays already a prominent role which resembles in its complexity scattering processes on surfaces (cf. Ch. 2.2.3 and Ch. 2.4). Therefore, the development of the following model focuses on light scattering at the macroscopic particle's surface to bridge this gap in the theory.

Churnside [3] and Marron and Schroeder [4] show in their experiments that the observation of scattering on a greater object's surface, or outermost layer, may be sufficient to induce a full decay of the autocorrelation function. In Marron and Schroeder's

light scattering experiment, a turnable aluminum disc was sprayed with white lacquer and illuminated with a laser. The configuration of the surface determines the decay's shape and decorrelation time of the autocorrelation functions. This finding shall now be practiced to develop a new methodology for the analysis of the autocorrelation functions obtained by DLS experiments. Inspired by the ray-tracing algorithms as common investigation method in geometrical optics, we want to find a reformulation for the scattering vector of the intermediate scattering function.

From Ch. 4.4 we know, that for diffusive scatterering particles, with similar scattering abilities as the rotating disc in Marron et al.'s experiment, we observe two distinct decays of the autocorrelation function. Both decays were isolated such that both may be analyzed individually. The decay at later times ($\tau \approx 10^{-2}\,s$) was already identified as transit of the rough particle through the laser beam and thus as its transitional motion. The decay at earlier times ($\tau \approx 10^{-6}\,s$) is induced by an individual motion of the particle, since no interference effects may be possible due to the lack of further particles in the scattering volume as potential explanation for that decay [5]. For rigid bodies, vibrational effects due to e.g. short-term deformations or shape instabilities are out of question. Thus, only the rotation of the sphere about its own barycenter may constitute another type of motion and may thus provoke another decay at such early times.

The rotation of a diffusive scattering particle shall now become amenable to analysis with help of the "Rough Particle Model" (RPM) developed below. The particle surface is assumed to consist of numerous tiny scattering elements involved in the scattering processes, cf. Ch. 2.2.3, where the caused phase shifts will accurately be observed. Particular geometries of the model sphere in space will be considered as well as the influence of surficial brightness distributions by analyzing the correlation function's weighted amplitude term. This model shall later serve to analyze laboratory experiments (cf. Ch. 6).

The following section Ch. 5.1 explains the fundamental idea of the model and provides a general expression for the field autocorrelation function (FACF) as well as for the intensity autocorrelation function (IACF). In the ensuing sub-sections (Chs. 5.1.1 and 5.1.2) a more accurate description of the phase and amplitude terms, respectively, will

be discussed. In Ch. 5.2, particular expressions for specific sphere geometries in the respective reference frame will be provided, followed by parameter studies in Ch. 5.3. The chapter will be closed with a brief conclusion in Ch. 5.4.

5.1. Model principles based on surface scattering

The idea is to consider the scattered light from all contributing illuminated surface elements of the sphere and do the statistics over all detected phase shifts. The registered phase depends on the scattering element's location on the sphere's surface that is determined by the surface element's spherical coordinates. Thus, the actual rotation of the sphere can be characterized by the angular velocity ω, which is encoded in the autocorrelation function's phase term.

For rough granular particles with diameters much greater than the wavelength of the incident light, we consider the physics of scattering on surface structures, cf. Ch. 2.2.3. We expect a monochromatic plane wave incident on an auxiliary plane E_1 as illustrated in Fig. 5.1. The plane, being tangent to the surface point closest to the light source, mimics the scattering events as if the curved surface was flat and all scattering surface entities have the same distance to the laser. This implies, that the incident light is unscattered when arriving at each of the surface points to obey the single-scattering limit. The same accounts for the detector registering the scattered light from plane E_2, respectively. The time-dependent location $\vec{r}_P$ of element P on the sphere's surface determines the respective extra distances l_a and l_b to the incident plane and the auxiliary scattered plane for that particular surface element with respect to other surface elements. The distinct extra paths among the surface elements then cause the optical path differences that induce the sought phase shifts. $\bar{q}$ describes in Fig. 5.1 the equatorial scattering plane as reference plane.

To analyze the phase shift contribution of each surface element following the rotational motion, we start again with the general expression for a collective electric field E_G that results from the superposition of the electric field contributions from each surface scattering entity of the rotating particle, just as in Eq. 2.64, with index P indicating

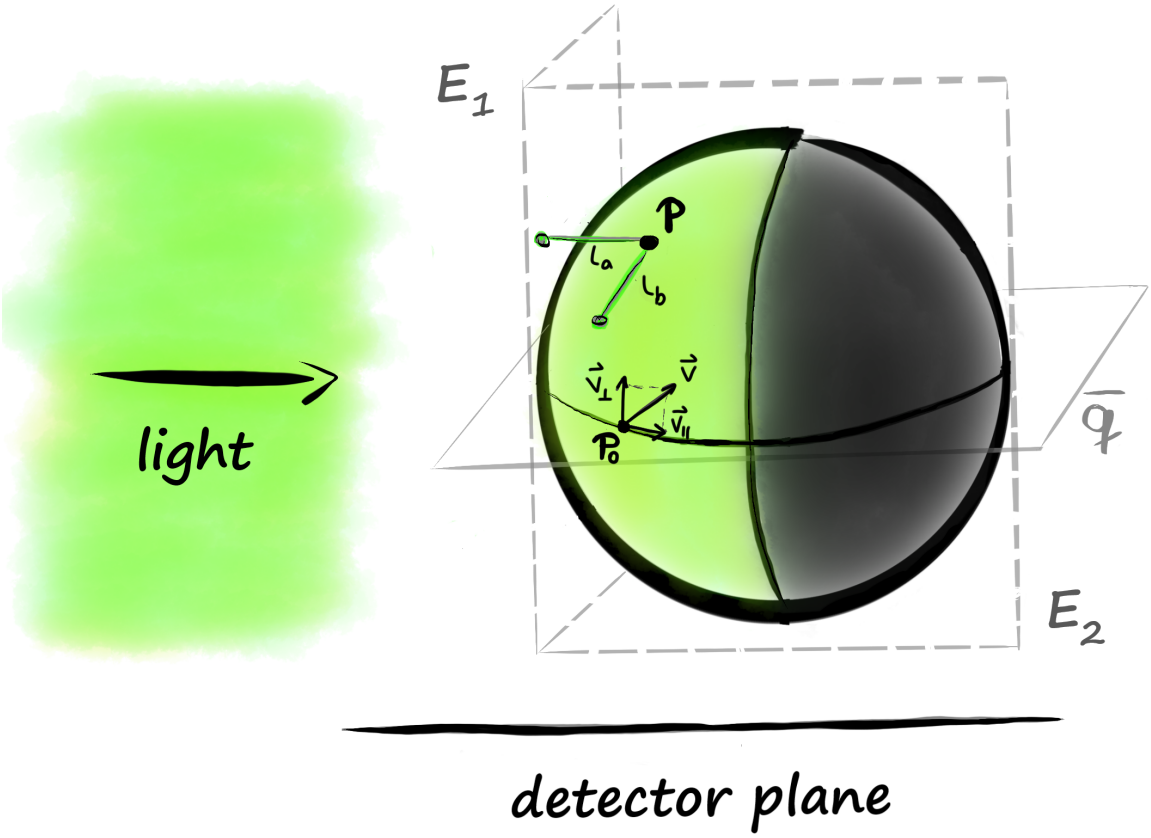

Figure 5.1.: The sphere's situation of illumination in the experimental setup from Ch. 4. The laser light is incident on the sphere from the left side of the picture, only illuminating the particle's left hemisphere. The light is detected by a detector in the detector plane after the scattering event. The horizontal equatorial scattering plane is denoted as reference plane $\bar{q}$. The auxiliary planes E_1 and E_2 are provided by the sphere's physically closest surface point towards the light source or the detector, respectively. The individual incident and scattered path contribution for each surface point are given by l_a and l_b, which are enclosed by the point P and the respective plane. The reference point P_0 marks the center of the sphere segment of interest. Each surface element has a tangential velocity $\vec{v} = \vec{v}_\perp + \vec{v}_\parallel$. Thereby, $\vec{v}_\parallel$ is determined to always be parallel to $\bar{q}$. The component $\vec{v}_\perp$ is respectively perpendicular.

the particular surface element:

$$E_G(t) = \sum_p E_p(t) e^{-i\Delta\alpha_P(t)} \tag{5.1}$$

and with $\Delta\alpha_P(t) = \vec{q} \cdot \vec{r}_P(t)$. The phase ϕ is renamed to α to avoid confusion with the spherical coordinate ϕ. $\Delta\alpha_P(\tau)$ is the abbreviation for the phase difference

$$\Delta\alpha_P(\tau) = \alpha_P(\tau) - \alpha_P \qquad \text{with} \qquad \alpha_P(\tau) = \alpha_P + \omega\tau. \tag{5.2}$$

The angular velocity ω denotes thereby the angular velocity of the particle responsible for the phase shift. Following the same logic as in Ch. 2.3.2 for the calculation from Eq. 2.64 to Eq. 2.67, we arrive at:

$$\langle E_G(t) E_G^*(t+\tau) \rangle = \sum_P \langle |E_P|^2 \rangle \langle e^{i\Delta\alpha_P(\tau)} \rangle \tag{5.3}$$

Thereby, the following assumptions, see Goodman [6], are considered: First, we assume that the amplitudes and phases are independent of each other and of other phases and amplitudes. Second, for very rough surfaces, we expect the phases to be equally distributed between $-\pi$ and π such that $\langle \alpha_P \rangle = 0$ and that the correlation area is very small such that it can not be resolved. As third requirement, we assume that the phases will fluctuate much faster than the amplitudes. A shift in phase occurs if the scatterer moves at least one wavelength [5], such that the time scales of phase fluctuation for a rotating particle of $r = 1\,\text{mm}$ with an angular velocity $\omega = 0.1\,\text{ms}^{-1}$ are of the order of $\tau = \frac{\lambda}{\omega r} = 10^{-9}\,\text{s}$ for visible light. The characteristic length on which the amplitude significantly changes is of the order of one radius. Thus, the respective time scale for amplitude fluctuations is given by about 10 ms. The estimation shows that the amplitude should fluctuate on much greater time scales than the phase and therefore, the amplitudes may be assumed to be constant.

We only want to consider selected points on the spherical scatterer's surface, namely the elements which are illuminated by the laser beam and that are simultaneously facing the direction of the detector (see Fig. 5.1) such that only a quarter of the complete sphere's surface is of particular interest. The surface area of this sector will

in the following also be referred to as region of interest. A straightforward approach to only take the relevant contributions into account is to sum up all contributions in that area of interest via the surface integral over that segment S:

$$\langle E_G E_G^*(\tau)\rangle = \int_S A^2 e^{-i\Delta\alpha(\tau)} dS \tag{5.4}$$

A^2 refers to the squared amplitude term that depends on the location of the scattering entity on the sphere's surface describing the scattering ability of that entity. The shape of granular particles may be approximated in the simplest way as spherical. Thus, the Cartesian expression above is transformed into spherical coordinates.

$$\langle E_G E_G^*(\tau)\rangle = \int_{\theta_{\min}}^{\theta_{\max}} \int_{\phi_{\max}}^{\phi_{\max}} A^2(r,\theta,\phi)\, e^{-i\Delta\alpha(r,\theta,\phi,\tau,\omega)}\, r^2\, \sin(\theta)\, d\theta\, d\phi \tag{5.5}$$

Since we approximate the particle as a sphere, the distance of the surface entity to the particle's barycenter represented by the radius r is assumed to be constant, because surficial height variances which would locally elongate or shrink the radius are magnitudes of orders smaller than the mean radius of the particle. The integral boundaries for θ and ϕ have to be selected according to the orientation of the particle's spin axis in space since the polar angle θ gives the deviation from the z-axis and the azimuth angle ϕ is always measured in the respective x-y-plane. The boundaries will be, for now, denoted as $[\theta_{\min}, \theta_{\max}]$ and $[\phi_{\min}, \phi_{\max}]$. In the following, the z-axis will always be considered to be the spin axis of the particle. A particular expression for the phase term and the amplitude term of Eq. 5.5 will be provided in the subsequent sections Chs. 5.1.1 and 5.1.2.

The used correlator computes from fluctuating intensities an autocorrelation function of the form $g_2(\tau)-1$. We use the Siegert relation [7], cf. Eq. 2.88, to convert $\langle EE^*(\tau)\rangle$ to $g_2(\tau)-1$ in order to gain the ability to analyze measured intensity autocorrelation functions with the RPM model. Thereby, we reformulate $\langle EE^*(\tau)\rangle$ to $G_1(\tau)$. $g_1(\tau)$ is then the field correlation function normalized by the intercept value. The requirement for the application of the Siegert relation is the validity of the central limit theorem such that the total scattered electric field obeys Gaussian statistics [6]. The necessity is to ensure a high number of entities that scatter light at the same time which is

given for a rough surface, cf. Ch. 2.2.3. Each surface entity may be considered as "a scatterer" such that the scattered light is randomized and all phase shifts ranging from 0 to 2π are equally probable. Then, the electric fields are expected to be normally distributed. Therefore, we reformulate Eq. 2.88 for our purposes to:

$$g_2(\tau) - 1 = \left| \frac{\langle E_G E_G^*(\tau) \rangle}{\langle E_G E_G^*(0) \rangle} \right|^2 \tag{5.6}$$

Eq. 5.5 is then transformed into an intensity autocorrelation, measurable by correlators, by simply squaring that field expression after normalization with its intercept value.

5.1.1. Functional analysis of the phase term

The phase shifts encoded in $\Delta\alpha(r, \theta, \phi, \tau, \omega)$ will be determined via Eq. 2.36 [2], where the location of the scattering entity $\vec{r}(\tau)$ on the rotating particle is time dependent:

$$\Delta\alpha(r, \theta, \phi, \tau, \omega) = \vec{q} \cdot \vec{r}(r, \theta, \phi(\omega, \tau)) \tag{5.7}$$

Since quasi-elastic scattering is assumed, $\vec{q} = |\vec{q}|$ (see Eq. 2.32). Therefore, the phase difference origins from the temporally changing locations of the scattering elements on the surface when the particle rotates. The scatterer's location is expressed by the spherical coordinates r, θ and a time-dependent azimuth angle

$$\phi(\omega, \tau) = \phi + \omega\tau \tag{5.8}$$

The time-dependence of the azimuth angle is caused by the rotation of the rigid particle about its spin axis defined here to be the z-axis. Thus, when the particle spins with an angular velocity ω, the ϕ-coordinate will change for a surface element, however the corresponding polar angle will remain the same.

The phase α_P, induced by light being scattered at a discrete surface element P, consists of a random phase contribution $\delta\alpha_P$ and a deterministic term $L_p(\tau)$, reflecting the light path, which is not altered randomly as $\delta\alpha_P$, but systematically as the sphere is rotating

with a discrete angular velocity

$$\alpha_P(\tau) = \frac{2\pi}{\lambda} L_P(\tau) + \delta\alpha_P. \tag{5.9}$$

L_P generally describes the extra travelled distance of light respective to the auxiliary planes E_1 and E_2 depending on the scattering element's position on the surface:

$$L_P = l_a + l_b \tag{5.10}$$

For the two elements at the poles, l_a and l_b are maximal and consequently L_P is maximal as well. The lowest values are expected for elements located on the sphere's equator due to the shortest distances to the respective auxiliary planes.

In order to investigate the random phase contribution $\delta\alpha_P$, we recall the assumptions made by Goodman [6] regarding light scattering on rough surfaces. First, no preferred propagation direction by the light wave after being scattered is assumed such that over the interval of $[-\pi, \pi]$, each phase of the scattered field from a surface element is equally probable. Therefore, $\delta\alpha$ is equally distributed over that interval. This results in $\langle\delta\alpha_P\rangle$=0 and therefore in $\langle\delta\alpha_P\delta\alpha_{P'}\rangle$=$\delta^*{}_{PP'}$ with δ^* denoting the Dirac-function. The Dirac-function is equal to unity if P=P' and equal to zero otherwise. Thus, the contribution of $\delta\alpha_P$ may be neglected here.

Consequently, the difference between two phases is then only dependent on the deterministic terms

$$\Delta\alpha_P(\tau) = \alpha_P(\tau) - \alpha_P = \frac{2\pi}{\lambda}\Delta L(\tau) \tag{5.11}$$

where the temporal change of l_a and l_b identifies the optical path difference between two time steps $\Delta L(\tau)$ that causes the detected phase shifts:

$$\Delta L(\tau) = l_a(\tau) + l_b(\tau) - (l_a + l_b) \tag{5.12}$$

Depending on the scattering entity's position on the sphere, the optical path length will change with time since l_a and l_b change their magnitudes. When points approach the poles, l_a and l_b increase attaining their maximum directly at the poles. The lowest values for l_a and l_b are found on the equator at the touching point on the respective

plane. Noteworthy here is that an entity travelling with time within a plane parallel to the equatorial scattering plane $\bar{q}$, l_a and l_b change but not their respective ratio and thus not their total sum, such that there $\Delta L(\tau) = \Delta L$. Therefore, we expect the greatest changes in $\Delta\alpha_P(\tau)$ from entities travelling perpendicular out of $\bar{q}$. The investigation of the sphere's spin axis orientation with respect to the setup geometry has thus such an importance. After finding an expression for the amplitude term of Eq. 5.5, particular phase term expressions based on a selection of spin axis orientations will be provided in Ch. 5.2.

5.1.2. The Gaussian spot as amplitude term

The amplitude term reflects the complexity of local light intensity distribution based on the local scattering abilities of the surface elements. For example, if the amplitude term equals a constant value, e.g. $A(r, \theta, \phi) = 1$, an uniform surface is assumed [4] where each scattering entity is illuminated with the same light intensity and scatters the light in the same manner as all of its neighboring scatterers. This is though an idealized scenario. A suitable description for most natural occurring surfaces is the Gaussian intensity distribution with the intensity peak being located in the geometrical center [6]. The brightness decays exponentially towards the outer bounds. This ansatz covers a broad range of problems from rather specular reflections to diffusive reflections. The Gaussian intensity distribution as an expression for the amplitude term will be discussed in the following. That expression shall then describe the scattering abilities of smoother and rougher surfaces more accurately within the scope of the RPM. In the following, this brightness distribution on the sphere's surface will be referred to as Gaussian spot.

The principle of such a Gaussian spot relies on weighting the brightness of the scatterers according to their position on the sphere by a Gauss function of the form

$$A^2(r, \theta, \phi, t) = e^{-\frac{d^2(r,\theta,\phi,t)}{2b^2}} \tag{5.13}$$

with d as the distance between two points: an arbitrary surface element $\mathrm{P}(\mathrm{r}, \theta, \phi)$ and the brightest element $P_0(r, \theta_0, \phi_0)$ (center of Gaussian spot) serving as reference. We note, that in Ch. 5.1, we assumed the amplitude to be constant as well as the radius

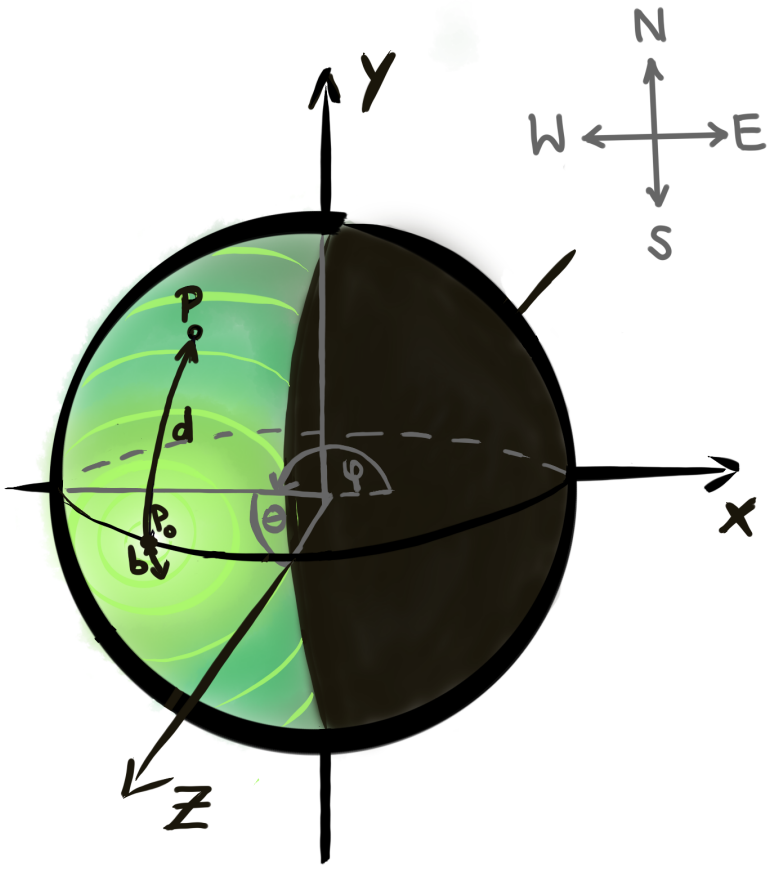

Figure 5.2.: Visualization of the Gaussian spot on a rough sphere. The light incidents on the left hemisphere. The right hemisphere is not illuminated. The distance between the center of the Gaussian spot P_0 and any point P on the particle's illuminated surface section is denoted as d. P_0 is located on the sphere's equator $\theta = 45°$. The colors ranging from light green to dark green indicate high to low intensity values of the scattered light. The brightness decreases gradually towards the margins of the considered sphere segment. The standard compass points are given in the upper right corner to provide further options of guidance. The north-south axis aligns here with the y-axis and the east-west axis with the x-axis.

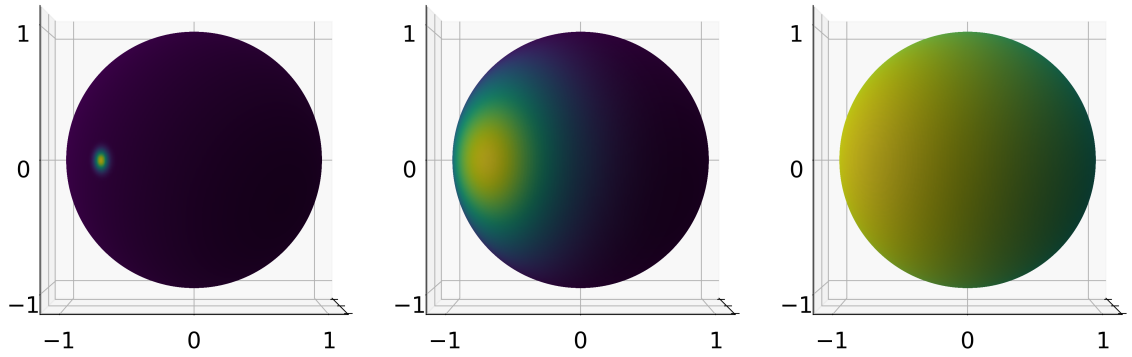

(a) Narrow Gaussian spot (b) Broad Gaussian spot (c) Very broad Gaussian spot

Figure 5.3.: Simulations of the brightness distribution on unit spheres depending on the width of the Gaussian spot. The laser is incident from the left-hand side. The colors scale from yellow to dark blue for intensities from high to low values. The laser is incident from the left-hand side. The colors scale from yellow to dark blue for intensities from high to low values. Due to the spot's small half-width (b=0.05), panel a) shows a great portion specular reflection that is typical for reflective surfaces, e.g. metal surfaces. In b), a Gaussian spot distribution with a greater variance (b=0.5) was calculated such that b) shows the scattering behavior of a rougher surface causing a significant contribution of diffuse scattering apart from specular reflections. In panel c), a very rough surface with b=2 was assumed showing a well distributed illumination indicating that high roughness by diffuse reflection only, as for example in case of the moon being illuminated by the sun.

to have a constant magnitude. The factor b determines the standard deviation of the Gaussian distribution. A schematic visualization of a Gaussian spot on the illuminated sector of a particle is provided in Fig. 5.2. Observable here is that the brightness of the scatterers decreases with increasing vicinity to the sphere's poles and with approaching the margins of the region of interest.

A Gaussian spot enables to describe the degree of specularity or diffusivity respectively by determining the parameter b, as illustrated in Fig. 5.3 a)-c). The narrower the spot, the more specular the reflection of the incident light is expected to be. In case of a very focused spot with b=0.05 (a), the portion of diffusive scattered light is so small that the reflected light component predominates and the surface may be considered smooth and reflective like metal surfaces. On the contrary, with b=0.5 the Gaussian

spot broadens with increasing surface roughness (b) merging into a very rough surface (c) for very large b-values, as e.g. b=2. An example for the latter case would be sunlight which is scattered diffusively from the moon's surface.

It is tempting to assume that the actually brightest surface entity, being the center of the Gaussian spot, should be the one facing in the direction of the incoming laser light, sitting directly in the scattering plane (leftmost point in the figure). However, from the perspective of a detector mounted orthogonal to the opto-mechanic axis of the laser, the apparent brightest entity is located at P_0 since in this point, strong reflection occurs according to Snell's law (cf. Eq. 2.48) such that the angle of the incident light equals the angle of the scattered light $\alpha_i = \alpha_s = 45°$. The portion of specular reflected light in the registered scattered light then decreases with distance from P_0.

In order to describe the distance d in Eq. 5.13 particularly, we use the principle of orthodromes from geography linking two points on a sphere's surface by the direct distance on great circles. Orthodromes are identified with help of the spherical law of cosines such that the distance on a sphere with radius r is expressed as [8]

$$d = r\ \cos^{-1}(\sin(\gamma_P)\sin(\gamma_{P0}) + \cos(\gamma_P)\cos(\gamma_{P0})\cos(\lambda_P - \lambda_{P_0})). \tag{5.14}$$

Hereby, $\cos^{-1}$ denotes the arc cosine. The variables γ and λ describe the geographic latitude and longitude, respectively. A transformation of the coordinate system is necessary since the geographical coordinate system assumes $\gamma = \frac{\pi}{2}$ at the north pole and $\gamma = -\frac{\pi}{2}$ at the south pole. However, in the general spherical coordinate system, the spin axis z pierces through the north pole of the geographical system and θ ranges from 0 to π from north to south pole. λ though is defined similar to ϕ since the meridian poses the reference for the longitude and the meridian may be arbitrarily defined in a spherical coordinate system with the spin axis pointing upwards. Thus, the only necessary conversion between both coordinate systems is

$$\gamma = \frac{\pi}{2} - \theta. \tag{5.15}$$

Eq. 5.14 may then be reformulated in the spherical coordinate system as

$$d = r\ \cos^{-1}\left(\sin\left(\frac{\pi}{2}-\theta_P\right)\sin\left(\frac{\pi}{2}-\theta_{P_0}\right)+\cos\left(\frac{\pi}{2}-\theta_P\right)\cos\left(\frac{\pi}{2}-\theta_{P_0}\right)\cos(\phi_P-\phi_{P_0})\right) \tag{5.16}$$

and the final amplitude term has the form

$$\boxed{A^2(r,\theta,\phi) = e^{-\frac{1}{2b^2}(r\ \cos^{-1}(\sin(\frac{\pi}{2}-\theta_P)\sin(\frac{\pi}{2}-\theta_{P_0})+\cos(\frac{\pi}{2}-\theta_P)\cos(\frac{\pi}{2}-\theta_{P_0})\cos(\phi_P-\phi_{P_0})))^2}} \tag{5.17}$$

The values for $P_0(\theta_{P_0}, \phi_{P_0})$ vary due to the distinct reference geometries for each case of axis orientation and have to be specifically determined. The complete integral expressions comprising θ- and ϕ-dependent amplitude and phase terms for different spin axis orientations will be presented in the next section (Ch. 5.2).

5.2. Integral solutions for distinct spin axis orientations

If a particle is spherical and rigid, its surface elements will not perform relative motions with respect to each other but rather move as a collective respective to the particle's barycenter. The angular velocity of the sphere $\vec{\omega} = \frac{\vec{v}}{\vec{r}}$ will be the same for every surface element, however, due to the sphere's curvature a distribution of tangential velocities of the elements exists. The tangential velocity increases with an element's vicinity to the equator such that points on the equator experience the maximal speed, points near the poles the minimal speed. The tangential velocity of each point is composed of a parallel and perpendicular component $\vec{v}_\parallel$ and $\vec{v}_\perp$, respectively, such that $\vec{v} = \vec{v}_\parallel + \vec{v}_\perp$, see Fig, 5.1. $\vec{v}_\parallel$ is in the following always, independent of the orientation of the sphere's spin axis, oriented parallel to the reference scattering plane $\bar{q}$ and $\vec{v}_\perp$ is respectively perpendicular oriented. When calculating the field autocorrelation function (FACF), contributions from all surface elements in the region of interest will be summed up. Thus, the tangential velocity distribution on the surface directly impacts the outcome. The higher the tangential velocity of a point, the faster the state of the system changes respective to the state at $\tau = 0$. Consequently, the FACF will decay faster. If more points with higher tangential velocities than with lower velocities are found in the

region of interest, the contributions from faster tangential velocities will in sum weigh higher than the slow velocities resulting in a faster decaying FACF than in the opposite case. Thus, a proper distinction of the spin axis orientation including distinct sets of points transiting in the illuminated sphere segment is inevitable.

The spin axis orientations confining particular cases and their derivations are discussed in the subsequent sections: First, the spin axis piercing through the center of the illuminated segment will be examined such that only the slower moving or even resting elements contribute to the FACF. In the opposite case, where the fastest elements are constantly illuminated, the FACF is expected to decay very fast. Additionally, options where the axis aligns with the day-night line such that the fastest and the slowest moving segments are probed simultaneously (full range of motion) are highlighted. We may distinguish the two most extreme deviations from the former mentioned cases: The spin axis levelled in the equatorial plane and pointing towards the collimator or laser (sphere rolls), as well as the axis pointing upwards (sphere rotates about vertical axis like e.g. the Earth in space).

5.2.1. Spin axis in the center of observation

The first spin axis orientation, which is to be investigated, is the axis piercing through the center of the illuminated sphere segment P_0. The arrangement of the Cartesian axes is illustrated in Fig. 5.4 a). The spin axis defining the z-axis is shifted to an angle of 45° between the opto-mechanic axes of the collimation optics and the laser beam. The x- and y-axis adapt to the z-axis. Thus, the angle relevant for the description of the rotation is $\phi(\tau)$, see Eq. 5.8, giving information about the angular velocity ω of the spinning particle. The spherical coordinates θ and ϕ of point P are defined by the deviation of the z-axis and in the x-y-plane with help of the auxiliary point P', respectively.

For the calculation of the path length difference we use the Hesse normal form, in particular its so-called difference formula [9]

$$d(P, E) = |(\vec{h} - \vec{g}) \cdot \vec{n}_0| \tag{5.18}$$

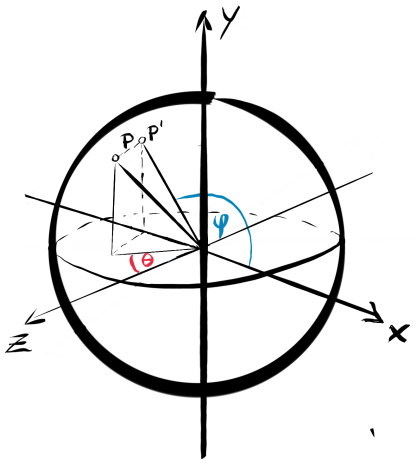

(a) Spin axis puncturing the brightest point P_0

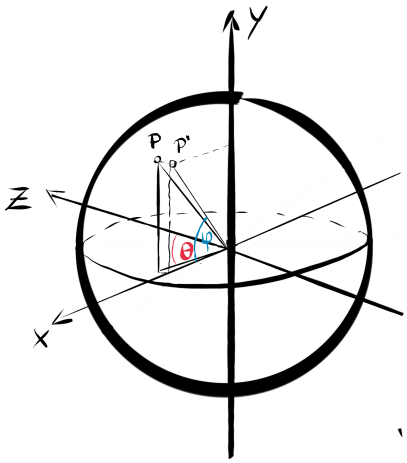

(b) Spin axis shifted about 09° to the left of case a)

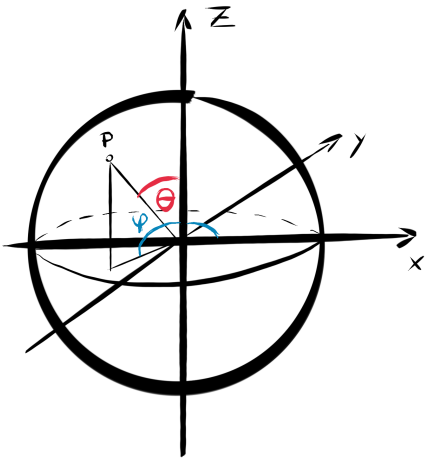

(c) Spin axis is pointing upwards

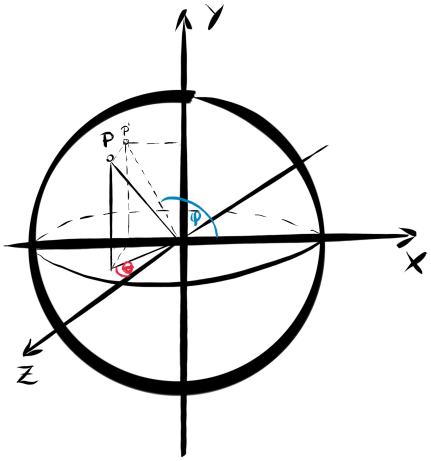

(d) Spin axis aligned with the collimator

Figure 5.4.: Schematic sketches of spheres with different axis orientations, showing the relevant ranges for the spherical coordinates θ (red) and ϕ (blue) of a point P. The point P′ indicates the projection of P onto the x-y-plane in order to determine ϕ. a) and b) show the particular cases, where the spin axis or the equator, respectively, run through the brightest surface point P_0. In panel c), the spin axis is orthogonal to the scattering plane by pointing upwards. d) represents the case of the spin axis aligning with the collimator's opto-mechanical axis.

d describes the distance of a point P, and its position vector $\vec{h} = (x_h, y_h, z_h)^T$ from the coordinate system's origin, with respect to a plane E that has a support vector $\vec{g}$ and the normal vector $\vec{n_0}$. The additional path lengths l_a and l_b may then be computed similar to d respective to their corresponding plane E_1 or E_2.

Here, the distance d equals the radius of the sphere since the auxiliary plane is tangent on the sphere's outermost point. The normal vector

$$\vec{n_0} = \frac{\bar{n}}{|\bar{n}|} \tag{5.19}$$

is determined in dependence of the x- and z-axis orientations such that for the incident components E_1 and l_a, we receive

$$\bar{n} = (-1, 0, 1)^T \qquad \text{and} \qquad |\bar{n}| = \sqrt{(-1)^2 + 1^2} = \sqrt{2} \tag{5.20}$$

$$\vec{n_0} = \frac{1}{\sqrt{2}}(-1, 0, 1)^T. \tag{5.21}$$

The distance d=r, may then be reformulated as

$$d = \frac{1}{\sqrt{2}}(-x + z). \tag{5.22}$$

The resulting path difference w.r.t the incident light components:

$$d(P, E_1) = \left| -\frac{x_p}{\sqrt{2}} + \frac{z_p}{\sqrt{2}} \right| - r \equiv l_a \tag{5.23}$$

In order to adapt to the spherical geometry, Eq. 5.23 is reformulated in spherical coordinates

$$l_a = \left| -\frac{r \sin(\theta)\cos(\phi)}{\sqrt{2}} + \frac{r \cos(\theta)}{\sqrt{2}} \right| - r. \tag{5.24}$$

The same principle applies for the components linked to the scattered light, such that $\bar{n} = (1, 0, 1)^T$ and correspondingly

$$l_b = \left| \frac{r\sin(\theta)\cos(\phi)}{\sqrt{2}} + \frac{r\cos(\theta)}{\sqrt{2}} \right| - r. \tag{5.25}$$

Both paths l_a and l_b then add together and the resulting optical path distance may be determined as

$$\Delta L = 2r\left(\frac{\cos(\theta)}{\sqrt{2}} - 1\right) \tag{5.26}$$

with a dependence on θ only. Surface points in the vicinity of the axis will then spin in small circular tracks around P_0. The diameters of those circles grow with greater θ.

The phase α_P of a point P at a specific time t is given by

$$\alpha_P = \frac{2\pi}{\lambda}\Delta L = \frac{4\pi r}{\lambda}\left(\frac{\cos(\theta)}{\sqrt{2}} - 1\right). \tag{5.27}$$

However, θ is time-independent and the relevant variable to describe the rotation would be $\phi(\tau)$ (cf. Eq. 5.8) which is not present in the equation above. In conclusion, the rotation of the particle is here insignificant for the decay of the autocorrelation function, similar to the situation as if the sphere stayed at rest. The phase shifts thus would only be noticeable between scattering events occurring on different circular tracks on the sphere but not with time. The phase shift from Eq. 5.11, only depending on θ, finally equals 0:

$$\Delta\alpha_p(\tau) = \frac{2\pi r}{\lambda}\left(\frac{\cos(\theta)}{\sqrt{2}} - 1 - \frac{\cos(\theta)}{\sqrt{2}} + 1\right) = 0 \tag{5.28}$$

This gives a time-independent phase term in the field autocorrelation function. The integral boundaries are determined by the possible ranges of positions identified by θ and ϕ in the contributing region of the sphere. For this geometry, we find the field autocorrelation function with the respective boundaries

$$\boxed{\langle E_G E_G^*(\tau)\rangle = \int_{\frac{\pi}{2}}^{\frac{3\pi}{2}} \int_0^{\frac{\pi}{2}} A^2(r,\theta,\phi) r^2 \sin(\theta) e^0 d\theta d\phi = \text{const.}} \tag{5.29}$$

with a constant value for the entire time interval such that no decay occurs and a constant intensity of the scattered light is expected. Therefore, this case of axis orientation will be neglected in the further work.

5.2.2. Equator in the center of observation

The opposite extreme respective to Ch. 5.2.1 is if the scattering entities with the highest tangential velocity travel constantly through the center of the region of interest. The axis geometry is pictured in Fig. 5.4 b). The spin axis is here 45° shifted to the left of the incoming laser beam, such that the spinning sphere's equator is constantly illuminated, but the poles are not.

For the determination of the phase term, we follow the same logic as in Ch. 5.2.1. With the adaption of the correct coordinate system, we find $\bar{n}_1 = (1, 0, 1)^T$ and $\bar{n}_2 = (1, 0, -1)^T$ for the calculation of the distance between P and E_1 and E_2 respectively, such that

$$\vec{n}_0 = \begin{cases} \frac{1}{\sqrt{2}}(1, 0, 1)^T & \text{for } l_a \\ \frac{1}{\sqrt{2}}(1, 0, -1)^T & \text{for } l_b \end{cases} \tag{5.30}$$

and consequently

$$l_a = \left|\frac{x_p}{\sqrt{2}}\right| + \left|\frac{z_p}{\sqrt{2}}\right| - r \tag{5.31}$$

$$l_b = \left|\frac{x_p}{\sqrt{2}}\right| - \left|\frac{z_p}{\sqrt{2}}\right| - r. \tag{5.32}$$

After the conversion from Cartesian coordinates to spherical coordinates, we obtain for the optical path length

$$\Delta L(\tau) = 2r\left(\frac{\sin(\theta)\cos(\phi(\tau))}{\sqrt{2}} - 1 - \frac{\sin(\theta)\cos(\phi)}{\sqrt{2}} + 1\right) \tag{5.33}$$

Here, we find a dependence of the phase term on the angle ϕ which inherits a dependence on τ. By using Eq. 5.11 and Eq. 5.8, the temporal phase shift is expressed

as

$$\Delta\alpha_p(\tau) = \frac{4\pi r}{\lambda}\left(\frac{\sin(\theta)\cos(\phi(\tau))}{\sqrt{2}} - 1 - \frac{\sin(\theta)\cos(\phi)}{\sqrt{2}} + 1\right) \tag{5.34}$$

$$= \frac{4\pi r}{\lambda\sqrt{2}}\sin(\theta)\left(\cos(\phi+\omega\tau) - \cos(\phi)\right). \tag{5.35}$$

The usage of the theorem cos(a+b)-cos(a)=-2sin$\left(\frac{b}{2}\right)$sin$\left(a+\frac{b}{2}\right)$ simplifies the term above to

$$\Delta\alpha_p(\tau) = -\frac{4\pi r}{\lambda}\sqrt{2}\sin(\theta)\sin\left(\frac{\omega\tau}{2}\right)\sin\left(\phi+\frac{\omega\tau}{2}\right). \tag{5.36}$$

Thus, the surface integral with the correct integration boundaries reads as

$$\boxed{\langle E_G E_G^*(\tau)\rangle = \int_{-\frac{\pi}{2}}^{\frac{\pi}{2}}\int_{\frac{\pi}{4}}^{\frac{3\pi}{4}} A^2(r,\theta,\phi)e^{-i\frac{4\pi r}{\lambda}\sqrt{2}\sin(\theta)\sin\left(\frac{\omega\tau}{2}\right)\sin\left(\phi+\frac{\omega\tau}{2}\right)}r^2\sin(\theta)d\theta d\phi} \tag{5.37}$$

The coordinates of the center of the Gaussian spot P_0 are $\theta_0 = \frac{\pi}{2}$ and $\phi_0 = 0$. For this axis configuration, the amplitude term is then given by:

$$\boxed{A^2(r,\theta,\phi) = e^{-\frac{r^2}{2b^2}\left(\cos^{-1}\left[\frac{\sqrt{2}}{2}\left(\sin\left(\frac{\pi}{2}-\theta_P\right)+\cos\left(\frac{\pi}{2}-\theta_P\right)\cos(\phi_P)\right)\right]\right)^2}} \tag{5.38}$$

Eq. 5.37 contains an integral of type $f(x) = \int e^{\sin(x)}dx$ and thus its primitive can not be represented by elementary functions. Therefore, it has to be solved numerically to evaluate the field correlation function further. This is however unproblematic due to the integration between discrete boundaries.

The scattering entities move here almost perpendicular in and out of the equatorial scattering plane $\bar{q}$ since $\vec{v}_\perp \gg \vec{v}_\parallel$. Consequently, greater phase shifts in this case, respective to other geometries, are expected which result in smaller decorrelation times observable in the FACF.

5.2.3. Spin axis on day/night line

In the former cases of Chs. 5.2.1 and 5.2.2, we did not include the full range of possible tangential speeds of the surface elements but focused on either considerable contributions from barely moving surface entities or the fastest moving entities available. However, in reality, probing the full range of motions is highly probable since the spin axes of particles will not always align well with the setup geometry as presented above.

There is a great variety of possible orientations the spin axis may take on. However, not every case will be discussed in the frame of this thesis, though, two further special cases may be highlighted here. The two cases describe the scenarios, when the spin axis aligns with a Cartesian axis such that the equator and at least one pole will constantly be illuminated, contributing scattering information from scattering entities with the highest and slowest velocities, respectively. Thereby, the spin axis will always be found on the day/night line, hence at the margin of the region of interest.

5.2.3.1. Spin axis pointing upwards

We now consider the z-axis being oriented orthogonal to the equatorial scattering plane $\bar{q}$. This ensures that the equator as well as both polar regions are located in the region of interest. Information about the geometry of the problem including respective angle notations may be taken from Fig. 5.4 c).

As presented above, we use the Hesse normal form to determine the optical path difference with

$$\vec{n}_0 = \begin{cases} (-1,0,0)^T & \text{for } l_a \\ (0,-1,0)^T & \text{for } l_b \end{cases} \tag{5.39}$$

such that $|\bar{n}| = \sqrt{1^2} = 1$ in both cases and the distances between the surface entity P and the auxiliary planes are given by

$$l_a = |-x_p| - r \tag{5.40}$$

$$l_b = |-y_p| - r. \tag{5.41}$$

Thus, including the conversion to the spherical coordinate system, the optical path

length difference is equal to

$$\Delta L = r\left(-\sin(\theta)\cos(\phi(\tau)) - \sin(\theta)\sin(\phi(\tau)) + \sin(\theta)\cos(\phi) + \sin(\theta)\sin(\phi)\right). \quad (5.42)$$

The recurrent usage Eq. 5.11 and Eq. 5.8 allows to express the phase shift as

$$\Delta\alpha_p(\tau) = \frac{2\pi r}{\lambda}\left(\sin(\theta)\cos(\phi(\tau)) - \sin(\theta)\sin(\phi)) + \sin(\theta)\cos(\phi) + \sin(\theta)\sin(\phi)\right) \quad (5.43)$$

$$= \frac{2\pi r}{\lambda}\sin(\theta)\left(-\cos(\phi+\omega\tau) + \cos(\phi) - \sin(\phi+\omega\tau) + \sin(\phi)\right) \quad (5.44)$$

In order to simplify the equation above we use sin(a+b)-sin(a)=$2\sin\left(\frac{b}{2}\right)\cos\left(a+\frac{b}{2}\right)$ and cos(a+b)-cos(a)=-$2\sin\left(\frac{b}{2}\right)\sin\left(a+\frac{b}{2}\right)$:

$$\Delta\alpha_p(\tau) = \frac{4\pi r}{\lambda}\sin(\theta)\sin\left(\frac{\omega\tau}{2}\right)\left(-\cos\left(\phi+\frac{\omega\tau}{2}\right) + \sin\left(\phi+\frac{\omega\tau}{2}\right)\right) \quad (5.45)$$

Finally, with applying the theorem sin(a)-cos(a)=$\sqrt{2}\sin\left(a-\frac{\pi}{4}\right)$:

$$\Delta\alpha_p(\tau) = -\frac{4\pi r}{\lambda}\sqrt{2}\sin(\theta)\sin\left(\frac{\omega\tau}{2}\right)\sin\left(\phi+\frac{\omega\tau}{2}-\frac{\pi}{4}\right) \quad (5.46)$$

The resulting surface integral to describe the field correlation function is then

$$\boxed{\langle E_G E_G^*(\tau)\rangle = \int_{\pi}^{\frac{3\pi}{2}}\int_0^{\pi} A^2(r,\theta,\phi)e^{-i\frac{4\pi r}{\lambda}\sqrt{2}\sin(\theta)\sin\left(\frac{\omega\tau}{2}\right)\sin\left(\phi+\frac{\omega\tau}{2}-\frac{\pi}{4}\right)}r^2\sin(\theta)d\theta d\phi} \quad (5.47)$$

The Gaussian spot's center is located at $\theta_{P_0} = \frac{\pi}{2}$ and $\phi_{P_0} = \frac{5\pi}{4}$. The amplitude term is therefore given by:

$$\boxed{A^2(r,\theta,\phi) = e^{-\frac{r^2}{2b^2}\left(\cos^{-1}\left[\cos\left(\frac{\pi}{2}-\theta_P\right)\cos\left(\phi_P-\frac{5\pi}{4}\right)\right]\right)^2}} \quad (5.48)$$

The surface elements move along circular tracks in horizontal planes that are parallel to the equatorial scattering plane since $\vec{v}_\perp = 0$. Therefore, greater decorrelation times

of the FACF are expected, respective to cases where the tangential velocities of the surface elements show perpendicular components unequal zero, e.g. in Ch. 5.2.2.

5.2.3.2. Spin axis located in the scattering plane

In Fig. 5.4 d), the spin axis aligns with the collimator's opto-mechanic axis. Thus, the spin axis pierces through plane E_2 at the boundary between the illuminated and the dark hemisphere. Only one polar region is therefore considered relevant for the calculation of the FACF. From the collimator's perspective, entities on the equator will then move along the apparent contour line of the sphere. This configuration shows the most extreme variation in the horizontal plane of the spin axis respective to the case discussed in Ch. 5.2.1.

In accordance to Ch. 5.2.3.1, we find

$$\vec{n}_0 = \begin{cases} (-1,0,0)^T & \text{for } l_a \\ (0,0,1)^T & \text{for } l_b \end{cases} \tag{5.49}$$

such that with $|\bar{n}| = \sqrt{1^2} = 1$ we receive

$$l_a = |-x_p| - r \tag{5.50}$$

$$l_b = |z_p| - r. \tag{5.51}$$

The optical path length difference may be reformulated after coordinate transformations from Cartesian to spherical as

$$\Delta L(\tau) = r\left(\sin(\theta)\cos(\phi(\tau)) + \cos(\theta) - 2 - \sin(\theta)\cos(\phi) - \cos(\theta) + 2\right). \tag{5.52}$$

The phase shift is then given by

$$\Delta\alpha_p(\tau) = \frac{2\pi r}{\lambda}\left(-\sin(\theta)\cos(\phi(\tau)) + \cos(\theta) + \sin(\theta)\cos(\phi) - \cos(\theta)\right) \tag{5.53}$$

$$= \frac{2\pi r}{\lambda}\sin(\theta)\left(-\cos(\phi + \omega\tau) + \cos(\phi)\right). \tag{5.54}$$

We then here use again the identity -cos(a+b)+cos(a)=$2\sin\left(\frac{b}{2}\right)\sin\left(a+\frac{b}{2}\right)$ such that the expression above transforms to

$$\Delta\alpha_p(\tau) = -\frac{4\pi r}{\lambda}\sin(\theta)\sin\left(\frac{\omega\tau}{2}\right)\sin\left(\phi+\frac{\omega\tau}{2}\right) \tag{5.55}$$

and we obtain the time-dependent exponent of the phase term of the surface integral

$$\boxed{\langle E_G E_G^*(\tau)\rangle = \int_{\frac{\pi}{2}}^{\frac{3\pi}{2}}\int_0^{\frac{\pi}{2}} A^2(r,\theta,\phi)e^{-i\frac{4\pi r}{\lambda}\sin(\theta)\sin\left(\frac{\omega\tau}{2}\right)\sin\left(\phi+\frac{\omega\tau}{2}\right)}r^2\sin(\theta)d\theta d\phi} \tag{5.56}$$

$\theta_{P_0} = \frac{\pi}{4}$ and $\phi_{P_0} = \pi$ determine the Gaussian spot's center, such that:

$$\boxed{A^2(r,\theta,\phi) = e^{-\frac{r^2}{2b^2}\left(\cos^{-1}\left[\frac{\sqrt{2}}{2}\left(\sin\left(\frac{\pi}{2}-\theta_P\right)+\cos\left(\frac{\pi}{2}-\theta_P\right)\cos(\phi_P-\pi)\right)\right]\right)^2}} \tag{5.57}$$

Of course, instead of aligning the spin axis with the axis of observation, we could also align it with the incident laser light. This will however not change the final expression for the phase term in the equation above since only a respective change of absolute values of the pair l_a and l_b is caused. If we perform calculations for the latter case, the only necessary alteration is the change of the reference coordinate system. This will then alter the expressions for the normal vectors to $\vec{n}_0 = (0,0,1)^T$ for E_1 and $\vec{n}_0 = (1,0,0)^T$ for E_2 which form the basis for the distances l_a and l_b. Further, the integration boundaries will be adjusted. A closer look on the relevant spatial dimension show, that in both cases only the x and the z component are respectively important. The polarity for both cases might not agree, but the polarity of x and z in each case coincides, such that the outcome of ΔL will be sum-wise identical. Calculations from Eq. 5.52 onwards will thus be identical.

5.3. Parameter-dependent evolution of the correlation function

In this section, model predictions of the autocorrelation functions based on varying parameters are provided. Those studies shall serve to give suitable estimations on how

strongly the model depends on the course of particular variables and if identical results regarding the decorrelation times are provided by all models.

Apart from Eq. 5.29, all field autocorrelation functions commonly depend on the variables time τ, angular velocity ω and radius r. Thus, predictions on how the model will adjust to varying angular velocities and sphere sizes is of great interest for the further use of the model. Additionally, the effect of the Gaussian spot's half-width size b on the FACF is investigated by modelling a rather specular as well as a diffusive scattering behavior of the particle's surface. A time trace, identical to that provided by the ALV correlator, is used for the calculations to ensure proximity of the time scales of the computed results to the time scales of the autocorrelation functions obtained from laboratory experiments.

5.3.1. Influence of radius and angular velocity on the phase term

Figs. 5.5 a) to c) provide field autocorrelation functions for spherical particles where the angular velocity is a fixed value of $\omega = 0.1\,\mathrm{ms}^{-1}$. The particle radius r varies from $10^{-4}\,\mathrm{m}$ to $10^{-2}\,\mathrm{m}$. A homogeneous surface where every element possess the same scattering ability was assumed, such that $A^2(r,\theta,\phi) = 1$ and thus the FACF generally:

$$\langle E_G E_G^*(\tau)\rangle \sim \int_{\phi_{\min}}^{\phi_{\max}} \int_{\theta_{\min}}^{\theta_{\max}} e^{-i\Delta\alpha(r,\theta,\phi,\omega,\tau)} \sin(\theta) d\theta d\phi \tag{5.58}$$

where the discrete phase term expression for each case of spin axis orientation from Eqs. 5.37, 5.47 and 5.56, respectively, may be inserted. Figure 5.5 a) presents the calculated field autocorrelation functions for the case of the sphere's spin axis being oriented 45° to the left of the laser beam's opto-mechanical axis (cf. Ch. 5.2.2). Fig. 5.5 b) corresponds to the scenario with the spin axis pointing upwards (cf. Ch. 5.2.3.1) and 5.5 c) pictures the autocorrelation functions for the spin axis aligning with the collimator (cf. 5.2.3.2). The FACFs were normalized by $\langle E_G E_G^*(0)\rangle$. We receive FACFs with a single decay accompanied by oscillations due to the periodic functions in the exponential function's exponent.

The oscillations, which we can not assign a definite explanation yet, supposedly indi-

cate a degree of restoration of the initial surface scatterer configuration, and thus the scattered phase configuration, after some time. For example, from Fig. 5.5 a), we observe the first recurring peak for a particle size of 1 mm after $\tau_r = 4.5\,\mu$s. The distance, which a surface entity has travelled within that interval is estimated by $x = \omega \cdot r \cdot \tau_r$, such that with $\omega = 0.1\,\mathrm{ms}^{-1}$: $x = 10^4\,\mathrm{s}^{-1} \cdot 10^{-3}\,\mathrm{m} \cdot 4.5 \cdot 10^{-6}\,\mathrm{s} \approx \lambda$. Consequently, the element has travelled one wavelength to induce a decay of the FACF.

Greater radii shift the function to lower decay time values. For a particle of $r = 100\,\mu$m, the function decays within tens of microseconds whereas 1 cm-sized particles cause decays within hundreds of nanoseconds under similar conditions. Thus, the smaller the particle is, the slower the FACF will decay.

A likewise behavior is observable if the particle size remains constant, e.g. r=1 mm, but if the angular velocity ω of the spinning particle is varied from $0.01\,\mathrm{ms}^{-1}$ to $1\,\mathrm{ms}^{-1}$, cf. Figs. 5.6 a) to c). For $\omega = 0.01\,\mathrm{ms}^{-1}$, the FACF decays within tens of microseconds whereas an angular velocity of $1\,\mathrm{ms}^{-1}$ causes a full decay within hundreds of nanoseconds. In conclusion, the faster the particle spins, the faster the FACF will decorrelate.

Figures 5.5 d) and 5.6 d) show comparisons of the decay times for varying r and ω values, respectively, for the distinct spin axis orientations. The discrete values were obtained from taking the average of the τ-value of the last data point of the FACF's initial decay in the positive domain and the τ-value of the first data point in the negative domain. We observe a linear relation for all cases between τ and r as well as between τ and ω on logarithmic scales. Thus, increasing the radius or the angular velocity by one order of magnitude will cause decorrelation times an order of magnitude smaller. ω and r are related directly by the tangential velocity on the sphere's surface

$$\vec{v} = \vec{\omega} \cdot \vec{r}. \tag{5.59}$$

Thus, we conclude from the results above, that the tangential velocities of the surface elements determine the timescales of the field autocorrelation function's decay.

In case of the three chosen spin axis orientations, the distribution of the tangential velocities of the surface elements within the illuminated area of interest varies. Thus,

we obtain three different decorrelation time values under the same conditions, see Figs. 5.5 d) and 5.6 d). The highest τ-value under given conditions is always observed for the spin axis being orthogonally oriented to the reference scattering plane $\bar{q}$. The lowest τ-value, indicating the fastest decay, is always noted for case a), where the spin axis is found 45° shifted to the left of the laser beam's opto-mechanic axis.

This discrepancy in the predicted decorrelation times arises from the velocity distributions of the surface elements that traverse the illuminated region of interest in the particular cases, cf. Fig. 5.7. As mentioned in Ch. 5.2, the tangentially fastest elements are located on the sphere's equator, the slowest at the poles. In case a), only fast elements travel through the region of interest since the poles are not illuminated, but the elements on the equator and in its vicinity are. However, in b) the full range of tangential velocities is probed comprising equatorial elements as well as those of both poles. Case c) is the intermediate case between a) and b) since here, the equator elements traverse the region of interest, but slow elements from only a single pole region also contribute. Therefore, the average tangential velocity will be greater for case a) than for c) and b) respectively, with b) comprising the greatest portion of slowly moving elements of all three scenarios.

In conclusion, we note that it is necessary to distinguish between different spin axis orientations in the model since the geometry and the consequent tangential velocity distribution of the relevant scattering elements on the surface defines the decay times of the autocorrelation functions. However, all models show the same decay shape and the calculated values range in the same orders of magnitudes. Therefore, the approach may still be considered reasonable, even though we might compromise slight deviations from the actual decay times, if the orientation of the spin axis is not correctly identified. In real granular systems however, it is quite improbable that the spin axis perfectly aligns with one of the particular cases presented above. There is a great probability that the axis punctures the by the three axes spanned surface space. Thus, in such a situation, the spin axis will supposedly adapt to an averaged orientation, respective to those orientations presented above, and, still, a good accuracy in the investigations may be given.

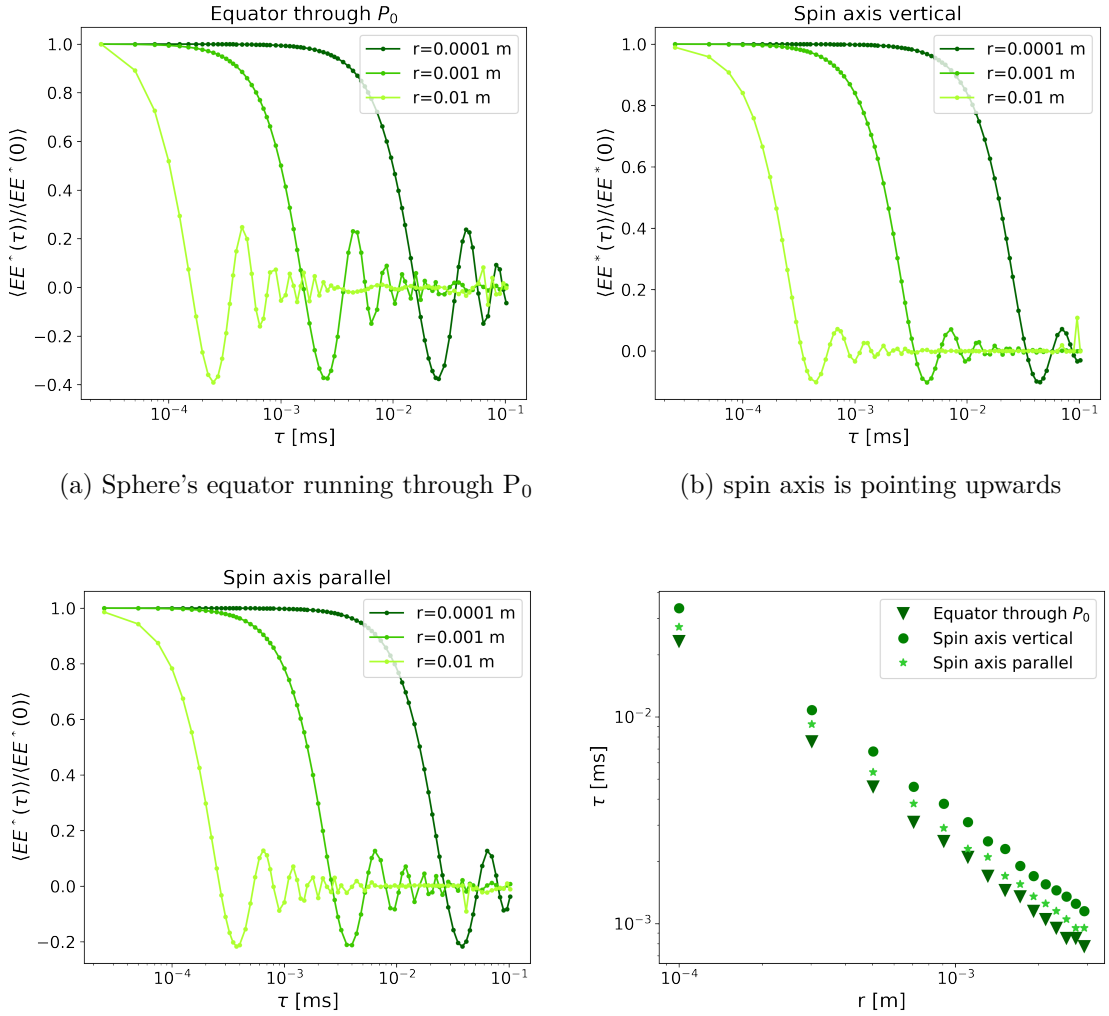

(a) Sphere's equator running through P_0

(b) spin axis is pointing upwards

(c) Spin axis aligning with the collimator

(d) Decorrelation time in dependence of particle radius

Figure 5.5.: The influence of the particle's radius r on the field autocorrelation function (FACF) for each discussed axis orientation. The autocorrelation function is a complex function of which only the real part is plotted here. a) shows the FACF for different radii in case of the sphere's equator running through the brightest point P_0, b) pictures the situation for an upwards pointing axis. In c), the spin axis aligns with the collimator's opto-mechanic axis. Panel d) gives the decorrelation times τ of the FACFs for each case (a)-(c) in dependence of a varying particle radius on logarithmic scales.

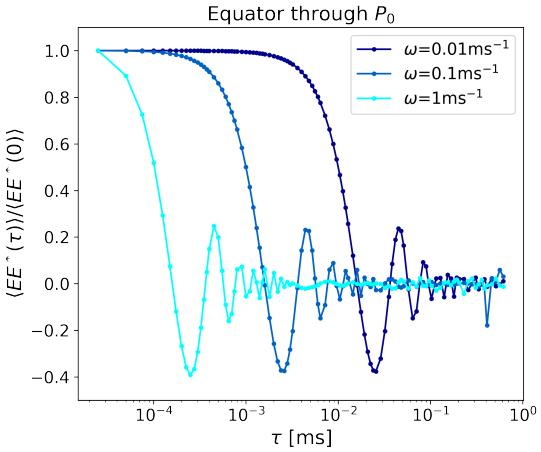

(a) Sphere's equator running through P_0

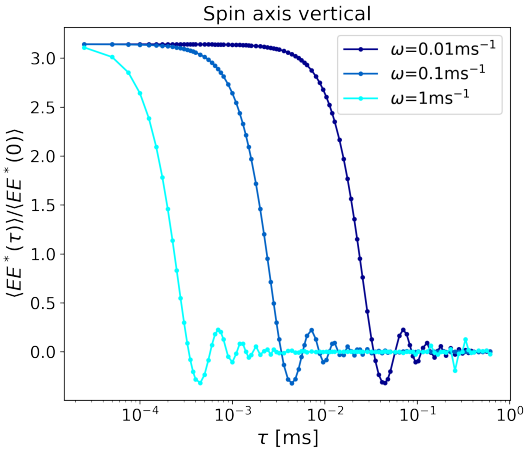

(b) spin axis is pointing upwards

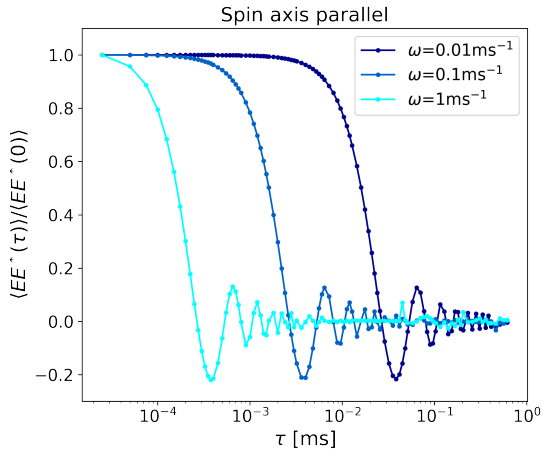

(c) Spin axis aligning with the collimator

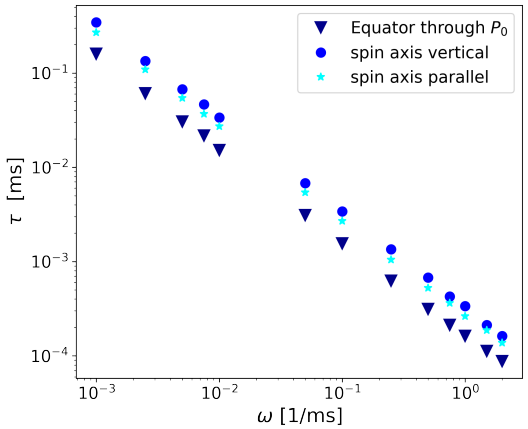

(d) Decorrelation time in dependence of particle's angular velocity

Figure 5.6.: The influence of the particle's angular velocity ω on the field autocorrelation function (FACF) for each discussed axis orientation. The autocorrelation function is a complex function of which only the real part is plotted here. a) shows the FACF for different angular velocities in case of the sphere's equator running through the brightest point P_0, b) pictures the situation for an upwards pointing axis. In c), the spin axis aligns with the collimator's opto-mechanic axis. Panel d) gives the decorrelation times τ of the FACFs for each case (a)-(c) in dependence of a varying angular velocity on logarithmic scales.

5.3.2. Effect of the Gaussian spot half-width on the amplitude term

Fig. 5.8 shows the normalized field autocorrelation functions for each orientation with the fixed values of r=1 mm and $\omega = 0.1\,\mathrm{ms}^{-1}$. For the amplitude term $A^2(r, \theta, \phi)$ the known expression from Eq. 5.17, depending on the spherical coordinates of a surface element, is inserted. The variable of interest is the half-width of the Gaussian spot

$$b(r) = \mathrm{w} \cdot r \tag{5.60}$$

which is here formulated in dependence of the particle radius r to ensure reasonable results. From Ch. 5.1.2 we know, that broad Gaussian spots represent rough surfaces. The smaller b, the more specular the scattering. The constant w denotes the ratio of the sphere's radius to the spot's half-width, which is assignable to the standart deviation of the Gaussian distribution. If w=1, the spot's brightest section is as wide as the radius of the sphere. Thus, if w>1, the entire spot would be broader than the particle itself, such that no significant brightness variations beyond w=1 may be expected. Then, the sphere's surface is assumed to be homogeneously illuminated.

In Figs. 5.8 a) to c), we see the calculated FACFs with a single decay accompanied by oscillations at later times for greater b-values. The b-value varies from 0.1r via 0.5r to $b = r$. The greater the b-value the broader also the probed velocity distribution on the sphere's surface. We observe no linear relationship between the decorrelation times τ and the chosen b-values. For example in case of a), if $b = 0.1$r, the function decays within a microsecond, for $b = 0.5$r we find $\tau \approx 3\,\mu$s and for $b = r$, the FACF decays in less than $20\,\mu$s.

Fig. 5.8 d) provides a comparison of a range of b-values for all three models, probing different tangential velocity distributions, on logarithmic scales. The discrete values were obtained from taking the average of the τ-value of the last data point in the positive domain of the FACF's initial decay and the τ-value of the first data point in the negative domain, similar to the procedure from Ch. 5.3.1. As also noted in Ch. 5.3.1, we observe here slightly different decorrelation times for all three models under the same conditions. For $b < 0.5$r, the τ-values decrease with increasing b-values. If

the spin axis is found in the $\bar{q}$-plane and shifted 45° to the left of the laser's opto-mechanic axis (case a)), the FACF experiences the fastest decays. The slowest decays are noted for the spin axis pointing towards the detector (case c)) for $b \geq r$. For greater b-values, the FACFs of case c) decay slightly faster than those of b). In case of b), the τ-values saturate for $b \geq 0.5$r at a specific value of $\tau \approx 3\,\mu$s. In contrast, the decorrelation times for c) decrease further until $b = r$. If the spin axis points in the direction of the collimator, $\tau \approx 2.5\,\mu$s is obtained for $b \geq r$. For case a), the lowest τ-values are always found saturating at less than $2\,\mu$s for $b \geq r$. Comparing again case a) with c), we note the same τ-trend but different magnitudes of τ. The comparably slower τ-values for c) origin from also including slower surface elements from one polar region in the calculations, cf. Fig. 5.7, which decrease the average surficial velocity and, consequently, increase the FACF's decorrelation time.

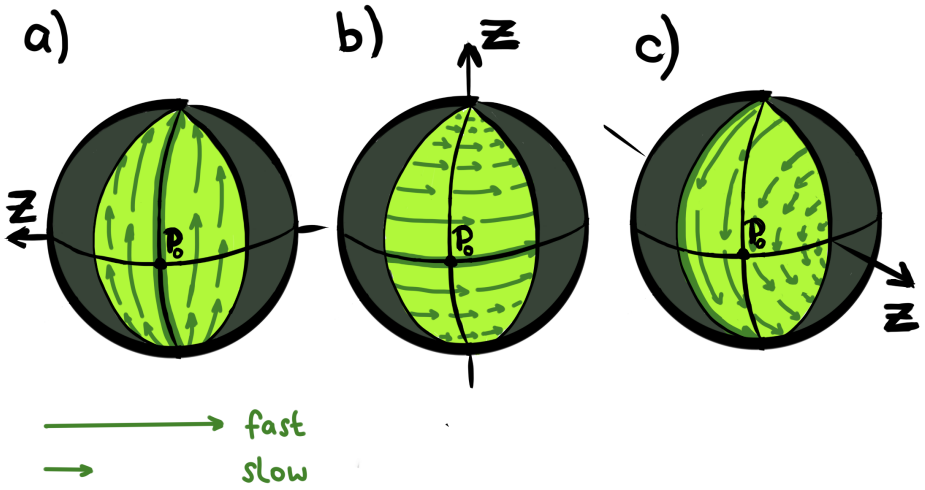

Figure 5.7.: This schematic sketch illustrates the tangential velocity distributions of the surface elements on the modelled spheres. The length of the arrow indicates the magnitude of the tangential velocity. The greatest magnitude at the sphere's equator is emphasized by a wider arrow. The highlighted green section represents the quarter section of the sphere that is illuminated and simultaneously facing the detector. The point P_0 shows the center of that section. The spin axis for each case is indicated by the corresponding z-axis. Case a) describes the sphere's equator constantly running through P_0, b) represents the case of a vertical spin axis and in c) the spin axis aligns with the direction of observation.

The saturation of τ arises from a combination of the probed surficial velocity distribution of the particle and the ratio between the width of the region of interest and the Gaussian spot's width. The region of interest comprises approximately a maximum width of r and a maximum height of 2r. In the particular case of b), the spot, centered around point P_0, is one radius wide if w= $\frac{1}{2}$ applies. Thus, it will then equal the horizontal width of the region of interest such that this region may be considered horizontally homogeneously illuminated for w= $\frac{1}{2}$ and beyond. In this particular case, the surface elements with the highest velocity cross that region. However, the upper and lower sectors of the region of interest, where for b) the polar regions of the sphere are found, need higher b-values to be weighted to the same extend as the surface elements near the equator region. Because those two regions are respectively small and provide only information about the slower moving elements, the decay times will not increase significantly further. In cases a) and c), the decorrelation times saturate for $b \geq r$, where all surface elements are expected to be equally bright such that no weighting of distinct contributions is relevant anymore.

Thus, we conclude that for very rough surfaces, i.e. great values of b, an average decorrelation time can be obtained quite easily for a sufficiently broad brightness distribution. However, for small b-values, which mimic the case of a reflecting surface, or also just a partially illuminated rough surface within the scope of this model, the probed surface element velocity distribution strongly impacts the resulting decorrelation times τ. From the figures above, we observe that under the same conditions, for rough surfaces, the FACF decays much faster than for specular scattering behavior, see Fig. 5.8 d). For specular reflecting surfaces, it is important to know, which region of interest is particularly being probed. Due to the small field of observation, changes in the velocity distribution have a significant impact on the temporal average of the FACF that is investigated.

In Fig. 5.9 a) to c), the intensity autocorrelation functions (IACF) are presented. The IACFs were obtained from the FACFs by using the Siegert relation, cf. Eq. 5.6. After squaring the normalized integral expressions, we observe that the magnitudes of the oscillation decrease significantly and that the functions decay from 1 to 0 as expected. The oscillations for greater b-values after the initial decay are notably small (less than

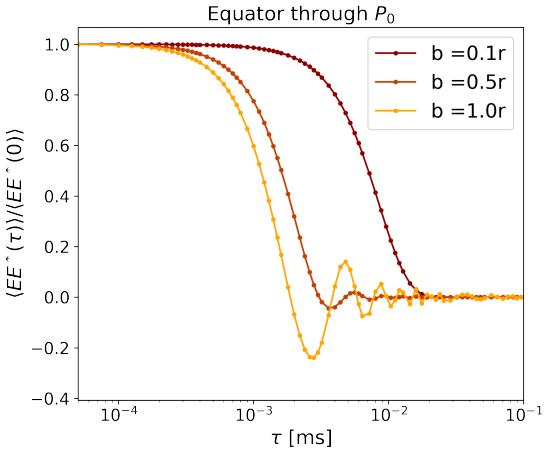

(a) Sphere's equator running through P_0

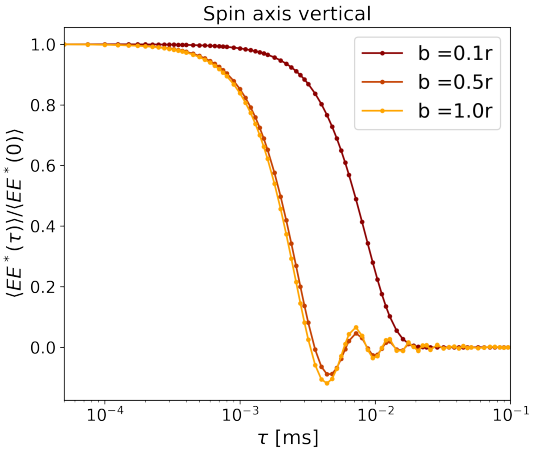

(b) spin axis is pointing upwards

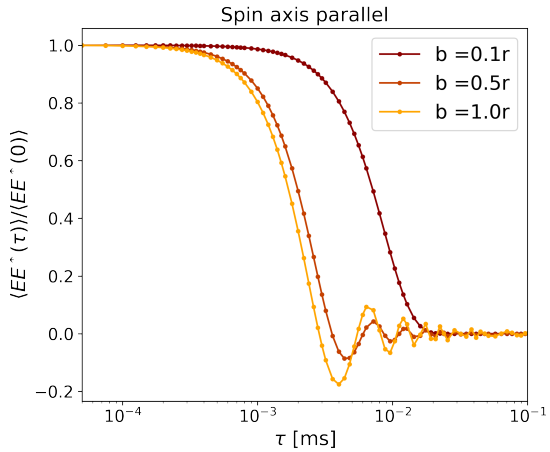

(c) Spin axis aligning with the collimator

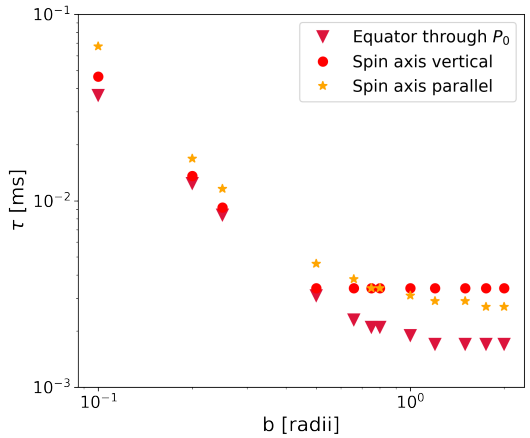

(d) Decorrelation time in dependence of the Gaussian spot width

Figure 5.8.: The influence of the Gaussian spot width b on the field autocorrelation function (FACF) for each discussed axis orientation. The autocorrelation function is a complex function of which only the real part is plotted here. a) shows the FACF for different spot widths in case of the sphere's equator running through the brightest point P_0, b) pictures the situation for an upwards pointing axis. In c), the spin axis aligns with the collimator's opto-mechanic axis. Panel d) gives the decorrelation times τ of the FACFs for each case a)-c) in dependence of a varying spot width on logarithmic scales.

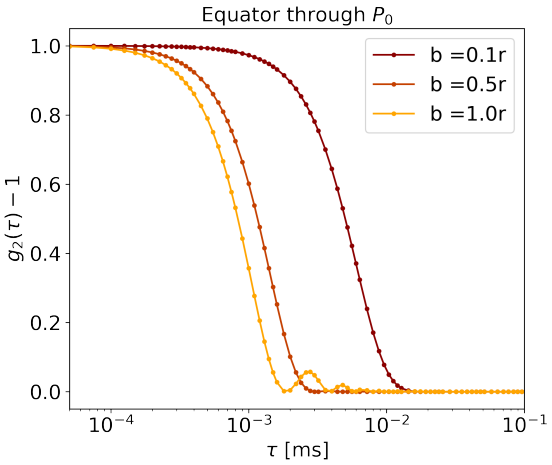

(a) Sphere's equator running through spot's center

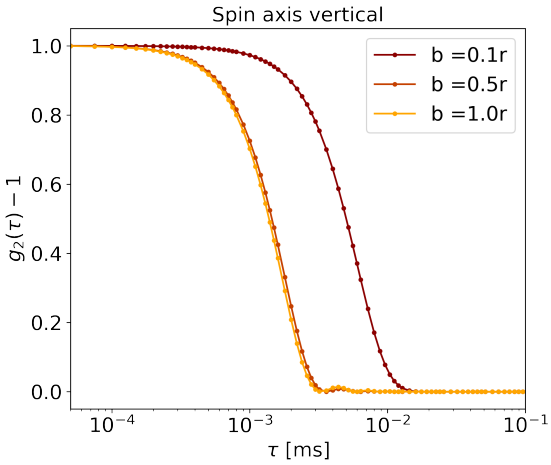

(b) spin axis pointing upwards

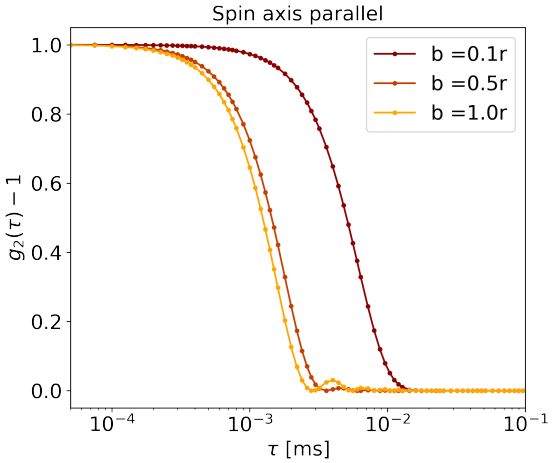

(c) Spin axis located in the scattering plane

Figure 5.9.: The influence of the Gaussian spot half-width b on the autocorrelation function $g_2 - 1$ for each discussed axis orientation. The fixed parameters for the estimation are a radius of r=1 mm and an angular velocity of ω=0.1 ms^{-1}. Above, each panel represents the ACFs for a specific orientation of the spin axis comparable to the former figures.

10% of the decay's amplitude) for all three cases. No oscillations are observable for small spot widths. When comparing the results with measured IACFs from Ch. 6, a reasonable similarity in shape will be asserted.

5.4. Conclusion

The aim of this chapter was to develop a model which permits the analysis of the autocorrelation function of a single diffusive scattering rotating macroscopic sphere. Due to the large particle radii compared to the incident light's wavelength, the scattering on the particle was treated here as a situation of scattering on homogeneous surfaces (cf. Ch. 2.2.3). The phase shifts in the scattered light are accessible by formulating the temporal field autocorrelation function of the scattered electric field as surface integral over all relevant scattering elements on the particle's surface.

The phase terms' exponents contain information about the light's wavelength, the particle size and the angular velocity, which the particle adopts. Thus, the concept may also be applicable to other types of radiation from the electromagnetic spectrum of light. We observed linear relationships between the field autocorrelation function's decorrelation time and the particle size and angular velocity, respectively, and thus also for the tangential velocity distribution, for a particular orientation of the particle's spin axis.

Different spin axis orientations were discussed since the distribution of the tangential velocities of the surface elements determines the time scales on which the autocorrelation functions decays. The geometry defines the evolution of the optical path difference of the incident light when scattered on the surface. The phase terms change accordingly (cf. Ch. 5.2). Motions out of the scattering plane show the most rapid changes in the optical path length difference and thus also in the scattered light's phases.

The amplitude term includes information about the by the surface elements scattered intensities based on the surface structure. The particle's surface is considered to be homogeneous such that the amplitude terms may be assumed to be time-independent. Only the location of the scattering element on the surface then defines the amplitude's magnitude, weighted by the selected brightness distribution on the surface. The surface's brightness distribution is here characterized by a Gaussian spot, which comprises expressions for rough surfaces as well as smooth and reflecting surfaces by using the corresponding spot half-width. Generally, smaller decorrelation times were obtained for broader brightness distributions, i.e. broader spot widths.

The RPM model may provide a first approach to the problem of light scattering on homogeneous particles with greater diameters. However, one should keep in mind that this model does not account for more than one polarization direction of light. Also, it was assumed that the amplitude is time-independent as all surface elements are expected to have the same scattering behavior. However, the expressions used exclude scenarios, where specific inhomogeneities in and on the surface cause a time-dependence of the amplitude term when the object rotates. Finding particular expressions for those scenarios is motivating further studies. Additionally, only four particular axis orientations were discussed. The model gains accuracy and provides more opportunities for the analysis of realistic scenarios if a general expression for all potential axis orientations is found. Further studies on this should also be motivated in the future. Effects like precession and nutation of the spin axis, which have also been neglected here, may be included in those studies. Those effects are relevant problems in view of time-dependent amplitude terms.

This model will be tested experimentally in the following chapter (Ch. 6) such that subsequently first steps on the investigation of the rotational granular temperature-like quantity within the scope of this experimental setup (Ch. 7) may be performed.

References

[1] C. F. Bohren and D. R. Huffman. *Absorption and scattering of light by small particles*. John Wiley & Sons, 2008.

[2] S. U. Egelhaaf. "Solution Scattering". In: *Soft condensed matter physics in molecular and cell biology*. Taylor & Francis, 2006, p. 38.

[3] J. Churnside. "Speckle from a rotating diffuse object". In: *JOSA* 72.11 (1982), pp. 1464–1469.

[4] J. C. Marron and K. S. Schroeder. "Speckle from rough rotating objects". In: *Applied optics* 27.20 (1988), pp. 4279–4287.

[5] B. J. Berne and R. Pecora. *Dynamic light scattering: with applications to chemistry, biology, and physics*. Courier Corporation, 2000.

[6] J. W. Goodman. “Statistical properties of laser speckle patterns”. In: *Laser speckle and related phenomena*. Springer, 1975, pp. 9–75.

[7] A. Siegert. *On the fluctuations in signals returned by many independently moving scatterers*. Radiation Laboratory, Massachusetts Institute of Technology, 1943.

[8] P. Wongapiwatkul, P. Laosinchai, and B. Panijpan. “Enhancing conceptual understanding of trigonometry using Earth geometry and the great circle”. In: *Australian Senior Mathematics Journal* 25.1 (2011), pp. 54–63.

[9] F. Lemmermeyer. *Hurwitz und die eulersche Identitaet*. `https://www.mathi.uni-heidelberg.de/~flemmermeyer/publ/hurwitz.pdf`. Accessed: 2023-01-18.

6. Experimental validation of the rough particle model (RPM)

The concept of the rough particle model (RPM) from Ch. 5 is now to be experimentally validated. For this purpose, experimental conditions must be created, where the rotational motion of a particle will be deterministic while a stable orientation of the rotational axis is ensured. Consequently, the experiment may be repeated countless times and the rotational speed can be reproduced each time. Thus, the case of a sphere rolling along an inclined plane with the axis of rotation pointing in the direction of the collimator will be investigated in support of Ch. 5.2.3.2. Due to the rolling motion along the plane, the sphere adopts a specific translational speed, which corresponds to the rotational speed. As soon as the sphere leaves the plane, it continues to rotate with the same rotational speed, which is however now independent of the translational motion, i.e. the fall of the sphere. If the contribution of the translational motion as in Ch. 4 is isolated, the rotational motion of the sphere is the only remaining mode of motion of the sphere which is to be analyzed.

The idea is not only to generate DLS data but also to verify the results visually by using a camera. The camera data is then evaluated with the method of image particle velocimetry (PIV). The angular velocity of the rotating sphere is extracted from both methods and will be compared to determine the quality of the RPM model from Ch. 5.

In the following section Ch. 6.1, the used experimental setup will be presented and particular thoughts regarding the arrangement of the components will be discussed. In Ch. 6.2, the collected dynamic light scattering data will be processed, followed by an

analysis of the camera data with particle image velocimetry (PIV) in Ch. 6.3. In the final section Ch. 6.4, the results from both methods will be compared and conclusions are drawn.

6.1. Setup arrangement

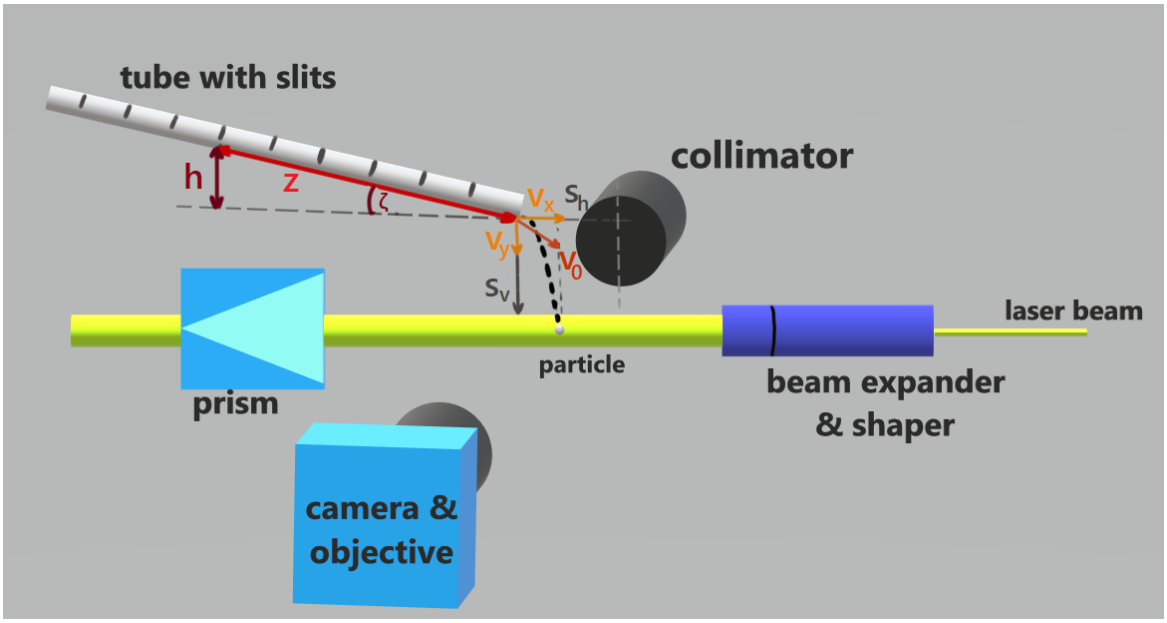

Figure 6.1.: A schematic drawing of the used experimental setup. The detection optics as well as the laser, including the beam shaping optics, from prior experiments are kept. Particles roll down an inclined plastic tube before passing through the laser beam with a velocity $v=v_x+v_y$. The tube is mounted with a distance s_v above the laser and a horizontal distance s_h respective to the center of the collimator's aperture. The inclination of the tube is marked by ζ, accompanied by the height h and distance within the tube z to define the start position of the rolling particles at the respective slit. The slits are indicated representatively by the dark lines on the tube. A prism with flanked sides is additionally installed when photos are taken to ensure sufficient illumination of the particle from all sides.

The experimental setup is pictured in Fig. 6.1. Most of the components from the previous chapters (camera plus objective lense, laser and beam shaping optics) are kept, but again a change of equipment regarding the drop mechanism of the particles

is necessary. PTFE spheres with a diameter of 2.0 mm are used as scatterers (cf. Ch. 4.4).

An important requirement for the usage of PIV in Ch. 6.3 is to ensure that the sample is uniformly illuminated such that brightness contrasts on the sphere's surface only occur due to the intentionally painted black spots as reference marks for the PIV processing algorithm. Otherwise, misinterpretations due to unwanted shadows on the sphere's surface may arise. In this experimental setup, the only light source with a sufficiently high intensity to let the sphere be adequately illuminated, on images taken with exposure times of about 100μs, is the laser which, however, only illuminates the particle's right hemisphere in the photos, cf. the inset in the left panel of Fig. 4.11. By using a prism whose angled flank surfaces reflect the light back towards the particle, an illumination with the same light intensity of the left hemisphere is assured. From the beam shaper optics' perspective, this prism is positioned behind the falling particle. The prism, however, was only used when no DLS measurements were performed but only photos were taken. Otherwise, no single scattering of the laser light would be guaranteed. We may perform the DLS and the camera measurements separately due to the findings in Ch. 6.2.

The inclined plane is realized by a plastic tube that is aligned with a predetermined angle of inclination ζ above the upper bound of the laser beam. That distance between the beam's top and the tube's tip is denoted as s_v. s_h marks the horizontal distance of the tube's tip with respect to the plane running through the center of the collimator's aperture and the geometric center of the objective. The tube is aligned with the center ray of the incident laser beam, such that the sphere's axis of rotation points in the direction of the collimator. In order to realize different rotational speeds, the particle starts from specific start positions in the tube, which, according to the law of conservation of energy, result in different roll and thus rotation speeds. Therefore, small slits were cut in the tube's top half into which small plastic plates were inserted acting as stoppers to keep the particles at their starting position until the experiment begins. The removal of the stoppers then causes the sphere to start rolling and subsequently the sphere drops into the laser beam.

To assure an optimal feeding of light scattered in 90° into the collimator's aperture,

that has its maximal efficiency in its geometrical center, an estimation of the sphere's horizontal flight distance is useful to place the tip of the tube in the most profitable position with respect to the aperture. The observation volume is limited by the dimensions of the collimator's aperture and, depending on its velocity, not every trajectory might be detectable. When the sphere leaves the inclined plane at its tipping point, the sphere's trajectory will change due to the effects of gravity such that the trajectory resembles the parabolic path of a thrown object like for example a projectile.

Because of the variance of the rotational speeds on one hand and the flown horizontal distance x_h after leaving the tube's tip as consequence of the range of roll speeds within the tube on the other hand, predictions of the rotational speeds in dependence of the start level are beneficial. The start level is hereby determined by the point P(z,h) which implies the length of the travelled tube segment z, that the sphere is rolling down on, and the local start height h that is dictated by the inclination angle, see Fig. 6.1. We use the conservation of energy. Assuming that the potential energy E_{pot} of the particle can be converted into kinetic energy E_{kin} such that:

$$E_{\text{pot}} = E_{\text{kin}} \tag{6.1}$$

Further it is assumed that the rolling resistance may be neglected in this experiment since the sphere ideally only touches the tube in a single point. The kinetic energy may further be distiguished into contributions from the translational and the rotational motion, respectively, such that:

$$E_{\text{kin}} = E_{\text{transl}} + E_{rot} \tag{6.2}$$

$$mgh = \frac{m}{2}v^2 + \frac{J}{2}\omega^2 \quad \text{with } J = \frac{2}{5}mr^2 \tag{6.3}$$

where m denotes the mass of the sphere, g = 9.81 $\frac{m}{s^2}$ the gravitational acceleration, h the height of the sphere's bottom point on the inclined plane, i.e. start height, and v the spheres translational velocity. Its angular velocity is called ω and J represents the massive sphere's moment of inertia depending on the sphere's radius r. The direct

relation between the translational and angular velocity is given by

$$v = \omega r. \tag{6.4}$$

With trigonometry the height of a point on the inclined plane may be reformulated by the sine of the inclination angle and the point's distance z with respect to the tip of the plane

$$h = \sin(\zeta) z. \tag{6.5}$$

By cancelling the masses in Eq. 6.3 and inserting the relation above we obtain

$$2g \sin(\zeta) z = v^2 + \frac{2}{5} v^2 \tag{6.6}$$

$$v = \sqrt{\frac{10}{7} z g \sin(\zeta)} = \sqrt{\frac{10}{7} g h} \equiv v_0. \tag{6.7}$$

The translational velocity of the rolling sphere and consequently the initial velocity v_0 of the falling process and thus the parabolic trajectory depends, according to Eq. 6.7, on the start position of the spheres in the tube which is linked to the tube's inclination. The velocity is however independent of a sphere's properties as e.g. the radius or the mass. Trigonometric functions may be used again to give a rough estimation of the horizontal and vertical velocity components v_x and v_y, respectively, as depicted in Fig. 6.1

$$v_x = v_0 \cos(\zeta) \tag{6.8}$$

$$v_y = v_0 \sin(\zeta) \tag{6.9}$$

such that the estimation of the horizontal x-component of the particle's flight distance may be determined by:

$$x_h = v_x \sqrt{\frac{2 s_v}{g}} = v_0 \cos(\zeta) \sqrt{\frac{2 s_v}{g}} \tag{6.10}$$

Consequently, the horizontal distance flown by the sphere increases with the start level on the inclined plane. Due to the cosine or sine relation, respectively, there is no linear relation between the degree of inclination and parameters like the start level height or

the particle's horizontal velocity component as presented in Fig. 6.2 for the inclination angle ζ ranging from 1° to 90°.

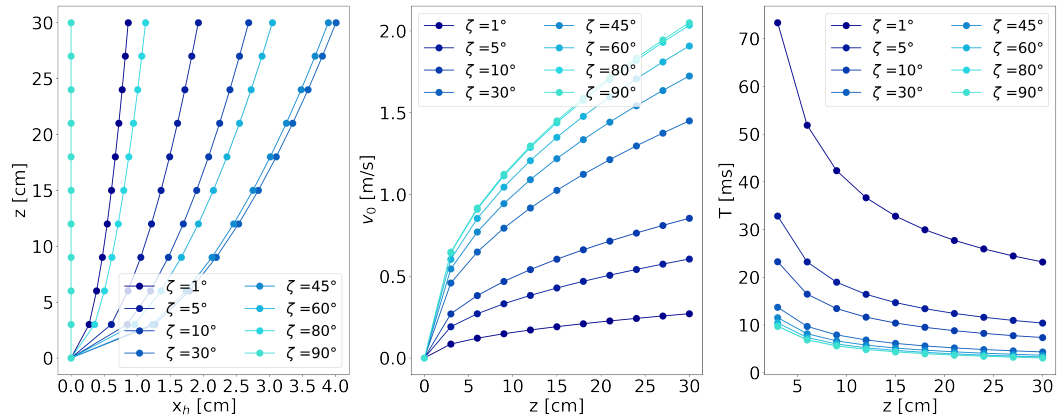

Figure 6.2.: Calculation of flight parameters respective to a variety of inclination angles ζ ranging from 1° to 90°. The left figure shows the interplay of the start position variable z in the tube with the horizontal flight distance a particle encounters when leaving the tube. The evolution of x_h is not monotonic with ζ and z, but has a point of return at about $\zeta = 33°$. The figure in the middle represents the dependence of the particle's velocity at the tube's tip v_0 on the start position z. The higher ζ, the greater v_0 for the corresponding start position. On the right side, the relation between the time the particle needs to fulfill a revolution T and z is illustrated for different ζ. The greater the plane's inclination, the faster the particle rotates.

In figure 6.2 a), the relation between the start level point P(z,h), in particular z, and the horizontal flight distance x_h from the tipping point are shown. A higher start point accompanies a greater horizontal flight distance. With decreasing ζ the range of the x_h covered increases showing a greater difference between the x_h of very small z with respect to greater z. For example, for $\zeta = 45°$ a start level point P(z=3 cm,h) corresponds to a horizontal distance of $x_h = 1.25$ cm whereas for P(z=30 cm,h) a $x_h = 3.9$ cm is expected. The maximal range of values is found at an inclination angle of $\zeta \approx 33°$. For smaller ζ, the range of h_x-values decreases again due to the lesser horizontal speed of the sphere fighting against gravity. For $\zeta = 90°$ which resembles a free fall, $x_h = 0$ for all ζ and all start levels.

Estimations based on Eq. 6.7 are shown in Fig. 6.2 b). The velocity increases with z

or also with ζ. For greater inclination angles, e.g. $\zeta = 60°$, the diversity of velocities with respect to the start position becomes highly significant such that along the total length of the tube of 30 cm a variation of v_0 from $\approx 0.6\,\frac{m}{s}$ to $\approx 1.8\,\frac{m}{s}$ is possible. In contrast, for smaller inclination angles, the impact is not as severe.

In Fig. 6.2 c), the period of one rotation of the sphere

$$T = \frac{2\pi r}{v_0} \sim \frac{1}{z} \tag{6.11}$$

is estimated in dependence of the start level position z. The greatest values for T, describing a slow rotation, are achieved by a small inclination angle and a small start level height. The sphere's rotational speed increases consequently with increasing start height or inclination of the tube resulting in a small period. The greatest variety of angular velocities for a single arrangement of the tube may be expected for small inclination angles.

In conclusion, we see that a proper installation of the tube is necessary to achieve the best results. Our aim is to investigate a significant range of angular velocities for a single setup configuration. By choosing a suitable horizontal distance of the tube's tip with respect to the collimator's aperture center the greatest number of experiments, involving varying start heights, may be performed without rearranging the tube. Thus, the reproducibility of the experiment will be facilitated. Also, a rather smaller angle of inclination should be used to have on one hand a greater range of angular velocities and consequently of periods T in one experiment but also on the other hand to keep the variety of small horizontal distances covered such that most of the attempts pass the laser volume in front of the collimator's aperture.

6.2. DLS data processing

Once the correct alignment of the tube has been set up, the DLS experiment can start. We want to test if the rotational speed of the sphere is clearly deterministic by, first, proving that the obtained angular velocity is reproducible for every start level by comparing several measurements from the same start level. Further, we want to

investigate if, with increasing start level, the sphere's angular velocity is also increasing. If both assumptions are true, we may consider the setup to be well calibrated and that the obtained angular velocities reflect the true physical angular velocity which is then to be verified with the PIV analysis in Ch. 6.3.

The inclination angle $\zeta = 3.25°$ is used for the following experiments. The total tube length is $z_{\mathrm{tot}} = 30\,\mathrm{cm}$ and slits for different start level points P(z,h) were cut every 3.0 cm such that a total number of 10 levels of investigation are possible at once. The lowest level h1 is found at z=3.0 cm and the highest level h10 corresponds to z=30.0 cm. Furthermore, the tip of the tube is mounted with $s_v = 0.5\,\mathrm{cm}$ above the upper edge of the laser beam and approx. $s_h = 1\,\mathrm{cm}$ apart from the collimator's center.

After first calibration attempts, a range of possible start levels may be selected. In the arrangement above, the intensity measurements of the scattered light indicate the starting heights h2 to h6 as most suitable, which correspond to the tube segment lengths z=6.0 cm to z=18.0 cm. Level h4 provides the optimal trajectory that runs nearly in front of the collimator's center. The levels h2, h3, h5 and h6 show trajectories that slightly deviate, respectively, from the optimal case. However, in the data presented below the detector received sufficiently strong intensity signals such that a variation of presumably smaller to larger rotational speeds may be observable.

The first question which is to be answered is if the angular velocities are reproducible in that sense that for each start level the same ω-values are obtained repetitively. This trend would show the deterministic nature of the rotational velocity in the experiments. For this purpose, experiments with the particle starting at a specific level were performed four times. The results may be exemplarily found for start level h4 in Fig. 6.3.

The left panel of Fig. 6.3 shows the non-normalized data of the late decays on linear time scales of all four runs for start level h4. Analogue to Ch. 4.4, the data is fitted with the ACF of a trapezoid, see Eqs. 4.25 and 4.26. Data and processing for the other cases ranging from h2 to h6 are listed in Ch. A.

The intercept value at $g_2(\tau = 0) - 1$ varies depending on the flight trajectory of the

particle with respect to the collimator since the amount of light seen by the collimator optics differs. The more light is received by the collimator, the higher the recorded intensity and thus, the higher the ACFs intercept such that the signal-to-noise ratio increases. The signal heights H, referring in the recorded intensity trace to the input count rate in kHz, for all tries take on solid values of H≈5. Generally, the values agree on the magnitudes for each parameter H, A and B. The first segments of the data are well fitted. However, the last fit segment shows a small deviation of the data trend. Due to the existing noise level, the sharp ends of the trapezoid flanks are contorted. But overall, the signal-to-noise ratio is high indicating a good data quality such that the decays may be separated.

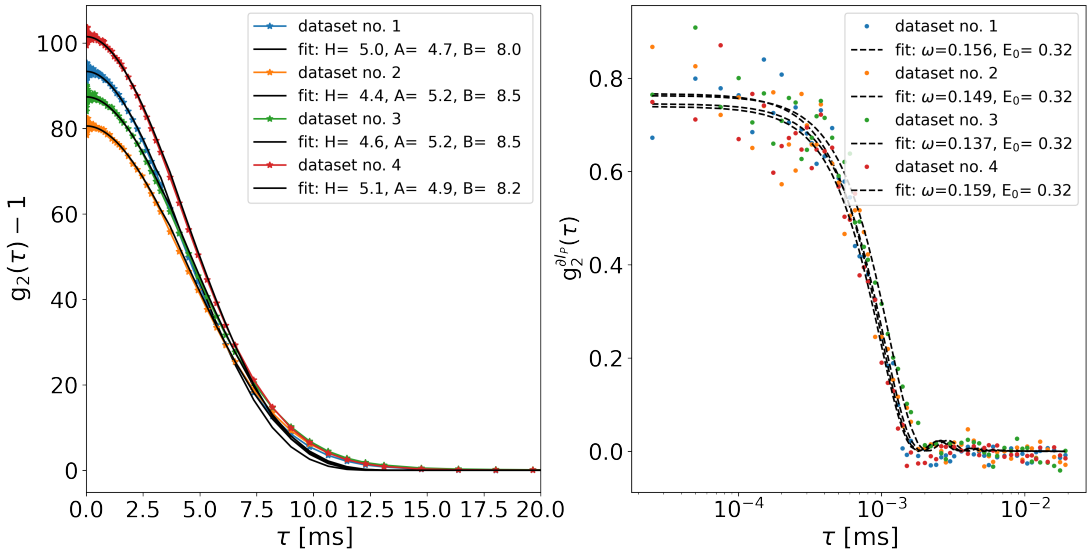

Figure 6.3.: The fitting of several autocorrelation functions of a rotating PTFE sphere passing through a laser beam. In all cases, the particle starts from position h4 in the tube. The left plot shows the late decays on linear time scales which are fitted by the autocorrelation function of a trapezoid. The right plot shows the fitting of the data from the early decays $g_2^{\partial I_P}(\tau)$ on logarithmic time scales with the corresponding function from the RPM (cf. 5.2.3.2). The fit parameters for both decays are denoted in the respective legend.

In case of h4, two data sets may be fitted with the expression for a broader plateau

and narrower flanks, two for a rather spiky trapezoidal signal approaching a triangular shape. The averaged data set adapts more to the trapezoidal signal shape. However, all data sets show half-widths of approximately 8 ms such that the transit of the spheres through the laser beam is expected to last about 16 ms. The time by which the ACFs in the left panel of Fig. 6.3 reaches $g_2(\tau) = 0$ constitutes likewise approx. 16 ms. This suggests that all trajectories are similar which supports the aspect of reproducibility of the experimental situation.

However, in contrast to the experiment from Ch. 4.4, the shape on the particle's trajectory is supposedly different here. In the former experiment, the particle fell following a straight line starting from above the laser volume down to the collection container. Thus, a clear distinction between the trajectory segments where the particle was approaching or retreating the laser volume resulting in equally wide flanks and the particle transiting the laser beam (the trapezoid's plateau) is possible. The plateau's width equals thereby the laser beam width such that the translational velocity of the particle can be determined. But in case of the particle rolling off the tube's tip, the parabolic path comprises supposedly a trapezoid "leaning" to one side. The particle crosses the laser beam not simply in a straight line but in a parabola due to the horizontal velocity component being greater than 0. In the experiment from Ch. 4.4, $v_h \approx 0$. This parabola extends the actual path through the beam such that this path segment and consequently the signal's plateau becomes larger than the beam width. Further, the parabolic trajectory may be laterally wider above the laser beam than beneath it due to the changing ratio of the horizontal to the vertical velocity component when the particle approaches the ground. Thus, the trapezoidal signal shape will not be as symmetric as it used to be in Ch. 4.4 but will have flanks of different widths. This circumstance induces fitting difficulties regarding the flank width B-A but also the plateau half-width A for the algorithm where a symmetric trapezoid is assumed. The signal half-width B though remains unaffected. Thus, we might not be able to determine a clear translational velocity for the particle here, but the approach is sufficient to eliminate the contribution of the number fluctuations in the measured ACF such that the early decay may be investigated further.

In case of the other start positions h2 to h6, we observe, that the transit time for the

particles starting from h2 and h3 is slightly longer than for particles starting from h4 or higher. Due to the smaller acceleration time in the tube resulting from a smaller z, the particles possess a smaller horizontal velocity component. When leaving the tube's tip the total velocity is smaller with respect to the velocities obtained when starting at higher positions. Thus, the particle requires more time to transit the laser beam.

The right panel of Fig. 6.3 shows the data of the early decay $g_2^{\partial I_P}(\tau)$ after isolation and the corresponding fits with the RPM expression from Eqs. 5.56 which have been squared due to the application of the Siegert relation, cf. Eq. 2.88. The principle of the Gaussian spot was used to parameterize the amplitude term of the fit function. The standard deviation of the Gaussian peak is given by the parameter b in dependence of the particle's radius. We assume the PTFE particle to have an increased roughness such that the portion of specular reflection is small compared to the diffusive portion. In the model fits, a value of b=1 corresponding to a spot width of 2 radii is assumed. $E_0 = \sqrt{g_2^{\partial I_P}(\tau = 0)}$, describing the squareroot of the intercept value, serves as constant factor within the amplitude term to facilitate the fitting of the data for the algorithm. The fit parameter ω in Eq. 5.56 gives the angular velocity of the rotating particle.

From the shapes of the decays we may conclude that on one hand the data is not very noisy due to the clear decay form and on the other hand that the ACFs exhibit nearly the same values for the decorrelation time and the angular velocity. The values for the angular velocities range from $0.14\,\mathrm{ms}^{-1}$ to $0.16\,\mathrm{ms}^{-1}$, such that the variance from the mean value ($\langle\omega\rangle = 0.15\,\mathrm{ms}^{-1}$), is equal to or less than $0.01\,\mathrm{ms}^{-1}$ and thus, less than 10% from the mean.

From the data and fits obtained for the other start levels (cf. Figs. A.1 to A.4) where the flight trajectories are expected to deviate more strongly from the optimal case, the more distinct scattering of data points indicates a higher noise level. The increased noise level lessens the reliability of the results for those start levels. From the fit parameters, we may observe a higher variance of the angular velocities with respect to the mean value for the specific start level. This variance increases with the assumed deviation of the particle's flight trajectory from the ideal trajectory. Therefore, the data sets of h2 and h6 should be treated more cautiously than the other cases. In case of h2, the acquisition of many usable trajectories was problematic due to their

significant distance to the aperture's center of the collimator. Thus, those trajectories may be considered not as reliable as for example the trajectories obtained with start level h3. Especially one trajectory deviates in Fig. A.1 from the course of the other trajectories and distorts the final result if all trajectories will be averaged. However, the data of h2 is presented here to provide a first impression of the trend of the angular velocities for lower start positions. For the more reliable h2 data a smaller angular velocity with respect to those obtained from h3 is perceptible. However, in sum the results of the levels h2 to h6 indicate the ability to reproduce deterministic angular velocities with this experimental setup.

The second question, which is now to be answered with help of Fig. 6.4, is if the decay time τ increases with start level height. From the knowledge gained in Chs. 5.1.1 and 6.1 we expect that the ACFs decay time decreases with increasing angular velocity of the particle which is the consequence of the particle spinning faster as the start level is increased. The cases presented in the figure are the averaged ACFs for the respective start levels of h2 to h6. Thus, a greater variety of rotational speeds should be achieved within this experiment.

The top left panel of Fig. 6.4 shows the late decay of the averaged autocorrelation functions for all start levels on linear time scales. The fit parameter values agree with those found in Fig. 6.3. The remaining panels of Fig. 6.4 from left to right and top to bottom show the fitting of the average ACFs for each start level h2 to h6, respectively, with the squared expression of Eq. 5.56 at very early times after the isolation from the late decay. The values for the angular velocities ω show the expected dependence on the start level. The lowest level h2 exhibits the lowest angular velocity of $\omega = 0.11\text{ms}^{-1}$. The higher levels show respectively higher values ranging from $\omega = 0.13\text{ms}^{-1}$ to $\omega = 0.17\text{ms}^{-1}$ for h3 to h6.

However, the value of h5 and h6 adopt almost the same value with ω for h5 being even slightly higher than the estimated ω for h6. This may arise from either fitting issues of the algorithm or from a rather physical reason like the proximity of the start levels in the tube. In Fig. 6.2 b) and c) , the values for h5 and h6 at $\zeta = 1°$ and $\zeta = 5°$ are very much alike such that this may also be expected to be true for $\zeta = 3.25°$. In contrast to lower start levels, higher rolling and thus rotational velocities are obtained

when a particle starts rolling from h5 and h6, respectively. Further, the deviation from the ideal trajectory is accompanied by lesser signal strengths and thus a worse signal-to-noise ratio, such that for now, the results from h5 are rather considered to be plausible. The data set with the best quality is here h4, whereas h2 shows the noisiest data.

In conclusion, we see that the predictions from the former section regarding the relation between the start level of the particle in the tube and the rotational speed are experimentally valid. The longer the sphere has time to adapt to the rolling motion which becomes faster with greater distance covered in the tube, the larger the angular velocities it shows when passing through the laser beam. The results are faster decaying autocorrelation functions. Further, we also see that the rotational speeds are reproducible for the corresponding start levels such that the problem may be investigated numerous times. This ability to reproduce the rotational speeds enables to perform DLS and PIV measurements separately. This is necessary since the PIV algorithm needs reference features on the sphere's surface in the images to track its motion. The procedure of tracking the particle's rotation in the photos and the obtaining of the angular velocity with PIV will be discussed in the following section.

6.3. Image processing using particle image velocimetry (PIV)

The angular velocities (orders of $\omega \approx 10^{-3}\mathrm{ms}^{-1}$) obtained in the former section with the method of DLS shall now be verified with the optical method of particle image velocimetry (PIV) to ensure the integrity of the results. PIV is often used in science and industry to characterize the flow behavior of samples [1].

With PIV the velocity field of an entire area within the flow is measured simultaneously instead of a single point as in optical point measurement techniques. PIV's greatest benefit is that it can provide physical insight into the overall flow behavior by mapping the flow field after extracting the data and visualizing the flow structures. A broad region of the sample is illuminated by a strong light source, e.g. a laser. The sample

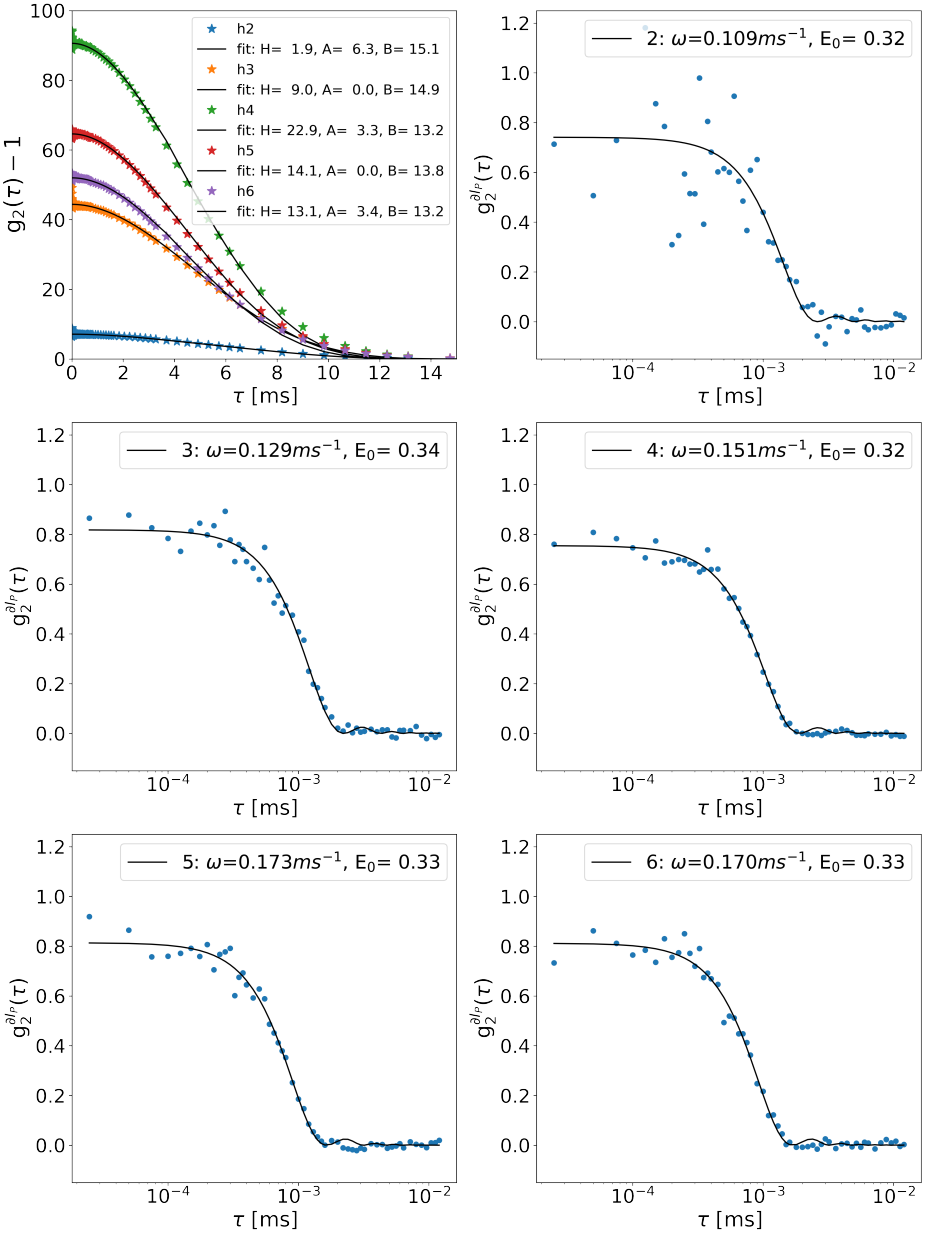

Figure 6.4.: Fit functions of the late and the early decays of the autocorrelation function $g_2(\tau)-1$ caused by a rotating PTFE sphere passing through the observation volume. The top left panel shows the late decays on linear time scales which are fitted by the autocorrelation function of a trapezoid. The other panels show the fitting of the data from the early decays $g_2^{\partial I_P}(\tau)$ on logarithmic time scales for a specific start position h2 to h6, respectively, of the particle in the tube (from left to right, from top to bottom). The corresponding fit parameters are listed in the respective legends.

is seeded with tracer particles which are assumed to reliably follow the flow dynamics. The motion of the tracer particles is then recorded by a camera. Thus, an estimation of the particle's velocity as well as the complete velocity field of the flow is possible. The recording of two successive images permits the determination of the particle displacement $\Delta\vec{s} = \vec{s}_1 - \vec{s}_2$ from the first frame to the second. The difference of the variables t_1 and t_2 describes the interval between the two frames taken, respectively. Thus, the speed and direction in the velocity field may be determined as

$$\vec{v} = \frac{\vec{s}_1 - \vec{s}_2}{t_1 - t_2}. \tag{6.12}$$

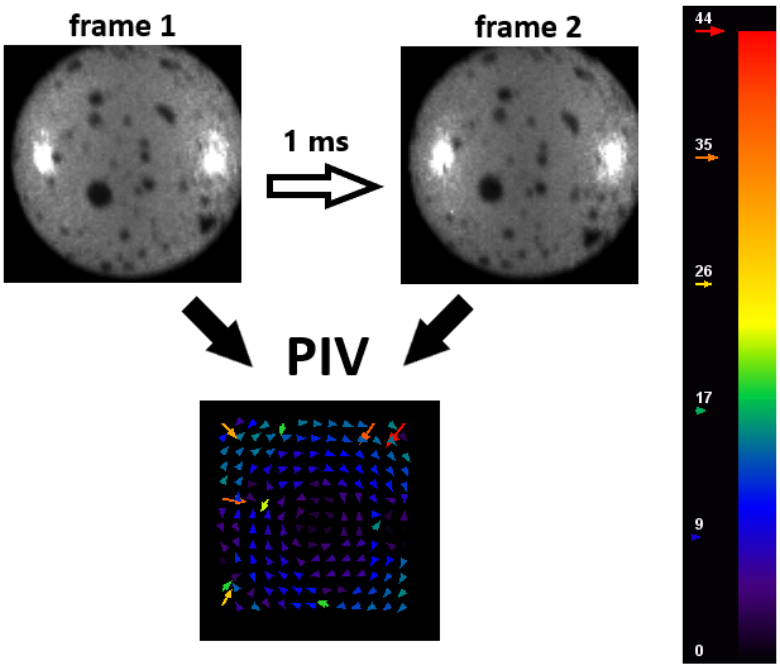

Figure 6.5.: An illustration of the processing steps with particle image velocimetry (PIV) on the recorded photos. Frame 1 and 2 show two subsequently taken photos of the particle. The passed time between both frames comprises 1 ms. After applying ImageJ's PIV plug-in, a colored correlation map with arrows indicating the velocity of the moving features from frame 1 to 2 is created, shown below the photos. The corresponding velocity scale is shown at the right margin of the illustration ranging from 0 to 44 $\frac{\text{px}}{\text{ms}}$.

However, no specific velocity of single tracer particles is detected. The local velocity of a small area of the measurement plane is calculated by statistical means based on

the identification of particle patterns. Usually, 2D crosscorrelation schemes are applied to the two recorded frames (gray value patterns), which are divided into small interrogation windows [2]. The interrogation window's pattern from the first frame is then correlated with some region of equal size in the second frame. Thereby, the interrogation window will be shifted pixel-wise in the vicinity of the interrogation window's location in the first frame. The result is a local correlation map. The maximum correlation value in the map indicates the most probable displacement of the particle pattern of that respective interrogation window [3, 4].

For the application of this technique to our problem, we paint the white spheres with numerous tiny black dots with lacquer from a spray can. Those dark spots function the same way on the sphere's surface as the tracer particles in a flow. Since we learned in Ch. 6.2 that we are able to control the particle's angular velocity, we may perform the DLS and the camera measurements separately. Therefore, we actually may partially paint the sphere. If a painted sphere would be used in the DLS experiment, alterations in the scattered light due to e.g. local absorption effects or local changes in the refractive index were caused. A series of frames is recorded by the high-speed camera every millisecond while the particle passes through the laser beam with a rotational motion around its spin axis as visualized in Fig. 6.5. Both photos look almost alike, however a slight clockwise rotation of the sphere after 1 ms may be observed.

The PIV algorithm used here is the plug-in PIV, in particular its option iterative PIV (Basic), of Fiji's image processing software "ImageJ". The plug-in follows the same concept as regular PIV techniques [5]. The user may choose up to three interrogation window sizes in one procedure. The map in Fig. 6.5 (bottom image) shows the resultant velocity field with the corresponding legend on the right margin of the figure. The arrows represent the tangential velocities broken down into speeds and directions of the detectable surface features in the two photos above with 188 x 188 pixels each. The dimensions of the images are referred to as the dimensions x and y. For the calculation of the velocity field the interrogation window size was set to 24 px and the search window to 72 px. The search window size should always be larger or equal to the interrogation window such that the existence of the feature, represented by the interrogation window, in the searching area is ensured. The vector spacing was 12 px,

respectively.

The majority of arrows show a circular pattern with the arrows pointing in a clockwise manner. The slowest speeds are found in the center of the figure. The speeds increase with increasing distance from that center, agreeing with the expected physics observable for a turning sphere or disc. However, there are arrows which have quite high values of $25\,\frac{\text{px}}{\text{ms}}$ and more. Further, the arrows do not align with the majority of arrows following the flow pattern. Those outliers may arise from correlating window margins lacking some discrete information about the flow.

In order to minimize the errors caused in the calculated correlations and also to take the effect of the tangential velocity of a particle increasing with distance to the objects center into account, the complete data cloud obtained by the PIV plug-in is analyzed. In Fig. 6.6, the tangential velocity data v obtained by the PIV plug-in in dependence of the distance towards the center r, is presented exemplarily for h6. The other cases are listed in Ch. B. The tangential velocity v increases with radius r, such that with help of linear regression the angular velocity ω of the particle may be determined. The slope m of the regression line of the form y=mx+n with the offset n=0 provides the values for the angular velocities such that

$$\omega = \frac{v}{r}. \tag{6.13}$$

The center point of the sphere on the photos does not move. Thus, no v>0 may be expected there such that the choice of n=0 is reasonable. The radius $r = \sqrt{x^2 + y^2}$ was determined by the positional arguments x and y of the arrows given in the data sheet of the PIV analysis, the tangential velocities are directly found in the sheet.

The spread of values deviating from that regression line indicates the quality of the method. If there are many outliers such that the data cloud broadens significantly, the quality of the measurement lessens. In Fig. 6.6, we see that apart from a few outliers for greater radii, the scattering of the data points of the cloud is quite low indicating a good quality.

Finally, with this method, we observe the same behavior of the angular velocity with

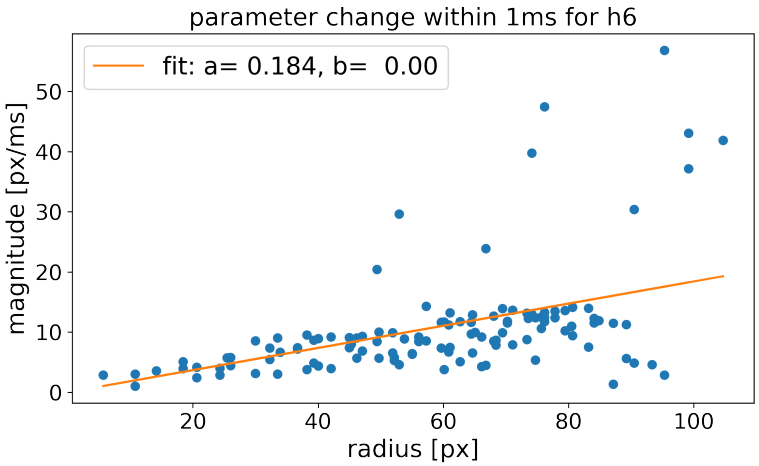

Figure 6.6.: Exemplarily: The tangential velocities v in $\frac{\text{px}}{\text{ms}}$ in dependence of the feature's distance r to the center of the photo. The values were obtained by using the PIV method for the case of the sphere starting at level h6. The dots represent the data whereas the linear graph illustrates the linear regression fit of the form $v = a \cdot r + b$ to determine the angular velocity of the particle.

start height of the particle on the inclined plane. For h2, an angular velocity of $0.11\,\text{ms}^{-1}$ was found. The angular velocity increases with start height, reaching an angular velocity of $0.18\,\text{ms}^{-1}$ for h6. The degree of agreement between both methods, the PIV and the DLS measurements (cf. Ch. 6.2) shall be discussed in the following section Ch. 6.4 where both results will be compared and a final conclusion regarding the entire experiment will be drawn.

6.4. Comparison of methods and resume

The final aims of the experiment are, first, to compare the results obtained with DLS and PIV in Chs. 6.2 and 6.3, to show the applicability of the RPM model (cf. Ch. 5) to a laboratory experiment, but also, to assess the quality of the setup calibration. In the DLS experiments, the data quality was sufficient throughout the experiments. Though, better signal-to-noise ratios for trajectories running closer to the aperture's center of the collimator were observed. The data set for h4 is considered to be the most reliable. Results from h2 and h6 should therefore be treated comparably cautious. The PIV data quality is good, since a proper illumination of the sphere as well as enough detectable surface features were provided. The scattering of the data points in Ch. B is still reasonable, such that reliable values for the angular velocities were obtained.

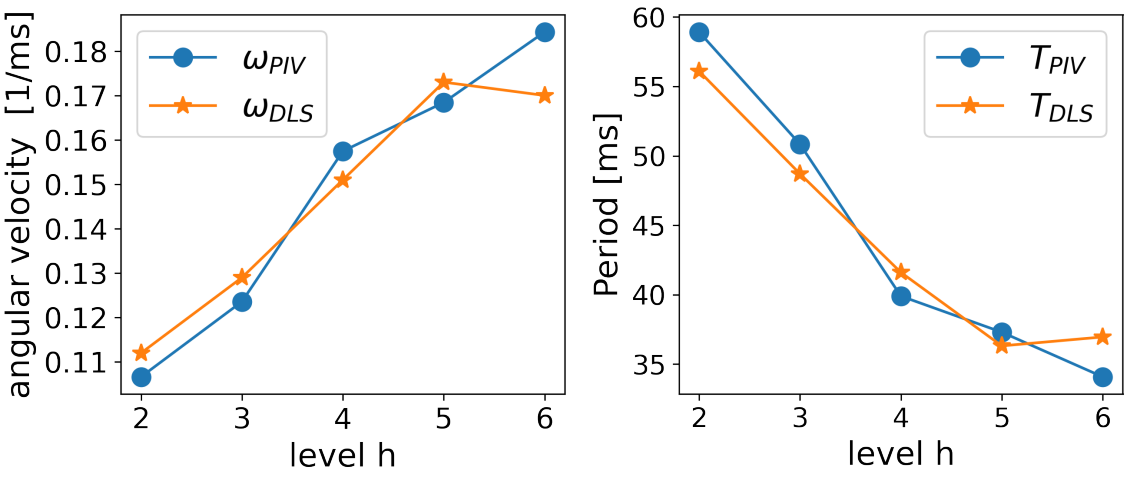

Figure 6.7.: Comparison of the angular velocities ω (left window) and periods T (right window) obtained by PIV (blue line with dots) and DLS (orange line with stars), respectively. Both parameters are shown in dependence of the particle's start level in the tube.

The results of the DLS data processing showed, that the angular velocities may be controlled by allowing the particles to start from predetermined start positions. The higher the start position, the higher the angular velocity. The adapted angular velocities were reproducible for each start position, cf. exemplarily Fig. 6.3. A similar behavior of the angular velocity increasing with start level was observed with the PIV

method, cf. exemplarily Fig. 6.6. A comparison of the results of both methods is shown in Fig. 6.7.

The left panel of Fig. 6.7 shows the obtained angular velocity for each method respective to varying start positions of the particle in the tube. The agreement between the angular velocities ω_{DLS} and ω_{PIV} for each start position is good. The difference between both velocities is generally $\Delta\omega \approxeq 0.005\mathrm{ms}^{-1}$. An exception is given for h6, where $\Delta\omega \approxeq 0.014\mathrm{ms}^{-1}$. However, the small discrepancies support the credibility of the ω_{DLS}-values from h3 to h5. Also, since the agreement of both angular velocities for h5 is comparable to those obtained for lower start heights, the ω_{DLS}-value h6 is considered here as outlier.

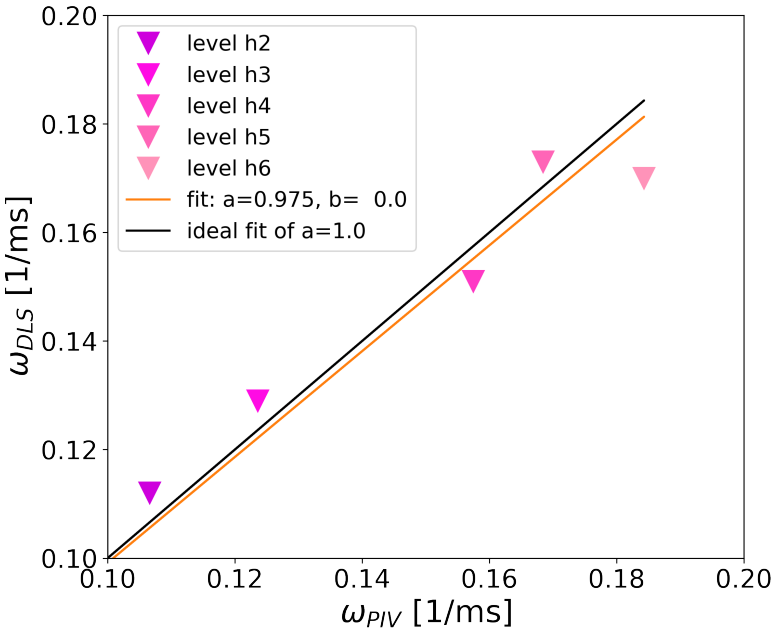

Figure 6.8.: The direct comparison of the angular velocities ω obtained by DLS and PIV for start levels h2 to h6 (triangles). The solid black line represents the ideal case of $\omega_{\mathrm{DLS}} = \omega_{\mathrm{PIV}}$ by having a slope equal to 1 and an offset of 0. The orange line results from the fit of the form y=ax+b to examine deviation of the slope from the ideal.

Further, we may conclude from the coherent trend of the angular velocities of both

methods, that the RPM model from Ch. 5 is able to resolve the angular velocity of a rotating macroscopic rough sphere. As further proof of concept, the direct comparison of ω_{DLS} and ω_{PIV} in Fig. 6.8 is fitted with a linear function of the form y=ax+b, where b=0, illustrated by the orange solid line. If the slope a=1, then ω_{DLS} and ω_{PIV} are identical, as indicated by the solid black line. The slope of the angular velocities comprises to 0.975, monitoring a small error of 2.5 % with respect to the ideal case.

As a measure of accuracy of the angular velocities obtained from the PIV method, the periods were calculated from the angular velocities of both methods, see the right plot of Fig. 6.7. Those values were then compared to the rotational velocities visible in the recorded image sequences of about 15 frames. The calculated periods match the extrapolated times for a complete turn of a surface feature about the center, indicating a high credibility. However, an entire revolution could not be recorded since the particle needs less time to pass through the observation volume than it needs to rotate once. For h2 in particular, the rotation takes about twice as much time.

In conclusion, the RPM model provides a suitable methodology to investigate the controlled rotational motion of a single rough and macroscopic particle after rolling down an inclined plane. In fact, the rotational motion of the optically diffusive particle induces the decay of the ACF at early times, firstly noted within this work in Ch. 4.4. The angular velocity ω may be extracted from the DLS experiment with the RPM such that estimations about the rotational granular temperature may come into further reach. A first attempt will be made in Ch. 7, where a measurement series of single, but directionally unguided, particles falling through a funnel will be performed. The experiment resembles an in some sense idealized effluence of particles in an hourglass. The data will be evaluated with all discussed spin axis configurations from Ch. 5.

References

[1] M. Raffel, C. E. Willert, J. Kompenhans, et al. *Particle image velocimetry: a practical guide*. Vol. 2. Springer, 1998.

[2] R. D. Keane and R. J. Adrian. "Theory of cross-correlation analysis of PIV images". In: *Applied scientific research* 49.3 (1992), pp. 191–215.

[3] M. Atkins. "Velocity field measurement using particle image velocimetry (PIV)". In: *Application of Thermo-Fluidic Measurement Techniques*. Elsevier, 2016, pp. 125–166.

[4] R. Lindken and S. Burgmann. "Laser-optical methods for transport studies in low temperature fuel cells". In: *Polymer electrolyte membrane and direct methanol fuel cell technology*. Elsevier, 2012, pp. 425–461.

[5] Q. TSENG. *Tutorial for the iterative PIV plugin*. `https://sites.google.com/site/qingzongtseng/piv/tuto`. Accessed: 2022-12-02. 2022.

7. Measuring the granular temperature in an hourglass-like experiment

Based on the results of the former chapters, we are able to determine the translational velocity (cf. Ch. 4) and the angular velocity (cf. Chs. 5 and 6) of a macroscopic rough sphere with our DLS setup. From those variables, the corresponding granular temperatures may be identified. One application may be an hourglass-like laboratory experiment with pre-defined requirements. An hourglass [1] is a conjunction of two glass bulbs, which are symmetrically and vertically connected by a narrow neck. The device is used to measure short time intervals. The upper bulb contains granular matter, which passes in a regulated flow through that neck. This matter is a system of macroscopic particles as described in Ch. 2.1.1. The laboratory experiment below will resemble granular particles passing through a hourglasses neck but with a controlled flow procedure.

In the following, we will briefly discuss theoretical thoughts regarding the experiment and how the experiment was particularly performed to investigate the system's rotational granular temperature, cf. Chs. 7.1 and 7.2, respectively. The results will be presented in Ch. 7.3, followed by a brief discussion of the experiment's outcome. In the end, the chapter will be summarized in Ch. 7.4.

7.1. Theoretical considerations

We consider the particle system to be a very dilute granular gas as the macroscopic particles will be inserted separately into the observation volume. Thus, collisions among the particles are obviated. The determination of the translational granular temperature is as straight forward as described in Eq. 2.1. The particles will drop one-by-one in a vertical line through the observation volume. From Ch. 4 we know how to obtain information about the particle's velocity from its vertical transit through the laser beam. The time the particle takes to pass the laser volume is hidden in the total plateau width 2A of the recorded intensity signal. Thus, the particle's velocity reads as

$$v = \frac{s}{2A} \tag{7.1}$$

with s representing the distance between the upper and the lower bound of the laser beam. $\langle v \rangle$ is then calculated as average over all individually measured velocities. The translational granular temperature is then given by:

$$\Theta_{\text{trans}} = \frac{1}{N}\sum_{i=1}^{N} \delta v_i^2 = \frac{1}{N}\sum_{i=1}^{N} (v_i - \langle v \rangle)^2 \tag{7.2}$$

From Chs. 5 and 6, we know how to extract the angular velocity of particle falling through the observation volume of our setup. This angular velocity is necessary to determine the rotational granular temperature of a particle in view of Eq. 2.1. However, since the angular velocity is also a vector, it contains information about the speed of rotation but also about the direction, which is determined by the position of the spin axis in space.

The challenge in this experiment is the indeterminacy of the exact orientation of the spin axis such that its approximate position can only be guessed as a first attempt of investigation. Further, the spin axis' direction may even vary by precessing when passing the observation volume. In Chs. 5.2.2 through 5.2.3.2, we discussed special cases of axis orientations in view of the region of interest on the sphere's surface in

the experiment. Notably in Fig. 5.6, the three distinct phase terms lead to different decay times even though the conditions, as the given particle diameter and the angular velocity, are exactly the same for all three models. Conversely, different angular velocities for the same decay time of the auto-correlation function would be expected with those model fits. However, in reality, there will be only a single angular velocity for a particle independent of the axis orientation.

Thus, since the orientation of the particle's spin axis can not be (pre-)determined, the most probable axis orientation is selected. Vectors, like the spin axis vector, can be disassembled and may be expressed as composition of three vectors in the three-dimensional space, e.g. the basis vectors of the Cartesian reference system. Assuming, that all three options occur with equal probability, averaging those should give a reasonable estimation for now. The most probable orientation here is determined by taking the average of all cases discussed above, which do align with the Cartesian basis vectors: the spin axis pointing upwards $\vec{\omega}_{\perp}$ as well as the spin axis parallel to either the opto-mechanic axis of the collimator $\vec{\omega}_{\parallel_c}$ or the laser beam $\vec{\omega}_{\parallel_l}$, respectively, such that

$$\vec{\omega} = \frac{1}{3}\left(\vec{\omega}_{\perp} + \vec{\omega}_{\parallel_l} + \vec{\omega}_{\parallel_c}\right) \tag{7.3}$$

This of course only defines the spin axis to pierce through the upper half of the illuminated region of interest. If the axis runs through one of the other sphere segments, the polarity of the vector components change, however, the absolute value of the angular velocity, which is here of actual interest, is independent of the axis orientation. Thus, the attempt is to determine the most probable angular velocity by using those three models and average their results. Additionally, effects like precession and nutation of the spin axis may falsify the results. Thus, if those effects occur, the axis anyhow can not be clearly determined and averaging may be the most efficient way to approach this problem for now.

Known from Ch. 5.2.3.2, the expression for $\vec{\omega}_{\parallel_c}$ and $\vec{\omega}_{\parallel_l}$ give the same results, such that both may be assumed to be equal $\omega_{\parallel_c} = \omega_{\parallel_l} \equiv \omega_{\parallel}$. In conclusion, we obtain the absolute value of the angular velocity of a particle in this experiment as

$$\omega = \frac{1}{3}\left(2\omega_{\parallel} + \omega_{\perp}\right) \tag{7.4}$$

Of course, different axes may be selected to be averaged, e.g. the spin axis running through the center of the Gaussian spot $\omega_\times$ or this axis rotated about 90° such that the sphere's equator crosses the Gaussian spot's center $\omega_\circ$. However, those cases only represent a single incident. As soon as the axis deviates only to a small degree from this position, the result will be significantly different. In contrast, the axes chosen in Eq. 7.4 rather represent a series of options for the spin axis. Further, $\vec{\omega}_\parallel$ is found half-way from $\vec{\omega}_\circ$ to $\vec{\omega}_\times$ such that it may be considered already as average of both options.

The rotational granular temperature in the experiment below for N particles may then be determined by using an expression similar to Eq. 2.2

$$\Theta_{\mathrm{rot}} = \frac{1}{N}\sum_{i=1}^{N}\delta\omega_i^2 = \frac{1}{N}\sum_{i=1}^{N}\left(\frac{(2\omega_\parallel + \omega_\perp)_i}{3} - \langle\omega\rangle\right)^2 \tag{7.5}$$

with $\delta\omega^2$ being the variance of a particle's angular velocity from the average angular velocity.

7.2. Data acquisition

The experimental setup remains to a large extend the same as for the experiments of Ch. 4.4, see Fig. 4.4. The particles were dropped through a funnel to guide them through the laser beam in front of the center of the collimator's aperture in a straight trajectory. The funnel imitates the lower end of the hourglass' neck. The significant difference to the former experiment is the absence of the water-filled cuvette, such that the particle will not cross a water reservoir in front of the collimator but air only. The inclusion of suspended solids in the water may cause additional noise which is here avoided. Due to the lower viscosity of air with respect to water, faster transits through the laser beam are expected then observed in Ch. 4.4.

50 spheres of 2.0 mm diameter and with a density of $\rho = 2200\frac{kg}{m^3}$ for polytetrafluoroethylene (PTFE) were dropped one after another into the observation volume. Each measurement lasts 10 s. That number of particles has to pass the laser volume solitary to ensure that inter-particle interference effects as well as inter-particle collisions are

avoided. The translational and angular velocities for each particle are extracted as done before in Ch. 4 and 6. Consequently, the 50 velocities are averaged to generate the mean values $\langle v \rangle$ and $\langle \omega \rangle$.

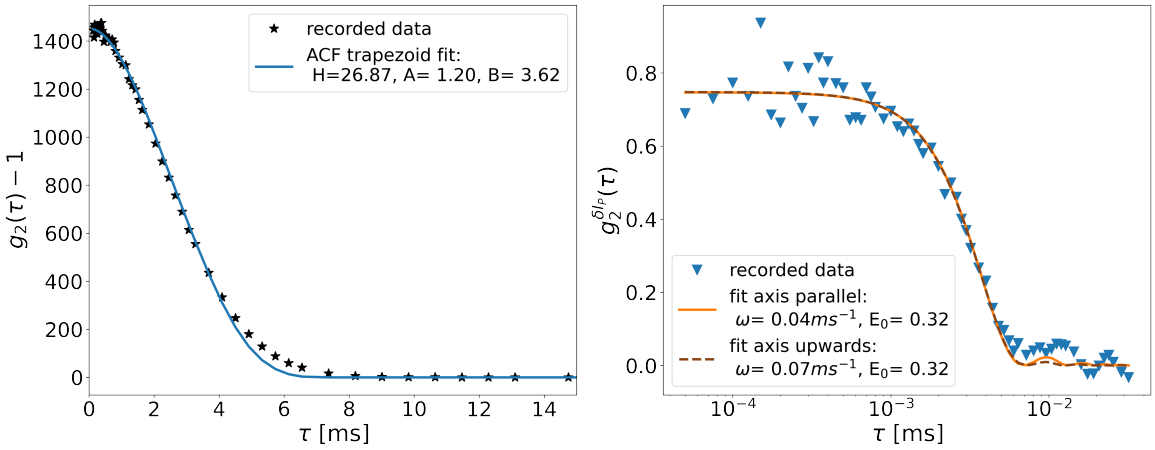

Figure 7.1.: The measured autocorrelation function of one arbitrarily selected particle (out of 50 runs) obtained in the hourglass-like experiment. The left window depicts the isolated early decay on linear time scales. The right panel shows the function's decay at early times of the recorded auto-correlation function on logarithmic time scales. The corresponding fit parameters are denoted in the legends.

Fig. 7.1 shows exemplarily the recorded auto-correlation function for an arbitrary selected particle. The left panel shows the late auto-correlation function decay on linear time scales from which the duration of the particle transition through the observation volume may be extracted. Recalling the laser width of s=14.7 mm and assuming, that the particle trajectories are parallel to the vertical, the particle's velocity is estimated with Eq. 7.1. Since A is one of the fit parameters for the late decay of the auto-correlation functions, the values may be easily obtained from the legend of the left panel of Fig. 7.1.

In Fig. 7.1, the function reaches 0 at about 7.5 ms which agrees with the fit parameter 2B also being approx. 7 ms. In the comparable experiment from Ch. 4.4 in water, the signal width 2B equals approx. 38 ms. In conclusion, the particle needs about 5 times longer to pass the beam in water then it does in air. The right figure illustrates the early decay on logarithmic time scales. The fit parameters for the angular velocity

with both models give values of $\omega_{\parallel} = 0.04\,\mathrm{ms}^{-1}$ and $\omega_{\perp} = 0.07\,\mathrm{ms}^{-1}$.

7.3. Results and discussion

The translational velocities and the respective variances for all 50 spheres are pictured in Fig. 7.2. The left panel shows the velocity values for each measurement as black dots. Their average value is indicated by the purple line. The highest recorded velocity is $v = 3.1\,\frac{\mathrm{mm}}{\mathrm{ms}}$ whereas the lowest velocity is $v = 1.7\,\frac{\mathrm{mm}}{\mathrm{ms}}$. The calculated mean velocity of all 50 particles equals $\langle v \rangle = 2.125\,\frac{\mathrm{mm}}{\mathrm{ms}}$.

The values of the purple triangles in the right figure of Fig. 7.2 were obtained with

$$\delta v^2 = (v - \langle v \rangle)^2. \tag{7.6}$$

We note values of the orders of $10^{-5}\,\frac{\mathrm{mm}^2}{\mathrm{ms}^2}$ ranging to almost $1\,\frac{\mathrm{mm}^2}{\mathrm{ms}^2}$. The majority of data points however shows a variance of $10^{-2}\,\frac{\mathrm{mm}^2}{\mathrm{ms}^2}$ to $10^{-1}\,\frac{\mathrm{mm}^2}{\mathrm{ms}^2}$ from the mean velocity. With

$$\Theta_{\mathrm{trans}} = \langle \delta v^2 \rangle \tag{7.7}$$

we obtain as translational granular temperature $\Theta_{\mathrm{trans}} = 0.084\,\frac{\mathrm{mm}^2}{\mathrm{ms}^2}$. Θ_{trans} is visualized as black line in the right panel of Fig. 7.2. The presence of those greater deviations from the mean translational temperature may exist due to odd trajectories which are not parallel to the vertical such that a longer transit time is recorded. Since the particles are not individually accelerated in the funnel, deviations of the individual speeds with respect to the mean value supposedly only arise due to oblique trajectories caused by many contacts with the funnel walls. Thus, the measured time of 2A may not be assigned to the laser width in order to calculate the particle's translational velocity. Otherwise, significantly smaller velocities are expected due to larger transit times.

With Eq. 7.4, the angular velocities for each particle were calculated. The exemplary result for an individual case is illustrated in the right plot of Fig. 7.1. The visualization of all 50 values may be found in Fig. 7.3. In the left-hand graph, the estimated angular velocities ω for each measurement are marked with black dots and show values roughly between $0.02\,\mathrm{ms}^{-1}$ and $0.42\,\mathrm{ms}^{-1}$. The averaged angular velocity, indicated by the

red line, is $\langle\omega\rangle = 0.090\,\mathrm{ms}^{-1}$. The maximal variance from the mean value is about $0.3\,\mathrm{ms}^{-1}$ which is about 3 times larger than the average value. In the majority of cases, the deviation only conducts values of less than $0.06\,\mathrm{ms}^{-1}$ such that the majority of the spheres spin with approx. the same angular velocity and extreme deviations from the mean angular velocity are relatively rare.

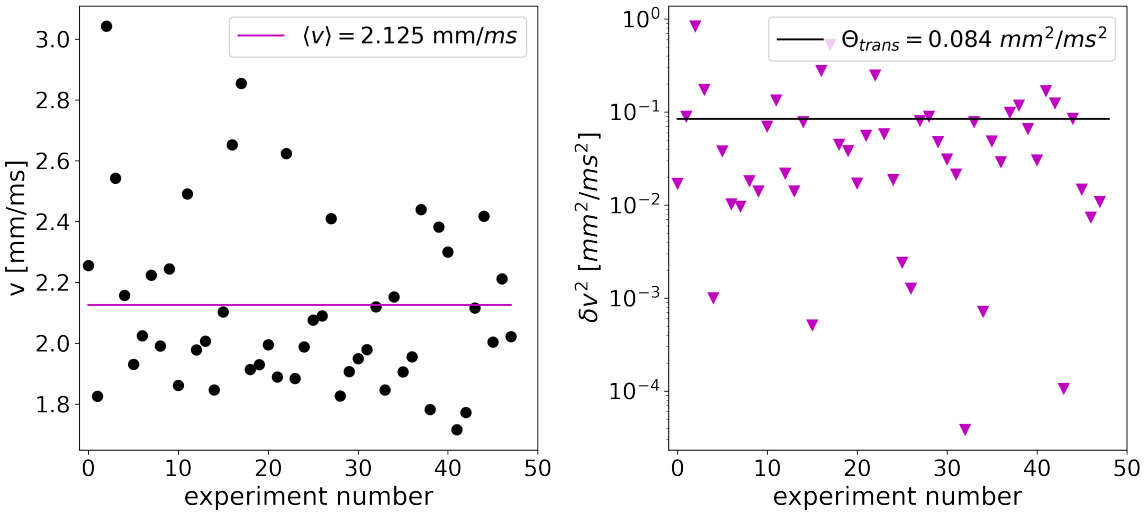

Figure 7.2.: The calculation of the translational granular temperature based on the obtained data in the hourglass-like experiment. The left panel shows the extracted translational velocities v for each of the 50 experiments as black dots. The velocity average $\langle v\rangle$ is obtained from those 50 individual experiments marked as purple line. The individual variance from the mean value δv^2 is presented as purple triangles in the plot to the right, from whose average value of the translational granular temperature Θ_{trans} may be directly determined. The translational granular temperature for this system is represented as black line in the graph on the right-hand side.

On the right side of Fig. 7.3, the squared variance of the angular velocities with respect to the mean value according to

$$\delta\omega^2 = (\omega - \langle\omega\rangle)^2 \tag{7.8}$$

is shown for each of the 50 experiments. The differing angular velocities may be the result of a varying number of collisions between the particle and the trunk wall of the

funnel. Due to the contact of the wall and a specific point on the particle's surface, the sphere will gain a torque that leads to rotation. Consequently, the rotational speed but also the direction of spin and thus the spin axis orientation will be changed with each collision. As soon as the particle leaves the funnel, no further torque promoting the particle rotation may be generated and only energy through translation may be gained. Depending on the number of the collisions in conjunction with the location of the touching points on the sphere's surface, the torques will add up and lead to fast spinning spheres or, if subsequent contact points are found on two opposite walls, they will partially cancel each other out.

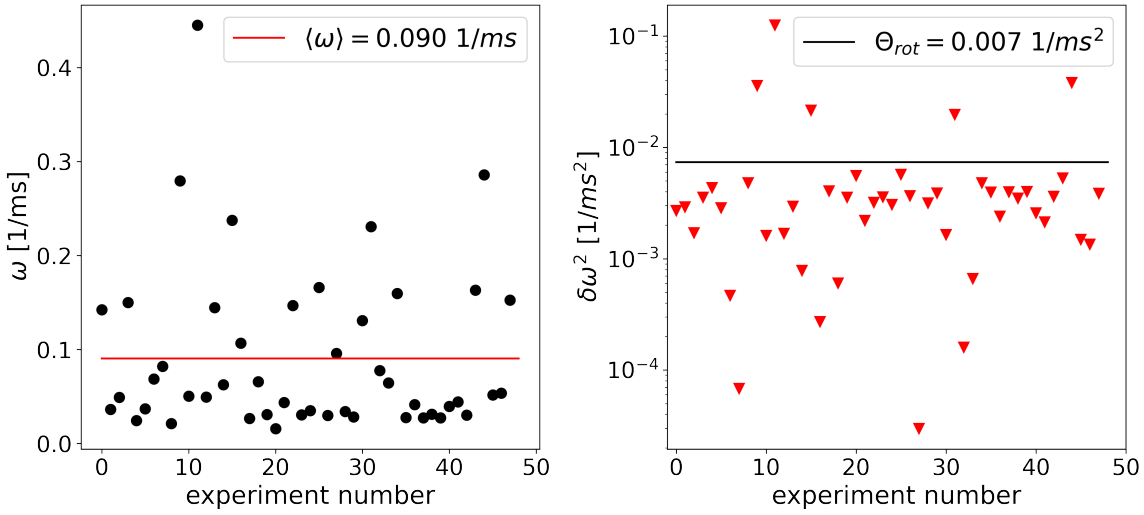

Figure 7.3.: The calculation of the rotational granular temperature based on the obtained data in the hourglass-like experiment. The left panel shows the extracted moduli of the angular velocities ω for each of the 50 experiments as black dots. The angular velocity average $\langle\omega\rangle$, obtained from those 50 individual experiments, is marked as red line. The individual variance from the mean value $\delta\omega^2$ is presented as red triangles in the plot to the right from whose average value of the rotational granular temperature Θ_{rot} may be directly determined. The rotational granular temperature for this system is represented as black line in the graph on the right-hand side.

The final step to provide a granular temperature for this system is to take the average of all variances $\delta\omega^2$ and use Eq. 7.5 to gain the systems granular temperature

$$\Theta_{\mathrm{rot}} = \langle\delta\omega^2\rangle. \tag{7.9}$$

Θ_{rot} is represented by the black line in the right panel of Fig. 7.3. The line symbolizes a value of $\Theta_{\mathrm{rot}} = 0.007\,\mathrm{ms}^{-2}$.

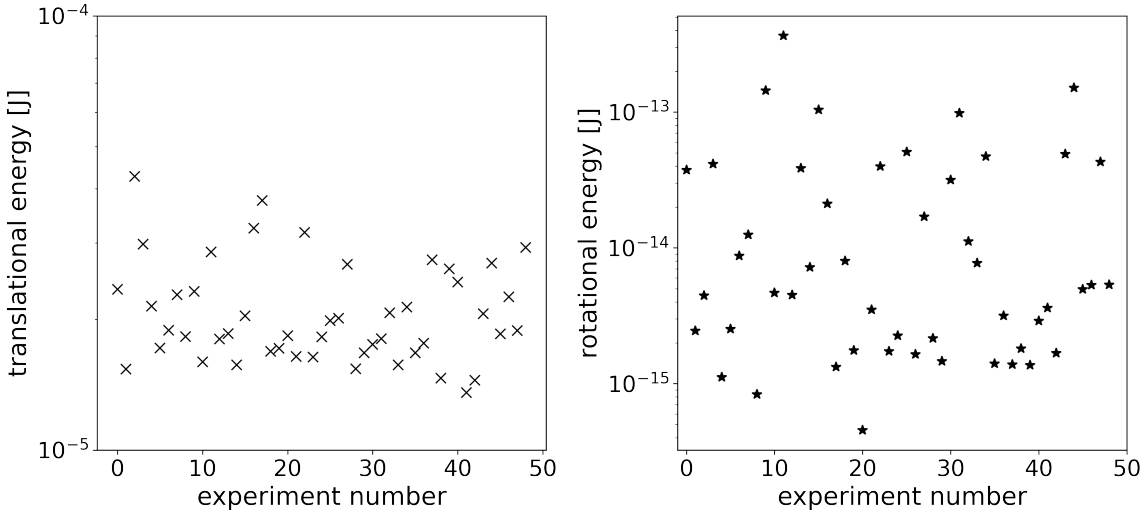

Figure 7.4.: The left panel shows the translational kinetic energy for all 50 particles that travelled through the laser beam. The values are presented on a logarithmic ordinate to provide a better comparison of the magnitudes with the values in the panel on the right. On the right-hand side, the rotational kinetic energy for each particle is represented on a logarithmic scale. All kinetic energies are given in Joule.

Granular gases are generally considered to be a non-equilibrium system where the equipartition of energies does not hold. In Fig. 7.4, the magnitudes of the translational and rotational kinetic energies were estimated with

$$E_{\mathrm{kin}} = \frac{m}{2}v^2 \tag{7.10}$$

$$E_{\mathrm{rot}} = \frac{I}{2}\omega^2 \tag{7.11}$$

in order to revise if the energy is equally distributed among the translational and rotational degrees of freedom. The values of the mass m and the moment of inertia I were taken from Ch. 6.1. Fig. 7.4 a) shows values of approx. 10^{-5} J for the translational kinetic energies of the particles whereas Fig. 7.4 b) provides values ranging from 10^{-15} J to 10^{-13} J such that both differ by orders of magnitudes. This great difference supports the concept that equipartition does not hold for the granular gas in this experiment.

7.4. Conclusion

The experiment performed above shows an idealized case of an hourglass-like system probed with DLS. An estimation of the translational and rotational granular temperature was attempted by determining the translational and rotational velocities of the particles. 50 particles passed the observation volume, one after another, such that the particles could be observed individually but also, theoretically, as group.

By using the method from Ch. 4, the translational velocity of a particle could be determined. The time for the observation volume transit was measured and used for the computation of the velocity. The translational granular temperature was then obtained by calculating the mean variation of a particle's velocity respective to the mean velocity of all particles.

The angular velocity of the particle, resulting from the particle's rotation, was estimated with the concept from Ch. 5. The rotational granular temperature was then identified by calculating the mean variance from the ensemble's mean angular velocity. However, the exact spin axis orientation of a probed particle is unknown. Thus, none of the in Ch. 5 discussed cases could be particularly selected to interpret the data. We assumed that all spin axis orientations, found in the plane that is spanned by the three basis vectors of the reference coordinate system, are equally probable and that the spin axis of the probed particle is found among those. Therefore, the average angular velocity, calculated from the three angular velocities obtained with the RPM expressions for the axes aligning with the corresponding basis vectors, was considered to approximate the angular velocity of the particle.

This is however just a first attempt of finding a solution to the actual problem. A more sophisticated solution for the determination of the correct axis is necessary. A first prospective ansatz may be to find further integral expressions in the scope of the RPM. The increased number of known axes would increase the accuracy of the estimation of the particle's spin axis orientation when averaging. Thus, a more reliable value for the angular velocity may be obtained.

From the respective velocity values, the translational and rotational kinetic energies

were estimated. The great difference in the order of magnitudes shows the absence of equipartition between the degrees of freedom for this system.

Finally, the procedure presented above is only applicable, if the solitariness of a particle in the observation volume is assured. If more than one particle would be present, as it is expected for usual hourglasses, the methodology would reach its limits, since inter-particle interference effects were excluded in the considerations. Sudden phase difference caused by directional changes of the flight trajectories or shape deformations due to inter-particle collisions would impede the analysis of the granular temperatures further. Also, the principle does yet only account for macroscopic rough spheres that comprise an inhomogeneous composition. An extension of the principle to multiple particle systems or to particles with shape or compositional variations may be motivated in future studies.

References

[1] C. T. Veje and P. Dimon. "The dynamics of granular flow in an hourglass". In: *Granular matter* 3 (2001), pp. 151–164.

8. Conclusion

8.1. Summary

The aim of this study was to investigate dynamic light scattering (DLS) on macroscopic particles, which exceed the wavelength of visible light ($\approx 500\,\mathrm{nm}$) by far. The particle sizes considered here are of the order of millimeters. Since a granular particle comprises such a large diameter, the particle may be assumed to be an agglomeration of many tiny scattering entities instead of only a single scattering entity. Thus, the complexity of only a single macroscopic particle is expected to cause a significant impact on the decay of the measured autocorrelation function (ACF) in DLS experiments. The particular subject here was to analyze how extensive a single granular particle affects the outcome of a DLS measurement and to investigate the consequent phenomenons, which may be read from the resulting autocorrelation function.

The data obtained in DLS experiments on single moving macroscopic particles showed that such a particle is indeed optically sufficiently complex, such that its motion will induce a full decay of the recorded autocorrelation function. Depending on the type of material and its optical properties, a late decay at the orders of several milliseconds as well as a decay at times of microseconds were recorded.

The late decay was noted for every tested homogeneous particle, independent of the material it is composed of. The decorrelation occurs due to the number fluctuations in the observation volume, i.e. the particle being present or absent, cf. Ch. 4. The sudden presence of a scatterer causes a significant sudden increase in the recorded intensity. The analysis of the intensity signal showed that its shape may be approached by a trapezoidal function. The flanks refer then to the particle's entrance and exit in

the observation volume, respectively, and the plateau gives the period of the entirely illuminated particle travelling through the laser beam. The translational velocity of the particle may then be determined from the trapezoid's plateau width, if the beam diameter is known. The analytic form of the calculated autocorrelation function of a trapezoid signal agrees well with the shape of the recorded late decay such that the shape of the late decay may be attributed to the translational motion of the particle passing through the observation volume.

The contribution from the number fluctuations was then successfully separated from the early decay of the ACF. The isolation of the contributions permits to analyze the decay at early times without effects of the particle's translational motion.

The ACF's early decay is caused by the motion of the particle's surface entities respective to its barycenter, here the rotation of the sphere. Depending on the configuration and number of scattering entities on the surface, which will vary with the particle's material, the shape as well as the decorrelation time of this ACF segment will differ. The roughness of the surface is thereby decisive. Examples for a rough, a reflecting and transparent particles were presented. A pure, smooth and transparent particle ("ideal scatterer") does not possess such a decay at early times, whereas an opaque, rough particle shows a distinct early decay. An ideal scatterer may be used to observe particle translation only. Thus, the focus of further studies in this thesis lay on such diffusive scattering particles.

In order to understand the scattering process on the surface of a diffusive scattering particle, and to interpret the obtained ACF properly, the rough particle model (RPM) was developed (see Ch. 5). The model sums up all scattering contributions of all scattering surface entities in the region of interest. The model comprises a Gaussian distribution as amplitude term to simulate a realistic brightness distribution on the surface. The functional form of the phase term was derived by considering the phase shifts in the scattered light from each relevant surface element in consideration of the particle rotation. The RPM provides an estimation of the angular velocity of the spinning particle in dependence on the geometric orientation of the spin axis. Model predictions were provided by varying the significant parameters of particle radius, angular velocity and width of the brightness distribution to show the range of the model's applicability.

In conclusion, the distribution of the tangential velocities of the surface elements is the dynamical property defining the time-scales on which the autocorrelation function decays.

A particular scenario of the RPM was tested experimentally (see Ch. 6). The obtained DLS data, and consequently the results for the angular velocity, were verified by particle image velocimetry (PIV) on images recorded with a high-speed camera. The estimated angular velocities from both methods agree within an estimated error of 5%. Thus, the RPM from Ch. 5 is considered to be reliable.

At last, all presented principles were tested in an experiment in which the translational and rotational velocities could be measured, cf. Ch. 7. The measurement procedure resembles an idealized case of grains running through hourglass' neck. The respective granular temperatures were determined from the estimated translational and rotational velocities. Since the amount of kinetic energy hidden in the translational and rotational motion differ in orders of magnitude, the equipartition theorem may be considered to be invalid here, as expected for non-equilibrium systems.

Overall, the most important lesson learned, with the DLS experiments performed on macroscopic particles, is that the decays of the autocorrelation function for such particles are not only triggered by the relative motion of the particles with respect to each other, as assumed for particles with $d \leq \lambda$, but that simply the presence of a single moving granular particle induces at least one distinct decay. If the particle is sufficiently rough or exhibits other inhomogeneities as shape variations or complex internal structures, motions like rotation, vibration or temporal deformations produce a full decay on early time scales. The insights gained by considering light scattering on macroscopic particles as light scattering on surfaces, constituting an ensemble of scattering surface entities, may be used to further build on in the future for a more comprehensive understanding of the particular scattering processes on granular media. First ideas will be shared in the subsequent section.

8.2. Outlook

A classical granular particle possess some surface roughness, may comprise an irregular shape including surface asperities and may also have impurities of other matter. We initially decreased its complexity in the presented experiments to the most ideal case and then increased the complexity again step by step. By considering ball lenses, we started with a transparent, spherical particle that has a smooth surface and no complex internal structure such that only the particle's translation is observable with DLS. When performing experiments with optically diffusive particles, the complexity was increased by investigating spherical granular particles that possess a significant surface roughness. Consequently, effects linked to the particle rotation appeared in the DLS data. Thus, the selection of a more irregular particle shape may be the next step. As a start, ellipsoidal particles may be investigated. By having three symmetry axes, ellipsoids are more complex than spheres but possess a regular shape though, such that scattering processes still remain predictable with the current state of knowledge [1]. If rough ellipsoids are to be investigated with help of the RPM, more comprehensive expressions for the axes orientations must be formulated by e.g. taking the average of many more than only three possible axis orientations. This model improvement may already be profitable when one is still investigating spheres. After successful investigations, the shapes may become even more irregular to approximate a real granular particle further.

The RPM was discussed for homogeneous, diffusive scattering spheres. Within our experiments, we also tested reflecting spheres as well as transparent spheres whose scattering abilities differ from fully diffusive scattering particles. Thus, similar concepts for DLS on those particles have to be established, respecting the differing scattering abilities. In case of the reflecting particles, the amplitude term in the field autocorrelation function could easily be changed to a very narrow Gaussian spot by adjusting the spot width. The adaptation of the phase term may be more challenging since other considerations about the contributing light paths are necessary, e.g. the increased portion of specular reflections in the scattered light. The expression for the field autocorrelation function of a transparent particle may then emerge as case of scattering in a small number of points on the spheres mantle. Supposedly, reflective scattering will be the

dominant scattering mechanism.

Granular particles however do not occur solitarily in nature but in a bulk. Therefore, another aim is to extend the concept of the RPM to a multiple particle scenario. First, the effect of the translational motion of many particles in one system should be observed. A suitable method would be to prepare a fluidized bed with ideal scatterers. DLS measurements on such a fluidized bed containing those particles would give insight not only on the number fluctuations but also on the interference effects of the scattered light as stated by Berne and Pecora [1]. In the beginning, the amount of scatterers in the fluidized bed should be little such that the particles will not tend collide. Collisions would lead to faults on the particle surface and thus to a distinct surface roughness. Those surface roughnesses would then again cause a detectable motion of the surface entities. Also, the effects of number fluctuations and interference effects may superpose in the recorded autocorrelation function. In order to analyze only the interference effects of two particles or more, experiments in microgravity may be of interest. If driven by external forces, the particles will change their location but a fluctuating number of particles in the observation volume could be avoided. The complexity of the system may then be increased again by using rough particles to gain a more comprehensive understanding of how the individual particle motions, but also bulk motions, in a fluidized bed may be analyzed with DLS with help of the here presented methodology.

References

[1] B. J. Berne and R. Pecora. *Dynamic light scattering: with applications to chemistry, biology, and physics*. Courier Corporation, 2000.

Appendices

A. DLS data from particles rolling down an inclined plane

In this chapter, additional dynamic light scattering data to the experiment performed in Ch. 6.2 is provided. The data was obtained by observing a single rough particle passing through the observation volume after rolling down an inclined plane.

The particles started from different start levels on the inclined plane to generate spinning spheres with distinct angular velocities. For each start level, several runs were performed to show the reproducibility of the generated angular velocities for a specific start level. The respective data sets are systematically sorted from a low start level (h2) to the highest start level (h6). The points in the figures below indicate the measured auto-correlation function's (ACF). The left panel in each plot show the ACFs at late times, the right panels give information about the early decays of the ACFs. The data was fitted with the respective analytic expression for the decay, cf. Chs. 4 and 5, indicated by the colored lines.

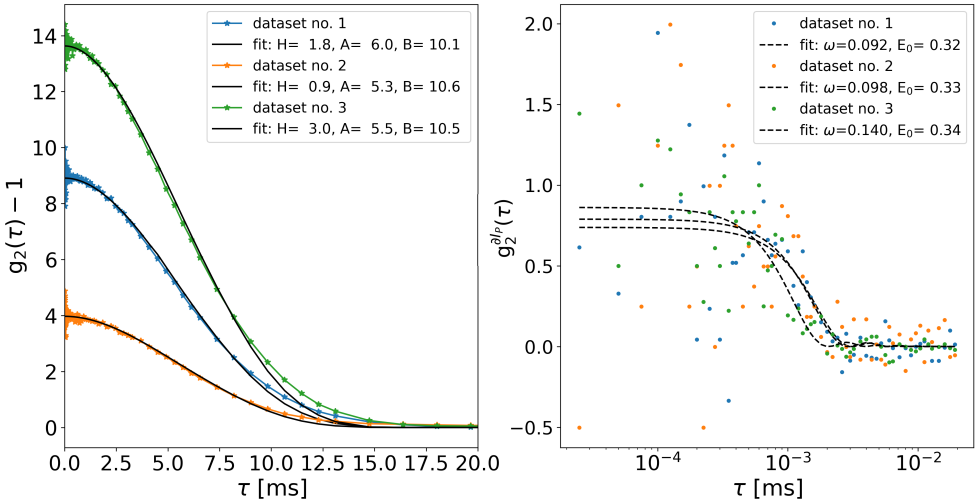

Figure A.1.: The fitting of autocorrelation functions of a rotating PTFE sphere passing through a laser beam. In all cases, the particle starts from position h2 in the tube. The left plot shows the late decays on linear time scales which are fitted by the autocorrelation function of a trapezoid. The right plot shows the fitting of the data from the early decays $g_2^{\partial I_P}(\tau)$ on logarithmic time scales with the corresponding function from the RPM (cf. 5.2.3.2). The fit parameters for both decays are denoted in the respective legend.

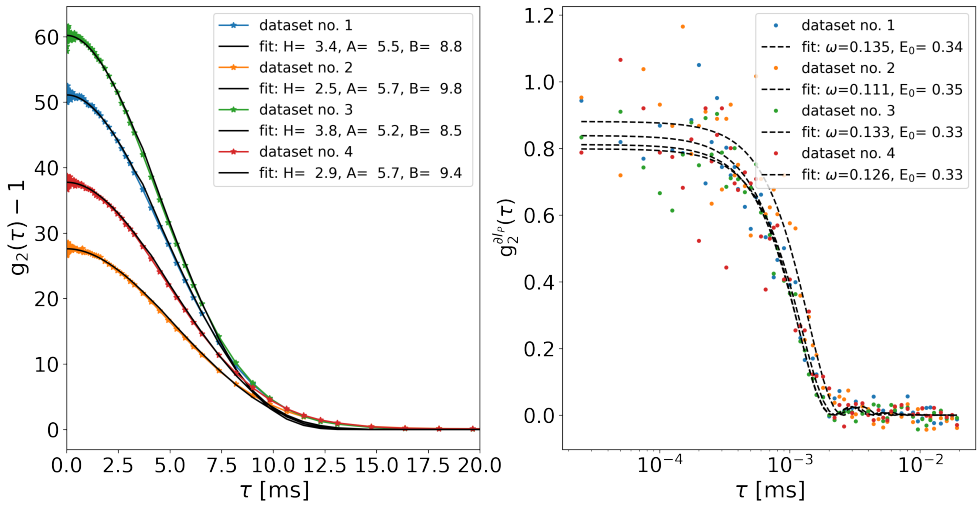

Figure A.2.: The fitting of autocorrelation functions of a rotating PTFE sphere passing through a laser beam. In all cases, the particle starts from position h3 in the tube. The left plot shows the late decays on linear time scales which are fitted by the autocorrelation function of a trapezoid. The right plot shows the fitting of the data from the early decays $g_2^{\partial I_P}(\tau)$ on logarithmic time scales with the corresponding function from the RPM (cf. 5.2.3.2). The fit parameters for both decays are denoted in the respective legend.

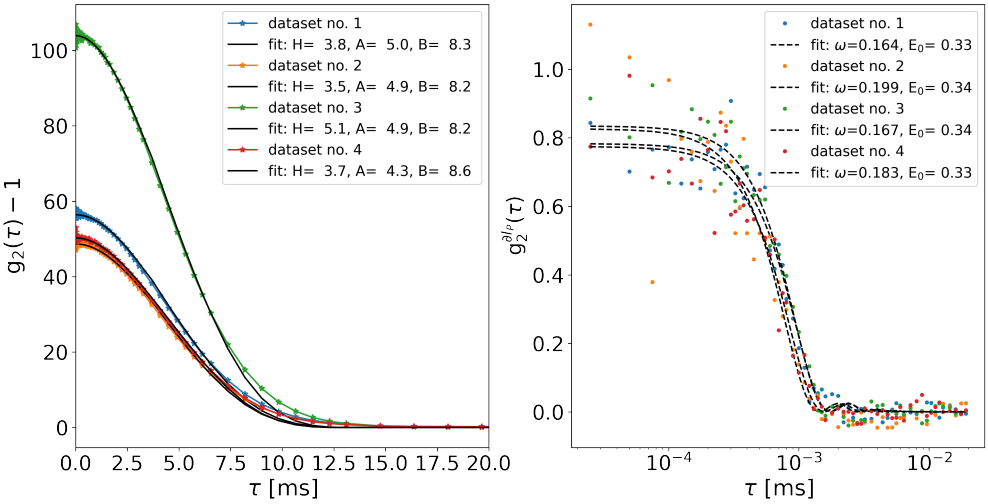

Figure A.3.: The fitting of autocorrelation functions of a rotating PTFE sphere passing through a laser beam. In all cases, the particle starts from position h5 in the tube. The left plot shows the late decays on linear time scales which are fitted by the autocorrelation function of a trapezoid. The right plot shows the fitting of the data from the early decays $g_2^{\partial I_P}(\tau)$ on logarithmic time scales with the corresponding function from the RPM (cf. 5.2.3.2). The fit parameters for both decays are denoted in the respective legend.

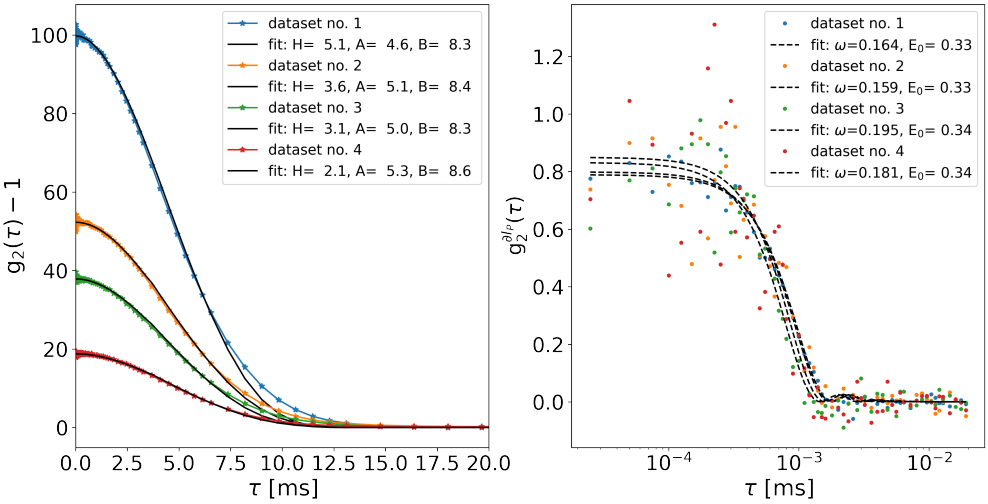

Figure A.4.: The fitting of autocorrelation functions of a rotating PTFE sphere passing through a laser beam. In all cases, the particle starts from position h6 in the tube. The left plot shows the late decays on linear time scales which are fitted by the autocorrelation function of a trapezoid. The right plot shows the fitting of the data from the early decays $g_2^{\partial I_P}(\tau)$ on logarithmic time scales with the corresponding function from the RPM (cf. 5.2.3.2). The fit parameters for both decays are denoted in the respective legend.

B. Results from PIV analysis for all start positions

Here, additional data from the PIV analysis from Ch. 6.3 is provided. The order of the plots below is given from the lowest start level (h2) to the highest start level (h6). The data was obtained by observing a single rough particle passing through the observation volume after rolling down an inclined plane with a high-speed camera. The motion of the features on the rotating sphere were then tracked with the "PIV"-PlugIn of the image processing software ImageJ. The obtained data is visualized by the blue dots. A regression line was used to find the sphere's angular velocity ω.

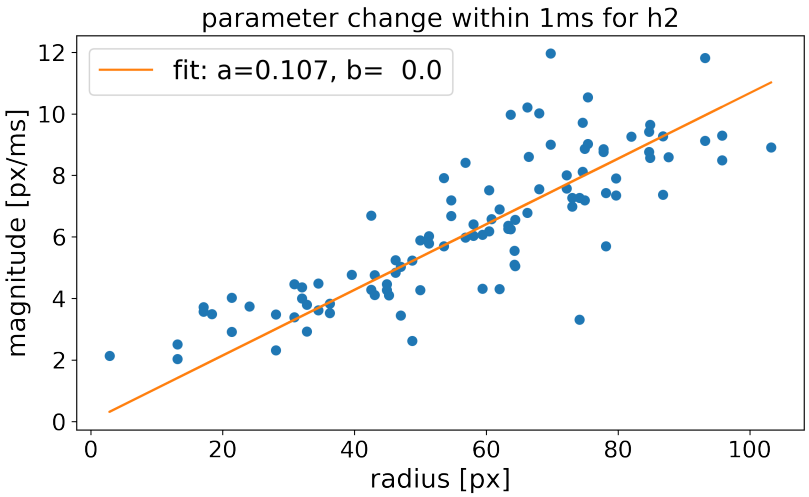

Figure B.1.: The tangential velocities v in $\frac{\text{px}}{\text{ms}}$ in dependence of the feature's distance r to the center of the photo. The values were obtained by using the PIV method for the case of the sphere starting at level h2. The dots represent the data whereas the linear graph illustrates the linear regression fit of the form $v = a \cdot r + b$ to determine the angular velocity of the particle.

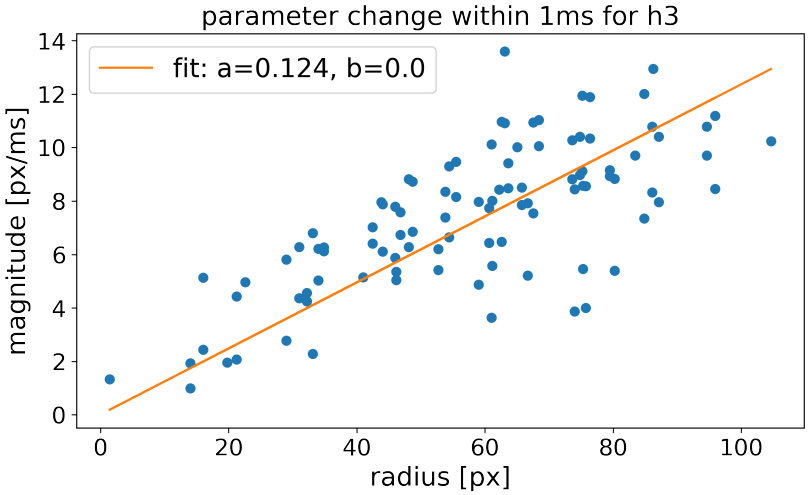

Figure B.2.: The tangential velocities v in $\frac{\text{px}}{\text{ms}}$ in dependence of the feature's distance r to the center of the photo. The values were obtained by using the PIV method for the case of the sphere starting at level h3. The dots represent the data whereas the linear graph illustrates the linear regression fit of the form $v = a \cdot r + b$ to determine the angular velocity of the particle.

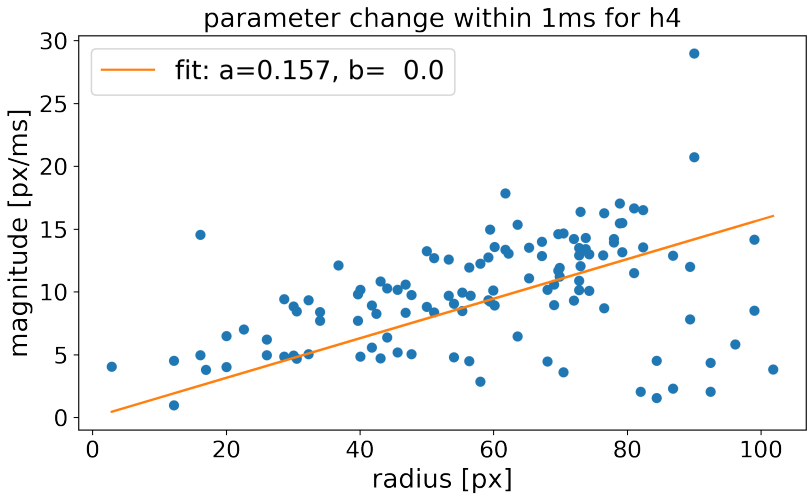

Figure B.3.: The tangential velocities v in $\frac{\text{px}}{\text{ms}}$ in dependence of the feature's distance r to the center of the photo. The values were obtained by using the PIV method for the case of the sphere starting at level h4. The dots represent the data whereas the linear graph illustrates the linear regression fit of the form $v = a \cdot r + b$ to determine the angular velocity of the particle.

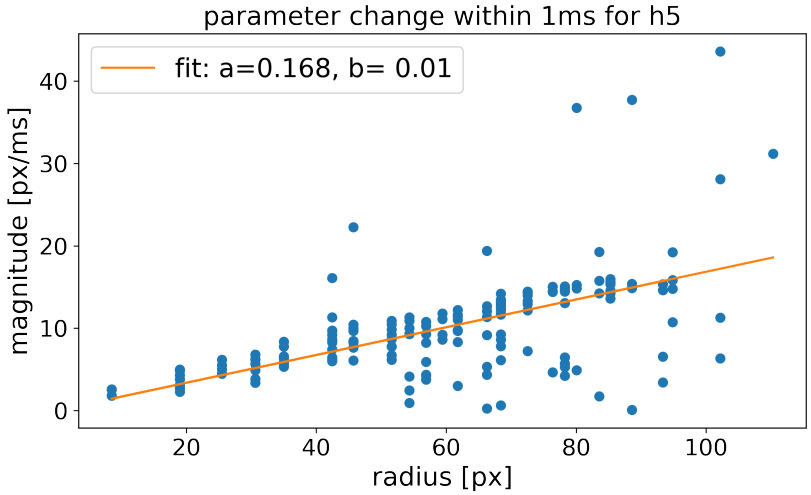

Figure B.4.: The tangential velocities v in $\frac{\text{px}}{\text{ms}}$ in dependence of the feature's distance r to the center of the photo. The values were obtained by using the PIV method for the case of the sphere starting at level h5. The dots represent the data whereas the linear graph illustrates the linear regression fit of the form $v = a \cdot r + b$ to determine the angular velocity of the particle.

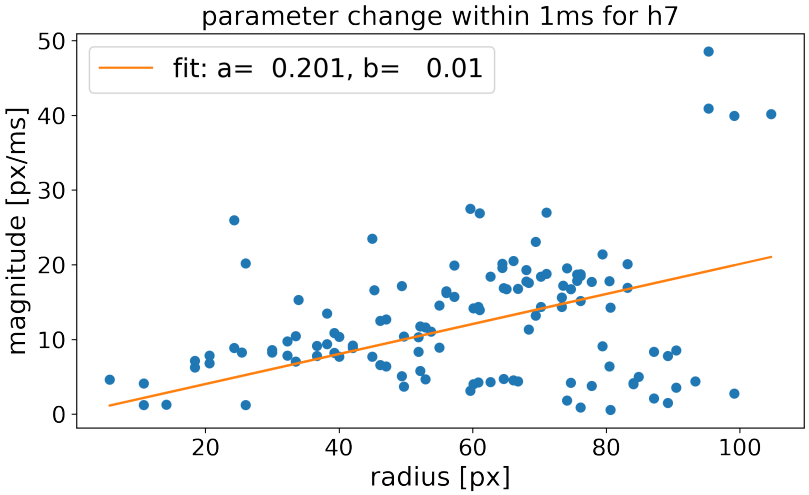

Figure B.5.: The tangential velocities v in $\frac{\text{px}}{\text{ms}}$ in dependence of the feature's distance r to the center of the photo. The values were obtained by using the PIV method for the case of the sphere starting at level h7. The dots represent the data whereas the linear graph illustrates the linear regression fit of the form $v = a \cdot r + b$ to determine the angular velocity of the particle.

List of Figures

Danksagungen

Bei der Erstellung dieser Doktorarbeit wurde ich über die Jahre hinweg von vielen Menschen unterstützt, bei denen ich mich an dieser Stelle bedanken möchte.

Allen voran möchte ich mich bei meinem Doktorvater Prof. Dr. Matthias Sperl für die Möglichkeit bedanken, diese Arbeit anfertigen zu dürfen und somit weitere Erfahrungen in der Forschung sammeln zu können. Ich möchte mich auch für das entgegengebrachte Vertrauen bedanken, mich für meine Doktorarbeit von den bisherigen erlernten Fachgebieten zu lösen und mich einer, für mich, komplett neuen Thematik stellen zu dürfen.

Meinem Prüfungskomitee bestehend aus Prof. Dr. Matthias Sperl, Prof. Dr. Barbara Milow und Prof. Dr. Stephan Schlemmer möchte ich dafür danken, dass sie sich der Aufgabe angenommen haben meine Arbeit zu bewerten. Besonders hervorheben möchte ich meine Wertschätzung gegenüber Prof. Dr. Barbara Milow, die sich der Aufgabe, meine Arbeit zu begutachten, sehr kurzfristig angenommen hat.

Ein besonderer Dank gilt Dr. Philip Born für die ausgezeichnete Betreuung bei der Umsetzung der gesamten Arbeit. Durch die entgegengebrachte Geduld, Hilfsbereitschaft und Begeisterung für die Thematik wurde ich stark motiviert und konnte stetig an der Aufgabe wachsen. Durch Diskussionen über Grundlagen, sowie komplexeren Themen, habe ich mein Wissen stetig erweitern können.

Für die Unterstützung bei der Bildbearbeitung besonders schwierigere Fälle, der Wortfindungsstörungen während des Schreibprozesses, sowie der Geduld und Unterstützung während der Anfertigung dieser Arbeit möchte ich mich bei meinem Ehemann Mirko Tim Künstler herzlich bedanken. Insbesondere in der Schlussphase der Promotion hat

er mich emotional gestärkt.

Bei meinen Kollegen Dr. Philip Born und Dr. Wolf Till Kranz möchte ich mich bedanken, dass sie sich die Zeit nahmen, meine Arbeit korrekturzulesen und mir wertvolle Tipps bei der Anfertigung gaben. Maximilian Thienel möchte ich ebenfalls für die Unterstützung danken.

Ich möchte mich für sehr fruchtbare Diskussion während des gesamten Prozesses bedanken bei Dr. Philip Born, Raphael Kessler, Dr. Wolf Till Kranz und Ya-Chun Wang.

Bei Ya-Chun Wang und Dr. Olivier Coquand möchte ich mich für eine stets sehr angenehme Büroatmosphäre, sowie fachlichen aber auch privaten Austäuschen bedanken. Für ein stets angenehmes Arbeitsklima bedanke ich mich bei der gesamten Arbeitsgruppe.

Für die sehr spontanen technischen Unterstützungen durch Konstruktionen nach Maß und die damit einhergehende Erleichterung beim Experimentieren möchte ich mich bei Raphael Kessler und dem Werkstatt-Team des Instituts für Materialphysik im Weltraum am Deutschen Zentrum für Luft- und Raumfahrt in Köln bedanken.

Ich möchte mich weiterhin bei meinen stets motivierten Praktikanten, die ich während meiner Forschungszeit betreuen durfte, Henk Hustadt und Ema Salugova, bedanken. Durch ihre kompetente Unterstützung bei Laborversuchen und der Datenauswertung wurden viele zielführende Erkenntnisse gewonnen.

Für die liebevolle Unterstützung während meiner Kindheit, meines Studiums und der anschließenden Doktorarbeit, die nicht nur finanzieller Natur war, sondern auch aus Geduld und essentiellen Ermutigungen bestand, möchte ich mich bei meinen Eltern Ilian und Katrin Dossow ganz herzlich bedanken.

Erklärung zur Dissertation
gemäß der Promotionsordnung vom 12. März 2020

Diese Erklärung muss in der Dissertation enthalten sein.
(This version must be included in the doctoral thesis)

„Hiermit versichere ich an Eides statt, dass ich die vorliegende Dissertation selbstständig und ohne die Benutzung anderer als der angegebenen Hilfsmittel und Literatur angefertigt habe. Alle Stellen, die wörtlich oder sinngemäß aus veröffentlichten und nicht veröffentlichten Werken dem Wortlaut oder dem Sinn nach entnommen wurden, sind als solche kenntlich gemacht. Ich versichere an Eides statt, dass diese Dissertation noch keiner anderen Fakultät oder Universität zur Prüfung vorgelegen hat; dass sie - abgesehen von unten angegebenen Teilpublikationen und eingebundenen Artikeln und Manuskripten - noch nicht veröffentlicht worden ist sowie, dass ich eine Veröffentlichung der Dissertation vor Abschluss der Promotion nicht ohne Genehmigung des Promotionsausschusses vornehmen werde. Die Bestimmungen dieser Ordnung sind mir bekannt. Darüber hinaus erkläre ich hiermit, dass ich die Ordnung zur Sicherung guter wissenschaftlicher Praxis und zum Umgang mit wissenschaftlichem Fehlverhalten der Universität zu Köln gelesen und sie bei der Durchführung der Dissertation zugrundeliegenden Arbeiten und der schriftlich verfassten Dissertation beachtet habe und verpflichte mich hiermit, die dort genannten Vorgaben bei allen wissenschaftlichen Tätigkeiten zu beachten und umzusetzen. Ich versichere, dass die eingereichte elektronische Fassung der eingereichten Druckfassung vollständig entspricht."

Teilpublikationen:

Dossow, L., Kessler, R., Sperl, M., & Born, P. (2021). *Dynamic light scattering from single macroscopic particles.* Applied Optics, 60(32), 10160-10167.

Köln, den 30.01.2023, Lisa Künstler

Erklärung zum Gesuch um Zulassung zur Promotion
gemäß der Promotionsordnung vom 12. März 2020

1. Zugänglichkeit von Daten und Materialien

Die Dissertation beinhaltet die Gewinnung von Primärdaten oder die Analyse solcher Daten oder die Reproduzierbarkeit der in der Dissertation dargestellten Ergebnisse setzt die Verfügbarkeit von Datenanalysen, Versuchsprotokollen oder Probenmaterial voraus.

- ☐ Trifft nicht zu.
- ☑ Trifft zu.
  In der Dissertation ist dargelegt wie diese Daten und Materialien gesichert und zugänglich sind (entsprechend den Vorgaben des Fachgebiets beziehungsweise der Betreuerin oder des Betreuers).

2. Frühere Promotionsverfahren

Ich habe bereits einen Doktortitel erworben oder ehrenhalber verliehen bekommen.
Oder: Für mich ist an einer anderen Fakultät oder Universität ein Promotionsverfahren eröffnet worden, aber noch nicht abgeschlossen.
Oder: Ich bin in einem Promotionsverfahren gescheitert.

- ☑ Trifft nicht zu.
- ☐ Trifft zu.

3. Straftat

Ich bin nicht zu einer vorsätzlichen Straftat verurteilt worden, bei deren Vorbereitung oder Begehung der Status einer Doktorandin oder eines Doktoranden missbraucht wurde.

Ich versichere, alle Angaben wahrheitsgemäß gemacht zu haben.

30.01.2023 Lisa Künstler